

ULTRA-HIGH PRECISION MACHINING OF CONTACT LENS POLYMERS

OLUFAYO, OLUWOLE AYODEJI
(s210026162)

2015

COPYRIGHT STATEMENT

The copy of this thesis has been supplied on condition that anyone who consults it understands and recognises that its copyright rests with the Nelson Mandela Metropolitan University and that no information derived from it may be published without the author's prior consent, unless correctly referenced.

ULTRA-HIGH PRECISION MACHINING OF CONTACT
LENS POLYMERS

By

Olufayo, Oluwole Ayodeji

Submitted in fulfilment/partial fulfilment of the requirements for the
degree of Doctor of Philosophy: Engineering: Mechatronics at the
Nelson Mandela Metropolitan University

July 2015

Promoter/Supervisor: Prof. Khaled Abou-El-Hossein

DECLARATION

I, *Oluwole Ayodeji OLLUFAYO & s210026162*, hereby declare that the *treatise/ dissertation/ thesis* for *Students qualification to be awarded* is my own work and that it has not previously been submitted for assessment or completion of any postgraduate qualification to another University or for another qualification.

.....

Official use:

In accordance with Rule G5.6.3,

5.6.3 A treatise/dissertation/thesis must be accompanied by a written declaration on the part of the candidate to the effect that it is his/her own work and that it has not previously been submitted for assessment to another University or for another qualification. However, material from publications by the candidate may be embodied in a treatise/dissertation/thesis.

ACKNOWLEDGEMENTS

Unto the Lord be the glory, honour and adoration for his infinite mercies and favour upon my life.

Sincere gratitude and appreciation go to my promoter, Prof Khaled Abou-El-Hossein, for his support and guidance through the period of study.

I would also like to acknowledge the Technology Innovation Agency /Department of Science and Technology of South Africa, National Research Foundation of South Africa (NRF) and Research Capacity development of NMMU for the financial support provided for this research.

Special gratitude also goes to my parents, Prof. and Dr (Mrs) Olufayo, who have instilled in me a deep love for the academics. You encouraged me to be an engineer like you. Thank you dad! To my big auntie, Prof (Mrs) Esther Titilayo Akinlabi, I say a big “Thank you”, for your support and mentorship. Also, my appreciation goes to my uncle Mr Akinlabi, my nephew and niece; Akinkunmi, and Stephanie, I also thank Dr and Mrs F. A. Emuze, Dr and Mrs K. A. Olowu, Mrs Olutobi, Liliane Creppy, Mr. Emmanuel Oyeyemi and my dear sister Mrs. Motunrayo Oyeyemi. Special thanks also to my one love and best friend, Samira, who believed in me though this period of my studies.

I remain grateful to all my friends, colleagues; Timothy Otieno, John Fernandes, Ikho Bambiso, Dr. Michael Ayomoh and Munir Kadernani who have supported me in many ways through this period of study. Further thanks go to Prof. Theo van Niekerk and members of AMTC / Siemens who have been of great support throughout my time at the Nelson Mandela Metropolitan University. Thank you.

ABSTRACT

Ultra-High Precision Machining of Contact Lens Polymers

Olufayo, O. A.

Faculty of Engineering, the Built Environment and Information Technology

P.O. Box 77000, Nelson Mandela Metropolitan University,

Port Elizabeth, South Africa

July, 2015

Contact lens manufacture requires a high level of accuracy and surface integrity in the range of a few nanometres. Amidst numerous optical manufacturing techniques, single-point diamond turning is widely employed in the making of contact lenses due to its capability of producing optical surfaces of complex shapes and nanometric accuracy. For process optimisation, it is ideal to assess the effects of various conditions and also establish their relationships with the surface finish. Presently, there is little information available on the performance of single point diamond turning when machining contact lens polymers. Therefore, the research work undertaken herewith is aimed at testing known facts in contact lens diamond turning and investigating the performance of ultra-high precision manufacturing of contact lens polymers.

Experimental tests were conducted on Roflufocon E, which is a commercially available contact lens polymer and on Precitech Nanoform Ultra-grind 250 precision machining. Tests were performed at varying cutting feeds, speed and depth of cut. Initial experimental tests investigated the influence of process factors affecting surface finish in the UHPM of lenses. The acquired data were statistically analysed using Response Surface Method (RSM) to create a model of the process. Subsequently, a model which uses Runge-Kutta's fourth order non-linear finite series scheme was developed and adapted to deduce the force occurring at the tool tip. These forces were also statistically analysed and modelled to also predict the effects process factors have on cutting force. Further experimental tests were aimed at establishing the presence of the triboelectric wear phenomena occurring during polymer machining and identifying the most influential process factors.

Results indicate that feed rate is a significant factor in the generation of high optical surface quality. In addition, the depth of cut was identified as a significant factor in the generation of low surface roughness in lenses. The influence some of these process factors had was notably linked to triboelectric effects. This tribological effect was generated from the continuous rubbing action of magnetised chips on the cutting tool. This further stresses the presence of high static charging during cutting. Moderately humid cutting conditions presented an adequate means for static charge control and displayed improved surface finishes. In all experimental tests, the feed rate was identified as the most significant factor within the range of cutting parameters employed.

Hence, the results validated the fact that feed rate had a high influence in polymer machining. The work also established the relationship on how surface roughness of an optical lens responded to monitoring signals and parameters such as force, feed, speed and depth of cut during machining and it generated models for prediction of surface finishes and appropriate selection of parameters. Furthermore, the study provides a molecular simulation analysis for validating observed conditions occurring at the nanometric scale in polymer machining. This is novel in molecular polymer modelling.

The outcome of this research has contributed significantly to the body of knowledge and has provided basic information in the area of precision manufacturing of optical components of high surface integrity such as contact lenses. The application of the research findings presented here cuts across various fields such as medicine, semi-conductors, aerospace, defence, telecom, lasers, instrumentation and life sciences.

TABLE OF CONTENTS

ACKNOWLEDGEMENTS	V
ABSTRACT	VI
TABLE OF CONTENTS	VIII
ABBREVIATIONS	XII
NOMENCLATURE	XIII
LIST OF TABLES	XIV
LIST OF FIGURES	XVI
GLOSSARY OF TERMS	XXI
CHAPTER 1 INTRODUCTION	1
1.1 Preamble.....	1
1.2 The general concept for the study.....	1
1.3 Optical manufacturing techniques for contact lenses	2
1.4 Significance of the study	4
1.5 Problem statement	4
1.6 Research aim and objective	5
1.7 The hypothesis statement	6
1.8 Research scope	6
1.9 Structure of the thesis	7
CHAPTER 2 LITERATURE REVIEW	8
2.1 Introduction	8
2.2 Eye polymer optics.....	8
2.3 Contact lenses and their materials	10
2.3.1 Classes of polymers used in medicine	13
2.3.2 Fabrication of contact lenses	15
2.3.3 Commercially available contact lens materials	17
2.4 Manufacturing of contact lenses.....	20
2.4.1 Spin casting	21
2.4.2 Plastic injection moulding	22
2.4.3 Ultra high precision machining technique	24
2.4.4 Research & barriers in the ultra-high precision manufacturing of polymers	28

2.4.4.1	Elastic recovery in polymer machining	29
2.4.4.2	Diamond wear in polymer machining	30
2.4.4.3	Tribo-chemical wear in polymer machining	30
2.4.4.4	Triboelectric wear in polymer machining	33
2.5	General behaviour of polymers in diamond machining	39
2.5.1	Parameters to evaluate surface roughness	42
2.6	Modelling of ultra-high precision machined polymers.....	43
2.6.1	Response surface method.....	43
2.6.1.1	Box-Behnken response surface method	44
2.6.2	Atomistic Simulation methods.....	45
2.6.3	Molecular Dynamics (MD) Simulation method.....	46
2.6.4	MD simulation of machining operations	48
2.6.5	MD simulation in polymer machining	50
2.6.5.1	Principles of MD simulation and model	51
2.6.5.2	Some potential energy functions in MD simulations.....	53
2.7	Summary.....	56
 CHAPTER 3 MOLECULAR DYNAMICS SIMULATION OF POLYMERS.....		57
3.1	Introduction	57
3.2	Molecular properties of Roflufocon E lens.....	58
3.3	Molecular structure of contact lens polymers	59
3.4	Use of MD in nanomachining simulation	63
3.5	Methodology of MD simulation of Polymer nanomachining.....	65
3.5.1	Pre-processing and export of molecular structure	66
3.5.2	Main MD processing	68
3.5.3	Post processing and visualisation.....	68
3.6	Molecular Dynamics (MD) constituent parts.....	69
3.6.1	System configuration	69
3.6.2	The workpiece	70
3.6.3	The tool.....	71
3.7	General overview of MD simulation conditions.....	72
3.7.1	Initialization.....	72
3.7.2	Boundary conditions	72
3.7.3	Relaxation of the system	74
3.7.4	Potential energy function	74
3.7.5	Scope of the simulation	76

CHAPTER 4	EXPERIMENTAL PROCEDURES.....	77
4.1	Introduction	77
4.2	Experimental setup	78
4.3	Workpiece	81
4.4	Diamond tool.....	82
4.5	Surface finish measurements (Atomic Force microscopy)	83
4.6	Cutting force measurements	86
4.6.1	Measurement instruments	86
4.6.2	Cutting mechanics	87
4.7	Electrostatic discharge measurements	90
4.7.1	Electrostatic sensor	91
4.7.2	Electrostatic humidity procedure.....	93
CHAPTER 5	RESULTS AND DISCUSSION	94
5.1	Statistical evaluation of factors affecting surface finish of contact lens polymers	94
5.1.1	Theoretical value to surface finish	95
5.1.2	Determination of appropriate polynomial equation to represent RSM model	102
5.1.2.1	ANOVA analysis of the response surface quadratic model for surface roughness.....	104
5.1.2.2	Determination of significant factors influencing surface roughness	106
5.1.3	Analysis of cutting chips	110
5.1.3.1	The influence of rake angle on material properties of the workpiece	117
5.1.3.2	The influence of cutting parameters on material properties of the workpiece	118
5.1.4	Experimental observations of factors affecting surface finish	119
5.1.5	Summary of results.....	121
5.2	Predictive modelling of cutting force at the tool tip	123
5.2.1	Summary of results.....	128
5.3	Predictive modelling of cutting force and the influence of cutting parameters	128
5.3.1	Summary of results.....	134
5.4	Statistical evaluation of triboelectricity.....	135
5.4.1	Analysis for triboelectric phenomenon at 60% relative humidity	135
5.4.2	Analysis for triboelectric phenomenon at 40% relative humidity	147

5.4.3	Analysis for triboelectric phenomenon at 20% relative humidity	159
5.4.4	Modelling summary	163
5.4.5	Conclusion and physics of the triboelectric phenomenon	164
5.4.6	Summary of results.....	165
5.5	Molecular modelling overview of polymer nanomachining	166
5.5.1	Introduction.....	166
5.5.2	Thermodynamic information analysis	166
5.5.3	Comparison of various potentials between tool and workpiece	169
5.5.4	Correlation of MD results to machining conditions.....	175
5.5.5	Summary	180
CONCLUSION		181
RECOMMENDATION		186
REFERENCES.....		187
PUBLICATIONS		201
APPENDIX A: ULTRA-PRECISION G-CODE.....		203
APPENDIX B: POLYMER USAN WORKSHEET		206
APPENDIX C: LAMMPS.....		207

ABBREVIATIONS

ADC	- Allyldiglycol carbonate
AFM	- Atomic Force Microscopy
ANOVA	- Analysis of Variance
CL	- Contact Lens
EWC	- Equilibrium Water Content
FDA	- Food Drug Administration
FEM	- Finite Element Analysis
GP	- Gas permeable
HDPE	- High Density Poly Ethylene
HEMA	- Hydroxyethyl Methacrylate
IOL	- Intraocular Lens
IR	- Infrared
MD	- Molecular Dynamics
NMMU	- Nelson Mandela Metropolitan University
PC	-Polycarbonate
PDMS	- Poly (dimethyl-siloxane)
PE	- Polyethylene
PHEMA	- Polyhydroxyethyl Methacrylate
PMMA	- Polymethyl Methacrylate
PP	- Polypropylene
PS	- Polystyrene
UHPM	- Ultra-high precision machining
RH	- Relative Humidity
RGP	- Rigid Gas Permeable
Rpm	- Revolution per minute
RSM	- Response Surface Method
SEM	- Scanning Electron Microscope
SMSS	- Sequential Model sum of squares
SPDT	- Single Point Diamond Turning
UHPDT	- Ultra High Precision Diamond Turning
RDX	- Cyclotrimethylenetrinramine

NOMENCLATURE

(F_c)	- Advancing force in the direction of cutting (N)
(F_y)	- Uniaxial force perpendicular to the F_x during cutting
(F_z)	- Vertical downward force on the tool (N).
D	- Depth of cut (μm).
f	- Feedrate ($\mu\text{m}/\text{rev}$).
ϕ	- Diameter.
V_c	- Cutting speed (rev/min)
Φ	- Shear angle
β	- Friction angle
α	- Rake angle
μ	- Coefficient of friction
t_2	- Uncut chip thickness
t_1	- Sheared away thickness
ω	- Width of tool
l	- Length of tool
h	- Tool thickness
E	- Young's modulus of material
ε	- Strain

LIST OF TABLES

Table 2.1	FDA grouping and modern RGP materials, divided into four groups based on their contents.	17
Table 2.2	Properties of common optical polymers [26].....	18
Table 2.3	Types of contact lens buttons and their respective properties	19
Table 2.4	Summary of triboelectric charging mechanisms by Williams [64] ..	36
Table 2.5	Comparison of some atomistic simulation methods [13].....	46
Table 2.6	Comparison of nanometric cutting and conventional cutting mechanics [13]	48
Table 3.1	Monomers of Roflufocon E and ending bonds.....	61
Table 3.2	Assignment of CP/MAS ¹³ CNMR Chemical Shifts of PMMA [108] and Roflufocon E	63
Table 3.3	Monomer ratios per molecule in Roflufocon E	63
Table 3.4	Comparison of Some Atomistic Simulation Methods[13]	64
Table 3.5	Parametric values used in MD simulation.....	70
Table 3.6	Quantification of atoms per element type	70
Table 3.7	Physical properties of diamond tools	71
Table 3.8	Parametric values used in MD simulation.....	72
Table 4.1	Diamond machining parameters of contact lens polymer	81
Table 4.2	Workpiece and Diamond tool geometry.....	82
Table 4.3	Surface measurement matrix of experiments	85
Table 4.4	Specification of electrostatic sensor	91
Table 5.1	Experimental runs and results of Surface Roughness.....	94
Table 5.2	Sequential model sum of squares (SMSS) analysis for surface roughness.....	103
Table 5.3	Lack of fit test for surface roughness.....	103
Table 5.4	ANOVA for model coefficient for Surface Roughness in UHPM of contact lens polymer.....	104
Table 5.5	Experimental run and results of surface roughness	110
Table 5.6:	Cracking and microstructural ripple occurrence on cutting chips based on high cutting depth at SEM different image magnification	113

Table 5.7	Smooth and large folding on cutting chips based on low cutting feed	115
Table 5.8	Tear edges on cutting chips at low depth of cut and cutting speed	116
Table 5.9	Analysis of Force at the tool-tip for the experimental runs.....	126
Table 5.10	Experimental run 15 ($0.15\text{m}^{-\text{sec}}$, $12\ \mu\text{m}^{-\text{rev}}$ and $25\ \mu\text{m}$) analysis of Force at the tool-tip.....	127
Table 5.11	Experimental run and results of cutting Force	129
Table 5.12	Lack of fit test for cutting Forces.....	130
Table 5.13	Sequential model sum of squares (SMSS) analysis for cutting Forces	130
Table 5.14	ANOVA for model coefficient for Cutting Forces in UHPM of contact lens polymer	131
Table 5.15	Experimental run and results of cutting Force	134
Table 5.16	Experimental run and results of Surface Roughness	135
Table 5.17	Sequential model sum of squares (SMSS) analysis for electrostatics at 60% humidity	139
Table 5.18	Lack of fit test for electrostatics at 60% humidity	139
Table 5.19	ANOVA for model coefficient for the electrostatics at 60% humidity in UHPM of contact lens polymer	140
Table 5.20	Sequential model sum of squares (SMSS) analysis for electrostatics at 40% RH	150
Table 5.21	Lack of fit test for electrostatics at 40% RH	151
Table 5.22	ANOVA for model coefficient for the electrostatics at 40% humidity in UHPM of contact lens polymer	151
Table 5.23	Sequential model sum of squares (SMSS) analysis for negative electrostatics at 20% humidity	162
Table 5.24	Lack of fit test for negative electrostatics at 20% humidity	162
Table 5.25	Polynomial equations to represent the developed models	163
Table 5.26:	Cutting parameters and interactions that significantly influence the triboelectric effect	163
Table 5.27	Comparison of various LJ force potentials during MD simulation	171
Table 5.28	Hybrid force simulation with (a) CPK; (b) VDW representation ...	174

LIST OF FIGURES

Figure 1.1	Taniguchi Curve [5]	3
Figure 2.1	Diagram of the eye and a contact lens	9
Figure 2.2	Diagram of the eye and positioning plane for an IOL implant [16] .	10
Figure 2.3	Typical IOL (a) traditional (b) plate designs [17]	10
Figure 2.4	Chart of contact lens classification	11
Figure 2.5	Homopolymers used in Medicine [20].....	14
Figure 2.6	The spin-casting process [21].....	22
Figure 2.7	Moulding process flow diagram, 3D mould design and machined mould.....	22
Figure 2.8	Ultra-precision machining technology [33].....	24
Figure 2.9	Ultra-precision diamond turning of freeform optics	25
Figure 2.10	Various optical objects used in critical industries [33].....	26
Figure 2.11	Ultra-precision diamond tools [40]	27
Figure 2.12	Ultra-precision machined lens wit 3D image and low form accuracy	28
Figure 2.13	Elastic recovery phenomenon after diamond cutting	29
Figure 2.14	Diamond tool wear [44].....	30
Figure 2.15	Methyl methacrylate (MMA) ester bond.....	31
Figure 2.16	Chemical wear on a diamond tool [46]	31
Figure 2.17	Lichtenberg figure on a diamond tool [9, 56]	34
Figure 2.18	Triboelectric series [63],	35
Figure 2.19	The Triboelectric Charge –(a) materials make intimate contact (b) materials separate (c) saturation point. Adapted from: Asuni [65] .	37
Figure 2.20	Flow concept of static charge [9]	37
Figure 2.21	Glass transition temperatures during machining [74].....	40
Figure 2.22	Three types of errors from turning operation: form, figure and finish [71]	41
Figure 2.23	Description of surface parameter [77].....	42
Figure 2.24	Box-Behnken statistical model	44
Figure 2.25	Schematic for multi-scale damage modelling [78]	47
Figure 2.26	MD simulation of nanometric cutting of silicon [82].....	49
Figure 2.27	Atomistic Interaction in Nanometric Machining [103].....	51

Figure 2.28	Atomistic Interaction in Nanometric Machining [103].....	52
Figure 2.29	Morse potential function and the effect of atomic distance on intermolecular force[82]	54
Figure 3.1	Chemical composition of Roflufocon E	59
Figure 3.2	Chemical structure of Roflufocon E molecule	60
Figure 3.3	Solid state CP/MAS ¹³ C NMR spectrum of Roflufocon E.....	62
Figure 3.4.	Software Methodology flowchart	65
Figure 3.5	Representative cross-linked epoxy chain (left), and amorphous cell composed of 10 epoxy chains from Material Studio	67
Figure 3.6	MATLAB shell window	68
Figure 3.7	CPK drawing method of Roflufocon E in VMD	69
Figure 3.8	(a) & (b) Crystal structure of the diamond atom as the cutting tool	71
Figure 3.9	Schematic of the MD Simulation of Nanometric Cutting.....	73
Figure 3.10	MD of simulation model of Roflufocon E (a) VDW (b) bonds representations.....	74
Figure 3.11	MD of simulation model of bonds acting on the polymer and tool within the boundary structure	75
Figure 3.12	Lennard-Jones interaction energy Aziz [131]	76
Figure 4.1	Sub-classifications of areas for investigation into UHPM process .	77
Figure 4.2	Precitech Nanoform 250 ultra-high precision machine	78
Figure 4.3	Precitech Nanoform 250 ultra-high precision machine	79
Figure 4.4	Diffraction and aspheric lens generating software (Diffsys)	80
Figure 4.5	Precitech Nanoform 250 Ultragrind machine controller interface ..	80
Figure 4.6	Diamond machining setup of contact lens polymers on UHPM	81
Figure 4.7	Roflufocon E contact lens button	81
Figure 4.8	Roflufocon contact lens button	82
Figure 4.9	Atomic Force Microscope/ Nano-indenter by CSM ®.....	83
Figure 4.10	Atomic Force Microscope setup for surface measurements.....	83
Figure 4.11	Surface AFM topographic images of contact lens	84
Figure 4.12	Force sensor setup schematic on UHP Machine.....	86
Figure 4.13	(a) Micro-force sensor (b) Charge amplifier (c) Data acquisition system	87
Figure 4.14	Diamond machining setup of Contact lens polymers on UHPM [136]	88

Figure 4.15	Diagram of (a) diamond cutting tool (b) cutting force representation	89
Figure 4.16	Setup for diamond turning of Contact lens polymer.....	90
Figure 4.17	Schematic for measuring the surface potential with electrostatic voltmeter.....	91
Figure 4.18	Electrostatic sensor (IZD10-510) [139].....	92
Figure 4.19	Sensor output vs charged potential for differing installation distance (IZD10-510) [139].....	92
Figure 4.20	Triboelectric setup for diamond turning of contact lens button	93
Figure 5.1:	Theoretical surface height for face turning operation [73].....	95
Figure 5.2:	Comparison between theoretical and experimental values of surface roughness as a function of depth of cut (a) at 2 $\mu\text{m}/\text{rev}$ feedrate (b) at 7 $\mu\text{m}/\text{rev}$ feedrate.....	96
Figure 5.3	Comparison between theoretical and experimental values of surface roughness as a function of feedrate (a) (at 10 μm depth of cut (b) at 25 μm depth of cut.....	97
Figure 5.4	Surface AFM topographic images of contact lens	102
Figure 5.5	Box-Behnken statistical model	103
Figure 5.6	Normal probability plot of residuals in surface roughness modelling	105
Figure 5.7	Probability plot of residuals vs. predicted points.....	105
Figure 5.8	Normal Probability plot of surface roughness vs speed.....	106
Figure 5.9	Normal Probability plot of surface roughness vs depth of cut.....	107
Figure 5.10	2D Normal Probability plot of surface roughness vs feed and depth of cut.....	108
Figure 5.11	3D Plot of the influence of feed and depth of cut on surface roughness.....	109
Figure 5.12	Lamella structure on the cutting chip (a) 2.5m/s, 7 $\mu\text{m}/\text{rev}$, 40 μm (b) 2.5m/s, 2 $\mu\text{m}/\text{rev}$, 25 μm	111
Figure 5.13	Photomicrographs made by SEM of cutting chips (Cutting conditions: $f = 30 \mu\text{m}/\text{rev}$, depth of cut = 10 μm) Jasinevicius et al. [138]	112
Figure 5.14	Photomicrographs made by SEM of cutting chip splits (Cutting conditions: $f = 30 \mu\text{m}/\text{rev}$, depth of cut = 10 μm)	112

Figure 5.15	(a) Diamond machining of a contact lens button (b) top surface of mounted lens button	120
Figure 5.16	Evaluation of force dissipation across the cutting tool	126
Figure 5.17	Normal probability plot of residuals in cutting force modelling	131
Figure 5.18	Probability plot of residuals vs predicted in cutting force modelling	132
Figure 5.19	Normal Probability plot of feed on cutting force	133
Figure 5.20	3D Plot of the influence of feed and depth of cut on cutting force	133
Figure 5.21	Chip build up on the diamond tool [55]	136
Figure 5.22	Basic cycle chart of the static charging during diamond machining of polymers [55]	136
Figure 5.23	Static charging effects in experiment 13 (60% - humidity)	138
Figure 5.24	Static magnitudes at 60% humidity experiments	138
Figure 5.25	Normal probability plot of residuals of statics at 60% humidity	140
Figure 5.26	Probability plot of residuals vs predicted response for the statics at 60% humidity	141
Figure 5.27	Behaviour of 60% RH in response to variation in feed at (a) 239 rpm (b) 2109 rpm (c) 3979 rpm.....	142
Figure 5.28	Behaviour of 60% humidity in response to variation in speed at (a) 2 μ m/rev (b) 7 μ m/rev (c) 12 μ m/rev	143
Figure 5.29	Behaviour of 60% humidity relative to interaction between feed and speed.....	144
Figure 5.30	Normal Probability plot of 60% relative humidity	145
Figure 5.31	3D Plot of the influence of feed and depth of cut on cutting force	146
Figure 5.32	Static magnitudes in high humidity experiments (40% humidity) .	147
Figure 5.33	Static charging fluctuations in experiment 4 at $s = 2109$ rpm, $f = 2\mu$ m/rev, $d = 40\mu$ m and 40% humidity).....	148
Figure 5.34	Chip builds up and static charging effects (40% humidity)	148
Figure 5.35	Static charging effects in experiment 12 at $s = 2109$ rpm, $f = 7\mu$ m/rev, $d = 25\mu$ m and 40% humidity.....	149
Figure 5.36	Static charging effects in experiment 15 at $s = 239$ rpm, $f = 12\mu$ m/rev, $d = 25\mu$ m and 40% humidity.....	150
Figure 5.37	Normal probability plot of residuals of statics at 40% humidity	152

Figure 5.38	Probability plot of residuals vs. predicted for the statics at 40% humidity	153
Figure 5.39	Behaviour of 40% RH in response to variation in speed at (a) 10 μ m (b) 25 μ m (c) 40 μ m	154
Figure 5.40	Behaviour of 40% humidity in response to variation in depth of cut at (a) 239 rpm (b) 2109 rpm (c) 3979 rpm	155
Figure 5.41	Interaction between feed and depth of cut (at 239 rpm)	156
Figure 5.42	Normal probability plot of electrostatic discharge at 40% relative humidity	157
Figure 5.43	3D Plot of the influence of parameters on electrostatic discharge at 40% humidity	158
Figure 5.44	Strong triboelectric effects at very low humidity	159
Figure 5.45	Triboelectric discharge effects during experiment 4 at $s = 2109$ rpm, $f = 2 \mu\text{m}/\text{rev}$, $d = 40 \mu\text{m}$ (20% humidity)	160
Figure 5.46	Triboelectric effect and sudden discharge at experiment 12 at $s = 2109$ rpm, $f = 7 \mu\text{m}/\text{rev}$, $d = 25 \mu\text{m}$ and 20% humidity	160
Figure 5.47	Comparison of cutting chip in experiment 4 & 12	161
Figure 5.48	Triboelectric effect and sudden discharge at experiment 6 at $s = 4109$ rpm, $f = 12 \mu\text{m}/\text{rev}$, $d = 25 \mu\text{m}$ and 20% humidity	161
Figure 5.49	Various cutting conditions during MD simulation	166
Figure 5.50	MD simulation of (a) temperature	167
Figure 5.51	MD simulation of energy	168
Figure 5.52	Hyper-elastic polymer property	169
Figure 5.53	MD of simulation model of Roflufocon	173
Figure 5.54	Various complexities involved in the cutting of polymers [147]	175
Figure 5.55	MD showing atomic movement within the silicon workpiece	176
Figure 5.56	Cutting force component of MD simulation of polymer	177
Figure 5.57	Temperature component of MD simulation of polymer	178
Figure 5.58	Energy observed during MD simulation of polymer	178

GLOSSARY OF TERMS

A

- **Acrylic** – related to resins or textile fibres made from polymers of acrylic acid or acrylates:
- **Aspheric** – property of a surface or lens deviating slightly from a specific spherical shape and relatively free from aberrations.
- **Astigmatism** - A defect in the eye or in a lens caused by a deviation from spherical curvature, which results in distorted images, as light rays are prevented from meeting at a common focus.

E

- **Elastomers** – any material such as natural or synthetic rubber, that is able to resume its original shape when a deforming force is removed.

F

- **Freeform** – a form of lens surface not organized in a planned conventional way; without restrictions or preconceptions.

H

- **Hydrogel** – a form of lens type whose liquid constituent composition is water.
- **Hydrophilic** – a form of lens which holds high affinity for water
- **Hydrophobic** – a form of lens or substance having little affinity for water or tending not to dissolve in, mix or be wetted by water.

L

- **Ligands** – an atom, molecule, radical or ion forming a complex with a central atom

N

- **Nanometric** – a term to describe measurements in the scale of study equal to one billionth of a meter and also equal to 10 Angstroms.
- **Neighbouring** – In atomic study, it defines distance found between atoms in a molecule and used to estimate conditions linked to molecular formation and force interaction.

P

- **Pair-potential** – In mechanics, it is a function that describes the potential energy of two interacting objects
- **Permeable** – a substance or material capable of permitted water passing through it.
- **Polymers** – a substance of high molecular weight derived by either the addition of many smaller molecules, or by the condensation of smaller molecules with the elimination of water.
- **Precision** – In mechanical study, it is the state of scientific exactness in accuracy.
- **Presbyopia** – a progressively diminishing ability of the eye to focus, caused by loss of elasticity of the crystalline lens. Also termed as farsightedness.

Chapter 1

Introduction

1.1 Preamble

Optics are a foundational component of our daily lives. Their applications transcend various spheres of human living such as electronics, medical and purely optical uses. Various sorts of optical materials exist; there is the collection of optical glasses, special materials (e. g. active laser glass, IR-Materials, sapphire), polymers, ultra-thin glass, high-precision optical components, wafers, and optical filter glasses. Applications of optics seen in the field of medicine are in the manufacture of vision lenses, fluorescence microscopy and phosphate laser glasses for dermatology. However, it can be stated that a great portion of optical materials used in medical research is focused on contact lenses.

In the years since polymers' introduction, contact lens technology has been increasing at a rapid rate. There have been improvements in manufacturing techniques, as well as an increase in the type of polymer used in the lens. Today, contact lenses can be manufactured via injection moulding or lathe techniques. While all injection moulding techniques provide easy and adequate solution to mass production of lenses, even so it is cost intensive for manufacturing prototype designs for specific medical needs. Therefore, the need to access the performance of ultra-high precision machining (UHPM) as an alternate technique suited for the manufacturing of high-end optics with divers surface profiles is necessary for improved contact lens production.

1.2 The general concept for the study

In a simple definition, optical lenses are worn in the eye to rectify vision [1]. Optical lenses are considered medical tools and can be worn for ocular rectification, aesthetic or therapeutic reasons. They provide a safe and effective way to visual conditions such as myopia, hypermyopia, presbyopia, and astigmatism. Some

applications of coloured contact lenses are however meant to enhance cosmetic appearance. They are used to change iris colour through tinted optic frames. Gupta and Aqil [2] in their article, reviewed the therapeutic contact lenses as an upcoming technology for ocular drug delivery. Their article discusses the various administration techniques discovered till now, i.e. soaking, particle laden contact lenses, molecular imprinting and ion ligands, etc. They conclude by stating the need for more efforts and techniques to make this novel concept to reach market after proper clinical trials. Patient compliance with timely delivery should be the aim in development of therapeutic contact lens [2].

The basic concept behind this medical application of optics is to place a thin plastic polymer lens over a layer of tears directly over the cornea as visual corrective substitute. Advantages of the contact lens over its predecessor, the spectacle, are its size and comfort. These lenses are also a preferred aesthetic choice for most people and could in certain medical cases provide better correction.

The idea behind this study is to provide insight into the optimisation of ultra-high precision machining of contact lens polymers and an evaluation of associated influential parameters.

1.3 Optical manufacturing techniques for contact lenses

The use of contact lenses for vision correction stresses on high precision and surface integrity in the nanometric ranges for lens functionality. Precision, the quality of being exact and accurate is one of the major properties in optics. Furthermore, optical aberrations on these lenses caused by geometrical deviations, surface roughness and sub-surface defects resulting from the fabrication process could greatly influence their functionality. Heinrich and Wildsmith [3] in their study, emphasize that the design, manufacture and metrology of contact lenses is a field heavily dependent on the existence and advancement of precision engineering.

Various manufacturing techniques for contact lens fabrication exist. Older fabrication methods such as moulding techniques span over an enormous range of manufacturing procedures and test configurations. These include spin casting, cast moulding and injection moulding. The manufacture of conventional contact lenses

often begins with the creation of moulds using a lathe and proceeds to the generation of the optical surface by the use of earlier mentioned moulding methodologies. Additional finishing procedures are then performed to achieve required optical quality [2]. Modern approaches however involve direct lathing of contact lens material in their unhydrated state, known as buttons [3]. At the present time the ultra-precision machining process of single point diamond cutting is regarded as an effective process for the generation of high quality functional surfaces. In nanotechnological lathing systems, surfaces with minimal defects in the superficial layer are produced from various materials especially from thermoplastic amorphous polymers of material composition designed for optical, photonic and bioengineering applications [4]. Taniguchi [5] in 1974 was the first to use the term “nanotechnology”. In his research he describes diverse measures of machining (Figure 1.1). Ultra-high precision machining (UHPM) is a machining method used to describe technologies with the highest possible dimensional accuracies achievable [5]. Most recent trends in machining address the removal of machine part at atomic level for highly precise surfaces that are employed in device parts for mechanical, optical and electronic applications. These trends corroborate Taniguchi’s model of increasing precision over time (Figure 1.1).

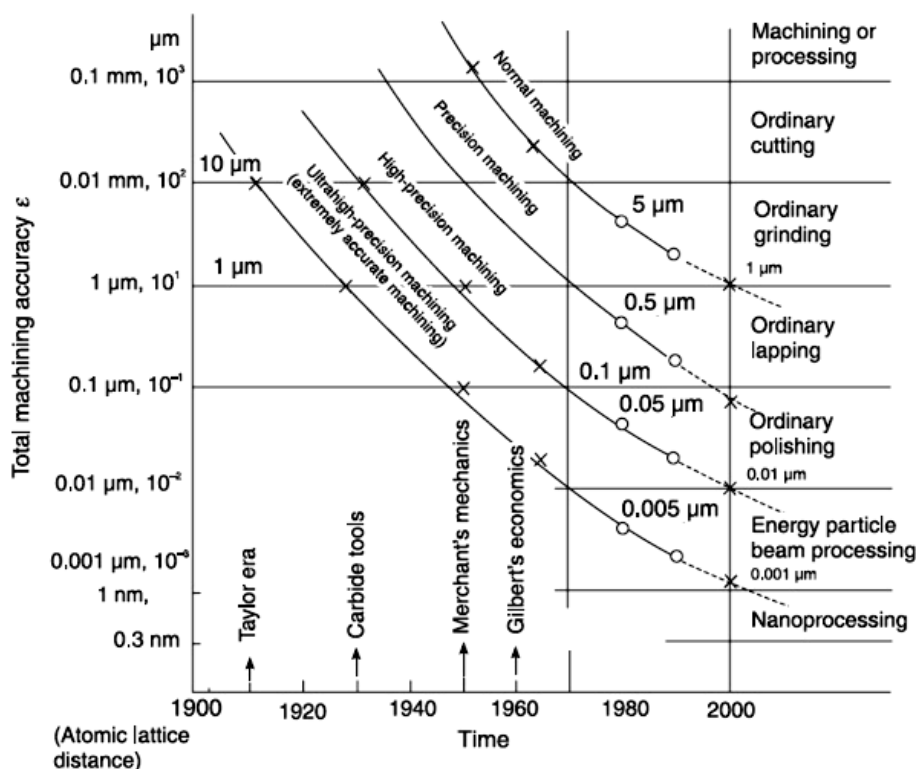


Figure 1.1 Taniguchi Curve [5]

Ultra-high precision machining (UHPM) has been used as a direct production method for making contact lenses due to its capability for high accuracy. Similarly, polymer machining has also been widely seen on the macro/nano machining landscape with polycarbonate, nylon and other plastics [6-8]. However, UHPM machining of these polymers within a few nanometric ranges of surface roughness is yet to be fully understood. Gubbels [9] in his research into glassy polymers expatiated on underlining mechanisms believed to be present in nanometric polymer machining. His research works forms part of foundational knowledge in micro-mechanisms identified between diamond and polymeric materials. His research further exposes the void present in the clear understanding of other underground mechanisms such as wear, effects of cutting parameter, electrostatics and atomistic reactions.

1.4 Significance of the study

The market of contact lens technology is well established in today's world. With annual increase, report shows estimates of about 125 million people wearing contact lenses worldwide in 2004 [10]. In 2011, worldwide contact lens market was estimated at \$6.8 billion with a growth of 11% over the previous year. In the same year, a demographic report showed that 67% of contact lens fits were to female users [11].

Based on the growing demand for the contact lens, an increase in the performance of the ultra-high precision of modern polymeric contact lens material would pioneer this field of bioengineering in South Africa. Furthermore, it creates an avenue for the manufacture of polymer lenses with specific design interface based on racial trait for the African landscape at low cost.

1.5 Problem statement

The need for high surface integrity and accuracy is imperative in contact lenses used in bioengineering applications [12]. The fabrication process of the contact lens is therefore an important process to control and produce functional lenses. However, based on its output accuracy, Single Point Diamond Turning (SPDT) is also highly

sensitive to changes within the machining environment. Thus instability could directly affect micro-forces occurring between the cutting tool edge and the workpiece and thus may lead to poor finishes. Therefore, evaluating the effects of cutting parameters on machining performance of the process is essential.

Furthermore, micro- and Nano-machining are known to occur at the tool tip in contact with the workpiece. This interface which contains few atoms or layers of atoms is not continuous as assumed by continuum mechanics [13]. Based on the scale of operation, atomistic simulation methods present possible solutions in evaluating nano conditions of cutting. This form of modelling is needed to further understand atomic responses and thus control quality of products at reduced costs.

Diamond tool edge is a major factor influencing optical geometry, surface roughness and sub-surface defects in the polymeric lens. The need to ascertain wear causing mechanisms and performance criteria influencing the process of contact lens fabrication is an integral part of identifying machining performance.

In conclusion, due to the limited amount of research in this field of polymer machining and especially at this scale of cutting, it is essential to ascertain sub-surface mechanisms responsible for degrading conditions in machined optical grade polymers, understand the correlations of forces to machining conditions and molecular shifts at the atomic level.

1.6 Research aim and objective

The aim of this research is to evaluate the performance of ultra-high precision machining of polymeric materials for contact lens manufacture, explain the triboelectric phenomena occurring in polymer nanomachining and identify the boundaries of machining parameters for optimal performance. The performance would be evaluated in terms of surface roughness.

The specific objectives of this research are:

- Evaluate the performance of ultra-high precision machining of a commercially available polymeric material used for contact lens manufacture;

- Create curve fitting models to study the effects of cutting parameters on surface finish and also the relationship of cutting force to cutting parameters;
- Determine the effects of electrostatic charging in nanomachining of polymers and its causative agents;
- Simulate a nanomachining process of polymers using the Molecular Dynamics (MD) method to understand underlying atomic phenomenon during cutting; and
- Validate the models using experimental results received.

1.7 The hypothesis statement

Monitoring sensing techniques and careful microscopic correlation and analysis of machining conditions can be used to estimate the influence of diamond turning parameters on the achievable surface roughness in the ultra-high-precision machining of polymeric lenses. A molecular dynamic simulation of contact lens polymers would assist in understanding subsurface sub-structural effects occurring during cutting.

1.8 Research scope

The research encompasses a detailed analysis of monitoring signals of the ultra-high precision cutting process at specific machining conditions. Machining parameters such as the feed rate, depth of cut, and speed were predetermined for experimental design. Monitored signals results obtained were used to model the surface integrity of the polymeric lens, determine the influential factors in machining, improve efficiency and assess wear mechanisms experienced. An analysis of triboelectric wear mechanism that usually accompanies diamond precision cutting of polymers was also performed. Furthermore, the research includes a molecular dynamics simulation of a prototype contact lens polymer and this was used to evaluate the atomic reaction during nanoscale machining of contact lenses.

1.9 Structure of the thesis

The thesis is subdivided into five chapters:

Chapter 1 explains the motivation, aim and the objectives of the research work.

Chapter 2 provides a review of the theory of nanometric machining, contact lens polymers and highlights various nanometric machining research works. It further reviews the molecular dynamics method, with consideration to the various thermodynamic ensembles, the commonly used interatomic potentials, algorithms for the integration of the equations of motion and examples of MD simulation in nanomachining.

Chapter 3 explains the methodology used for the MD simulation of nanometric machining of the contact lens polymer; the MD software used for the simulations and its hardware platform. It also shows the general overview of MD simulation systems.

Chapter 4 provides the experimental setup involved in the research. It includes the setup for the investigation of process factors affecting surface finish on SPDT of CL which observes the effects of speed, feed and depth of cut as cutting parameters influencing surface quality and creates a model using the response surface method, as well as the setup for investigation of triboelectric wear in the single point diamond turning of contact lens.

Chapter 5 explains the results obtained from each experimental test and displays all results obtained. It gives a statistical evaluation of cutting force and creates a model based on Runge-Kutta's equation to determine the actual force experienced at the tool tip and a model of the influence of cutting parameters on obtainable surface roughness. It also reveals the MD simulation results of single-pass nanometric machining.

The last section is a summary and conclusion of the contribution of this research work and proposes directions for future work.

Chapter 2

Literature Review

2.1 Introduction

A lens is an optical device which transmits or refracts light in a concentrated or diverged beam. Early records of lenses date as far back as ancient Greece and were applied as artefacts by artisans for fine work and magnification. Their use in modern applications has evolved and are now seen in medicine, astronomy, and imaging systems. Lenses over the years have evolved from various surface forms to suit various industrial applications. Examples of these forms are: spherical, aspheric, micro-prisms, freeform, and micro-lens arrays. Biomedical applications also employ lenses as prosthetics for correction of visual impairments such as congenital disorders, injury, and other medical conditions. These conditions could be treated using divers types of contact lenses.

Since the majority of biomedical optical applications is focused on visual correction, therefore; lenses are crucial, therefore, in ophthalmology studies. Biomedical lenses serve as substitute rectifying lenses to the damaged corneal surface. There are two basic types of biomedical lenses usually employed: contact lenses or intraocular lenses.

2.2 Eye polymer optics

Medical optical applications such as those related to the use of contact lenses however require high precision for relevance [14]. Surface integrity of dimensions in the nanometric scale (<10 nm) is necessary to cure visual imperfections. Biomedical ocular lenses are used to focus light beam on the retina for clear image formation (Figure 2.1). These lenses are necessitated due to imperfections found on the cornea of the eye leading to adverse medical conditions. Other medical uses of optics are seen in fluorescence microscopy and phosphate laser glasses for dermatology. However, most biomedical optical applications are focussed on visual correction.

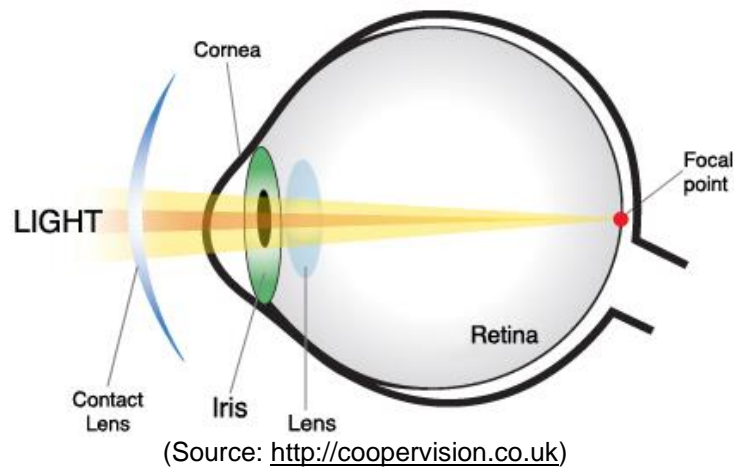


Figure 2.1 Diagram of the eye and a contact lens

Over the years, contact lenses have evolved to better suit various intricate medical conditions. One of the sub-conceptions of the contact lens is the creation of the intraocular lens. The invention of the implantable, biocompatible intraocular lens (IOL) for treatment in cataract surgery has been a ground-breaking medical discovery. Harold Ridley was the first to introduce the intraocular lens for visual correction in 1949 [15].

An intraocular lens (IOL) is an implantable contact lens in the eye, usually directly replacing the existing crystalline lens because it has been clouded over by a cataract, or as a form of refractive surgery to change the eye's optical power. An example of this lens type is shown in Figure 2.2. These lenses can be made from acrylic, silicone, or collamer polymers, designed as a one-piece lens or a multi-piece lens. Pseudophakic IOLs are most widespread type of IOL for cataract treatment. They permit a superior restoration of sight following the extraction of the cataractous crystalline lens. Its placement in a plane that approximates the plane of the normal lens prevents the optical and physical shortcomings of spectacle correction and prevents cultural contemptuous conventions associated with thick cataract glasses.

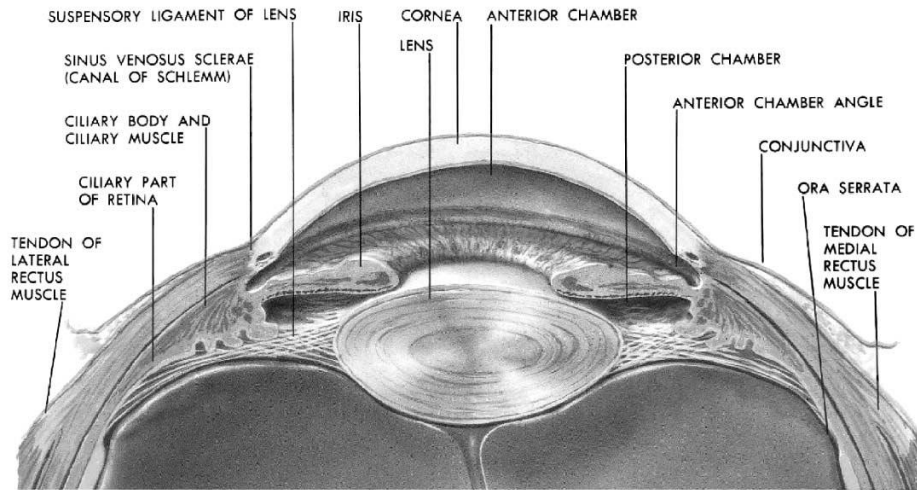


Figure 2.2 Diagram of the eye and positioning plane for an IOL implant [16]

IOLs share the same basic structure as contact lenses; a round, corrective central portion forms the lens. However, some IOLs are equipped with 2 arms, or haptics, for stable positioning within the eye. Most of today's IOLs are about a quarter of an inch or less in diameter and soft enough to be folded and injected through a syringe into the eye via a minute incision. Figure 2.3 shows a typical intraocular lens in both traditional and plate designs.

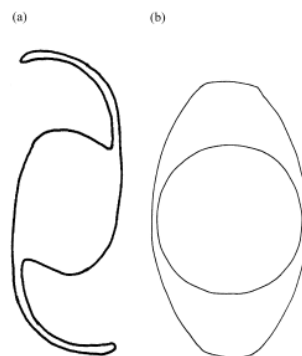


Figure 2.3 Typical IOL (a) traditional (b) plate designs [17]

2.3 Contact lenses and their materials

As earlier mentioned, a contact lens is a device worn in the eye to rectify vision [1]. Contact lenses (CL) could be classified by their primary functions or material composition. CLs are considered medical tools and can be worn for ocular

rectification, aesthetic or therapeutic reasons. They provide a safe and effective way to visual conditions such as myopia, hypermyopia, presbyopia, and astigmatism.

Three types of contact lenses exist based on materials composition. These are: soft, hard, and gas-permeable lenses. Figure 2.4 shows a detailed classification of contact lenses.

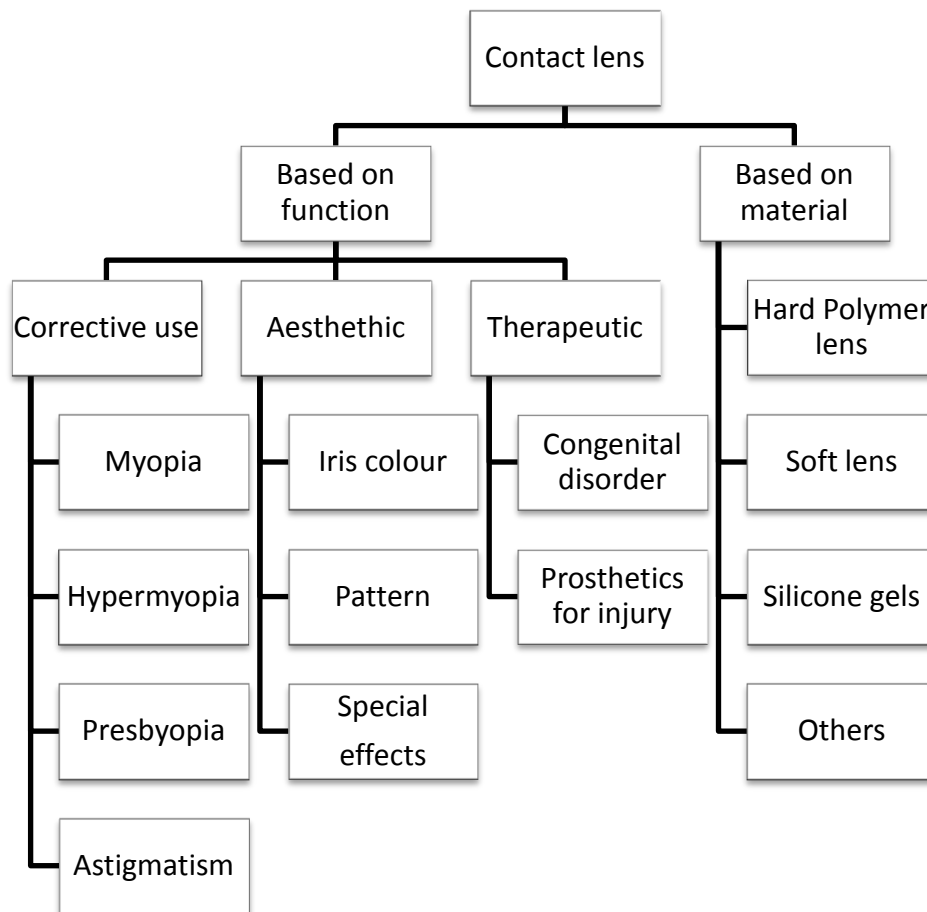


Figure 2.4 Chart of contact lens classification

The contact lens records date back to the end of the Second World War. Early invention of the optical lens was certainly not comfortable enough to attain well-known recognition. Prime lens recognition came from polymethyl methacrylate (PMMA or Perspex/Plexiglas) lenses. However, a known disadvantage of early PMMA lenses is that they did not allow oxygen to pass through to the cornea, which caused a number of adverse clinical events. Following this discovery, further research studies on PMMA by the copolymerization of methyl methacrylate with different monomers gave life to rigid gas permeable (RGP) lenses. Based on the

need for biocompatible polymers, the 2-hydroxyethyl-metacrylate (HEMA) soft lens hydrogel contact lens was then introduced leading to the evolution of a more versatile contact lens industry with new biocompatible polymers. Soft lens hydrogels, known as water-loving polymers are hydrophilic in nature and possess acceptable gas permeability.

A brief view of historical facts of the contact lens over the years is shown below [18]:

- 1508 Leonardo da Vinci illustrates the concept of contact lenses
- 1888 First contact lens manufactured from glass, by Adolph Eugene Fick
- 1936 Rohm and Haas create first contact lenses made from plastic
- 1948 Plastic contact lenses designed to cover only the eye's cornea
- 1965 Silicon elastomer lenses
- 1972 Introduction of soft contact lenses
- 1974 Introduction of RGP contact lenses
- 1988 Introduction of disposable soft contact lenses
- 1994 Introduction of one-day disposable soft lenses
- 1998 Silicone-hydrogel contact lenses first marketed
- 2010 Custom-manufactured silicone-hydrogel lenses became available

Another review of the soft lens evolution by Nicolson and Vogt [16] shows that the evolution has been driven by an increased understanding of the physiological needs of the cornea, beginning with the first hydrogel lenses developed by Wichterle, followed by a variety of high water hydrogels. Oxygen transmission requirements have been addressed through the use of siloxane and fluorosiloxane containing hydrogels. Further developments have been the appreciation of the importance of polymer phase morphology on lens movement on the eye.

While several factors can affect a lens' biocompatibility, perhaps the most important is the wettability of the lens; therefore gas-permeable lenses formed a compromise between the hard and soft lenses. These allow greater comfort yet with an optimal functionality. Soft and hard lenses employ a similar framework setup of refracting light by thickness and shape variation of the lens for vision correction. Various standards exist for contact lens design in specifying tolerance limits [19].

2.3.1 Classes of polymers used in medicine

There are many types of polymers used for biomedical purposes. They could be identified as homo-polymers or copolymers. Some common examples of general monomers seen in medicine (as shown in Figure 2.5) are Polymethyl Methacrylate (PMMA), Poly (2-hydroxyethyl methacrylate) Poly (HEMA), Polyethylene (PE), Polypropylene (PP) and Poly (dimethyl siloxane) (PDMS). These materials possess unique qualities related to permeability, strength, low-density and wettability [20]. Therefore, for the contact lens industry, lenses are influenced by their constituent base monomer. Figure 2.5 shows these common polymers used in medicine and their molecular structures. Soft lenses primarily are composed of HEMA while hard lenses originate from modification made to PMMA [21]. Furthermore, nearly all original RGP materials were chemical mixes of PMMA and silicon [22]. The addition of materials such as freely permeable silicon, and fluorine-based monomers to a polymer could produce resultant materials with increased physical properties such as wettability, permeability and flexibility but could also influence ionic properties.

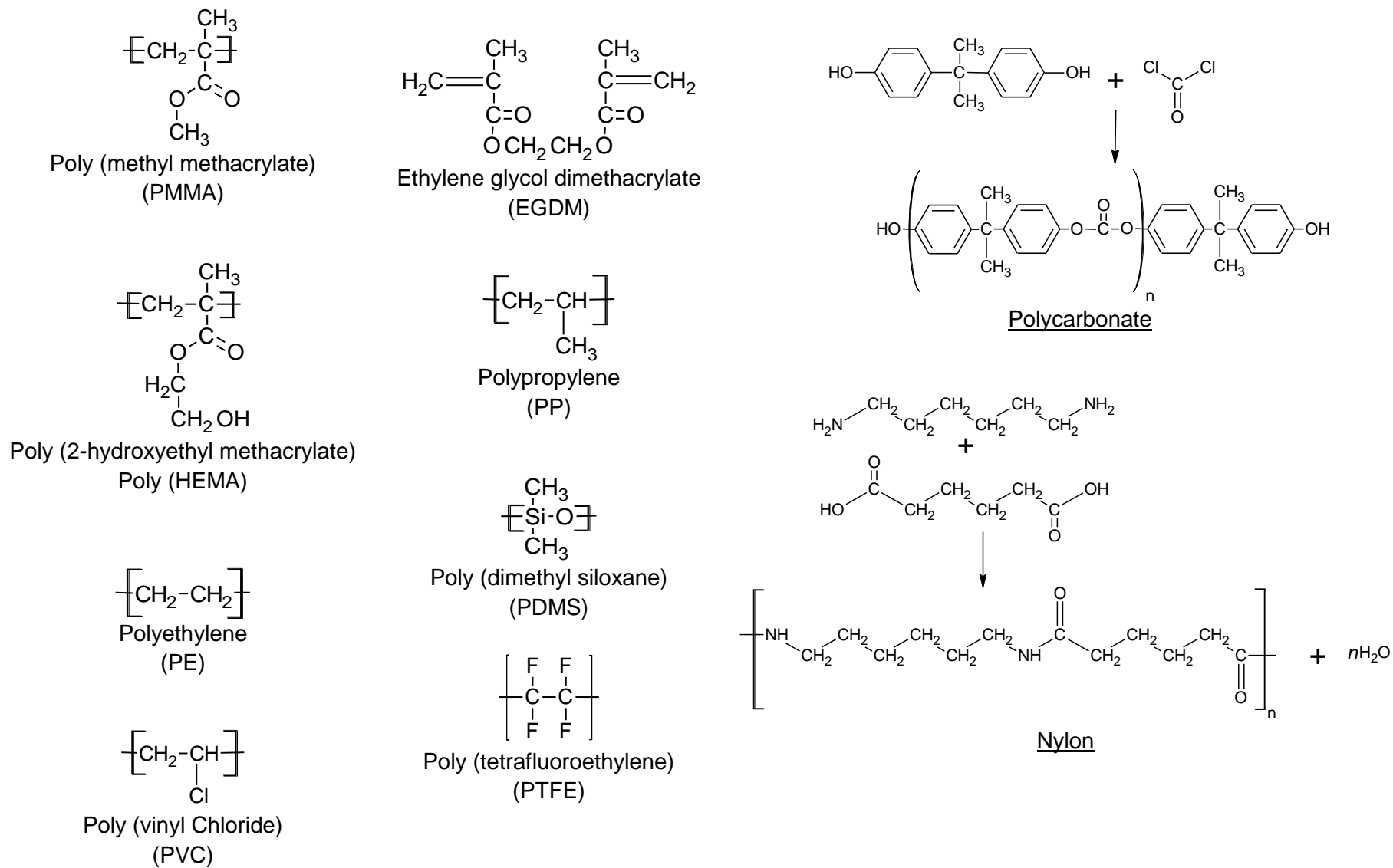


Figure 2.5 Homopolymers used in Medicine [20]

2.3.2 Fabrication of contact lenses

Chemistry is known to be the foundation of contact lens materials, and lens fabrication may be visualised as a form of "cooking" with ingredients and mixing/manufacturing steps. Known ingredients of contact lens materials include the monomers and polymers mentioned earlier in the previous section, which are combined into macromers and copolymers. These lenses are then processed to produce an optically clear, chemically stable, durable, oxygen permeable and wettable contact lenses polymer which is biologically inert.

Normally, carbon-based molecules are the basis for the original contact lens polymers including cellulose acetate butyrate (CAB) and polymethyl methacrylate (PMMA). Subsequently, newer contact lens polymers may be partially silicon-based (silicone-methacrylate and fluorosilicone acrylate) and hydrogel (silicone hydrogel) lenses. Final formulations of lens polymers only include constituents that improve lens features and characteristics. Beside the effects on surface wetting characteristics and water content, others link the polymers together (crosslinking) to achieve fitting equilibrium between stiffness, flexibility and durability [23].

More common monomers in contact lens materials include Snyder [23]:

- Methyl methacrylate (MMA), which contributes hardness and strength
- Silicone (SI), which increases flexibility and gas permeability through the material's silicon-oxygen bonds but has the disadvantage of poor wettability
- Fluorine (FL), which also adds a smaller degree of gas permeability and improves wettability and deposit resistance in silicone-containing lenses
- Hydroxyethyl-methacrylate (HEMA), the basic water-absorbing monomer of most soft lenses
- Methacrylic acid (MAA) and n vinyl pyrrolidone (NVP) monomers, both of which absorb high amounts of water and are usually adjuncts to HEMA to increase lens water content
- Ethylene glycol dimethacrylate (EGDMA), a cross-linking agent that adds dimensional stability and stiffness but reduces water content.

Some distinct monomers and additives may permit the polymer chains to change structure more freely within the material; others may prevent the transmission of ultraviolet light and yet others may aid the material repel dehydration.

A hydrogel polymer must possess certain physical properties if it is going to be suitable as a contact lens material. These include [21]:

- being optically transparent
- having a refractive index similar to that of the cornea, i.e. approximately 1.37
- being sufficiently oxygen-permeable
- having sufficient hydraulic permeability
- having sufficient dimensional stability
- having adequate mechanical properties
- being biocompatible in the ocular environment.

The equilibrium water content (EWC) for a lens is measured by:

$$\text{EWC} = \frac{\text{weight of water in polymer}}{\text{total weight of hydrated polymer}} \times 100 \quad (2.1)$$

Oxygen permeability was identified to be related to EWC in conventional hydrogels. This is linked to the movement of oxygen molecules through the water instead of the material itself. This relationship was identified as [21]:

$$Dk = 1.67e^{0.0397\text{EWC}} \quad (2.2)$$

Where Dk is the oxygen permeability constant.

Minor differences from the processing and material formula have great influence on the final chemical and physical properties of individual lens materials. For instance, adding NVP or MAA to a 38% (low-water content) HEMA monomer can result in a medium (about 50%) or even high (about 70%) final polymer water content. Adding MMA and/or EGDMA to HEMA increases material durability, elasticity and stability but decreases water content [23].

Various other properties of the polymers are altered in polymerisation. Properties such as electrical, magnetic, mechanical, acoustic and optical are amongst the most notable. Despite the widely accepted perspective of polymers been insulators, there

exists a separate class of polymers with conducting abilities. Many polymeric materials can be formed into thin, mechanical strong films and it is desirable to confer the additional property of electrical conductivity on polymers in addition to the flexibility and compatible advantages.

Table 2.1 combines the Food and Drug Administration (FDA) groups of contact lens polymers, and reviews some electrical properties achieved by observing the polymers' susceptibility to charge with their base constituents materials. In this research work, a "group three" fluoro-silicon acrylate polymer was studied.

Table 2.1 FDA grouping and modern RGP materials, divided into four groups based on their contents.

Group	Water content	Ionicity	Description	Material
I	Low (<50%)	Non-ionic	Contains no silicone or Fluorine	Cellulose acetate butyrate
II	High (>50%)	Non-ionic	Contains silicone but no Fluorine	Silicone acrylate
III	Low (<50%)	Ionic (<i>can charge</i>)	Contains silicone and Fluorine	Fluorosilicon acrylate
IV	High (>50%)	Ionic (<i>can charge</i>)	Contains Fluorine but no silicone	Fluorocarbon

Adapted from FDA tables in [23, 24]

2.3.3 Commercially available contact lens materials

There exist various industrial optical polymers available for use in today's market. Amidst optical polymers, Allyldiglycol carbonate (ADC), sometimes called CR-39, is popularly employed. This polymer was developed as a substitute for glass and is often called organic glass. It has almost the same refractive index, chemical resistance and similar mechanical properties as glass. ADC monomer has been used for many years in the manufacture of ophthalmic lenses. Nowadays more than 80% of ophthalmic lenses are made of ADC. Table 2.2 shows some other properties of common optical polymers like ADC used commercially [25].

Table 2.2 Properties of common optical polymers [26]

Unit	Acrylic	Acrylic Copolymer	Polystyrene	Poly etherimide	Poly-carbonate	Methyl pentene	ABS	Cyclic Olefin Polymer	Nylon	NAS	SAN	
Trade Name	Plexiglas	UVT	Styron	Ultem	Lexan	TPX	Acrylon	Zeonex	Poly-amide	Methyl	Styrene Acrylonitrile	
Refractive Index												
nf (486.1 nm)	1.497	—	1.604	1.689	1.593	1.473		1.537		1.575	1.578	
nd (589 nm)	1.491	1.49	1.590	1.682	1.586	1.467	1.538	1.530	1.535	1.533–1.567	1.567–1.571	
nc (656.3 nm)	1.489	—	1.585	1.653	1.580	1.464		1.527		1.558	1.563	
Abbe Value Vd	57.2	50–53	30.8	18.94	34	51.9		55.8		35	37.8	
Transmission	%1	92–95	92–95	87–92	82	85–91	90	79–90.62	90–92	88	90	88
Max Continuous	°F	161	190	180	338	255		253	179.6	199.4	174–190	
Service Temp.	°C	72	88	82	170	124		123	82	93	79–88	
Water Absorption	%3	0.3	0.25	0.2	0.25	0.15		<0.01	3.3	0.15	0.2–0.35	
Haze	%	1–2	2	2–3		1–3	5	12	1–2	7	3	3
dN/dT	x10 ⁻⁵ /°C	-8.5	-10 to -12	-12		-11.8–14.3		-8		-14	-11	
Color/Tint		Water clear	Water clear	Water clear	Amber	Water clear	Slight yellow	Water clear		Water clear	Water clear	

More recent inventions however are in the fluorosilicate materials, which possess added oxygen and wetting qualities. Numerous variations of fluorosilicate polymers exist, amidst which Roflufocon A, B, C, D and E manufactured by Contamac® Ltd, UK. These contact lens polymers buttons manufactured by Contamac® Ltd are well known for their improved wetting, oxygen permeability (Dk) index and flexibility. Table 2.3 shows the comparison of the most prominent Contamac® Ltd contact lens materials available in the market.

Table 2.3 Types of contact lens buttons and their respective properties

	Silicone Hydrogel	Gas Permeable		Hydrophilic	
Classification	Filcon V3	Focon III 2	Focon III 4	Filcon I 2	Filcon II 2
USAN*	Efrolcon A	Roflucon A	Roflucon E	Acofilcon B	Acofilcon A
Swell factor	1.63 at 20 °C	-	-	1.28 at 20 °C	1.36 at 20 °C
Water content	74-75%	-	-	49-50%	59-60%
Refractive index	1.375	1.450	1.432	1.417	1.400
Dry Refractive index	1.510	-	-	1.510	1.510
Light transmission	>99%	>97%	>94%	>94%	>94%
Handling tints	Blue	Blue/green	Blue	Blue	Blue
UV blocker	-	On request	On request	On request	On request
Diameter	12.70 mm	12.70 mm	12.70 mm	12.70 mm	12.70 mm
Thickness	Standard	4.70 mm	4.70 mm	5.00 mm	5.00 mm
Tensile Strength	0.39	-	-	0.35 MPa	0.14 MPa
Elongation to break	180	-	-	210%	140%
Modulus	0.35	-	-	0.36 MPa	0.16 MPa
Hardness (Shore D)	84	83	77	86	83
Cutting speed (RPM)	7-10,000	7-9,000	7-9,000	8-10,000	8-10,000
Permeability (ISO)	60	26	125		

*USAN - United States Adopted Names

As depicted in the Table 2.3, the Contamac® Ltd silicon hydrogel polymer possesses a high light transmission value greater than that of the other polymers but at an average permeability. Roflucon E as a gas permeable polymer possesses the highest permeability as compared to that of the other polymers shown. This is a desired feature to prevent dryness in the eyes in hot climatic regions such as those found in Africa. Also, this gas permeable polymer is the softest with a value of 77 Shore-hardness. For the hydrophilic polymers shown, though they possess a high water content level ranging from 50 to 60% and a high elongation index, nevertheless these polymers do not have a permeability constant value. Therefore, Roflucon E was the selected polymer in this study.

2.4 Manufacturing of contact lenses

The manufacture of biomedical lenses also requires high precision and tolerance with a surface accuracy of few microns or less [14]. Optical aberrations on these lenses caused by geometrical deviations, surface roughness and sub-surface defects of lens from the fabrication process could greatly influence the functionality. Heinrich and Wildsmith [27] state that the tools to evaluate manufacturability and compensation for system dynamics, as well as real-time process feedback are required in contact lens manufacturing of freeform surfaces. Special freeform contact lenses such as the toric lenses are just an entry level of freeform lenses. These lenses are used by patients that have significant complex wave-front aberrations. Therefore, it is necessary to understand and conduct a careful analysis of the optical fabrication process to achieve high optical precision irrespective of optical design.

Traditional optical fabrication spans over an enormous range of manufacturing procedures and test configurations. The manufacture of a conventional lens begins with a glass blank manufacturing and proceeds to the generation of the optical surface. This is done by various diamond shaping techniques such as grinding and polishing. In more recent approaches, IOLs are basically fabricated via compression moulds, injection moulds or precision machining technologies. Three basic techniques are identified for contact lenses manufacture.

They are:

- Spin casting method
- Moulding methods
- Ultra High precision machining.

Based on material choice and size requirement, moulding and spin casting of optical polymer components have long been used for high volumes, low cost and lightweight capability over precision cutting. However, these processes have not been readily accepted in the precision optical fabrication industry because of several difficult issues such as geometry deviation, inhomogeneous index distribution, birefringence and freeform fabrication. Machining has advanced to be a cost effective option for

polymeric materials, since for small to average sized batch production or specific designs, the cost of tooling for moulds and extrusion dies is insignificant.

PMMA lenses can be dry machined with acceptable surface finish due to the high stiffness of the material at room temperature. However, the industry trend is towards selection of more flexible polymers generally characterized by glass transition temperatures that are well below room temperature. The attractiveness of these polymers from a medical standpoint relates to a smaller incision during implanting as well as better oxygen permeability with some of the newer materials. However, machinability is a very difficult proposition for these polymers, since softer polymers lack the stiffness at room temperature to be machined with an acceptable surface finish. Nonetheless, GP lenses may contain very little water, remaining rigid on the eye. GP contacts are made with a computerized precision lathe cutting process similar to that used for lathe-cut soft lenses.

The next section briefly discusses each basic technique employed in the manufacturing of contact lenses, and points out the advantages and disadvantages observed.

2.4.1 Spin casting

Hydrogel lens designs have been successfully created by the original Wichterle method of spin casting for about 40 years. Spin casting offers the advantage of reliable production and low lens cost, However, this process is limited in optical powers as confined by the physical design of the lens [28]. Spin casting, unlike other methods such as lathing, is preferably aimed at the production of low volume to surface area ratio polymer lenses; it is also not employed in the production of polymeric lens susceptible to surface degradation [29]. Spin casting involves spinning the cast into which the monomer mix will be injected, whilst undergoing centrifugal forces, forcing the monomer to fill the required space provided for the lens shape. The injected polymer liquid spreads to the edges of the mould at specific speeds and defines lens properties. Figure 2.6 shows the various steps involved in spin casting, from the polymer insertion to packaging.

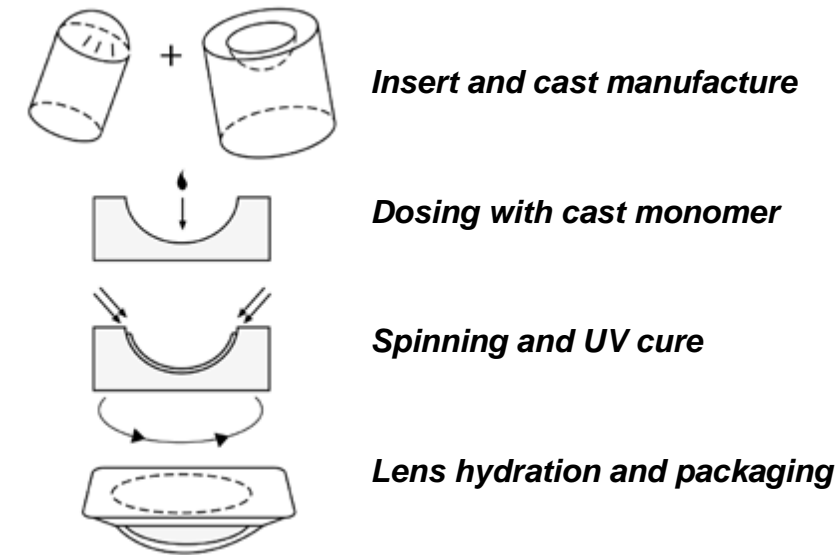
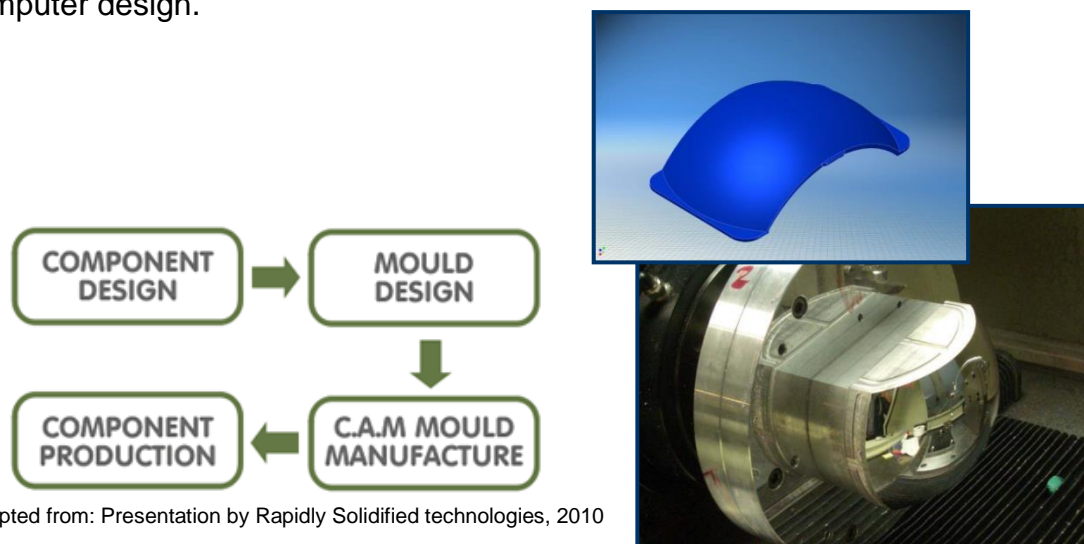


Figure 2.6 The spin-casting process [21]

In this process, the optical mould is responsible for the interior quality of the inner face of the lens. The final power of the finished lens is dependent on several factors. These are gravity, centrifugal force, surface tension, volume of monomer mix and spin speed [29]. This lens manufacturing process however faces issues during the creation freeform due to its low flexibility.

2.4.2 Plastic injection moulding

Moulding the lens can be carried out in several ways. The various available moulding techniques are spin cast, injection and compression moulding. Figure 2.7 shows a diagram of the moulding process flow, a sample manufactured mould and its computer design.



*adapted from: Presentation by Rapidly Solidified technologies, 2010

Figure 2.7 Moulding process flow diagram, 3D mould design and machined mould

Lenses produced from moulding techniques are seen in numerous technological applications such as surveillance systems, projection lenses, and optical heads. Injection moulding as an optical production method, offers a more reliable mass production moulding technique than its counterparts. This process presents a cost-efficient method for manufacturing optical surfaces such as flats, spheres and also aspheres that are meanwhile state-of-the-art in the field of plastic optics [30]. A review of the manufacturing process shows that moulded plastic is firstly injected at high pressure into the plastic mould and then it is allowed to cool and solidify before shaped lenses are extracted. The demands for image quality of optical components produced through injection moulds, however, are less severe than machining. Nonetheless, for the replication of optical plastic or glass components, moulding inserts with specific functional surface and subsurface requirements are needed to withstand the thermal and mechanical loads during the replication process and to ensure the desired optical part quality with a nanometric surface roughness and high form accuracy. Therefore, Brinksmeier et al. [12] in their research presented a process chain consisting of a thermo-chemical surface treatment and a sub-sequent diamond cutting process for the manufacturing of optical moulding inserts to achieve such surface requirements.

Despite its advantage in large production, injection moulding is faced with drawbacks in geometrical deviation of mould design and inhomogeneous index distribution during manufacturing [31]. The geometry deviation resulted from volume shrinkage and warpage are strongly dependent on process conditions. The inhomogeneous index distribution resulted from the residual stresses and non-uniform molecular orientation in the injection moulded parts. Plastic moulds are also limited in their flexibility in creating complicated geometries such as freeform based on mould design limitations. Furthermore, tooling expenses for injection moulded plastic optics differ greatly, with some more complex optics demanding more expensive tooling. These are the main reasons that injection moulded polymer optics are not particularly suited for all high precision applications. Therefore, the investigation into alternate machining processes with higher performance for high precision polymer lenses is essential and ultimate to providing an affordable high precision manufacturing process for satisfactory optical performance.

2.4.3 Ultra high precision machining technique

Ultra-precision machining dates back to 1966 and since then this technology has greatly progressed due to considerable advances in materials, tools and other supporting technologies [32]. Chiu and Lee [32] stated that the ultra-precision technique based on single-point diamond turning (SPDT) and ultra-precision diamond grinding (UPDG) have become an indispensable tool for economic making of ultra-high-quality products.

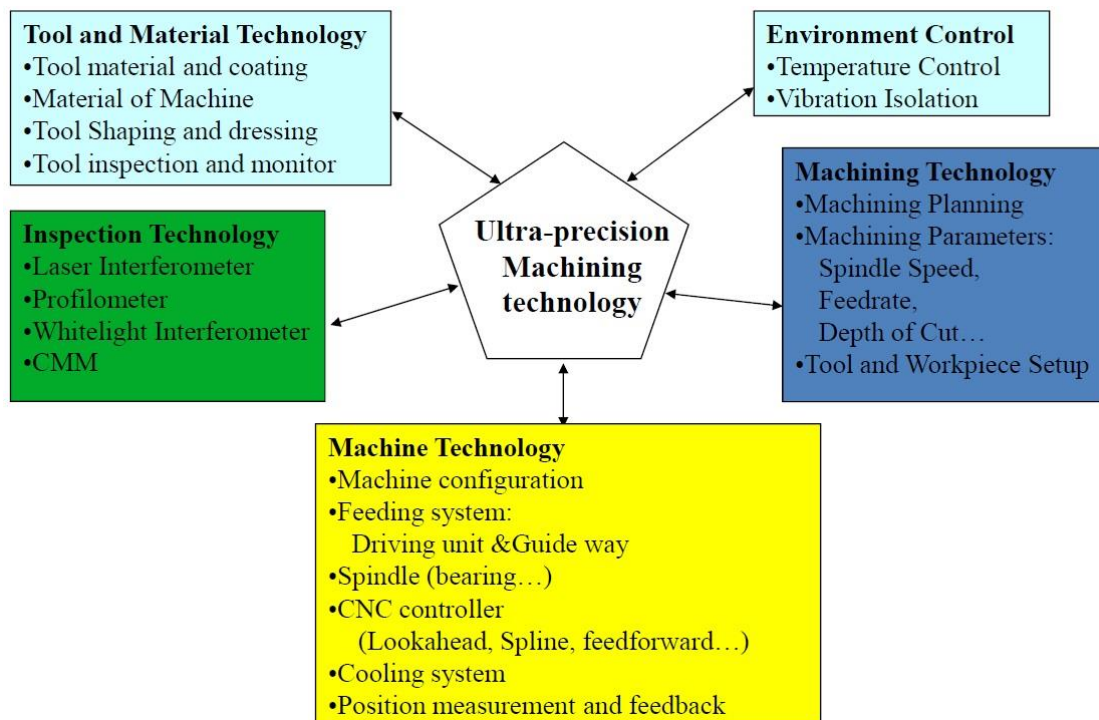


Figure 2.8 Ultra-precision machining technology [33]

Manufacturing of precision optics with diverse freeform surfaces is also a core component of contact lens production. Due to some isolated medical conditions, custom optical solutions have become a necessity in ophthalmology. Today's ultra-precision machining system is built on fundamental precision engineering principles coupled with leading edge technologies in controls, drive and feedback devices [34]. Ultra-high precision diamond turning (UHPDT) has thus become a generally acceptable manufacturing technique with the ability to produce freeform optics of various custom surface profiles for such applications. Some complex optical forms which can be produced through SPDT are: aspheric, toric and complex geometrical lens profiles. This optical manufacturing technique also boasts of a nanometric range

tolerance below $< 10\text{nm}$. UHPM techniques encapsulate tool and material technology, inspection technology, machining technology, Machine forms and environmental control (Figure 2.8). The growing market of precision, optics and micro technologies systems has pushed combined advances in process technologies, as well as measuring and testing quality assurance linked to this production process. Major advances in UHPM over the years have been achieved in the area of machine control, feedback systems, servo drives and general machining design [35].

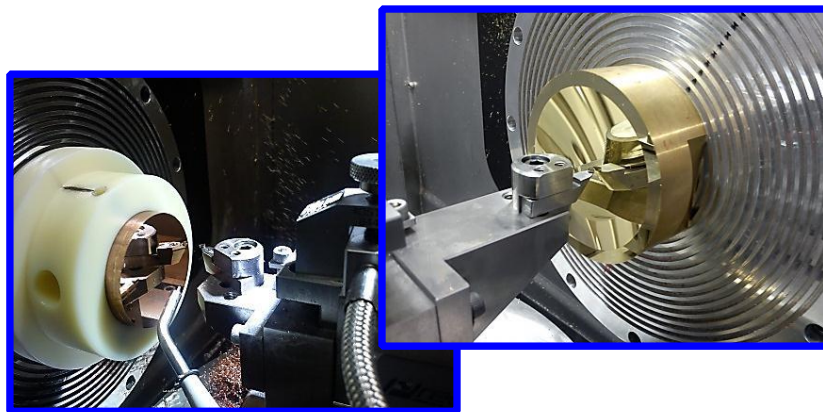


Figure 2.9 Ultra-precision diamond turning of freeform optics

At present, the ultra-precision machining of single point diamond cutting is the most effective process for the generation of high quality functional surfaces with minimal defects in the superficial surface layer [4]. This perspective is viewed from various materials, especially from thermoplastic amorphous polymers and their composition for optical, photonic and bioengineering applications. Applications of UHPM are seen in divers fields of study such as aerospace, automotive, solar energy harvesting, control and sensing, communication (fibre optics), entertainment (display devices) and medical. Figure 2.9 shows some applications in the use of ultra-precision diamond turning of free form optics. Figure 2.10 shows some various optical forms produced for distinct industrial uses.

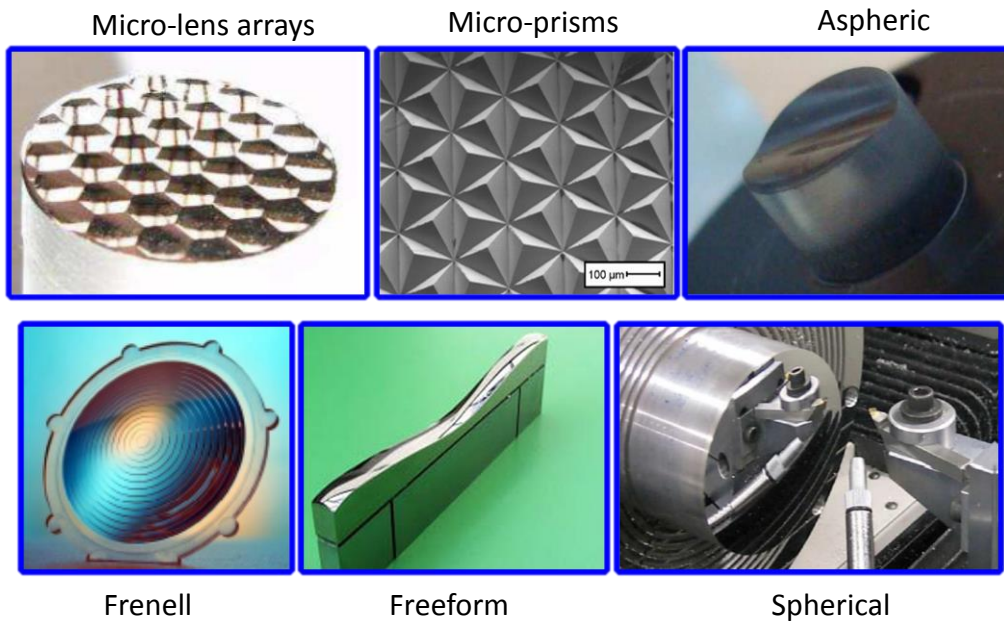


Figure 2.10 Various optical objects used in critical industries [33]

According to Bylinsky [36], it is estimated that the world market share value of ultra-high precision machines is approximately \$100 million with a constant growth rate of about 5% annually. Freedonia Market Research in 2011 identified the World demand for machine tool products rise to a strong 9.4% per year through 2014 to \$121 billion. In their survey they identified the global market for metal cutting machine tools to expand to 8.6% per year through 2014 to \$61 billion, with growth aided by a recovery in key end-use markets in the developed world. According to their research, metal cutting tools will continue to account for a majority of the total machine tools market in 2014 [37].

Currently, the technology of UHPM is found concentrated in established economies such as the United States, Germany and Japan, as well as emerging and economies, for example Brazil, India and South Korea. There is also a rapid growth in other countries such as Singapore and Hong Kong which mainly serve as high tech support to optical instruments.

Major advances in UHPM over the years have been achieved in the area of machine control, feedback systems, servo drives and general machining design [35]. A commonly used UHPM process in contact lens manufacture is single-point diamond turning (SPDT).

SPDT as a sub-form of UHP machining technique uses a finely polished monocrystalline diamond cutting tool (Figure 2.11). This nanometric process is capable of producing complex-shaped surfaces with a form accuracy of $1\mu\text{m}$ or less and roughness under 10 nanometres [38] as shown in Figure 2.12. Its capacity for high accuracy has also made this process widely used in the production of micro-electromechanical devices and medical optics [39]. Some complex optical forms which can be produced through SPDT are: aspheric, toric and complex geometrical lens profiles (Figure 2.10).



Figure 2.11 Ultra-precision diamond tools [40]

Based on its accuracy, SPDT is also highly sensitive to changes within the machining environment. Thus, instability could directly affect micro-forces occurring between the cutting tool edge and the workpiece and this may further result in poor attainable surface finish in optical manufacturing.

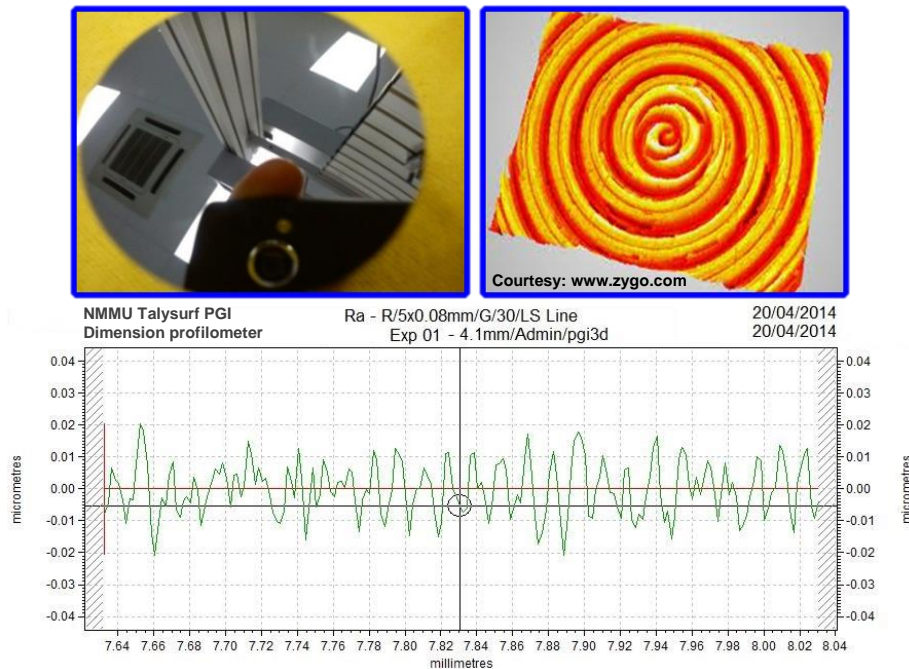


Figure 2.12 Ultra-precision machined lens with 3D image and low form accuracy

2.4.4 Research & barriers in the ultra-high precision manufacturing of polymers

Despite the increased acceptance and use of optics in the biomedical industry [14], nevertheless some challenges are still experienced in the manufacturing optical of polymers. These are experienced as geometrical deviation of mould design, wear and inhomogeneous index distribution occurring during optical manufacture. Furthermore, the effects of elastic recovery after machining hinges upon the choice of parameter combinations and machining conditions. These disadvantages constitute some of the barriers experienced in polymer optics manufacture. The section below evaluates some of the barriers and challenges in contact lens manufacturing.

Some additional barriers experienced in UHPM are:

- Machine programming for freeform surfaces
- Micro-chatters
- Thermal instability (environment control needed)
- The continuous development of new materials
- Unavailability of micro sensors for UHPM

2.4.4.1 Elastic recovery in polymer machining

Elastic recovery is the inherent ability of a material surface to return to a deformed state after unloading during cutting operation. It operates based on the rearrangement of atoms within the material based on changes in temperature, stress and strain experienced from loading. Elastic recovery of the deformed region after unloading yields to a change in the granular structure of the surface of the lens. This phenomenon in machining causes huge losses of surface quality in optics.

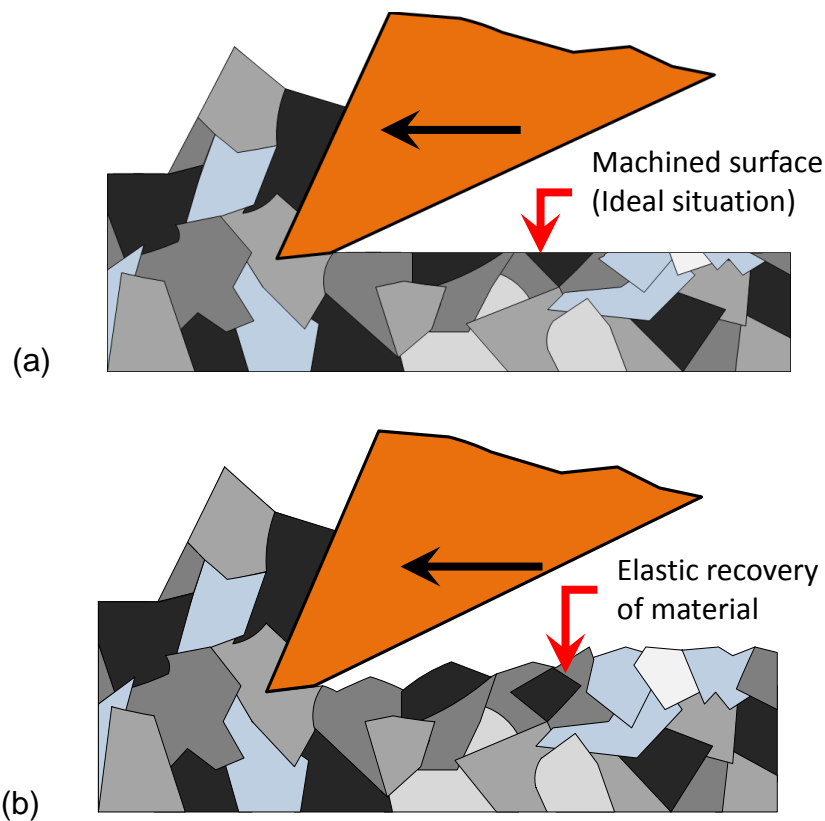


Figure 2.13 Elastic recovery phenomenon after diamond cutting

Gauthier et al. [41] in their study evaluated the elastic recovery of a scratch on a polymeric surface. Within their study, they modelled the recovery rate during full plasticity on PMMA around a moving conical/spherical tip. Also, Friedrich et al. [42] in their research show the elastic recovery and scratch resistance found in certain high performance polymers. From their research they explain the phenomenon of elastic recovery during the cutting of a commercial grade PMMA polymer. There is thus a need to consider the effects of elastic recovery in UHPM and take account of the grain structures of material during manufacturing of optics.

Figure 2.13(a) and (b) show the initial grain structure of an ideal machined surface and the actual surface reactions with elastic recovery of the grain structure after unloading.

2.4.4.2 Diamond wear in polymer machining

Despite high accuracy produced in UHPM of polymers, relatively large diamond wear formed on the tool may largely influence surface quality (Figure 2.14). Since no research work exists for this polymer it is necessary to consider a wider look at diamond wear in SPDT. Lane et al. [43] studied the thermo-chemical wear model and worn tool for single crystal diamond while cutting tool steel. In their study they identify diffusion based on elevated temperatures as a factor for wear formation in diamond tools. Abou-El-Hossein et al. [44] also in their research on rapidly solidified aluminium machining, identified a tribo-chemical reaction as a probable cause of wear formation at elevated temperatures. Other research works have identified other wear mechanisms found during the UHPM of polymers [4, 45]. Gubbels, van der Beek et al. [41] in their research on ultra-high precision turning of polymers identifies two dominant wear mechanisms, namely: Gubbels et al. [45]

- Tribo-chemical wear
- and triboelectric wear

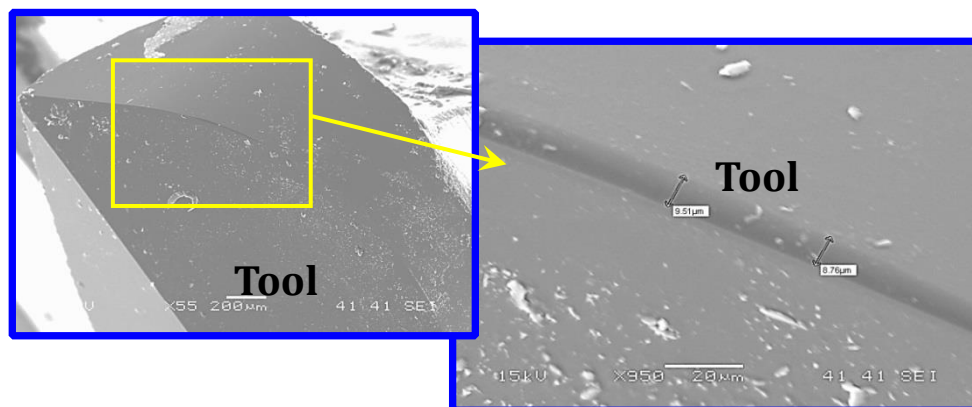


Figure 2.14 Diamond tool wear [44]

2.4.4.3 Tribo-chemical wear in polymer machining

This wear mechanism is also depicted as the breaking of the tightly bonded diamond lattice. When this happens, a carbon atom of the diamond may diffuse into the

workpiece, graphitize, and react with oxygen to form a dioxide, or with the workpiece to form carbide. In the monomer below (Figure 2.15), the ester bond in methyl methacrylate breaks away to combine with carbon atoms of the diamond tool under extreme temperatures leading to a gradual degradation of the diamond tool tip (Figure 2.16).

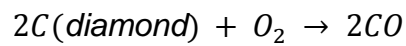
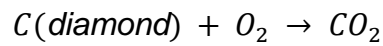
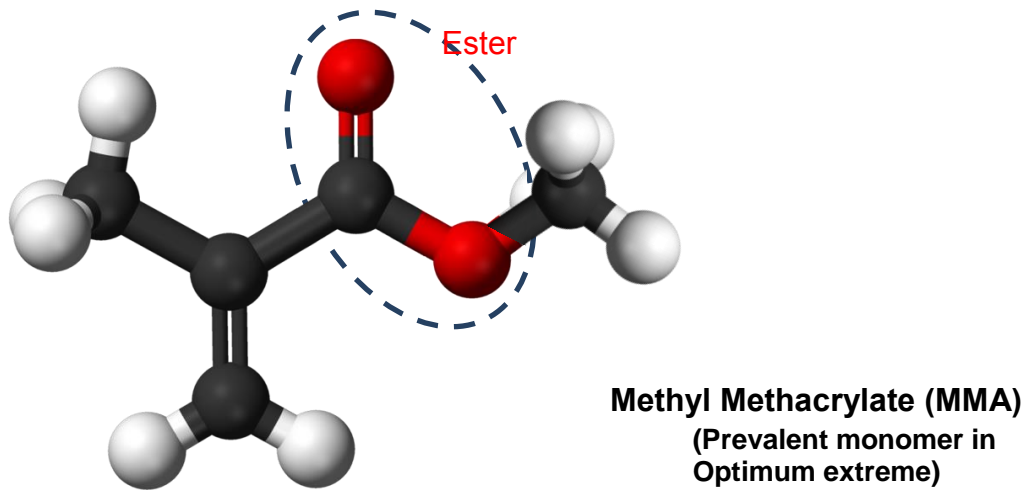


Figure 2.15 Methyl methacrylate (MMA) ester bond

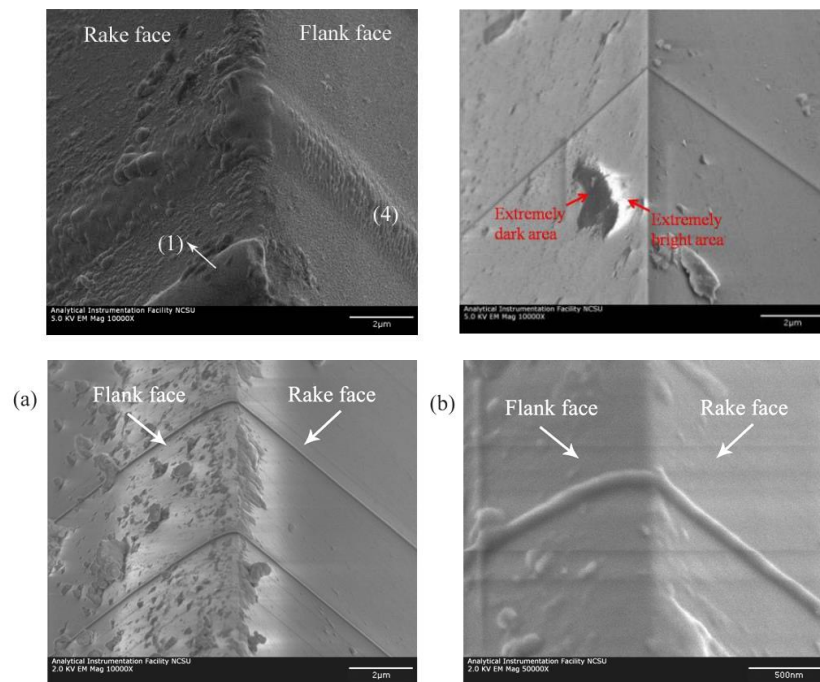


Figure 2.16 Chemical wear on a diamond tool [46]

Commonly used types of diamond wear are: adhesion, abrasion, tribo-thermal and tribo-chemical. These wear mechanisms are known to be able to operate independently or in combination with others during machining. Besides that fact, one of these mechanisms takes precedence in impact over others during research and is accountable for rapid tool wear. Adhesive wear based on the weak interactive forces of the workpiece causes the transference of mother material between workpiece and tool. This reaction is easily observed in macro and micro machining tools based on the types of cutting tools used. The adhesion reaction during cutting, however, is directed towards the softer material. In UHPM of contact lenses, adhesive reactions are drawn towards the polymer (the softer material) creating negligible adhesive effects on the tool. Therefore, adhesive wear is considered only as a collaborative wear mechanism in polymer machining. Abrasion in the same manner reacts based on the dissimilarity in the hardness of two materials. And thus based on hardness of diamond it is postulated its effects are minimal except in extensively prolonged polymer machining.

The influence of temperature cannot be ignored in tool wear formation. Research works have identified various temperatures recorded during diamond machining [47]. Jasinevicius et al. [47] identified the temperature during the single point diamond turning of non-ferrous metals. In their article of silicon crystal they established that the temperature on the cutting edge and rake face is not sufficiently high to thermally reduce diamond strength. Abdel-Aal et al. [48] in their paper indicated that the rise in workpiece surface temperature was comfortably lower than the thermal softening temperatures for non-ferrous metallic materials under the conditions applied. Particularly the temperature rise was of about 80 °C for germanium and less than 400 °C for silicon. According to Hurt and Decker [49], during diamond machining temperatures may reach values as high as 427 °C (or 700 °K). Such temperatures may influence the physical properties of the diamond. At additional levels of 700 °C diamond oxidizes in air to form gaseous by-products, such as carbon monoxide and carbon dioxide as shown in Figure 2.15. This oxidation effect from high temperatures represents a mechanism of wear-occurring polymer machining known as tribo-thermal wear which precipitates chemical wear formation. Other publications [50, 51] have identified cutting temperatures in diamond machining to be between 90-380 °C in turning metal alloys. Despite the number of studies done in temperature

measurement, machining is challenged by cutting scale and heat detection at that scale. Due to these challenges various attempts at estimating temperature have been devised, some of which relate the influence of some cutting parameters on temperature for estimation, FEA analysis of heat point and molecular simulation [51-53]. In plastics machining, Gubbels [9] integrated a thermocouple into the diamond tool for temperature measurement and identified temperatures obtained in machining to be around or above 200 °C.

Tribo-chemical wear can be explained in diamond turning by the chain scission of monomers which forms highly reactive radicals [54]. This chemical reaction could be observed by a “chipped” effect on the diamond surface. In their research Gubbels et al. [45] account wear patterns observed on PC and PMMA to chemical causes.

Another wear mechanism associated with elevated temperatures is Triboelectric wear which originates from the presence of tribocharging reflected by the adhesion of the chip around the tool [55, 56]. This form of wear was studied by Gubbels [9] who identified them to be one of major importance to diamond during the machining of glassy polymers.

2.4.4.4 Triboelectric wear in polymer machining

UHPM technology has also spurred research in the catastrophic wear of diamond tools when machining various materials [54, 57]. Despite all known advantages in nano-machining, UHPM of polymers using single point diamond tools is challenged by the presence of various wear mechanisms which affect surface quality. Currently there exists a limited amount of research work in polymer machining and diamond machining of contact lens polymers despite the great application of this technology in daily electronics. Current findings in the field still need additional experimentation for validation and expansion with a wider range of tested polymeric materials.

Despite its recognition as an adequate manufacturing technique for optical polymer production by various researchers [39, 58], another important cause of wear on the tool is due to triboelectric phenomenon. Contour Fine Tooling [56], a UK tooling firm, states that the wear in monocrystalline diamond tools when cutting polymers, is generally 5 to 10 times higher than when cutting copper with the same parameters. This phenomenon was explained by the difference in hardness between diamond

indicates the tendency of inclination in acquired charge of a material after tribocharging.

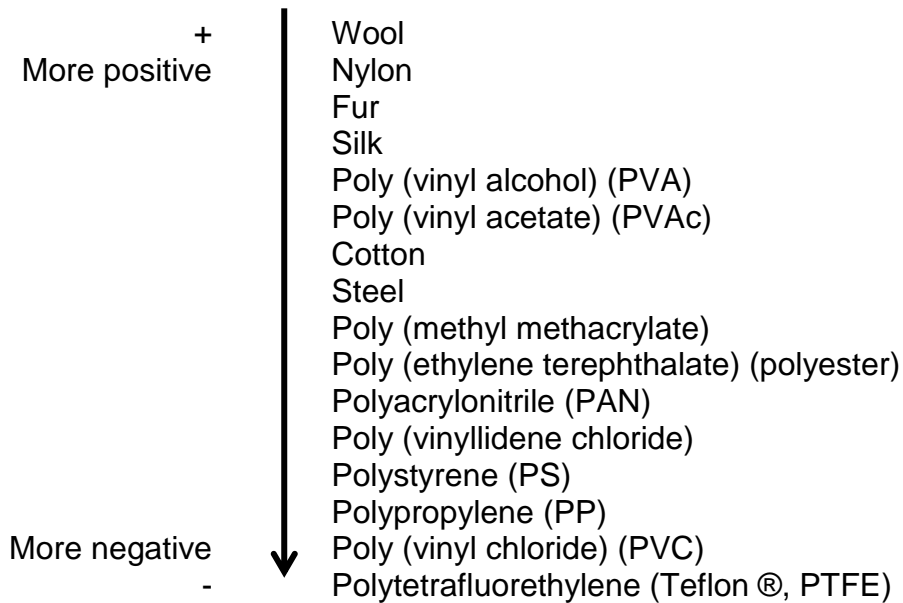


Figure 2.18 Triboelectric series [63],

Understanding the mechanism by which static charge is generated on or disappears from polymer surfaces has proven to be difficult. Questions remaining largely unanswered include [63]:

- The chemical and physical origins of the triboelectric series
- The mechanism of contact and tribocharging of polymer surfaces
- The mechanism by which the charge disappears from the surface after generation.

The mode by which materials applied to the polymer surface can substantially effect either the generation of static charge or the dissipation of the charge. Table 2.4 shows a summary of triboelectric charging mechanisms and how charges or ions move from one material surface to another

Table 2.4 Summary of triboelectric charging mechanisms by Williams [64]

Interface	Charge exchange agent	Interpretation
METAL-METAL	ELECTRONS	
METAL-INSULATOR	ELECTRONS	
Insulator non-ionic	Mobile transfer (hypothesis)	Mobile ions , when present predominate over other mechanisms
Insulator with mobile ions		
INSULATOR-INSULATOR	MOBILE IONS	Mobile ions , when present predominate over other mechanisms
Mobile Ions present		
Both non-ionic	MOBILE IONS H ₃ O+OH (in presence of water)	

In understanding the mechanism of contact and tribocharging of polymer surfaces, Figure 2.19 gives a pictorial explanation of the triboelectric formation. During triboelectric effect, electrostatic voltage is generated on materials surface due to the transfer of free electrons or ions during the rubbing action between the tool and the surface of the polymeric workpiece. This situation is derived from the electrons restriction in material due to their inability to escape from the material surface (Figure 2.19(a)). As electrons fail to reach a conducting path to ground a stage is reached where electrons jump across from a highly electron concentration surface to a surface lower magnitude until static saturation occurs (Figure 2.19(b)). They initially remain concentrated at the surface at the polymer due to its low atomic conductivity. At saturation, electrostatic potential difference exceeds the dielectric breakdown threshold of air (being the common medium between the material surfaces) through the path of least resistance for charge stabilization. This saturation point indicates high magnitudes and can be seen as a transient spark during static discharge (Figure 2.19(c)). Charge separation could occur through the following processes [9]:

- Rubbing of dissimilar materials
- Diffusion of charges in a living cell
- Convection separation of charge in clouds
- Chemical separation of charge in batteries.

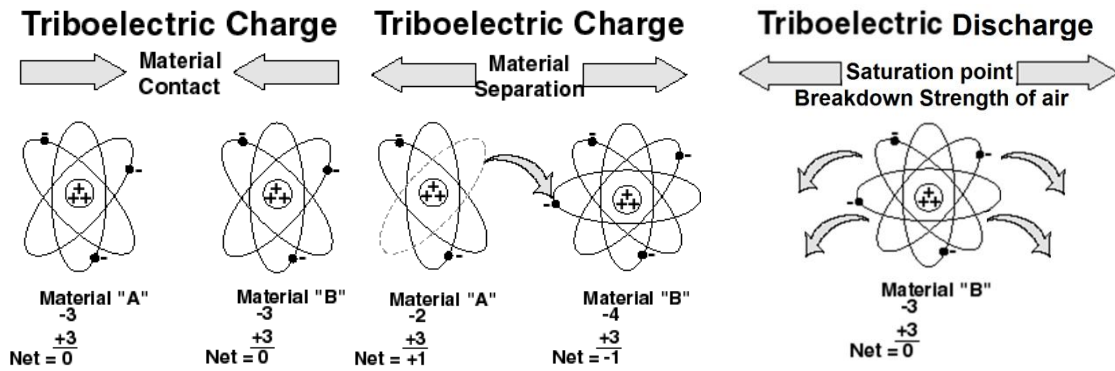


Figure 2.19 The Triboelectric Charge –(a) materials make intimate contact (b) materials separate (c) saturation point. Adapted from: Asuni [65]

Electrostatic which could be also identified as isolated charges is seen as in the charge concept flow in (Figure 2.20) which refers to the unintentional build-up static charges on material surfaces. This is created by the generation of ions. In reality, the Electrostatic phenomenon is as a consequence of the atomic nature of matter. It spurs of from an electrical atomic imbalance from the separation charge.

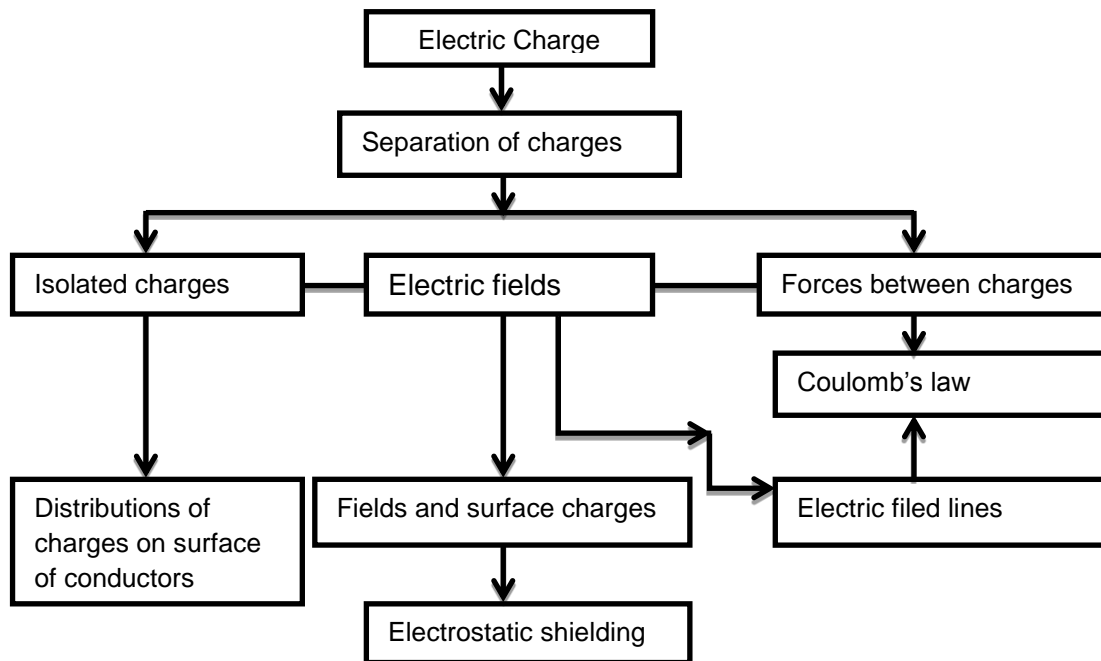


Figure 2.20 Flow concept of static charge [9]

This phenomenon is often found in non-conductors which trap freely moving electrons. Eq. 2.3 shows the potential voltage equation generated between dielectrics.

$$V = \frac{q}{C} = \frac{q \cdot d}{\epsilon \cdot A} \quad (2.3)$$

Where, V is the voltage difference, q is the charge, C the capacitance of the capacitor, ϵ is called the permittivity of the dielectric material between the plates, d the diameter and A is the area of the plates. Gubbels et al. [9, 66] in their study measured this static voltage using an electrostatic voltmeter, and using Eq. 2.3 linked the voltage to the estimated amount of charge to identify the amount of energy for electrostatic discharge. For evaluating triboelectric wear equation 2.4 below forms the baseline. It describes the kinetic energy (U) on an ion during acceleration.

$$U = E \cdot Q \cdot \lambda \quad (2.4)$$

Where, the energy U during acceleration, λ the mean free path of the particle and E is the electric field strength. For an electron in atmospheric air the mean free path is $\lambda_e = 10^{-5}$ m, and for an ion in atmospheric air the mean free path is $\lambda_i = 10^{-7}$ m. The acquired energy can be used for damaging the diamond surface by impingement of the particle and detachment of a carbon atom, which requires energy of 7.4 eV [9].

Williams [64] in a review of triboelectric charging of insulating polymers identified the effects of force exerted during polymer rubbing and depth of material removed as factors which influence static charge magnitude. Generally ESDs suggest a transfer of electrons from a high concentration surface to a lower concentration across dissimilar materials. From literature [60] it is identified that electrostatics transfer high electron concentration measured in Coulombs from a surface of a relatively negatively statically charged surface to a relatively positively statically charged surface.

A lucid explanation of charge in atoms is necessary to comprehend the principle ESDs occurring in UHPM. In insulating materials, electrons are not able to redistribute from the negatively charged area to the positively charged area due to the large band gap required to move electrons from the valence band to the conduction band. In conductor materials, electron conduction occurs easily because the energy band gap between the valence electron shell and the conduction band is infinitely small or they may overlap. In either case it takes very little to no energy to

promote an electron from the valence shell to the conduction band. This small amount of energy can easily be supplied by any thermal energy above zero K°. Conductive surfaces will, therefore, have uniform charge distributions as electrons are easily transported from regions of high concentration to areas of low concentration [60]. This follows the law of conservation of charge, which states: “that charge can neither be created nor destroyed, but only transferred from one entity to the other” [67].

Diaz and Felix-Navarro [68] created a semi-quantitative triboelectric series for polymeric materials. In their study they examine the influence of chemical structure and properties of the polymers on their charging magnitudes. Their study not only connects the results of various triboelectric series from research but also relates the overlapping results of several reports and gives an estimate of the relative charging capacity of numerous polymeric materials. They also reaffirm that charging results are due to proton or ion transfer between the surfaces in contact.

Experiments have also shown that relative humidity (RH) has a very big influence on the electrostatic charging and therefore, on the tool life. Below 60% RH strong electrostatic charging occurs; 60% to 70% RH is a transition area and above 70% RH no electrostatic charging is observed [56]. In a study on the influence of relative humidity on Aeolian electric field by Xie and Han [69], they found that low humidity below 30°C generated far higher magnitudes than higher humidity ranges. In their study, they explained the effects of high humidity in deionising sand particles from the wind vane fans.

2.5 General behaviour of polymers in diamond machining

Various polymeric materials have been machined in UHPM processes. Numerous research works have studied the various effects of machining polymers with diamond tools [4, 6, 7, 45, 70-73]. These materials range from polycarbonate (PC), polystyrene (PS), nylon and poly methyl methacrylate (PMMA) [6, 45] to industrial co-polymers.

Based on the differences between polymers and metals during machining, this section therefore gives a short introduction to the behaviour of polymers in

machining. Polymers, depending on their molecular weights, could respond as brittle or ductile materials. Intrinsic material behaviour in polymers could also be explained based on temperature. A study by Carr and Feger [70] on PC and PS, expresses that material is removed via ductile, brittle, or transitional mechanisms and this depends on polymer properties such as glass transition temperature (T_g), relaxation time, degree of crosslinking, and viscosity. Above glass transition temperatures, polymers enjoy thermodynamic equilibrium for ductile mode machining. However below this T_g (as seen in Figure 2.21), a thermodynamic condition called "aging" occurs. This condition yields a rough surface from the brittle fracture of the polymer after machining. Aging is caused by the shrinking of free volume space as lower temperature and atomic movement foster a readjustment of atomic positions. Gubbels et al. [72] in their research identified aging as an influential factor in mechanical response of a polymer.

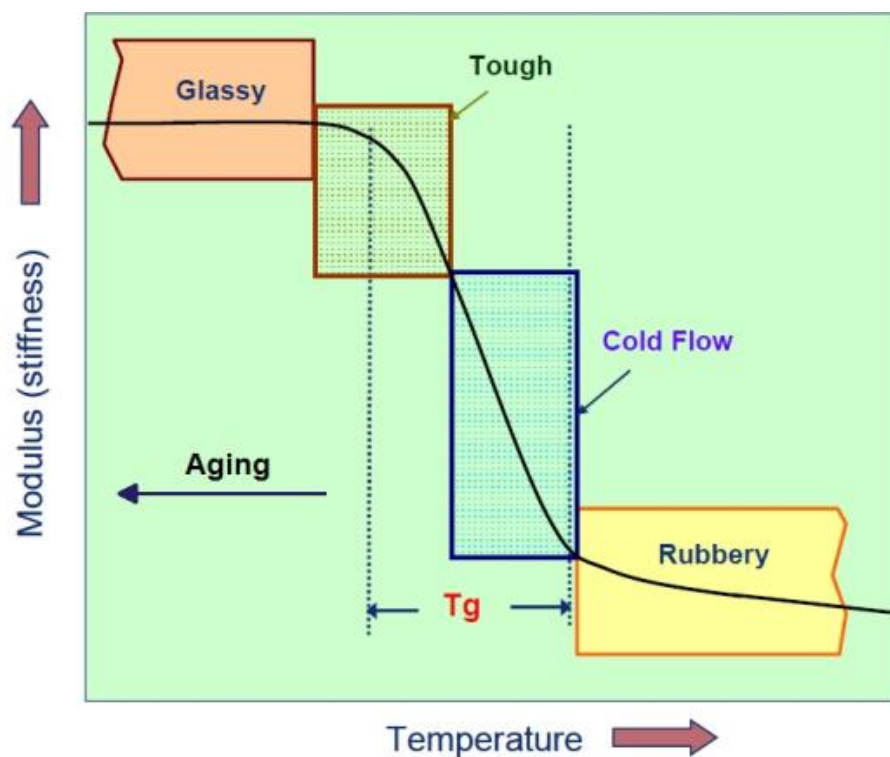


Figure 2.21 Glass transition temperatures during machining [74]

For a ductile workpiece, the melt viscosity of the polymer is important. The change from ductile to brittle mode in polymers could also be experienced on polymers by changing operating and tool parameters. Research [70] identifies that in brittle materials, the surface roughness is largely controlled by the rake face angle of the diamond.

Three main factors are known to influence the roughness and product shape [70, 73]. These are:

- Machine environment such as vibration isolation, temperature stability
- Process parameters e.g. cutting speed, depth of cut, feed rate and geometry of the diamond insert
- The physical and chemical properties of the material.

As discussed earlier, in polymeric materials, these physical properties of polymers are significant factors in determining the quality of the surface integrity. Surface deformations can be identified through specific defined optical errors. These errors and surface parameters are clearly explained below.

There are three types of errors that may occur on a machined surface during SPDT. These are the form, figure and roughness errors. Due to their close proximity in definition, these types of errors are identified by their causes. “Roughness error” is formed due to irregularities inherent in the machining process (e.g. cutting tool, and feed rates). “Figure error” or waviness may result from vibrations, chatter or workpiece deflections and strain in the material. “Form error” is the general shape deviation of the surface from the intended shape, neglecting variations due to roughness and figure error [71]. Figure 2.22 shows the three types of errors that may occur on a lens profile, after being machined by the diamond tool.

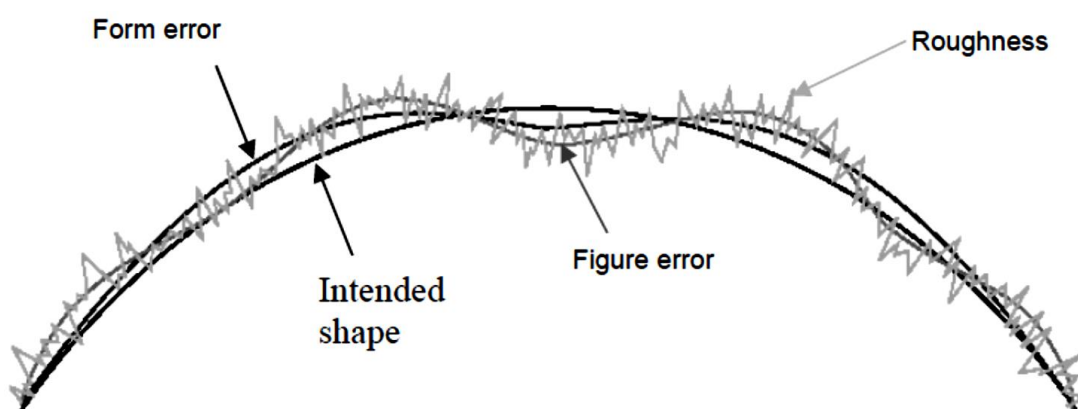


Figure 2.22 Three types of errors from turning operation: form, figure and finish [71]

This research consists of seven experiments derived from a combination of three machining parameters via a statistical approach. Each experiment would encompass a detailed analysis of the surface roughness of an area of $24 \times 24 \mu\text{m}^2$ of the lens

buttons using atomic force microscopy (AFM). Research has shown that AFM is a powerful characterization tool for polymer science, capable of revealing surface structures with superior spatial resolution. AFM is thus extremely useful for studying the local surface profile and roughness properties of a broad range of polymer material [75].

The results obtained were used to correlate the surface finish of the polymeric lens to influential cutting parameters.

2.5.1 Parameters to evaluate surface roughness

Surface roughness measurements are done using profilometer which directly measure the texture of a surface and represent the acquired surface in the form of profile graph [76]. The commonly used parameter for characterizing the surface roughness is the average roughness R_a which is defined as:

$$R_a = \left[\frac{1}{N} \int_0^N |z| dx \right] \quad (2.5)$$

Where $z=f(x)$ is the dimensional surface profile or roughness curve that can be obtained by several methods, L the length of the profile been accessed [76].

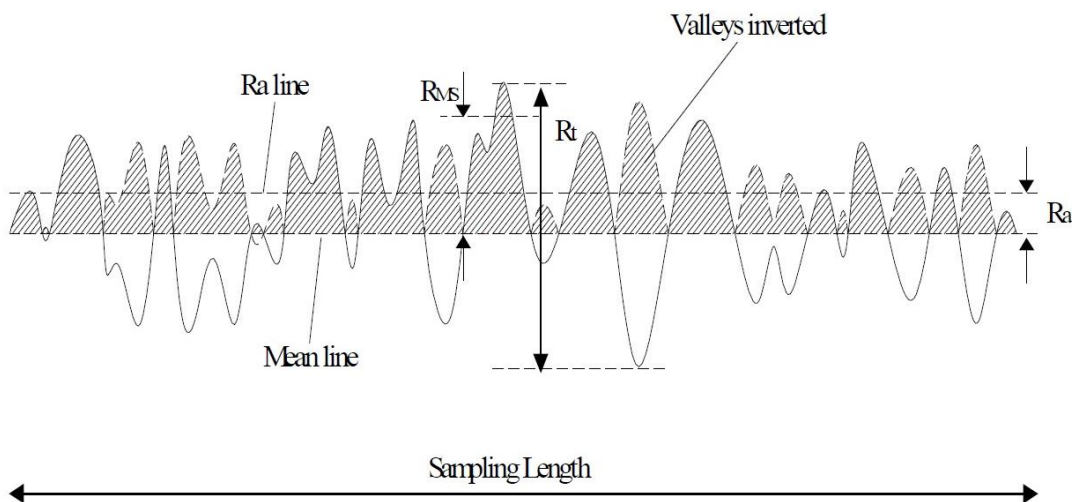


Figure 2.23 Description of surface parameter [77]

The Figure 2.23 shows a description of the surface parameters in estimating the surface roughness of an optical component. From the Figure, R_a shows an average band of mean roughness of the surface line based on the peak magnitudes of either side.

2.6 Modelling of ultra-high precision machined polymers

Different modelling methods have been employed to study machining operations. These methods range from statistical methods as mentioned in the previous section to graphically represented simulations such as curve fitting models. Dandekar and Shin [78] in their review of modelling of machining composite materials, identify methods such as finite element modelling (FEM), molecular dynamics simulations and multi-scale modelling as methods of interest in physical modelling techniques. Finite element simulations have been successfully used to predict flow of chip, fibre-based composite interactions and temperature change during cutting [78, 79]. The multi-scale modelling method alternatively, seeks to understand the evolution and progression of the damage from the molecular to the macroscale [78]. It is implemented by a modelling combination of atomic simulations and continuum mechanics solutions.

2.6.1 Response surface method

The response surface method (RSM) is a suitable method in establishing the effects of parameters in machining. This technique optimises responses which are directly influenced by known system variables using a developed spatial model. It does this by creating an n-dimensional surface using a collection of design techniques in the experimental study of relationship between the measured responses and a number of input descriptive variables. As a modelling technique, RSM seeks to establish the relationship between descriptive variables and single or more responses. The n-dimensional surface characterizes all balanced and possible designs. This surface consists of a finite number of points in space. These points are carefully selected and determined by a created response surface experiment software design and not the designer. These selected points can be used to interpolate other design points on the surface and establish predicted responses. Examples of response surface model techniques are the three-factorial design model, The Box-Menken (BB) model and the central composite design model (CCD). In summary, the response surface design can be used to perform predictions of parameters on created surface plot.

Generally, the response surface method is described as an equation in the form:

$$Y_u = \beta_o + \sum_{i=1}^W \beta_i X_i + \sum_{i=1}^W \beta_{ii} X_i^2 + \sum_{i,j=1}^W \beta_{ij} X_i X_j + \epsilon, \quad (2.6)$$

where Y_u , is the corresponding response, e.g. the surface roughness value (Ra) produced by the various process variables in UHPM and the X_i (1, 2 . . . , S) are coded levels of W quantitative process variables, the terms β_o , β_i , β_{ii} and β_{ij} , are the first and second order regression coefficients and ϵ the experimental error or the lack of system fit. The designer can rectify poor fitting of the model by adjusting design space and alternating levels of descriptive variables. The second term under the summation sign of this polynomial equation is attributable to linear effect, whereas the third term corresponds to the higher-order effects; the fourth term of the equation includes the interactive effects of the process parameters.

2.6.1.1 Box-Behnken response surface method

The Box-Behnken response surface method is a class of response surface design used in statistic modelling. This design class offers the possibility of addressing experimental boundaries and avoids factor combinations that are at extremes. It does this by creating a spatial representation of an experimental problem using centre points on frame edges and not corners of its spatial design. Extreme conditions depict parametric combinations found at the corners of its spatial model.

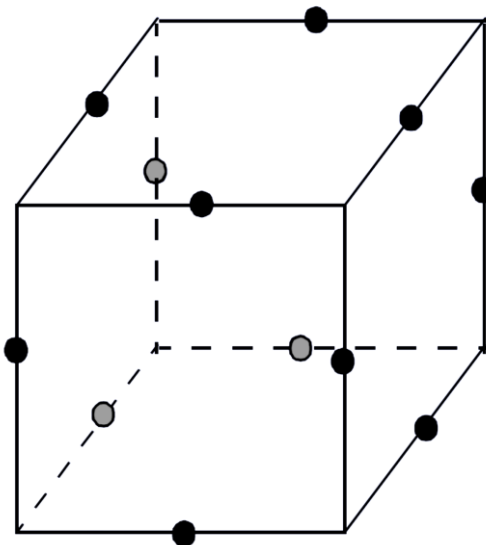


Figure 2.24 Box-Behnken statistical model

The Box-Behnken is an RSM method with three-level nearly orthogonal, resolution V design used for modelling factors with three levels. The slight non-orthogonal design

matrix is not a concern if the analysis is conducted using least squares regression. Figure 2.24 shows an example of a scatterplot diagram with various calculated spatial points used to determine the influence of descriptive variables on one or a set of responses. As shown earlier, for three factors, the Box-Behnken design does not include any corner points of the design space. Therefore, if the corner points are infeasible, the Box-Behnken design should be used to generate the quadratic curved response surface. Yet the disadvantage is that the BB design will produce a higher uncertainty of prediction near the corner points [80] but requires fewer data points for predictions. The main advantages of this experimental design method are that it only requires three levels for each factor; its design's ability to rotate and its lower requirement for experimental runs for 3 or 4 factors.

With the combination of parameters in diamond turning of polymers, RSM Box-Behnken can be applied to the polymer machining concept in response areas such as surface generation, cutting force determination and tribological wear determination. These various output responses from UHPM of polymers hold the necessary variables required for modelling and could be used to examine the impact of changing factors on the response.

2.6.2 Atomistic Simulation methods

There are numerous atomistic simulation methods that exist. Some commonly known are the Ab initio Molecular Dynamics Method, the Semi-empirical Molecular Dynamics method, the Empirical Molecular Dynamics method and the Monte Carlo Method. These various MD techniques have been applied in various spheres of molecular predictions and have different notable differences when applied. Table 2.5 shows the advantages and disadvantages of each method.

Table 2.5 Comparison of some atomistic simulation methods [13]

Method	Applications and Advantages	Disadvantages
Ab initio Molecular Dynamics Methods	More accurate solution	Computationally expensive –suitable for hundreds of atoms
Semi Empirical Molecular Dynamics Methods	A trade-off between ab-initio and classical MD methods. Can handle up to thousands of atoms	Less accurate solution than in ab initio methods
Empirical/Classical Molecular Dynamics Methods	Less computationally expensive than ab initio MD	Simulations are for shorter times than in MC
Monte Carlo Methods	More efficient /time saving, can be used for larger time frames, time is controllable	Doesn't allow the time evolution of the system in a suitable form for viewing

2.6.3 Molecular Dynamics (MD) Simulation method

MD studies as a modelling technique was initiated in the late 1950s at the Lawrence Radiation Laboratory (LRL) in the United States by Alder and Wainwright in the fields of equilibrium, as well as non-equilibrium statistical mechanics, to calculate the response of several hundred interacting classical particles using the then available highly powerful mainframe computers at LRL. Since then, MD simulation has been applied to a range of fields including crystal growth, indentation, tribology, low-pressure [81]. Amidst its numerous fields of applications, MD's have been seen in protein simulations and organic simulations, but in engineering its applications have been seen in indentation and nanometric cutting of materials. Figure 2.25 illustrates the full multi-scale schematics for the effects of damage occurring at the macroscale consistently involve damages along the full length of the scale. The need to observe nanoscale scale conditions to understand molecular mechanics of materials is essential [78].

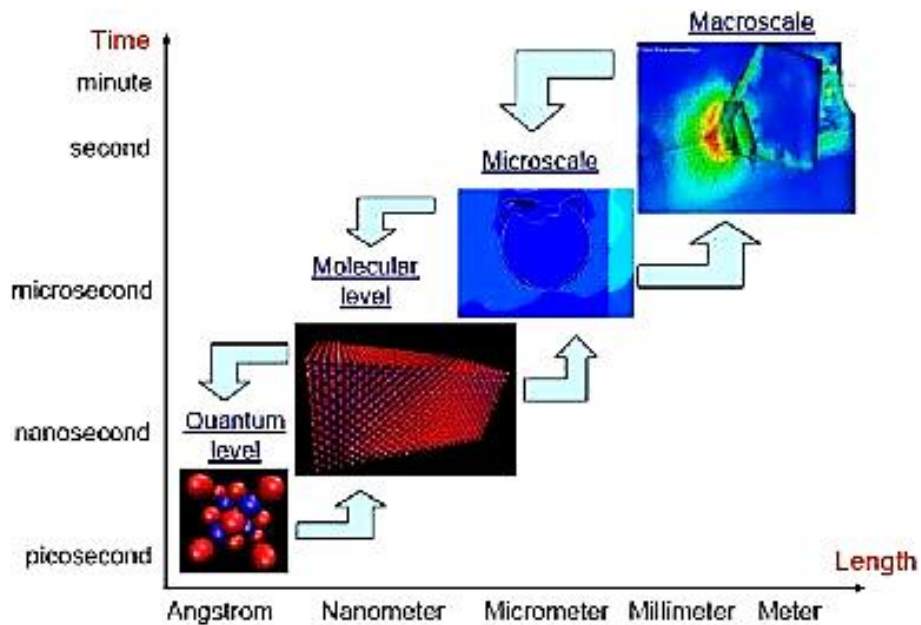


Figure 2.25 Schematic for multi-scale damage modelling [78]

Most nanometric MD simulations have been used in the simulation of single crystals due to the ease of determining molecular conditions, interatomic potential functions, and interatomic forces and are also based on reduced computational demands for single element simulations. Some examples are seen in the molecular dynamic modelling of silicon and copper [82, 83].

Table 2.6 below shows specific distinctions between conventional cutting and nanometric cutting. Also highlighted are relevant parameters to each cutting technique. The Table shows the suitability of molecular modelling for the nanometric cutting process due to the discrete molecular mechanics and the heterogeneous nature of its workpiece. At nanometric scale length, MD simulations are needed to adequately express the continuum representation of the problem.

Table 2.6 Comparison of nanometric cutting and conventional cutting mechanics [13]

	Nanometric Cutting	Conventional Cutting
Fundamental Cutting Principles	Discrete Molecular Mechanics	Continuum Mechanics
Workpiece Material	Heterogeneous	Homogeneous
Cutting Physics	Atomic Cluster Model	Shear Plane Model
Energy Consideration	Interatomic Potential Functional	Shear/Friction Power
Cutting Force	Interatomic Forces	Plastic Deformation
Chip Formation	Inner Crystal Deformation (Point Defects or Dislocation)	Inter Crystal Deformation (Grain Boundary Void)
Deformation and Stress	Discontinuous	Continuous
Cutting Tool Edge Radius	Significant	Ignored
Cutting Tool Wear	Cutting Face and Cutting Edge	Rake Face

2.6.4 MD simulation of machining operations

Molecular dynamics as a computer simulation technique uses a time-based statistical mechanics method to study the interrelation of atoms for conditions prediction and analysis. Estimation of atomistic information such as forces, bonds, angles and positions forms tools used in MD to statistically predict material conditions. Unlike the FEM, in MD simulation, nodes and the distance between nodes are selected not on an arbitrary basis but on more fundamental units of the material, namely, centres of the atoms could represent the nodes, the crystal lattice is similar to the FEM mesh and interatomic distance to the distance between nodes [81].

Thus the process can be reduced to the materials' fundamental units for analysis. Also, MD techniques give higher temporal and spatial resolution of the cutting process than is possible by a continuum mechanics approach. Consequently, certain phenomena of necessity neglected in continuum analysis can be effectively investigated by MD simulation [81].

Numerous researchers have used MD as a tool to assess cutting behaviour in diamond machining of various materials with distinct mechanical properties [84]. Oluwajobi and Chen also produced extensive work on MD simulation of nanomachining of copper [85, 86]. In their studies, they investigated various parameters in nanomachining such as minimum depth of cut, tool geometry and interatomic potential [84]. In addition, MD simulations results have also been successful in the past to address number of problems concerning the nanometric cutting process of brittle materials such as silicon [87-89]. Other works have been seen with nickel [90], nickel-titanium [91], zirconium and germanium [92, 93] and other materials.

Ultra-precision machining of monocrystalline silicon is key in microelectronics, micromechanical and optical element manufacturing; and thus the mechanism of nanometric cutting of monocrystalline silicon is a focused research topic. Molecular Dynamics (MD) simulation has provided an effective way for studying the removal of silicon at nanometric scale [84, 94]. Komanduri et al. [95] conducted an MD simulation of nanometric cutting of single-crystal, defect-free, pure silicon using the Tersoff potential. In their study the effects of rake angle, width of cut, depth of cut and clearance angle on material removal and surface generation were investigated. Olufayo and Abou-El-Hossein [82] in their research in the MD simulation of nanoscale silicon analysed the change in force during an MD simulation. Figure 2.26 shows the representation in their research of the nanometric cutting of silicon and the underlining atomic movement within the silicon workpiece. They identified MD as an efficient method in representing the nanoscale chip build-up.

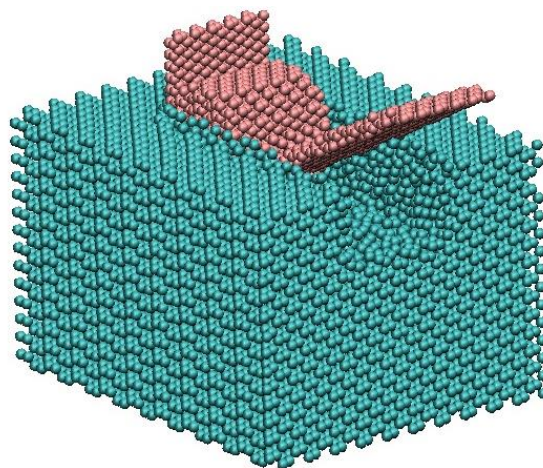


Figure 2.26 MD simulation of nanometric cutting of silicon [82]

Goel et al. [96] in their research investigated the atomistic aspects of ductile response of SiC during the nanometric cutting process. They discovered the presence of an sp^3 - sp^2 order-disorder transition which finally results in the graphitisation of diamond. This bread in the carbon coupling is as a cause of the formation of SiC-graphene during the nanometric cutting of SiC. Cai et al. [89] used MD to study the nanoscale ductile mode cutting of silicon. Their study observes the tool cutting edge and its effects on the shear stress in the workpiece material. Arafin et al. [97] discussed the effect of cutting edge radius in nanoscale ductile mode cutting of silicon wafer. The use of scanning electron microscope (SEM) images was employed to determine the subsurface quality and findings were further analysed based on Cai's MD study [89]. However, limited conclusive findings based on MD outcomes could be postulated. Aly et al. [87] conducted validation of MD simulated nanometric machining for silicon using a finite element analysis of force values. Their conclusion suggests several future perspectives to conclusively determine material behaviour. Various other researchers also highlighted the conditions in nanomachining of silicon using MD simulations based on investigations of cutting forces [89, 94], depth of cut , temperature [96], shear stress [89] and other parameters. Fang and Wu [98] performed MD simulations on multi-layered films. The films consisted of layers of aluminium, carbon and nickel. They observed jump-contact behaviour in some of their changing indentation conditions.

2.6.5 MD simulation in polymer machining

Molecular dynamic modelling of polymer is used in the field of chemistry for the reproduction of molecular compounds during design. This modelling technique offers a wide range of possibilities in modelling polymers, polymer chains and various structural make-ups in polymer building.

Limited research exists on nanoindentation of polymer material. There is a lack of adequate experimental validations in this area. A few other researchers' work have also sought to design of a reliable MD technique for predicting the physical properties of polymers from chain constitution [99]. Research work by Rocha et al. [100] nonetheless shows the application of MD in the nanoindentation of high density polyethylene (HDPE) polymer. Few articles portray research into the MD simulation of polymers. Starr et al. [101] performed the MD simulation on a bead spring polymer

surrounding a nanoscopic particle. In their study they observe the polymer/particle interactions. They identify the influence of surface interactions as an important factor in polymer dynamics.

Further research work by Chen et al. [102] studies the application of the MD technique on the cyclotrimethylenetrinramine (RDX) polymer. This energetic material (RDX) showed heating and decomposition of molecules during simulation. Representations of atomic motions within the material were also clearly captured by the MD simulation.

2.6.5.1 Principles of MD simulation and model

A brief overview of the principles of MD simulation below is given to assist in understanding its process and modelling procedures.

Atomistic representations identify all materials as atoms of various elements. These representations over a span in time (t), change in positions based on interatomic forces acting upon them and interact with their surrounding neighbouring atoms. Atoms within a molecule are further represented by spatial coordinates based on their constituent elements to determine their arrangement and spatial movements. Such coordinates are atomic distance \AA , bonds, bonds angles, dihedrals, improper and torsion coefficients. Figure 2.27 depicts a diagram of the atomistic interaction between the atoms within the tool and workpiece.

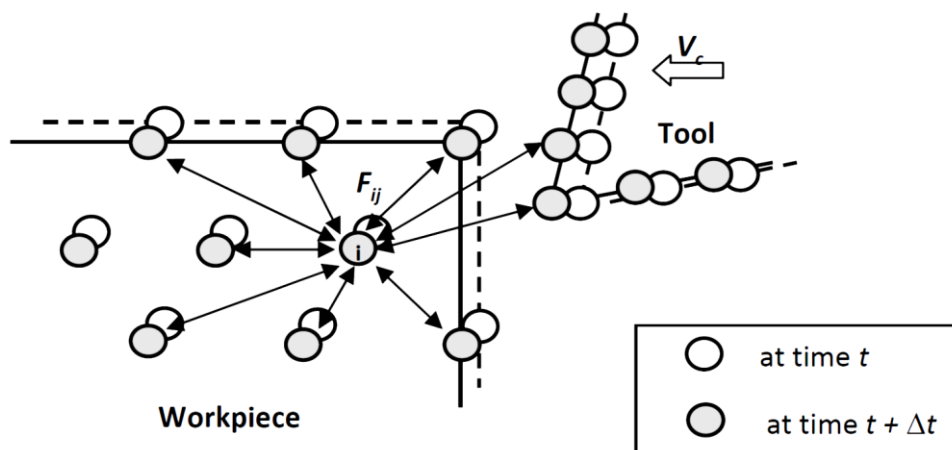


Figure 2.27 Atomistic Interaction in Nanometric Machining [103]

The atomic movement follows Newton's second law of motion based on the acting force experienced.

During nanometric machining after the three-dimensional tool made contact with the workpiece, the motion of the mobile atoms act according to Newton's second law of motion which can be computed from their interatomic forces. For a set of N particles or atoms,

$$F_i = m_i a_i \quad (2.7)$$

Where m_i is the mass of atom i , $a_i = \frac{d^2 r_i}{dt^2}$ the acceleration of the atom i and F_i is the force acting on atom i . The resultant force F_i acting on the forces can be obtained from a potential energy function, $E(r)$, which is a function of all atomic positions.

$$F_i = - \frac{\partial E(r)}{\partial r} \quad (2.8)$$

The energy function is instrumental in determining the accuracy of the MD simulation and the computational times. The general sequence of steps employed in an MD simulation can be seen in Figure 2.28.

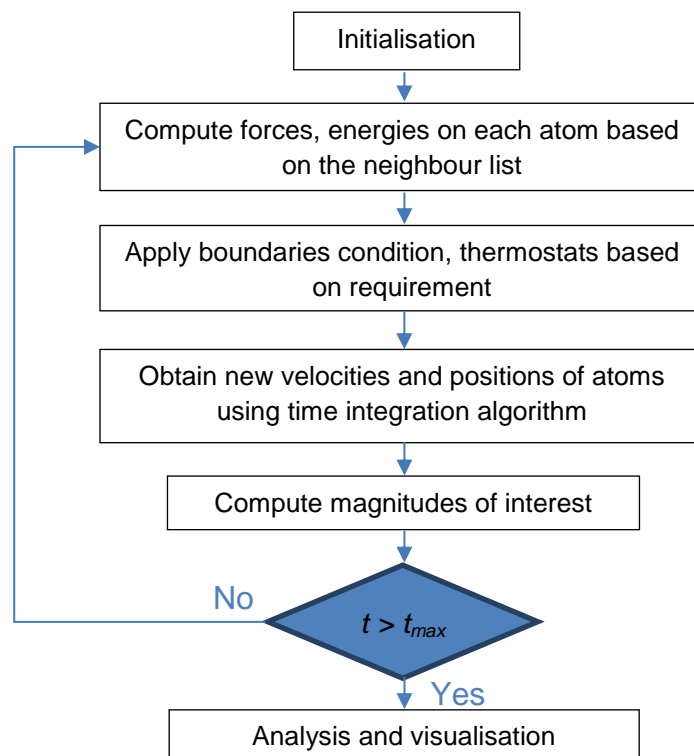


Figure 2.28 Atomistic Interaction in Nanometric Machining [103]

2.6.5.2 Some potential energy functions in MD simulations

During the estimation of force fields on atoms, cross-terms between all contributing atoms in a body could be considered. Such examples of cross terms are stretch-stretch, bend-bend, stretch-bend, stretch torsion etc. [84]. The presence of cross terms is used to characterise force potentials. Some known potential classes are:

- Class I: Harmonic potential with no cross terms e.g. CHARMM, AMBER
- Class II: Potential with cross terms and harmonic terms. It is aimed at producing both geometries and vibrational frequencies during simulation. E.g. COMPASS, PCFF, DREIDING
- Class III: The potential additionally accounts for electronegativity, polarizability and hyperconjugation.

Additional terms added to energy potentials aids in obtaining more accurate force fields. The points below identify some common interatomic force potentials used in MD simulations.

The most commonly used potential is the Lennard-Jones potential [84]; others are Morse potential, Born-Mayer potential, et cetera. These form part of the pair potentials, used for the interaction of a set of particles. In addition, there exist multi-body potentials such as Tersoff and embedded-Atom method (EAM) potentials.

Lennard-Jones potential energy function

The Lennard-Jones potential is given by the following equation [104]:

$$E = 4 \epsilon \left[\left(\frac{\sigma}{r} \right)^{12} - \left(\frac{\sigma}{r} \right)^6 \right] \quad (2.9)$$

Where E is the intermolecular potential between the two atoms or molecules. ϵ is the well depth and measure of attraction between the particles, r is the distance of separation between both particles, σ is the finite distance between particles at an intermolecular potential value of zero. It also indicates the maximum proximity two nonbonding particles can be to each other, also known as the van der Waals radius.

Morse potential energy functions

Morse potential is a pairwise potential energy function for bonded interactions. Many researchers have supplied different constants for the Morse potential for different materials [86, 94]. From Figure 2.29, the potential trails a reaction curve of energy to distance between atoms, yielding a repulsive force down the curve in the short range, attractive force along the rising curve in the medium range and a decay which stabilises in the long range of atomic force energy [82].

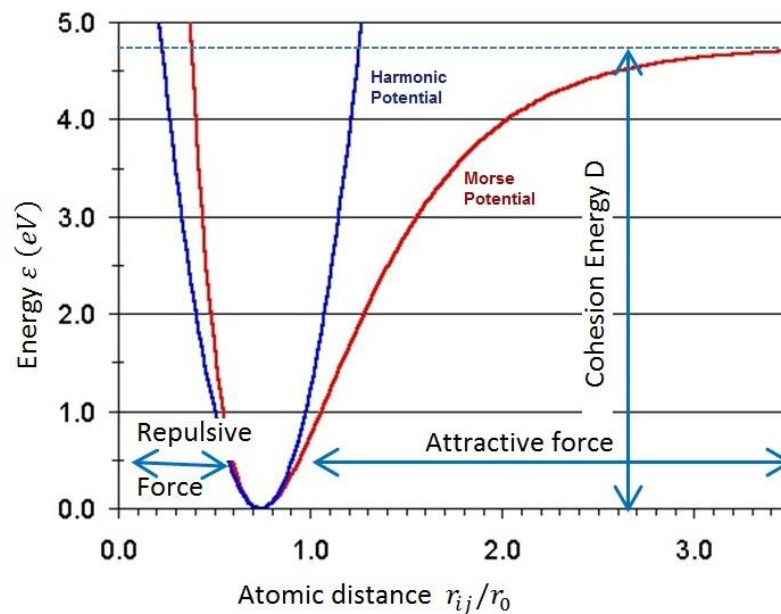


Figure 2.29 Morse potential function and the effect of atomic distance on intermolecular force[82]

$$\varphi(r_{ij}) = D(\exp[-2\alpha(r_{ij} - r_0)] - 2 \exp[-\alpha(r_{ij} - r_0)]) \quad (2.10)$$

Where $\varphi(r_{ij})$ is a pair-potential function, and D , α and r_0 correspond to the cohesion energy, the elastic modulus and the atomic distance at equilibrium, respectively. The Morse potential is known for its suitability for cubic metals.

EAM potential energy functions

The Embedded atomic model potential is given by the following equation [104]:

$$E = F_\alpha \left(\sum_{i \neq j} \rho_\beta(r_{ij}) \right) + \frac{1}{2} \sum_{i \neq j} \phi_{\alpha\beta}(r_{ij}) \quad (2.11)$$

where r_{ij} is the distance between atoms i and j , $\phi_{\alpha\beta}$ is a pair-wise potential function, ρ_β is the contribution to the electron charge density from atom j of type β at the

location of atom i and F is an embedding function that represents the energy required to place atom i of type α into the electron cloud.

Tersoff potential energy functions

The Tersoff potential models the total energy of the system as a sum of pair-like interactions. The potential function is based on the concept of bond order. In this potential, the strength of a bond found between two atoms is not constant, but depends on the local environment. The potential energy thus is in the form of [85]:

$$E(r) = \sum_i E_i = \frac{1}{2} \sum_i \sum_{i \neq j} V_{ij} \quad (2.12)$$

$$V_{ij} = f_c(r_{ij}) [a_{ij} f_R(r_{ij}) + b_{ij} f_A(r_{ij})] \quad (2.13)$$

where

$$f_c(r) = \begin{cases} 1, & r < R - D \\ \frac{1}{2} - \frac{1}{2} \sin \left[\frac{\pi}{2} (r - R)/D \right], & R - D < r < R + D \\ 0, & r > R + D \end{cases}$$

$$b_{ij} = (1 + \beta^n \zeta_{ij}^n)^{-1/2n} \quad (2.14)$$

where $E(r)$, E_i are the energies of interacting atoms, V_{ij} is the pair potential, R and D are cut-off parameters [85]. Also b_{ij} is a function of the cut-off radius.

The term ζ_{ij} (Eq. 2.14) defines the effective coordination number of atom i , i.e. the number of nearest neighbours, taking into account the relative distance of two neighbours $r_{ij} - r_{ik}$ and the angle between the atomic bonds (Eq. 2.15). This angle θ within function $g(\theta)$ has a minimum for $h = \cos(\theta)$, in which the parameter q determines how sharp the dependence on angle is, and p expresses the strength of the angular effect.

$$\zeta_{ij}^n = \sum_{k(\neq i,j)} f_c(r_{ik}) g(\theta_{ijk}) e^{[\lambda_3^3 (r_{ij} - r_{ik})^3]} \quad (2.15)$$

Where:

$$g(\theta) = 1 + \frac{p^2}{q^2} - \frac{p^2}{[q^2 + (h - \cos \theta)^2]} \quad (2.16)$$

$f_R(r)$ & $f_A(r)$ in Eq. 2.13, are the repulsive and attractive forces between atoms i and j can be represented as (Eq. 2.17) [87]

$$f_R(r) = Ae^{(-\lambda_1 r)}, f_A(r) = -Be^{(-\lambda_2 r)}, \quad (2.17)$$

2.7 Summary

In this chapter, a brief introduction into optics and their various applications in our society was shown. An inside look at optics in biomedical applications, identified contact lenses as one of the major applications of high end optics in medicine. Based on their constituting material base, contact lenses have different characteristics. Characteristics of importance to contact lenses are optical power, wettability, permeability, etc. For this reason, Roflufocon E (also known as Optimum Extreme) was selected as a polymer as choice in this study. Ultra-high precision machining amidst other manufacturing techniques was identified as a suitable contact lens manufacturing technique due to its ability to produce high-ends optics of various optical profiles. This technique is, however, challenged by the formation of tribo-chemical and triboelectric wear mechanisms which influence achievable surface quality. To control these wear mechanisms the need for an evaluation of this technique using an experimental and statistical approach is necessary. For evaluation two main techniques have been identified. These are: molecular modelling and the Box-Behnken statistical response surface method. These two modelling techniques offer a system for the evaluation of machining condition during the UHPM of contact lens polymers.

Chapter 3

Molecular Dynamics simulation of Polymers

3.1 Introduction

This section of the thesis is concerned with the modelling and simulation of Roflufocon E contact lens polymer as a tool to observe the nanomachining effects at molecular level. Prior to simulation, a back-track of some molecular properties of the polymer was performed to determine some properties of the polymer needed for simulation.

Predominantly, MD studies of the nanomachining were conducted by coding using the LAMMPS (Large Scale Atomic/Molecular Massively Parallel Simulator) which is an open source MD coding platform. The effects of some simulation conditions and observations are recorded in this study. Molecular dynamics is an atomistic simulation technique used to represent nanoscale interactions occurring between atoms of molecules. It involves the nanoscale depiction of interactive force mechanisms and arrangement found between atoms based on known potential constant known interatomic force potentials. This atomistic simulation method is founded on establishing adequate force potential and interaction between atoms for an appropriate representation of nanoscale interaction.

Although MD simulations allow the user to study many atomic scale physical phenomena, the drawbacks are that it is valid only for nanometric cutting. Furthermore, cutting speeds associated with MD simulations are not realistically implementable in experimentation, and its computational cost is too prohibitive for simulating macroscopic machining. An implementable MD simulation was generated and run in this research limited to computational demands exclusively to study the atomic scale physical phenomena of the material and not to validate its finding, but as a supplemental piece of information on its molecular sub-surface mechanism. Despite the fact that this simulation technique is not used to validate experimental results, it is carried out in the hope of understanding the properties of assemblies of molecules in terms of their structure and the microscopic interactions between them.

This serves as a complement to conventional experiments, enabling a deeper understanding that cannot be found out in other ways. [105]

Brinksmeier and Preuss [10] noted that mechanical engineers previously relied on knowledge of classical mechanics, electrodynamics and thermodynamics. While all of the mechanical, chemical and electronic properties of matter are governed by atomic motions and could be better understood through quantum mechanics, yet it was not absolutely necessary for working engineers to understand quantum physics because they were not dealing with individual atoms but with clusters. Now with the emergence of ultra-precision machining methods, such as diamond machining, this course of study is changing.

3.2 Molecular properties of Roflufocon E lens

Prior to modelling, a depiction of molecular properties of the selected contact lens polymer is essential. Roflufocon E, also known as Optimum Extreme, forms part of the optimum range GP contact lens polymers produced by Contamac®, Ltd. The optimum range of GP materials offers the lowest wetting angles in the industry, outstanding oxygen permeability and high stability, all to achieve one goal – on eye comfort. Optimum is FDA approved for a full range of indications such as myopia, hyperopia, astigmatism and aphakia. The balanced properties of Optimum make this material ideally suited for a range of lens designs such as toric, multifocal, kerataconusor corneas with a high oxygen demand. The Optimum range of materials also has FDA approval for the enhancement of surface wettability through the use of plasma treatment.

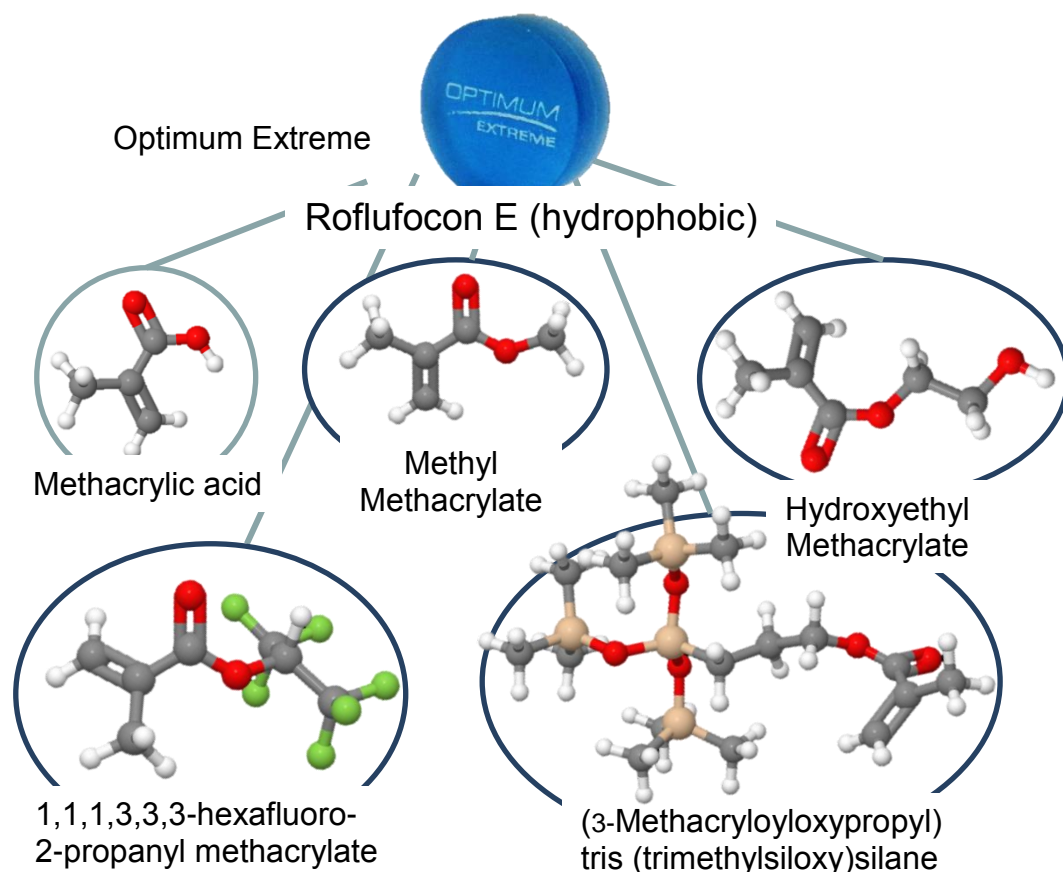


Figure 3.1 Chemical composition of Roflufocon E

Roflufocon E is a copolymer which comprises of methacrylic acid, hydroxyethyl methacrylate, methyl methacrylate and other fluoro and silane monomers. Methyl methacrylate (MMA) contributes hardness and strength while Fluorosilicon acrylate increases flexibility, gas permeability and wettability of the hydrophobic contact lens material. Figure 3.1 and Table 2.3 show the chemical composition of Roflufocon E lens material and a comparison of various contact lens buttons manufactured by Contamac® and their respective properties.

3.3 Molecular structure of contact lens polymers

As mentioned earlier, for a clear representation of Roflufocon E, one must obtain some properties such as spatial arrangement, polymerisation ratios and force fields present within the polymeric molecule. However, because of the commercial nature of the selected polymer and unavailability of some necessary information, a back-track method to estimate these properties of the polymer was employed in this study.

To obtain some of these parameters, an NMR (Nuclear Magnetic resonance) analysis of the polymer was conducted. The NMR analysis provides a spectrum of composing monomers ratios within the polymer.

NMR is a prominent technique for determining the structure of organic compounds. It uses the magnetic properties of the atomic nuclei in molecules, to derive specific information about its state. Through NMR analysis, information about the monomer ratios and molecular weights was obtained.

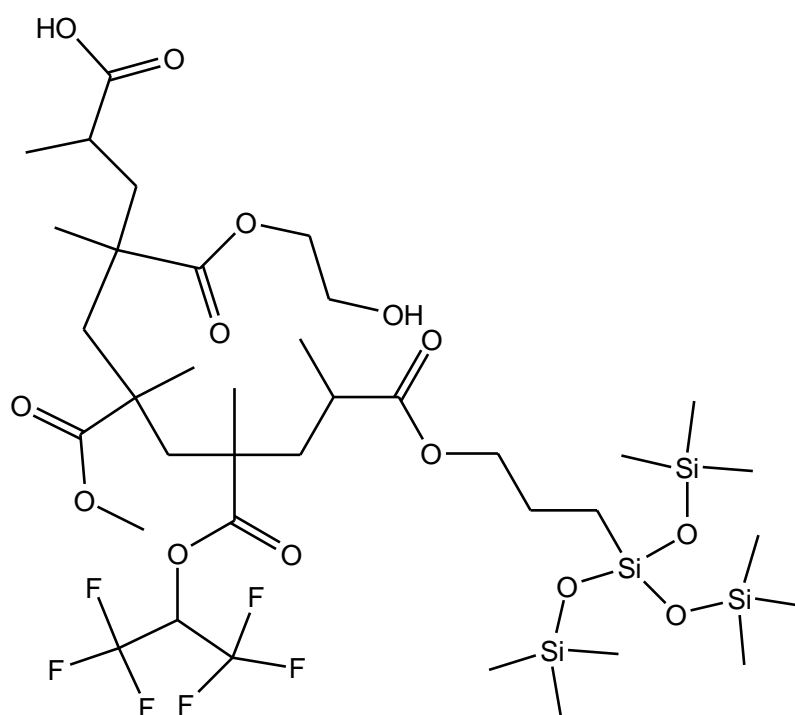


Figure 3.2 Chemical structure of Roflufocon E molecule

Table 3.1 Monomers of Roflufocon E and ending bonds

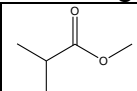
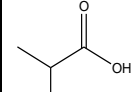
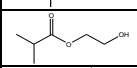
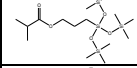
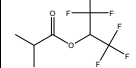
Roflufocon E Monomers	Terminal bonds/molecular weight		
Methyl Methacrylate (MMA)	$C_5H_8O_2$	100.11	
Methacrylic acid (MAA)	$C_4H_6O_2$	86.08	
Hydroxyethyl methacrylate (HEMA)	$C_6H_{10}O_3$	130.14	
(3-Methacryloyloxypropyl)tris(trimethylsiloxy)silane (TMS)	$C_{16}H_{38}O_5Si_4$	422.81	
1,1,1,3,3,3-hexafluoro-2-propanyl methacrylate (TFA)	$C_7H_6F_6O_2$	236.11	

Table 3.1 shows the constituent monomers in the polymer and their connecting end bonds. From the designed Figure 3.2, it can be seen that a proposed polymer molecule is arranged by combining just one ratio of each monomer. To obtain a more accurate representation of the polymer, an estimation of the monomer ratios is done in the study.

Nuclear Magnetic Resonance spectroscopic analysis (NMR)

Roflufocon E was mechanically crushed and subsequently ground using a mortar and pestle. The acquisition was performed at an ambient probe temperature of 25°C and dissolved in chloroform solvent ($CDCl_3$).

The 2D NMR spectra were recorded on an Agilent VNMRS Wide Bore 500 MHz NMR spectrometer in $CDCl_3$. Carbon-13(^{13}C) measurements were made at frequency of 125MHz, and calibrated with respect to the solvent signal. A 4mm HX MAS (X-channel Magic-Angle Spinning) radio frequency configuration probe was used to collect the NMR spectra. The MAS (magic-angle spinning) rate of 17 000 Hz was found to yield the best results. The spectra results obtained were successively Fourier transformed from associated NMR software, baseline corrected and the relevant peaks were identified.

A carbon-13NMR analysis of the polymethyl based methacrylate polymer did provide additional evidence as to the structure of this highly functionalized polymer. In interpreting of constituent monomers during the NMR analysis, a connection of

known peak values to chemical ending bonds is obtained from literature. The peak at 174.87 parts per million (ppm) corresponded to the carbonyl carbon. The peak at 120 ppm indicates the presence of the trifluoromethyl-ethyl ester monomer. It is postulated that the peak at 65 ppm must correspond to the methylene carbon adjacent to the hydroxyl group. Also, the peak at 54.25 ppm is assumed to correspond to the methylene carbon of the methacrylate group as seen by Rasmussen [106] in his research. The sharp peak at 45 ppm also corresponds to those seen in literature for methine carbon [106-108]. Rasmussen [106] and Souto [108] in their research work, identified the peak at 41 ppm to also correspond to the quaternary carbon of the methacrylate group. This shows resemblance to the minor peaks seen on the NMR spectra for the polymer. The peaks between 10 ppm to 18.5 ppm are presumed to corresponded to the methyl group found in MMA, MAA, HEMA, TMS, and TFA methacrylate group as seen in literature [108].

In this study, the methyl peak was very broad, so it was not possible to reliably determine the tacticity using this analytical method. The last major peak at 1 ppm is presumed to depict the trimethylsiloxy-silane group which possess a low chemical shift [109]. This analysis and the interpretations were not an unequivocal proof of the sequential arrangement of the polymer composition or its composition ratios, but nonetheless provided a baseline for replica in simulations. Table 3.2 shows some of the identified peaks in the polymers compared to PMMA. Figure 3.3 shows the solid state CP/MAS ^{13}C NMR spectrum of Roflufocon E.

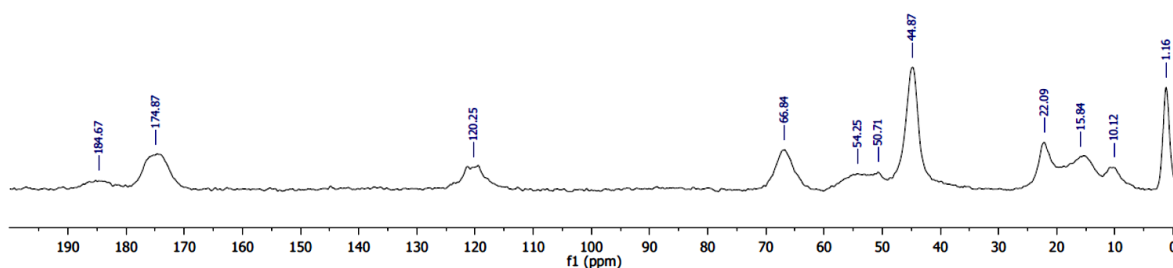


Figure 3.3 Solid state CP/MAS ^{13}C NMR spectrum of Roflufocon E

Table 3.2 Assignment of CP/MAS ^{13}C NMR Chemical Shifts of PMMA [108] and Roflufocon E

δ (ppm from TMS)					
	>C=O	-CH ₂ -	-OCH ₃	>C<	-a-CH ₃
PMMA	178.1	52.2	52.2	45.2	16.7
Roflufocon E	174.87	54.25	50.71	44.87	15.84

The assignments of the signals on the spectra of the copolymers are presented in Table 3.2. The resolved solid state CP/MAS ^{13}C NMR spectrum of the copolymer was obtained. Major peaks identified from the Roflufocon E signal are represented at 174.87, 120.25, 66.84, 54.25, 50.71, 44.87, 22.09, and 1.16 ppm. The spectra of the copolymers presented some similar peaks as PMMA, at essentially the same chemical shifts. These peaks represent end bonds of known monomers found within the analysis. From the NMR examination; the following estimation of the monomer ratio is obtained (Table 3.3). From the table a depiction of scaled values of the rations of the independent monomers are shown. The last entry in the table gives a full integer ratio of monomers.

Table 3.3 Monomer ratios per molecule in Roflufocon E

Roflufocon E				
MAA	MMA	TFA	HEMA	TMS
4	4	5.5	9.5	24
5	5	7	12	30

The next sections give examples of MD research work in nanomachining and introduce the chosen system flow in the thesis.

3.4 Use of MD in nanomachining simulation

The use of MD simulations in nanomachining is still an area of research under investigation. Table 3.4 shows a tabular presentation of some of the research works done over the years.

Table 3.4 Comparison of Some Atomistic Simulation Methods[13]

Reference	Year	Model	Potential/s used	Workpiece Material	Tool
Shimada et al[110]	1992	2D	Morse	Copper	Diamond
Rentsch and Inasaki [111]	1994	2D/ 3D	Lennard-Jones	Copper	Diamond
Komanduri et al[112]	1999	3D	Morse	Copper	Tungsten
Shimada et al[113]	1999	2D	Tersoff	Silicon	Diamond
Han et al[114]	2002	2D	Tersoff	Silicon	Diamond
Ye et al[115]	2002	2D/ 3D	EAM	Copper	Abrasive
Lin et al[116]	2003	3D	Tersoff	Silicon	Diamond
Cheng et al[117]	2003	2D	MEAM	Silicon	Diamond
Rentsch and Inasaki [118]	2006	2D/ 3D	EAM	Copper	Diamond
Shimizu et al[119]	2006	2D	Morse	Aluminium	Diamond
Pei et al[120]	2006	2D	EAM	Copper	Diamond
Cai et al[121]	2007	2D/ 3D	Tersoff	Silicon	Diamond
Shimizu et al[122]	2008	2D	Morse	Copper	Diamond
Noreyan and Amar[123]	2008	3D	Tersoff	SiC	Diamond
Oluwajobi[84]	2012	3D	More/Tersoff	Copper	Diamond
Olufayo and Abou-El-Hosseini[82]	2013	3D	Morse/Tersoff	Silicon	Diamond

*Adapted and expanded; from Oluwajobi [13]

From literature, there is no record of a nanomachining test involving the MD cutting of polymers. One research paper by Du et al. [124] investigates the velocity-dependent nano scratching of amorphous polystyrene. In their research a diamond probe is used to make micro scratching marks on polystyrene at a velocity of 500 m/s. Their simulations revealed that inter-chain sliding and intra-chain change of phenyl group rotation are two competing permanent deformation modes of polystyrene specimen. Tests of their research were conducted on a group of 400 packed polystyrene chains. This research study addresses an area of research into the actual nanomachining simulation of a commercially available optical grade polymer.

3.5 Methodology of MD simulation of Polymer nanomachining

There exist numerous MD software platforms available for simulation. Leading open source programs available are LAMMPS, XenoView, Metadise, et cetera. Each application has been identified with specific advantages for distinct simulations patterns. Oluwajobi [13] in his research work, compared both open-source and commercial based MD software to various MD applications. He identified these software's classifications based on their supported operating platforms and capabilities. Some observed capabilities are seen in modelling bimolecular systems, metals and ceramics, inorganics, polymers and proteins, as well as some general purpose-MD uses. Examples of such applications are CHARMM (Chemistry at Harvard Macromolecular Mechanics), GROMACS (Groningen Machine for Chemical Simulation), LAMMPS (Large-scale Atomic/Molecular Massively Parallel Simulator), Moldy, NAMD, TINKER, et cetera.

Based on the high computing demands MD simulations require, an 8 core with 2.93 GHz processing power computer was used for the simulation, with 8 Gigabytes of RAM and 1 terabyte of storage space. Additional virtual memory of 4 Gigabytes was created to ease on memory demands. In this thesis, LAMMPS, in combination with a VMD molecular viewer, was employed for the running of the simulation due to its variety of empirical potentials available and open source architecture. Oluwajobi [84] used LAMMPS in combination with OVITO® for the MD simulation of copper. Sun et al. [125] also used this tool in the determination of abrasive wear of nanoscale single crystal silicon. Figure 3.4 shows the software flow chart employed for the simulation.

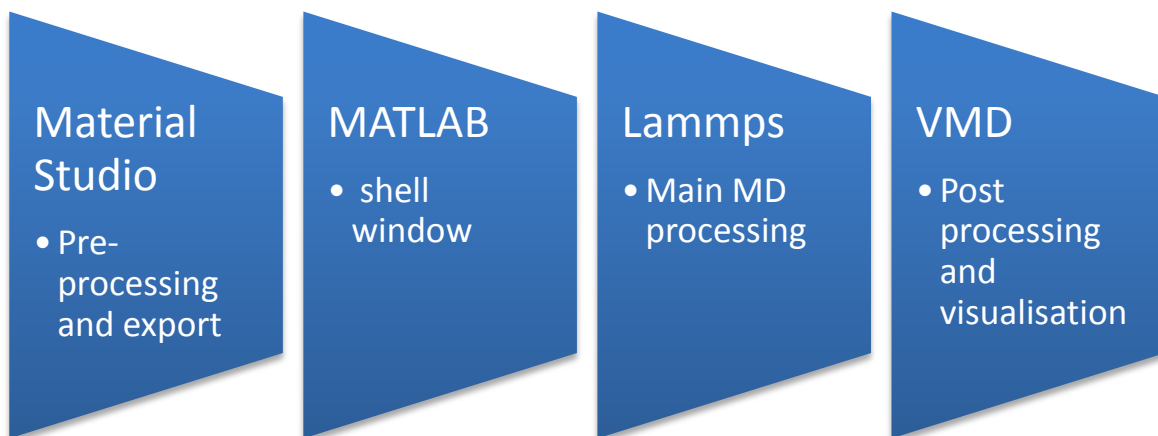


Figure 3.4. Software Methodology flowchart

3.5.1 Pre-processing and export of molecular structure

Initial pre-processing of molecular structure is the first step in polymer simulation as seen in Figure 3.4. Pre-processing and simulations were performed using Material Studio 6.0 software package. The Condensed-phase Optimized Molecular Potentials for Atomistic Simulation Studies (COMPASS) and Polymer Consistent Force Field (PCFF) were utilized in molecular mechanics (MM) and dynamics (MD) simulations.

Material Studio is a commercial program which can read a coordinate molecular file, generate bonds by distance, and angle topology. It is one of the few MD applications which possess the capability of assigning force fields on created molecular structures from existing potential files. This system technically regulates the force-field parameters for an intended molecular system using a "canned" force field. Despite its automatically calculated implementation, this technique of assigning requires a clear understanding of the fundamental structure of optimization algorithms and associated performance to make their application both efficient and correct in terms of their physical interpretation [126].

A canned force-field refers to a predefined force field coordinate built for general application to an associated type of molecule. These predefined force-field files allow you to omit all details except for the atom types, and bond topology, charges, and coordinates. They are normally found in MD platforms and easily assigned to molecules and atoms. Examples of canned force-fields are GAFF, DREIDING, COMPASS, CVFF, PCFF and UNIVERSAL. In fact, virtually all of the popular turn-key molecular modelling computer packages offer at least one "canned" force-field procedure with provisions for conducting energy minimizations and a variety of MD simulation procedures [127].

The PCFF and COMPASS are known as second generation or class II force fields. As members of consistent force fields family, they are parameterized against a wide range of organic compounds. PCFF is also applicable for polycarbonates, melamine resins, polysaccharides and inorganic materials, as well as for carbohydrates, lipids, and nucleic acids [128].

The COMPASS for field was created as an evolution from the PCFF field parameter. It is a commercial, ab-initio replica, with parameters suited for organic/inorganic

molecules, and polymers. Parameters included in this force field are categorized into valence and non-bonded interaction terms. Valence terms describe both diagonal and off-diagonal cross-coupling terms. However, non-bonded interactions depicted from short range van der Waals (VDW) and long range electrostatic interactions, are described by Lennard-Jones (LJ) 9-6 and coulombic functions, respectively [128]. Figure 3.5 shows a crossed linked epoxy chain of Roflufocon E polymer created in Material Studio in its amorphous form non-bounded and also bounded within a lattice. From the figure it can be seen how the polymer exists in its natural amorphous form; however, it is compressed within a lattice form to generate a flat surface for ease in simulated cutting.

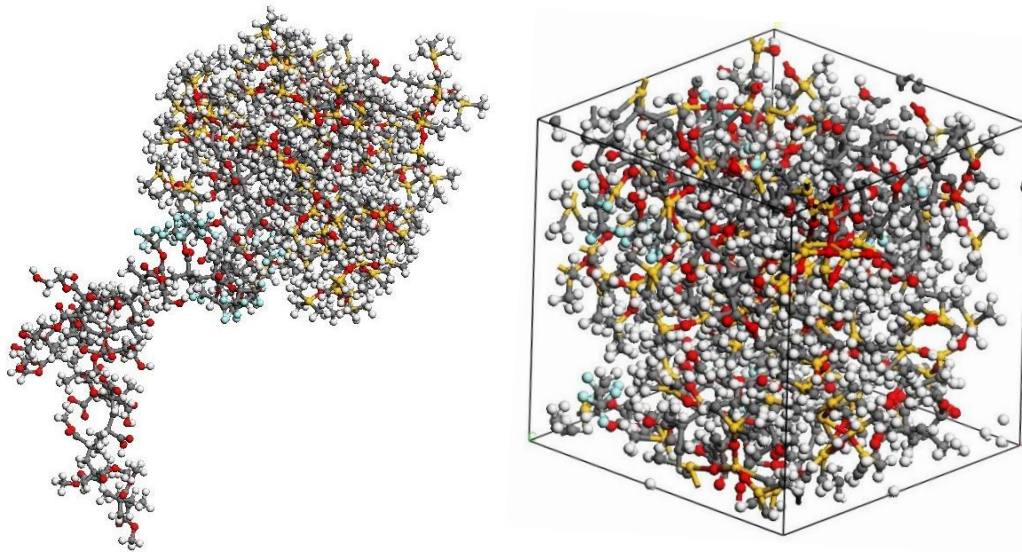


Figure 3.5 Representative cross-linked epoxy chain (left), and amorphous cell composed of 10 epoxy chains from Material Studio

The designed and modelled molecular systems from the pre-processing step were subjected to energy minimization using the combination of steepest descent and conjugate gradient (Fletcher-Reeves) algorithms, to reach the nearest local minimum just as seen from literature [128].

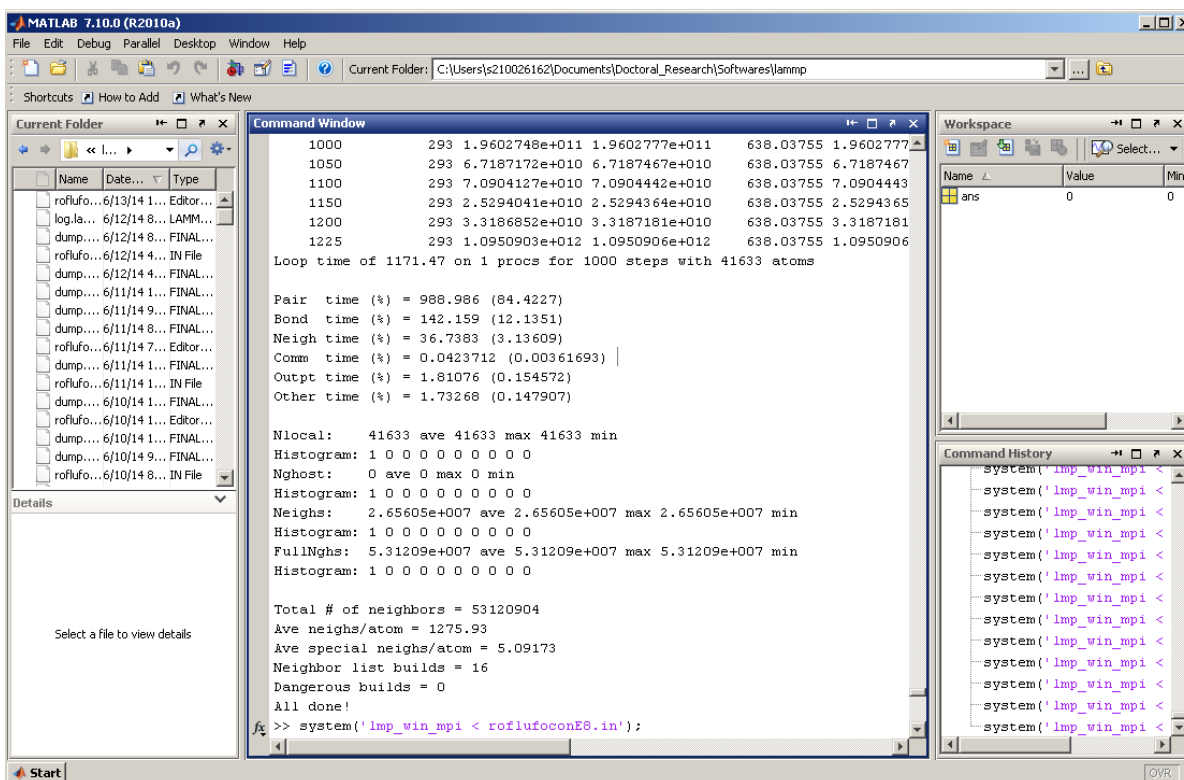


Figure 3.6 MATLAB shell window

3.5.2 Main MD processing

Due to LAMMPS software operating interface through a shell window, MATLAB was employed for interactive programming of LAMMPS MD files (Figure 3.6). LAMMPS as classical MD software runs on both single and parallel processing. It is used to compute the effects of force on molecular structures and implement the required potential and boundary conditions.

3.5.3 Post processing and visualisation

VMD (Visual Molecular Dynamics) is a commonly used visual molecular dynamics platform developed by the University of Illinois. It is used to generate 3D graphical representation of MD files and perform fairly moderate atomistic operations. Figure 3.7 shows a visual representation of the polymer through the CPK conventional drawing method. This representation (Figure 3.7) was generated during this study solely as a depiction of the visual appearance of the polymer and its individual atoms for an enhance performance view.

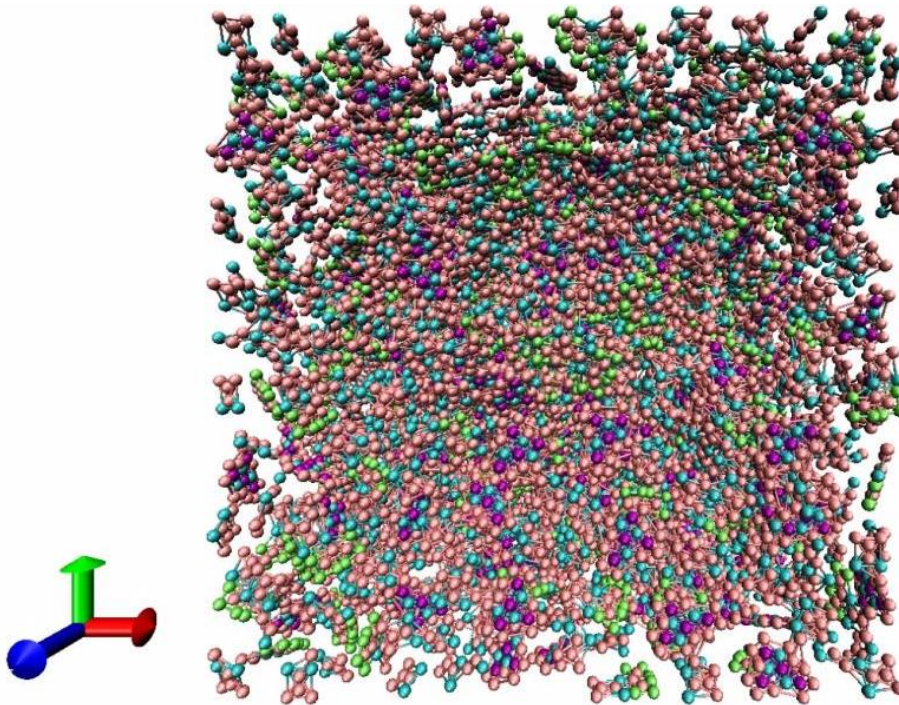


Figure 3.7 CPK drawing method of Roflufocon E in VMD

3.6 Molecular Dynamics (MD) constituent parts

In the creation of the simulation various parts and system conditions are to be considered for representation. These are: the tool, workpiece, initialization condition, boundary conditions and scope of simulation. The section below identifies each of the following sub-classes and gives a brief explanation of chosen setup employed at each of these levels within this thesis.

3.6.1 System configuration

Numerous configurations are set in the study; the simulated model specimen contains 41,633 atoms in total from the combination of its constituent part. Table 3.5 shows atomic counts of the various constituent parts of the simulated polymer. From the data file generated from material studio, atoms, bonds angle, impropers and their various types are obtained.

Table 3.5 Parametric values used in MD simulation

Component part	numbers
atoms	19216
bonds	19208
angles	36640
impropers	23096
atom types	16
bond types	23
angle types	50
dihedral types	65
improper types	37

3.6.2 The workpiece

The workpiece is described in Chapter 4. It is a fluoroacrylate polymer, commercially available for optical applications. Some physical properties of the polymer have been determined from its nanoindentation tests such as young modulus which has a value of 1.426GPa which was obtained from a nanoindentation test performed on the AFM.

During simulation after the generation of the polymer chain from material studio, the workpiece was constituted of the various quantities of its elements (Table 3.6). A Face centred cubic structure (FCC) was used to represent a crystal lattice which enclosed the atomic arrangement used for the workpiece. This atomic arrangement system possesses four atoms at the corners and one at the centre for each individual crystal face.

Table 3.6 Quantification of atoms per element type

Component part	numbers
Hydrogen	10992
carbon	5168
Oxygen	1760
Fluorine	336
Silicon	960

3.6.3 The tool

A diamond tool was simulated as the cutting tool used in the simulation. Based on the diamond being the hardest known substance, a rigid profile was adopted for the whole tool during cutting test. Known parametric properties of diamond are shown in Table 3.7 below.

Table 3.7 Physical properties of diamond tools

Chemical Symbol	C
Density	3500kg/m ³
Melting Point	3820K
Young Modulus	1050GPa
Thermal Conductivity	400W/mK
Crystal Structure	Diamond
Hardness	45GPa

Source : Oluwajobi [84]

The structure of the diamond is shown in the Figure 3.8. The figure shows the spatial arrangement of the repeating carbon atoms and the strong covalent bonds holding the structure. Figure 3.8a also shows 1,790 atoms of the cutting tool arranged in the diamond cubic crystal structure.

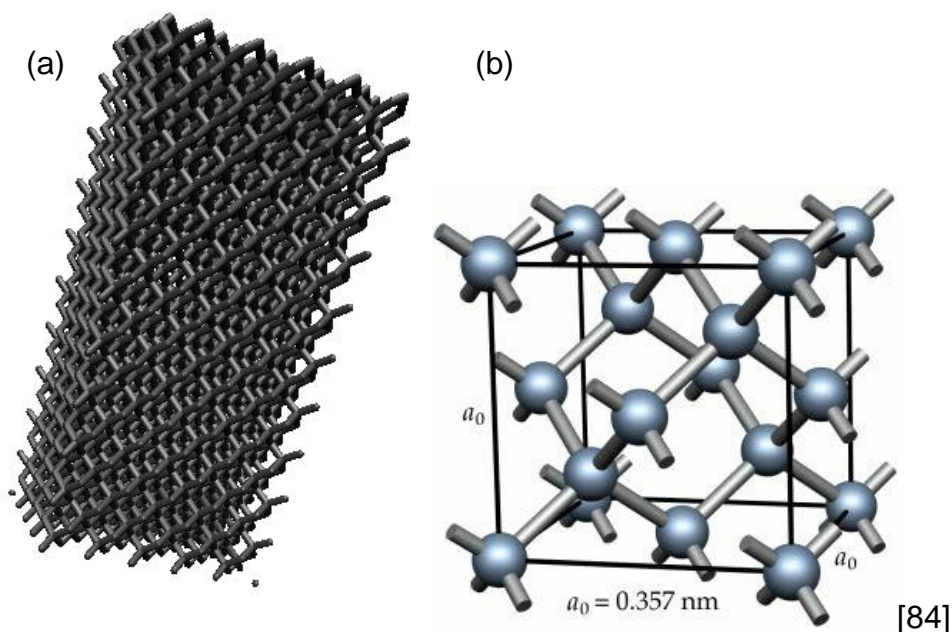


Figure 3.8 (a) & (b) Crystal structure of the diamond atom as the cutting tool

3.7 General overview of MD simulation conditions

3.7.1 Initialization

The Table 3.8 below gives a summary of the parametric values used in the course of the simulation. These simulation dimensions were chosen based on the processing limitation of the computer used.

Table 3.8 Parametric values used in MD simulation

Configuration	3D
Lattice constant (r0)	5.43 A0 (0.543 nm)
Diamond lattice (r1)	3.57 A0 (0.357 nm)
WP dimensions	18 r0 × 18 r0× 18 r0
Crystal orientation	[001]
Depth of cut	1.086 nm
Width of cut	1.428 nm
Cutting Speed	65 m/s
Temperature	293K
Time steps	0.2 fs (2 x 10 ⁻¹⁵)

The MD model was initialized by setting the atomic, bond, angle, dihedral and improper style used in the simulation. Class2 potential styles were used in all instances to correspond with applied Material Studio force field. Also, an FCC crystal structure and a lattice constant of 3.57 used in diamonds were used.

3.7.2 Boundary conditions

Boundary conditions were fixed as non-periodic and initial conditions for temperature and integration constants were set. Selected potential energy functions were then applied to simulate atomic reactions. A set control volume covering the area tool and workpiece of 144x X 144y X 144z is prepared with the predefined lattice crystal structure.

In nanometric machining, initial boundary conditions are set to recreate the effects of atoms within the workpiece and tool. A schematic diagram of the nanometric cutting simulation model is shown in Figure 3.9. The workpiece is divided into three different atomic zones: newton/movable atoms, thermostatic atoms and boundary atoms. The

boundary atoms have no set force acting on them, remain fixed during simulation and therefore avoid unexpected movement of the workpiece during cutting [129]. These atoms aid in maintaining lattice symmetry and reduce boundary effects during simulation. The thermostats layer is set to a temperature of 293°K which assists to dissipate high heat generated from cutting away from the cutting zone and implemented from the velocity scaling of the thermostat atoms in simulation.

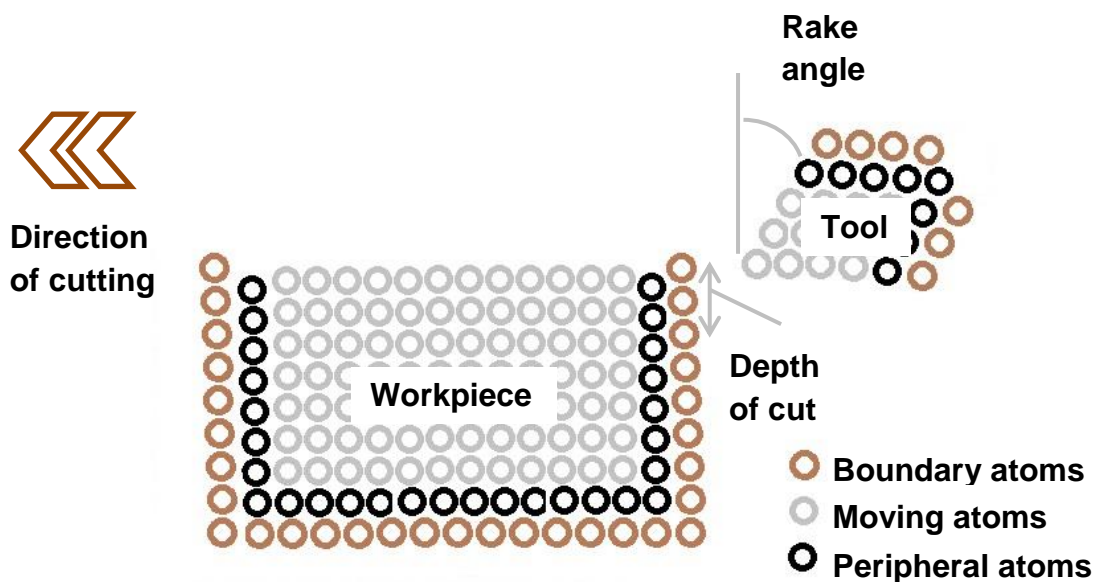


Figure 3.9 Schematic of the MD Simulation of Nanometric Cutting

The simulation portrayed in Figure 3.10, shows the atomic representation of the polymer using two different drawing representation methods; the Van der Waal representation and CPK technique. The simulation comprises of a single crystal diamond cutting tool with a nose radius of 500 nm.

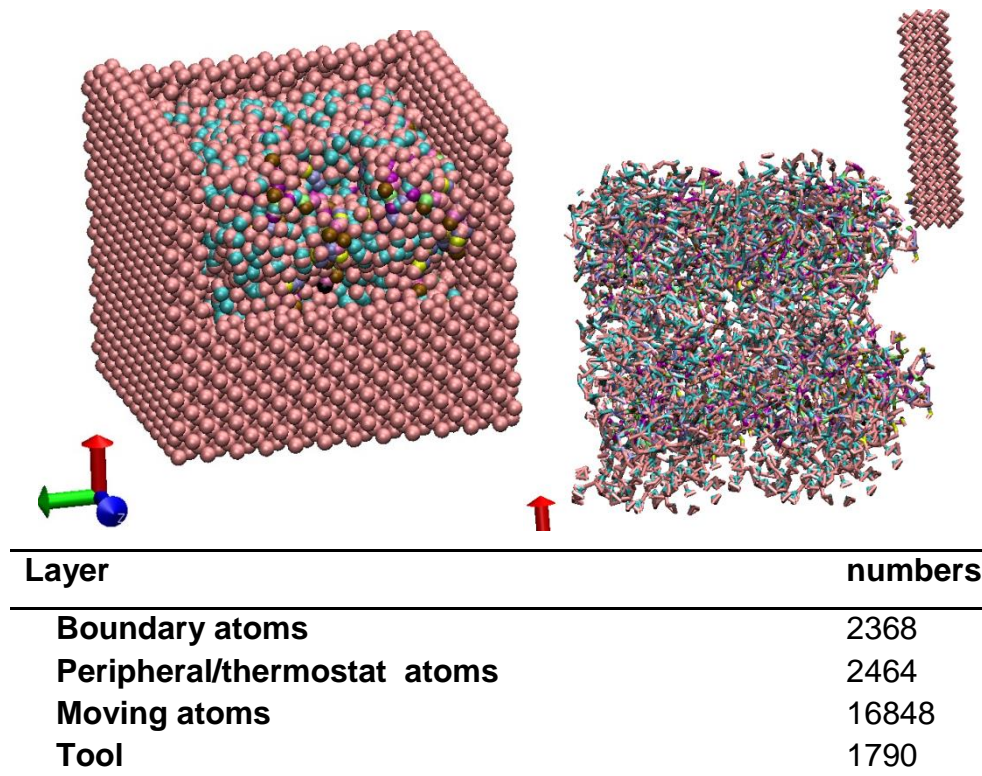


Figure 3.10 MD of simulation model of Roflufocon E (a) VDW (b) bonds representations

3.7.3 Relaxation of the system

Following to MD settings, the simulation is then brought to equilibrium by allowing current atoms settle to a relax state to mimic real materials [84]. This is done using an energy minimization of the system which was run during simulation by iteratively adjusting atom coordinates. A total of 10000 iterations were set with a stopping condition of 1.0×10^{-6} . This is used to find a potential energy minimum before nanomachining simulations begin to compute system dynamics for tool motion. At the end of initialization of a system, all setup parameters are given time to stabilise at this stage.

3.7.4 Potential energy function

Force potentials encompass the force fields interactions amidst the various atoms in a simulation. It accounts for the stability of the atomic environment and in turn defines the reliability and accuracy of MD simulation [130]. Three different force interactions exist amidst various atoms [94]:

- Amidst the workpiece atoms
- Between the workpiece and the cutting tool
- Within the cutting tool

The interactions possess different potential forces acting on the atoms during the cutting process. In this study, canned force fields consisted of Lennard-Jones 9/6 potentials and these were implanted between the atoms of the workpiece. The diamond tool as earlier stated was classified as a single rigid body and thus no forces were integrated amidst its atoms. The relations of some of the interacting forces between the diamond atoms and the polymer were defined using the Tersoff potential. From the Figure 3.11, a representation of the polymer, through combinations of both its CPK and bonds drawing, offers a representation of the generated MD assembly.

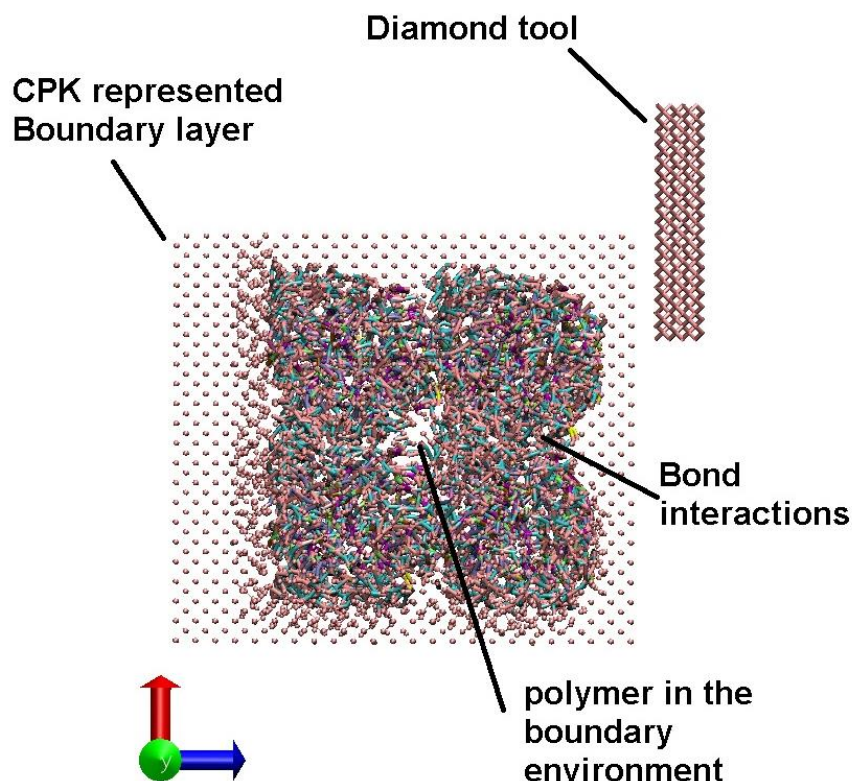


Figure 3.11 MD of simulation model of bonds acting on the polymer and tool within the boundary structure

The interactive force potentials are programmed in LAMMPS using the Lennard-Jones class II pair style. Figure 3.12 [131] indicates the influence of changing atomic

distance and interaction energy. In the LJ potential there are two basic parameters of importance: one parameter governs the strength of the attractive interaction and one of the repulsive interactions. Here, one parameter can be used as the minimal potential depth, and another as the atomic separation for the potential minimum i.e. σ and ϵ . At short distances the function is strongly repulsive, but at longer distances it actually becomes attractive [132]. These two parameters were altered in the running the experiments in this study to obtain a fitting simulation output.

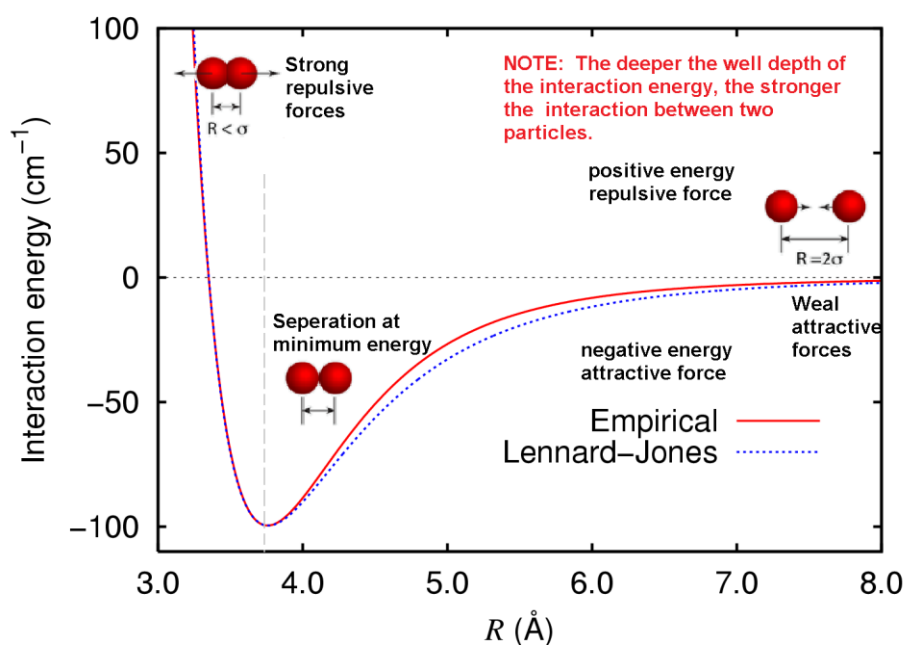


Figure 3.12 Lennard-Jones interaction energy Aziz [131]

3.7.5 Scope of the simulation

In this research study, the MD method is used purely for the study of the underlining mechanism during the nanometric machining using monocrystalline diamond tool to cut fluorosilicon acrylate polymer workpiece. The simulation only considers the applicability of canned forces in polymer simulation and evaluated force and energy changes.

Chapter 4

Experimental procedures

4.1 Introduction

As a diamond tool process, research works in UHPM have studied the wear, effects of tool geometry and influence of machine tools and control. Some research works have likewise beforehand addressed the effects of cutting parameters on the surface quality of various optical profiles and metallic materials. However, few research works exist in the evaluation of the diamond machining of polymers. Precision machining of polymers though has been in existence for a few decades now, yet is still an untapped field for new research investigation. This cutting edge technology with divers applications from medical, imaging and micro-electrical systems still needs an adequate prognostic system to ensure optimal performance.

This study seeks to address this gap in research and present an experimental approach for the prediction of the influence of process factors high precision machining of polymers. In this study an investigation into process factors and their effects on surface quality is determined. Figure 4.1 below shows the various sub-classifications areas for conducting an investigation into the UHPM process.

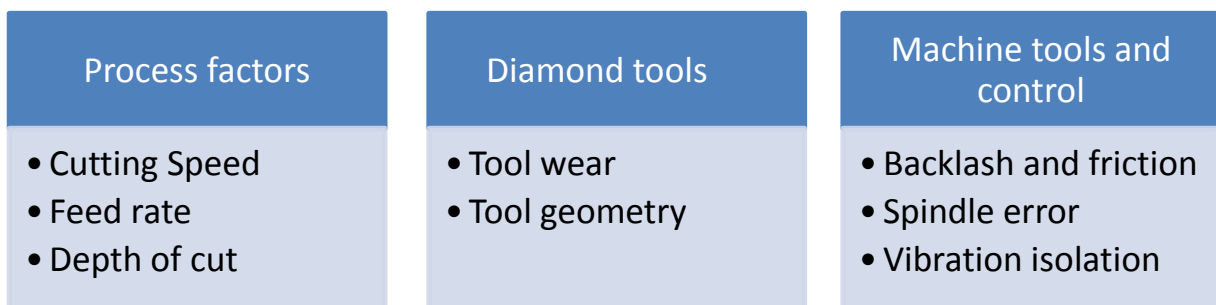


Figure 4.1 Sub-classifications of areas for investigation into UHPM process

This chapter gives an overview of the experimental setup used. A comprehensive description of equipment and components is also shown. These following sections address the type of cutting tool, workpiece, choice of machine, sensing methods and analytical steps employed in machining predictions.

4.2 Experimental setup

Machining tests were performed on the Precitech Inc. Nanoform Ultra-grind 250 ultra-high precision lathe which is available at the Nelson Mandela Metropolitan University, Precision engineering laboratory (Figure 4.2). The Nanoform 250 ultra-grind precision machine is a 4-axis diamond machining system designed for precision manufacturing of optics, optical moulds and mechanical components, ferrous and nonferrous. This precision machine is equipped with a vacuum chuck, ultra-high precision air-bearing spindle, granite base, oil hydrostatic slides and optimally located air isolation mounts [35]. The system is on a sealed natural base to eliminate machine contamination. Self-levelling isolation minimises vibration influences during machining. The system is driven by linear motors and hydrostatic oil bearing sideways, with advanced stiffness characteristics, provides ultimate performance. Nanoform 250 ultra-grind is also equipped with a spindle, which provides 25nm motion accuracy. The feedback resolution of the machining system is 1.4nm. Additionally, the programming resolution is 1.0 nm.

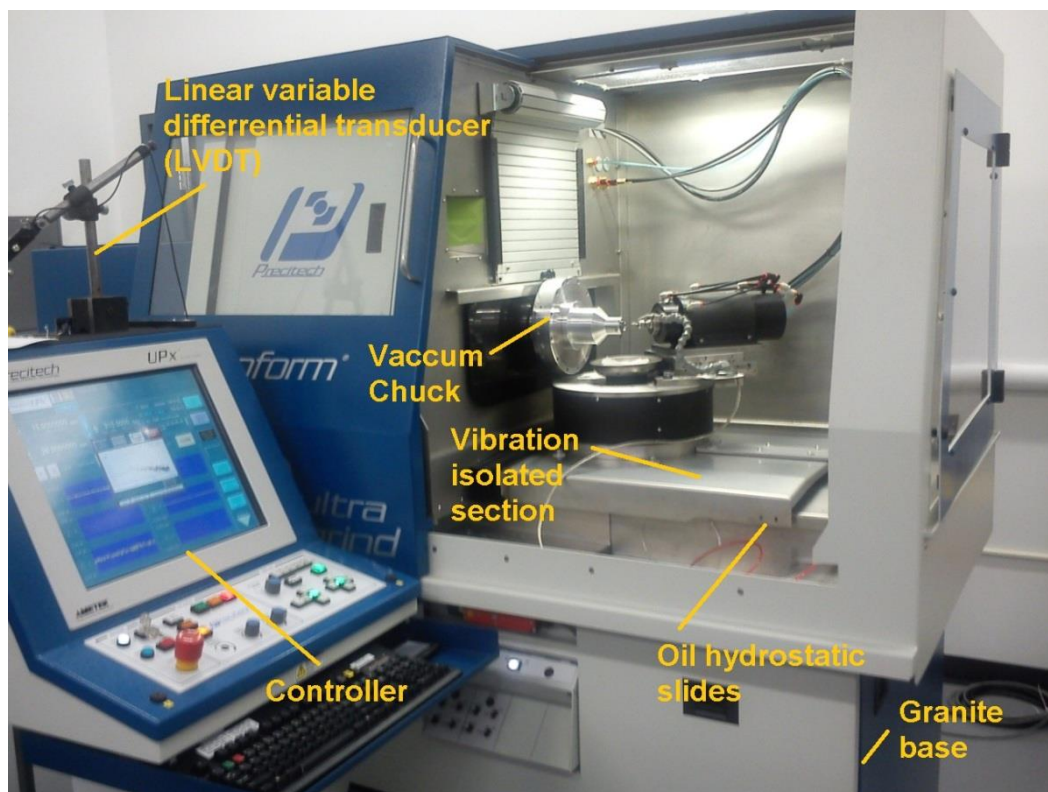


Figure 4.2 Precitech Nanoform 250 ultra-high precision machine

Specifications of the machine tool used can be summarised as follows:

- Slide travel: X-350 mm, Z-250 mm
- Maximum feedrate: 1500 mm/min
- Swing Capacity: 350 mm
- Load capacity: 68kg
- Work holding Spindle speed: <5000

Prior to machining, several calibration steps were done on the machine to ensure the accuracy of results. These steps range from the simple calibration, spindle balancing, workpiece alignment and tool capture. A spindle balance with an offset of 8nm was achieved prior to cutting with a workpiece alignment of less than 5µm swing. Figure 4.3 shows a preview of the spindle balance calibrating step performed.

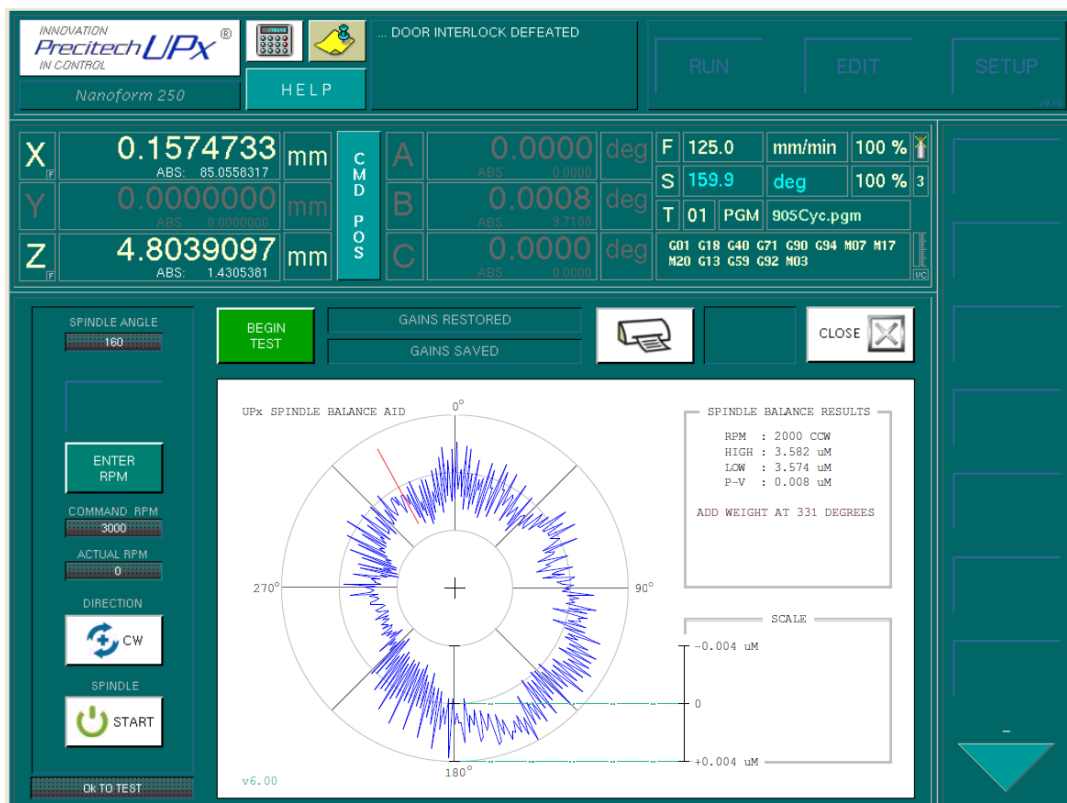


Figure 4.3 Precitech Nanoform 250 ultra-high precision machine

A diffractive and aspheric lens generating software called Diffsys® was used in designing the lens profile for machining (Figure 4.4). A machine “G-code” was prepared following the designed profile and then transferred to the machine controller. (See Appendix A for machine G-codes)

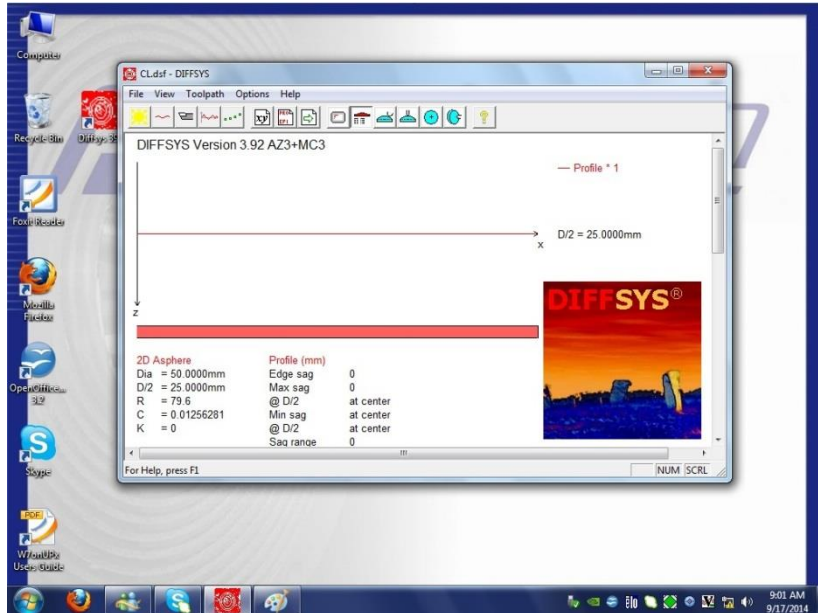


Figure 4.4 Diffractive and aspheric lens generating software (Diffsys)

Figure 4.5 and Figure 4.6 show the machine controller interface during machining experiments and the actual diamond machining setup of contact lens polymers on the high precision lathe. A highly sensitive piezoelectric micro-force sensor was also affixed below the diamond tool tip to monitor the cutting force experienced during cutting. Table 4.1 shows the diamond machining parameters used in the study.

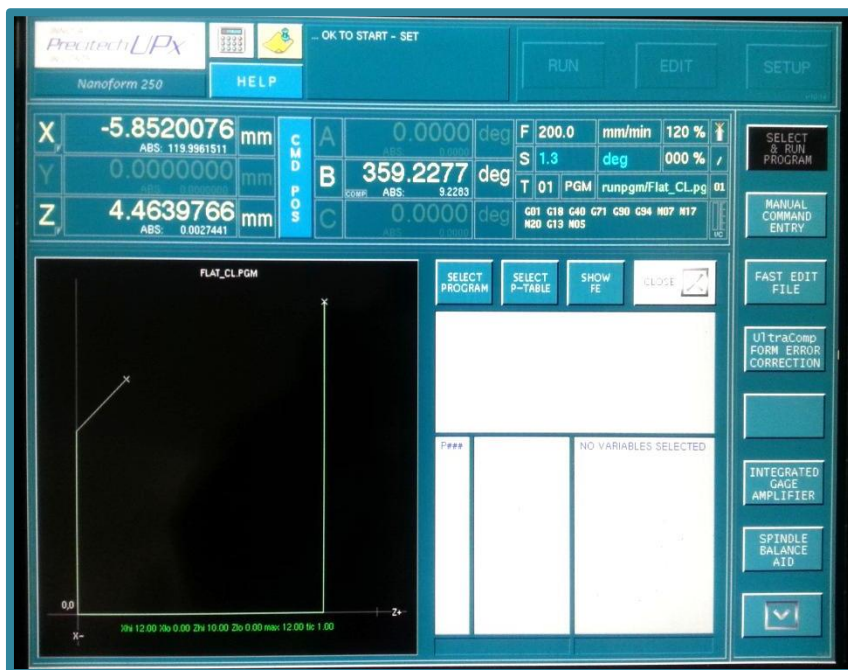


Figure 4.5 Precitech Nanoform 250 Ultragrind machine controller interface

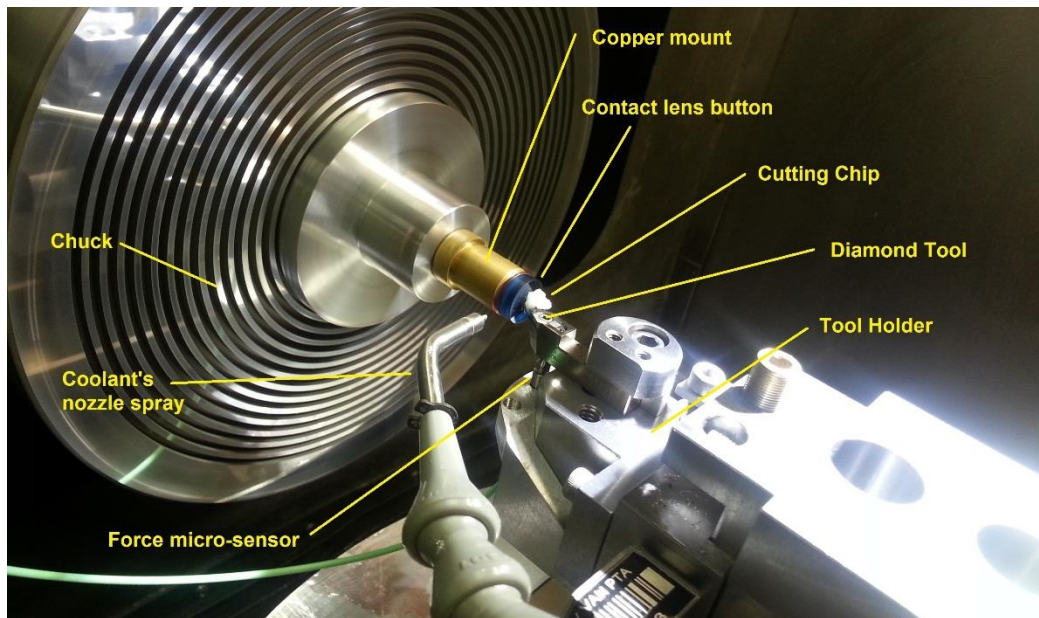


Figure 4.6 Diamond machining setup of contact lens polymers on UHPM

Table 4.1 Diamond machining parameters of contact lens polymer

Cutting Speed	0.15 m/s , 1.325 m/s, 2.5 m/s
Depth of cut	10 μm , 25 μm , 40 μm
Feed rate	2, 7 and 12 ($\mu\text{m}/\text{rev}$)

4.3 Workpiece

Roflucon E, which is a silicon-acrylate industrial grade contact lens copolymer, is used in this research. It is a rigid gas permeable polymer with hydrophobic properties. This commercially available contact lens polymer (Figure 4.7) is made by Contamac®, and is well known for its high permeability and wettable properties.

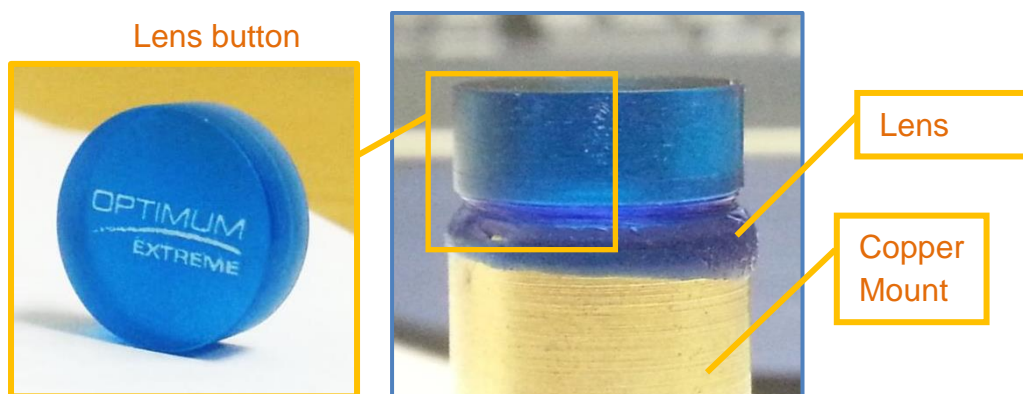


Figure 4.7 Roflucon E contact lens button

Based on these properties it was selected for this study. Roflufocon E as earlier mentioned in Chapter Two and Three, consists of methyl methacrylate which contributes to its hardness and a silicon acrylate for increased flexibility and permeability. The contact lens polymer was supplied as a button and block-mounted on a copper mount (Figure 4.7). Table 4.2 shows some the physical properties of the workpiece and diamond tool used.

Table 4.2 Workpiece and Diamond tool geometry

Workpiece		Silicon acrylate co-polymer
	Diameter	12.7 mm
	Thickness	5 mm
Tool		Single-crystal diamond
	Rake angle	-5°
	Relief angle	15°
	Tool nose radius	0.508mm

4.4 Diamond tool

Experimental testing was conducted on a range of cutting parameters using diamond tools. Contour® Ltd fine tooling monocrystalline diamond tool were employed to machine the polymer. Main geometry of the diamond tool used is presented in Table 4.2. Figure 4.8 shows a CAD drawing of the tool used during the study.

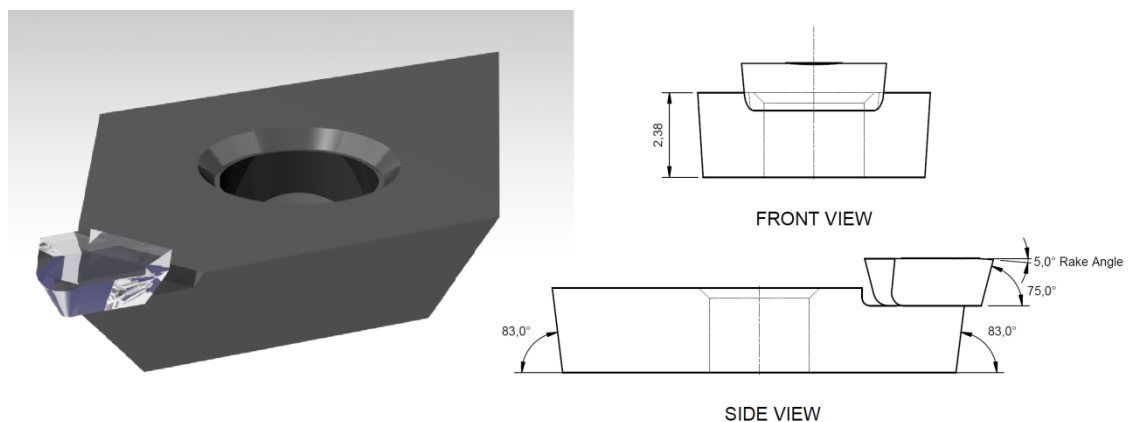


Figure 4.8 Roflufocon contact lens button

Various experimental procedures were performed during the research, based on surface roughness, measurement cutting force measurement and triboelectric measurement. The next sections address each of these procedures individually.

4.5 Surface finish measurements (Atomic Force microscopy)

Surface roughness measurements were performed on the CSM Nano indenter/Atomic force microscope which is available at the Nelson Mandela Metropolitan University (Figure 4.9). The AFM method is an extremely accurate and versatile technique for measuring surface topography at the nanoscale range. The technology possesses a very fine sensor tip mounted to the end of a small deflecting cantilever which is brought into contact with the front surface of the contact lens button. Figure 4.10 shows the AFM setup during surface roughness measurements.



Figure 4.9 Atomic Force Microscope/ Nano-indenter by CSM ®

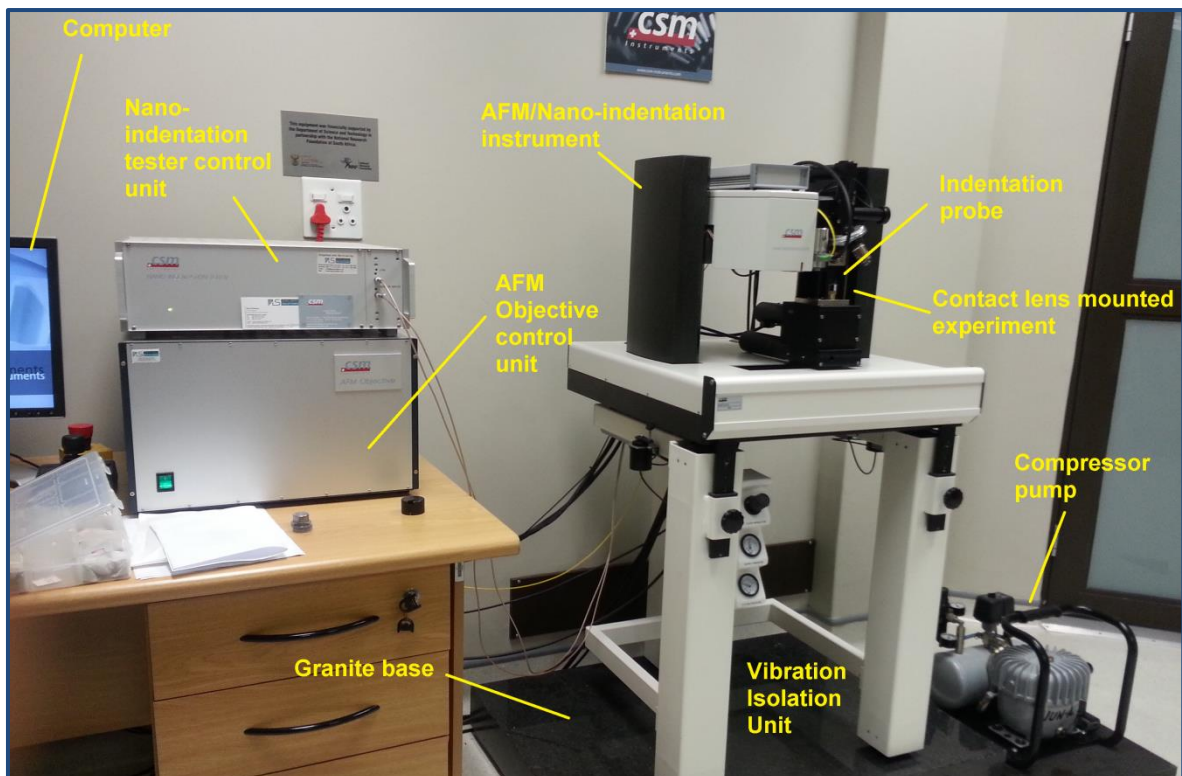


Figure 4.10 Atomic Force Microscope setup for surface measurements

During furrow scans, the indenter tip is moved across the surface in numerous line scans to produce a three-dimensional image of the surface with ultra-high resolution. The scribing direction is perpendicular to the machining axis. Though research works have shown greater roughness values in this direction, minimal effects are believed to be experienced at a polishing range (<10nm within few nanometres) of machining [133]. During furrowing of the measured area, a constant force is applied on the cantilever. Each test procedure involved the selection of a new testing site on the material specimen, followed by furrowing, and finally topographic measurement. The surface roughness was measured at three different positions on the surface of the workpiece: at the edge, centre of the radial axis and close to the centre of the workpiece. The measurements were compared and a variation of less than 0.3nm surface roughness was found. The measurements are done at 256 × 256 pixels and 24.42 × 24.42 μm. Statistical quantities of the measurement furrows are calculated and a topographic image representation is generated. Figure 4.11 shows an example of a 3D measured scan of the polymeric surface and statistical results of roughness.

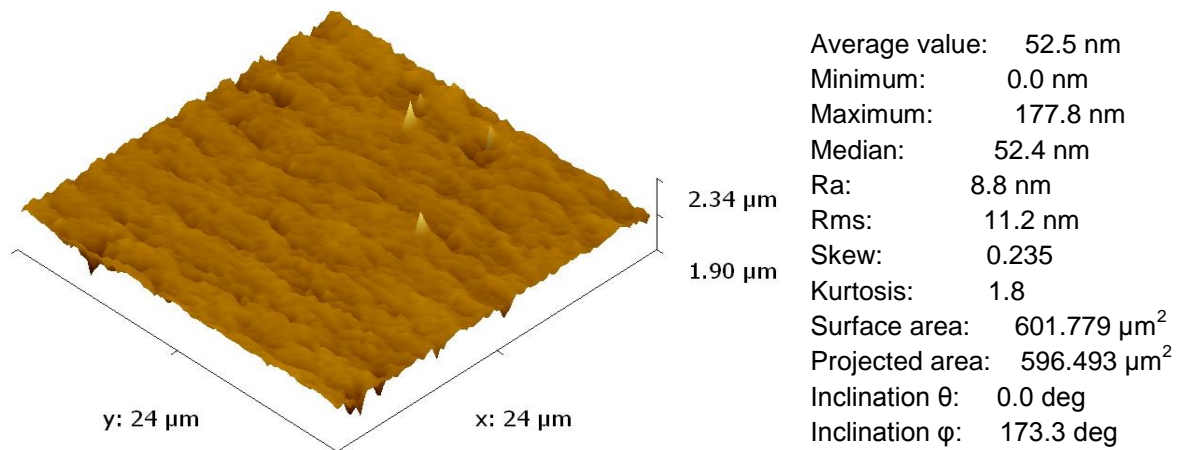


Figure 4.11 Surface AFM topographic images of contact lens

Experimental testing was conducted using a range of cutting parameters but at a fixed cutting depth of 25μm based on preliminary testing. Two distinct experimental procedures for roughness measurements were conducted. The first four experimental runs in Table 4.3 were used to evaluate the effects of the machining parameters on the surface roughness. From a choice of two different feed rates (0.15 and 2.5 m/s) based on recommended values set by the polymer manufacturer first experimental tests were run with changing speeds of (2 and 12 μm/rev).

Table 4.3 Surface measurement matrix of experiments

Exp. No.	Cutting speed (m/s)	Feed rate ($\mu\text{m}/\text{rev}$)	Depth of cut (μm)
1	0.15	2	25
2	0.15	12	25
3	2.5	2	25
4	2.5	12	25
5	1.325	7	25
6	1.325	7	25
7	1.325	7	25

The last three experimental runs in Table 4.3 focussed on the change in surface roughness and cutting force due to electrostatic charging. The parametric choice of this procedure was based on an average of the speeds and feeds of the first experimental procedure.

4.6 Cutting force measurements

This section of the experimental study considers the performance in the manufacture of UHPM contact lenses, by establishing the effects of the cutting force and its relationship with cutting parameters. Additionally a model is created to evaluate if the force sensor's position on a tool exerts an influence on recorded force values. The study therefore observes the cutting micro-force at the tool-tip and relates this to the cutting parameter. Figure 4.12 shows a schematic of the procedural steps for force measurements.

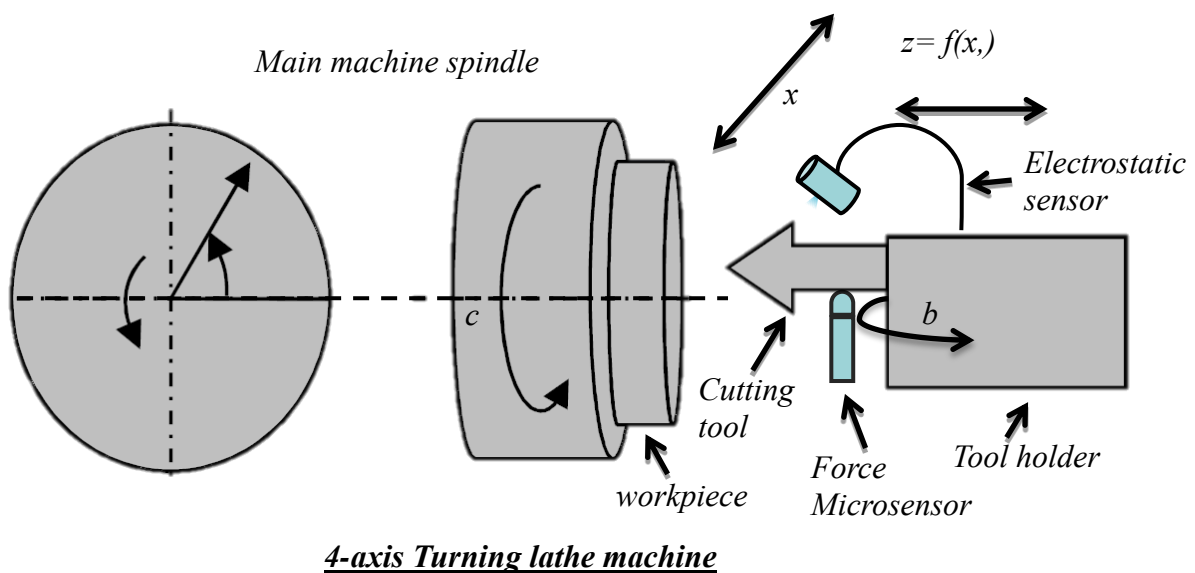


Figure 4.12 Force sensor setup schematic on UHP Machine

4.6.1 Measurement instruments

During the cutting force acquisition, a highly sensitive Kistler® piezoelectric as seen in (Figure 4.13a) was used. The micro-force sensor was affixed below the diamond tool to monitor the cutting force experienced during polymer cutting. The force sensor was set to a calibrated range of 0–20N at a sensitivity of -83,68pC/N. This sensor is plugged into Kistler® multichannel charge amplifier which converts sensor charge signals into a proportional output voltage (Figure 4.13b). This proportional voltage is further transferred through Kistler® Data acquisition system Type 5697 for force measurement and processing through Dynoware software.

Fifteen experimental force experiments were recorded based on the Box Behnken statistical from cutting parameters shown in Table 4.1. Three force measurements were collected for each experimental run and an average value of magnitude of the three was selected for the model.

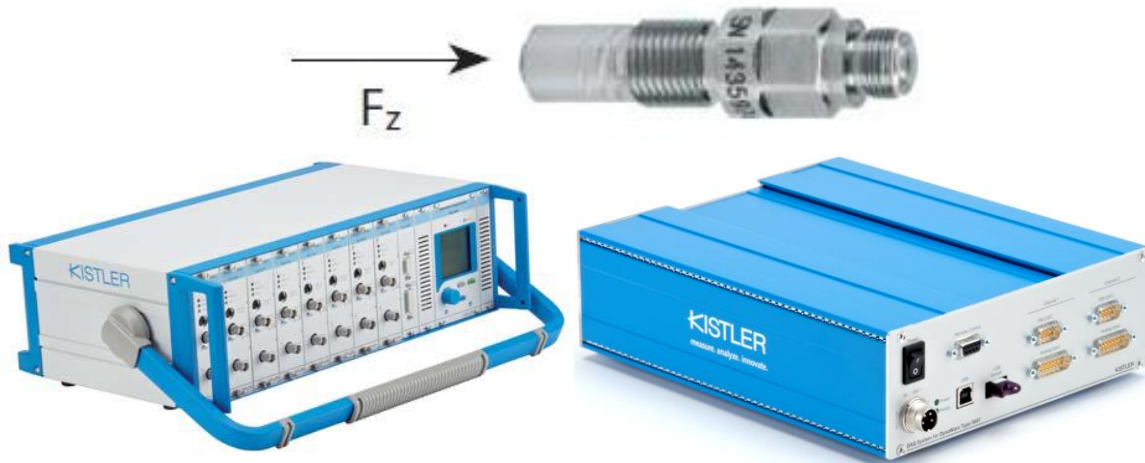


Figure 4.13 (a) Micro-force sensor (b) Charge amplifier (c) Data acquisition system

An understanding of the force mechanics occurring during cutting is helpful in interpreting acquired results. The sub-section below, gives a brief depiction of cutting mechanics involved in the study.

4.6.2 Cutting mechanics

From the literature [134, 135], micro-force sensing similarly could present an effective way in monitoring surface quality. During the modelling of micro-cutting forces occurring during diamond machining, it is essential to revisit the cutting mechanics equation linked to this diamond machining experimentation. Also, a brief insight into orthogonal force distribution in diamond turning for negative rake angle tools could assist in understanding the importance of cutting forces in UHPM. For this purpose, this section modifies known cutting mechanics equations to suit this experiment. The Merchant's model is the most famous approach of orthogonal cutting. It is extensively used in introductory courses on machining. In the model, the cutting edge is perpendicular to the relative cutting velocity between the tool and the workpiece (See Figure 4.14). The model could represent all forms of cutting levels and the materials are considered as continuous media.

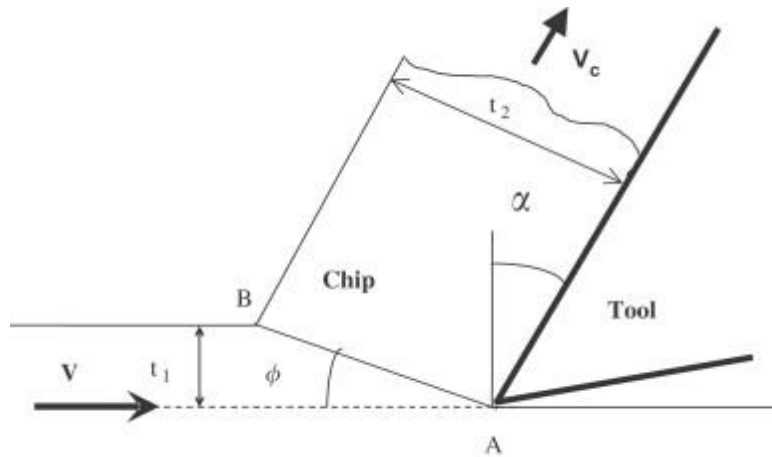


Figure 4.14 Diamond machining setup of Contact lens polymers on UHPM [136]

A metal chip with a width of cut (t_2) and uncut chip thickness (t_1) is sheared away from the workpiece. The cutting forces are exerted only in the direction of velocity V_c and uncut chip thickness, namely tangential force and feed force [13]. The Merchant's shear angle can be obtained from the equation below:

$$\phi = \frac{\pi}{4} + \frac{\alpha}{2} - \frac{\lambda}{2} \quad (3.1)$$

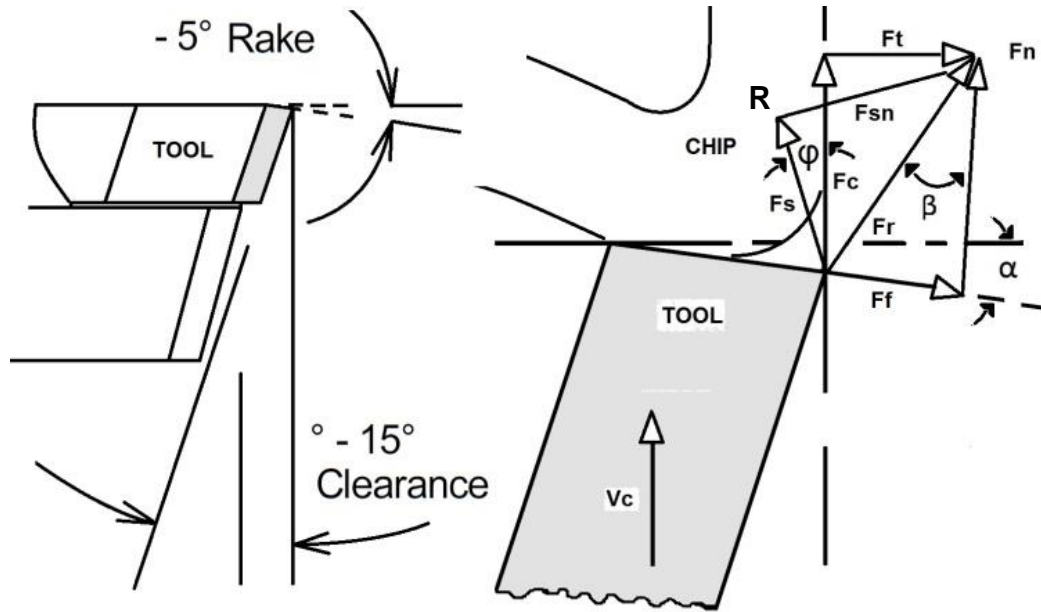
where α is the rake angle and λ is the friction angle defined by $\mu = \tan(\lambda)$, μ and is the coefficient of friction.

The following assumptions are considered for a cutting model to be applicable in representing machining operations:

- The tool tip is a perfectly sharp edge free of defects and alterations which could represent changes in force vectors
- The deformation is considered in only two planes (2D) for the action and direction of forces for representation
- Stresses on the shear plane are uniformly distributed i.e. considered as equal for the purpose of calculation
- The resultant force on the chip applied at the shear plane is equal, opposite and collinear to the force applied to the chip at the tool-chip interface [13].

Figure 4.15 below shows the cutting force interactions during the diamond turning operation. From the diagram below F_c , F_s , F_n , F_t , F_{sn} and F_r are the cutting force, shear plane force, normal force, thrust force, normal force along the rake plane of

the tool and resultant force during cutting. This orthogonal force diagram was readapted from [137, 138] using the negative rake angle of the tool for application in this thesis.



Adapted from orthogonal cutting force model [137, 138]

Figure 4.15 Diagram of (a) diamond cutting tool (b) cutting force representation

Where V_c is the cutting speed, ϕ , β and α are the shear angle, friction angle and rake angle. For a negative rake angle tool, the orthogonal cutting force can be interpreted as:

$$F_c = R \cos(\beta + \alpha) \quad (3.2)$$

$$F_s = \tau A_s = \tau (A_o / \sin\phi) \quad (3.3)$$

$$F_s = R \cos(\phi + \beta + \alpha) \quad (3.4)$$

Rearranging the equation 3.2, 3.3 and 3.4, the equation 3.5 is obtained.

$$R = F_s / \cos(\phi + \beta + \alpha) = (\tau A_o) / \sin\phi \cos(\phi + \beta - \alpha)$$

$$F_c = \tau A_o [\cos(\beta + \alpha) / \sin\phi \cos(\phi + \beta - \alpha)] \quad (3.5)$$

The derived model in Eq. 3.5 represents the factors associated with cutting forces during the UHPM of polymers using a negative rake angle. It could be used to predict underlining force factors at this scale of cutting responsible for cutting conditions.

4.7 Electrostatic discharge measurements

This setup observes a static charging effect and identifies the influence of speed, feed and depth of cut. It also observes environmental factors influencing the static build-up such as varying relative humidity. The influence of relative humidity and certain cutting parameters such as cutting feed rates were observed as factors in static charging. Figure 4.16 shows the setup for the triboelectric measurements.



Figure 4.16 Setup for diamond turning of Contact lens polymer

For the tests an electrostatic voltmeter was used and positioned at an installation distance of 25 mm from the workpiece as shown in Figure 4.17. Prior to experimental runs, contact lens buttons were lapped several times to flatten the surface area for measurement. Following lapping operation, the UHPM machine was wiped using anti-static foam cleanser and lenses were cleaned with a wet optical cloth to remove residual static charge generated during lapping. The surface potential within the UHPM machine was then checked using the voltmeter to ensure zero potential. Electrostatic data were acquired using NI PCI 6110 card.

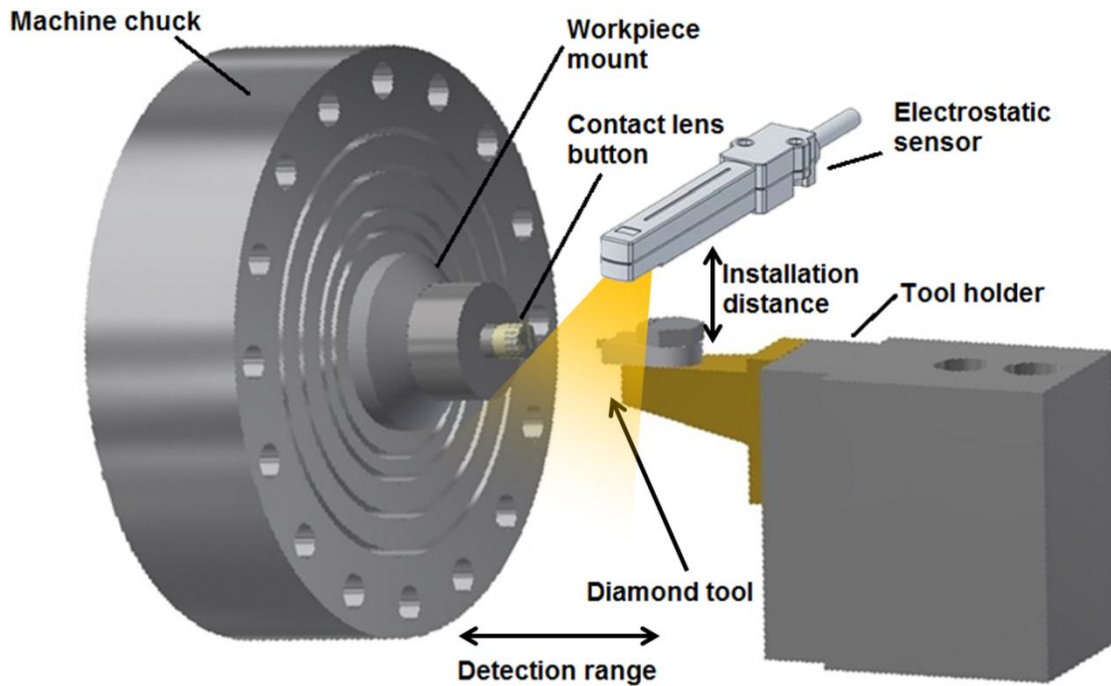


Figure 4.17 Schematic for measuring the surface potential with electrostatic voltmeter

4.7.1 Electrostatic sensor

Statics data acquired using the IZD- PZ510 electrostatic sensor by SMC® (Figure 4.18). An electrostatic sensor with a measuring range of 20kV was selected to cover the range of high electrostatic spikes generated during acquisition. Table 4.4 shows all the specifications of the selected electrostatic sensor.

Table 4.4 Specification of electrostatic sensor

Electrostatic sensor model	IZD10-510
Measuring range	+/- 20kV (when detection distance 50 mm)
Output voltage	1 to 5V (Output impedance Approx. 100ohms)
Effective detection distance	25 to 75mm
Linearity	+/- 5% F.S. (when 0 to 50°C, detection distance 50 mm)
Output delay time	Within 100ms
Source voltage	DC24V +/-10%
Power consumption	40mA or less
Operating ambient temp	0 to 50oC
Operating ambient humidity	35 to 85%Rh (Non-condensing)

The Figure 4.18 shows the electrostatic sensor and the setting for its installation distance to detection range. During the course of the experiment an installation distance of 25mm was used giving a concentrated detection range over the contact lens button. The sensor is also equipped with an inbuilt amplification circuit over an output range of 1 - 5V. This output voltage is later converted by the data acquisition software (LabVIEW®) to corresponding charge potential values using the graph in Figure 4.19.

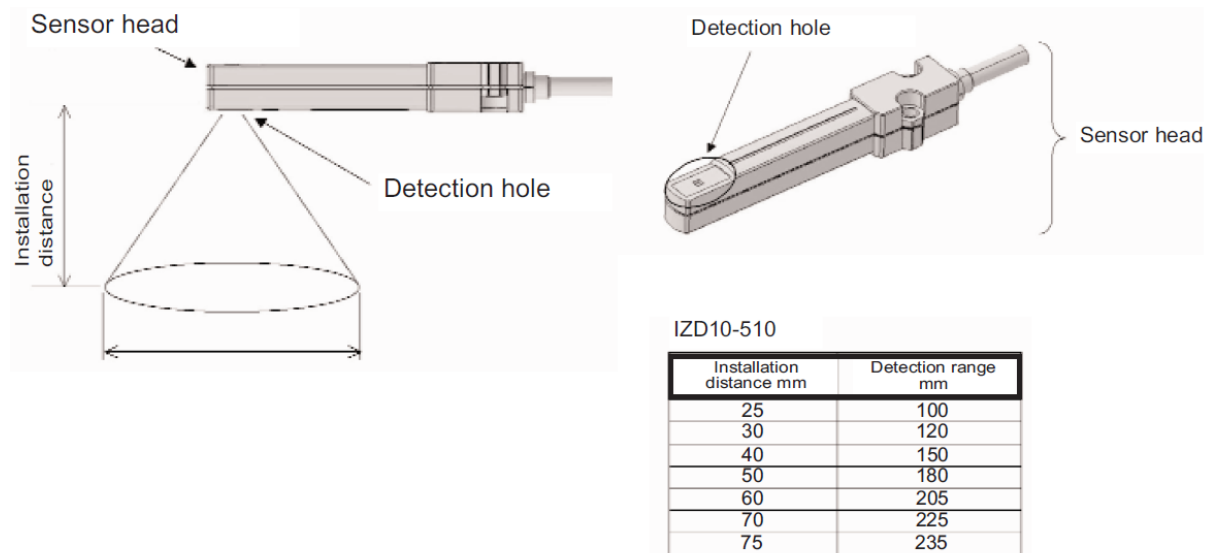


Figure 4.18 Electrostatic sensor (IZD10-510) [139]

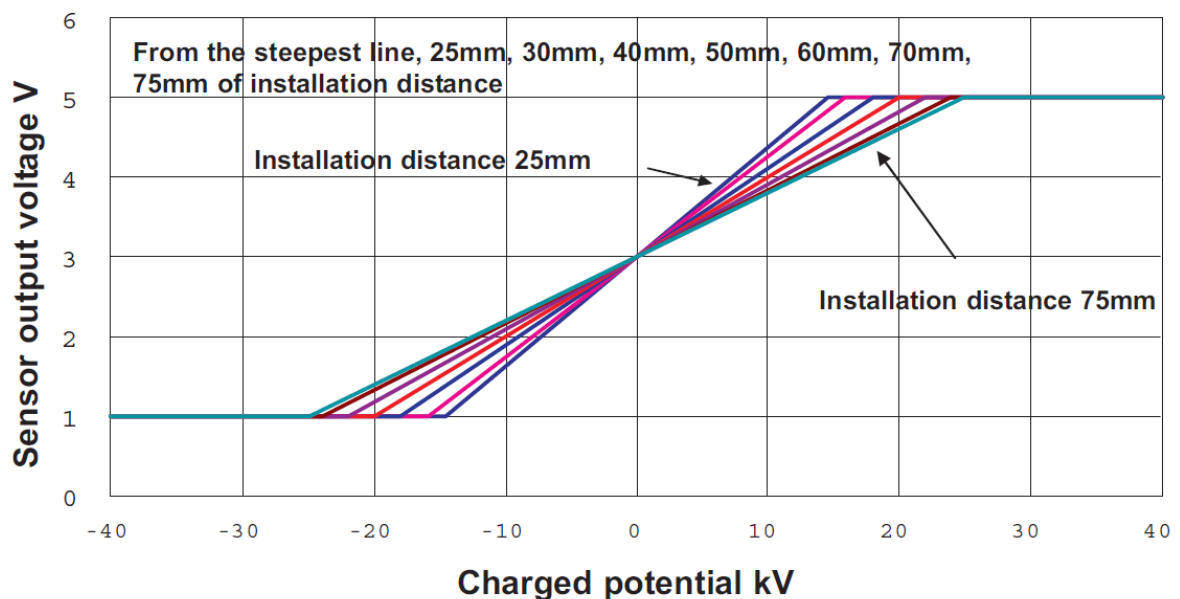


Figure 4.19 Sensor output vs charged potential for differing installation distance (IZD10-510) [139]

4.7.2 Electrostatic humidity procedure

Experimental tests were also conducted on the commercially available Contamac® Roflufocon E contact lens button which is an ionic contact lens copolymer. The lens buttons were block-mounted onto a copper mount for machining using low temperature optical wax (Figure 4.20). Additional experimental passes were run to ensure repeatability.

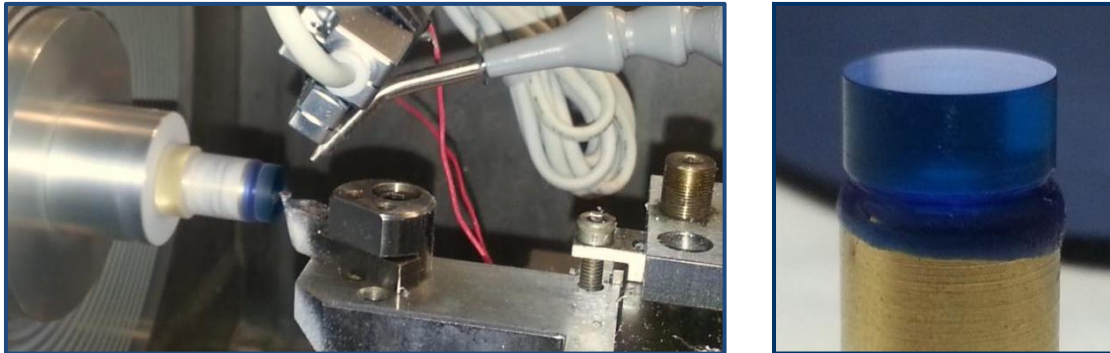


Figure 4.20 Triboelectric setup for diamond turning of contact lens button

Multiple electrostatics measurements passes were done per sample for repeatability and one repeatable value of the acquisitions was selected for the model. These were later broken into three sets of experimental runs conducted at varying relative humidity, to access the effects of humidity on static build-up. The 60%, 40% and 20% acquisition recorded the generated static charges hovering over the machined lens and cutting tool tip and took into consideration the changing polarities in static generations. The results were then analysed with a design of experiment software. The second order model was derived to obtain the empirical relationship between the two sets of response parameters and the machining variables speed, feed, and depth of cut. The analysis of variance (ANOVA) was used to check the adequacy of the second order model. The results for the three different relative humidity values are shown in the thesis.

Chapter 5

Results and discussion

5.1 Statistical evaluation of factors affecting surface finish of contact lens polymers

Fifteen experimental runs were carried out as listed in Table 5.1. The Surface roughness obtained from the contact lens machining runs was measured using the CSM Nano-indenter/Atomic Force Microscope. The acquisition measured an area of $24 \times 24 \mu\text{m}$ over the surface of the machined lens button to obtain an overview of the average surface roughness of the lens. Multiple measurement passes were done per sample for repeatability and one repeatable value of the acquisitions was selected for the model. These qualitative results are further supported by the peak-to-valley theoretical roughness results.

Table 5.1 Experimental runs and results of Surface Roughness

Run	Factors				
	A: Speed (m/s)	B: Feed ($\mu\text{m}/\text{rev}$)	C: Depth of cut (μm)	Theoretical Surface roughness (nm)	Actual Surface Roughness (nm)
1	2.50	2.00	25.00	0.98	8.8
2	0.15	7.00	40.00	12.06	12.6
3	1.33	7.00	25.00	12.06	14
4	1.33	2.00	40.00	0.98	6.1
5	2.50	7.00	40.00	12.06	11.2
6	2.50	12.00	25.00	35.43	12.9
7	0.15	2.00	25.00	0.98	4.5
8	0.15	7.00	10.00	12.06	13.6
9	1.33	12.00	40.00	35.43	9.8
10	2.50	7.00	10.00	12.06	20.4
11	1.33	7.00	25.00	12.06	14.6
12	1.33	2.00	10.00	0.98	15.5
13	1.33	12.00	10.00	35.43	8.8
14	1.33	7.00	25.00	12.06	17.3
15	0.15	12.00	25.00	35.43	12

5.1.1 Theoretical value to surface finish

Theoretical limits of surface finish exist for a material, tool and machine condition in machining. This theoretical finish is formed from the furrow trench curves left after feeding a circular shaped tool across a workpiece. The height of these furrows is calculated from the result of the relationship of the feed rate and the radius of the tool as seen in Eq. 4.1 [73]. Surface roughness parameters under investigation are the maximum peak-to-valley height R_t , and the arithmetic roughness R_a , respectively. In ideal conditions, the surface roughness profile is formed by the repetition of the tool tip profile at intervals of feed per workpiece revolution, S . The maximum peak-to-valley height, R_t and the arithmetic roughness, R_a , of an ideal e roughness profile [77] can be derived as follows (Figure 5.1):

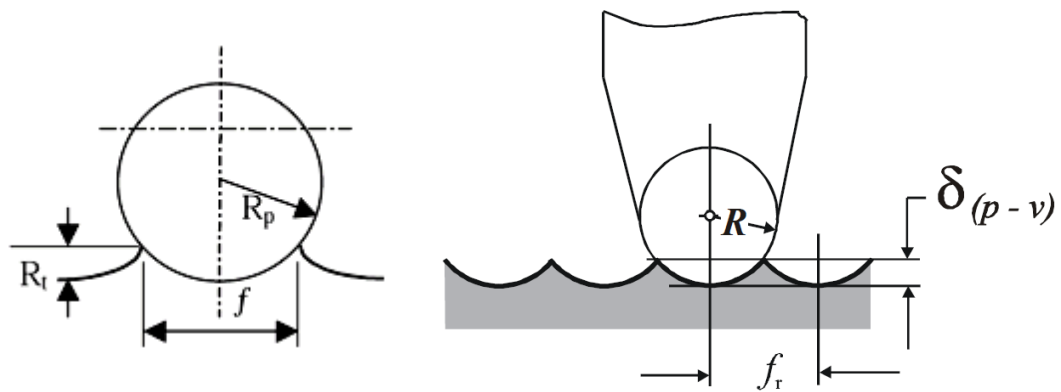


Figure 5.1: Theoretical surface height for face turning operation [73]

$$R_t \cong \frac{f^2}{8r} \quad (4.1)$$

$$R_a \cong 0.032 \frac{f^2}{r} \quad (4.2)$$

Where f is the tool feed rate in feed per revolution, and R is the tool nose radius, R_t is the peak-to-valley height, R_a is the average mean line of the roughness value during machining.

The maximum peak-to-valley height R_t , derived in Eq. 4.1 for an ideal roughness profile is referred as the theoretical roughness. Eq. 4.1 and 4.2 provide quantitative relationships among tool feed rate, tool nose radius, spindle speed and surface roughness. These are based on the assumption that there is no relative vibration between the tool and the workpiece [140].

Figure 5.2(a) and (b) show comparison of results between theoretical and measured surface roughness at fixed feedrates. It can be seen that with increasing depth of cut, variations of peak-to-valley roughness was found. At 2 $\mu\text{m}/\text{rev}$ feedrate, for lower values of depth of cut (10 μm to 25 μm), the roughness behaviour yielded lower roughness values with an increase in depth of cut. Similar results are observed at 7 $\mu\text{m}/\text{rev}$ feedrate, however with a more variations (Figure 5.2b). Literature [141] also has shown similar responses of increased depth producing contrary to norms lower roughness values.

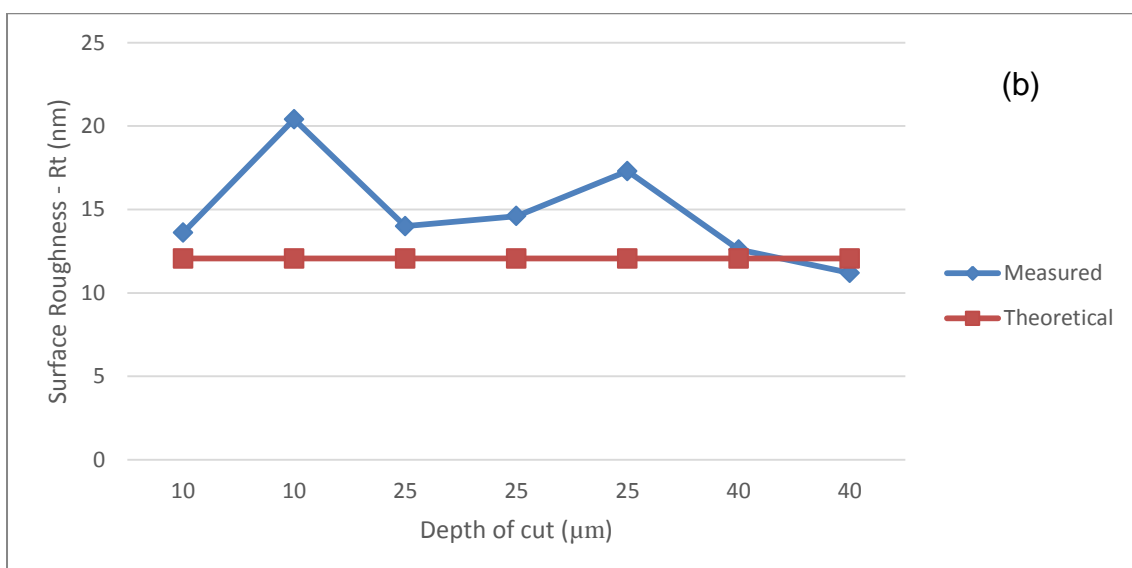
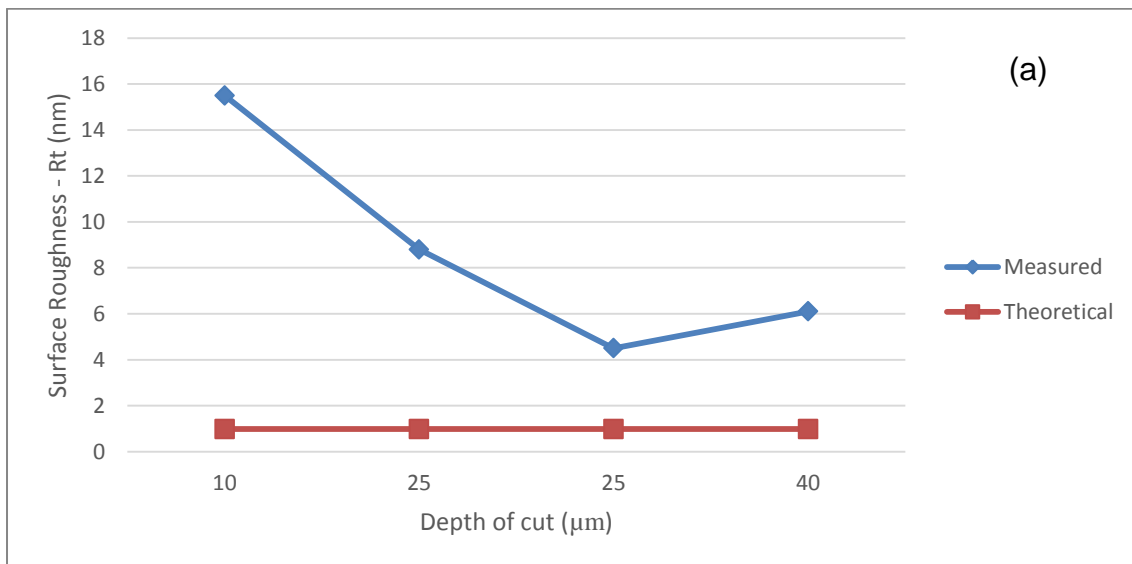


Figure 5.2: Comparison between theoretical and experimental values of surface roughness as a function of depth of cut (a) at 2 $\mu\text{m}/\text{rev}$ feedrate (b) at 7 $\mu\text{m}/\text{rev}$ feedrate

Analysing both experimental and theoretical value as a function of increasing feedrates at fixed depth yielded different results. Figure 5.3(a) and (b) shows these values of the peak-to-valley surface roughness (R_t) of the machined samples as a function of the feedrate.

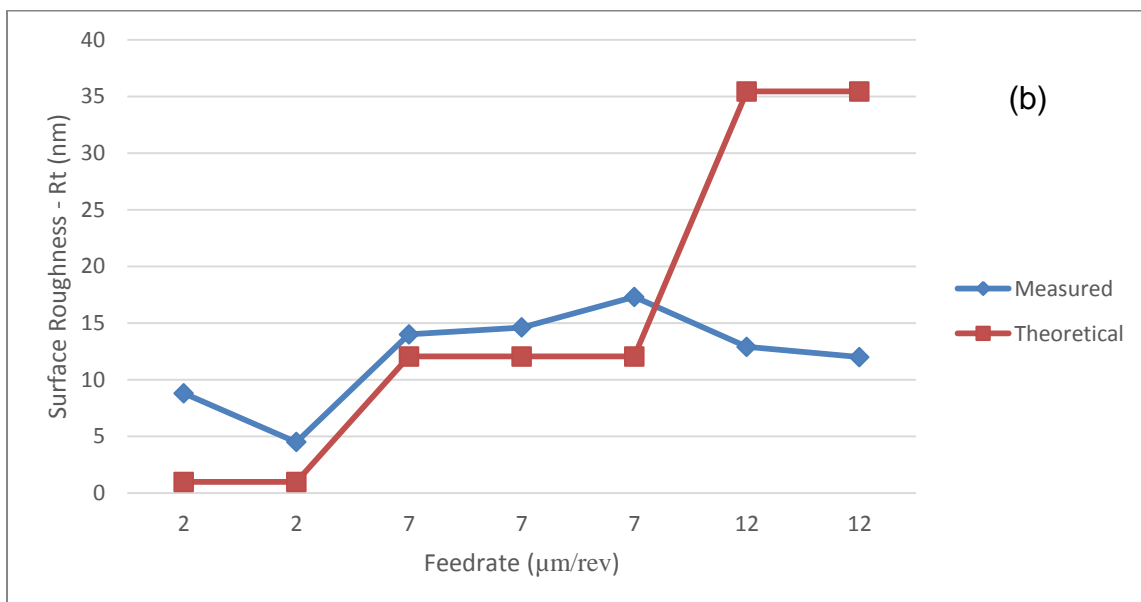
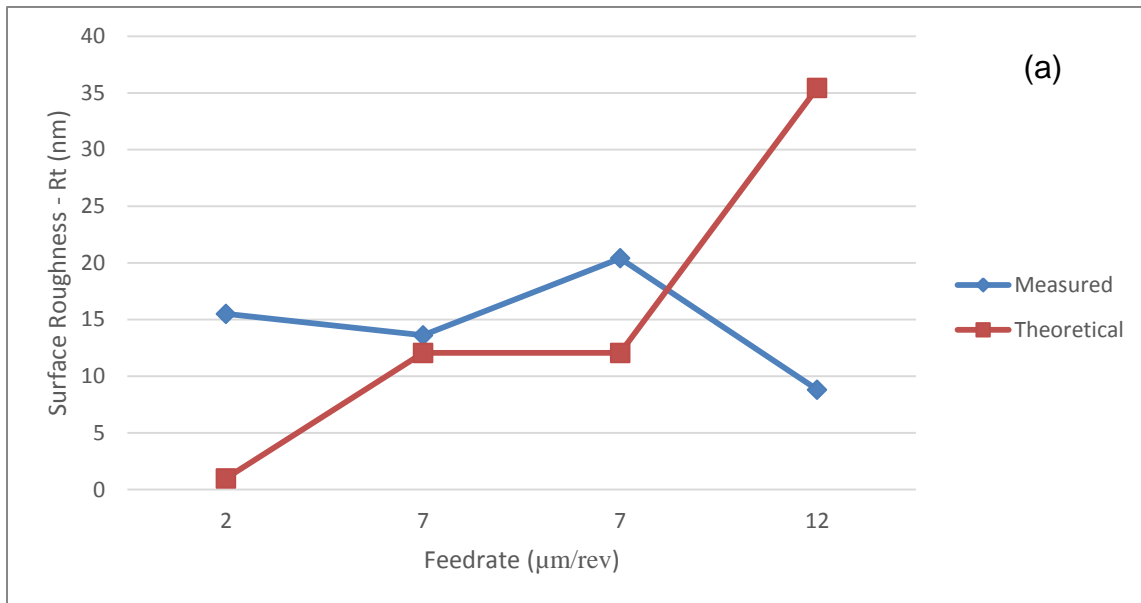


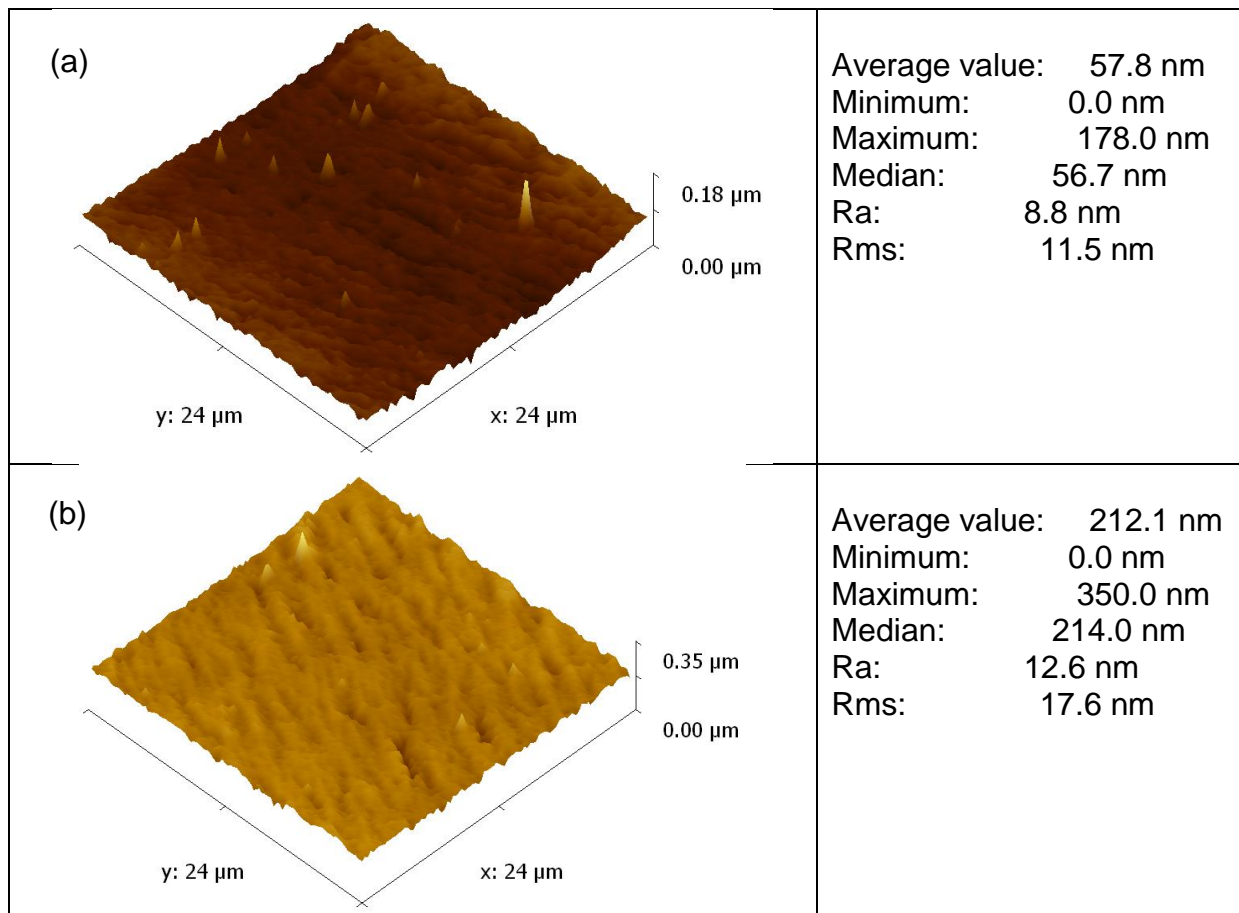
Figure 5.3 Comparison between theoretical and experimental values of surface roughness as a function of feedrate (a) (at 10 µm depth of cut (b) at 25 µm depth of cut

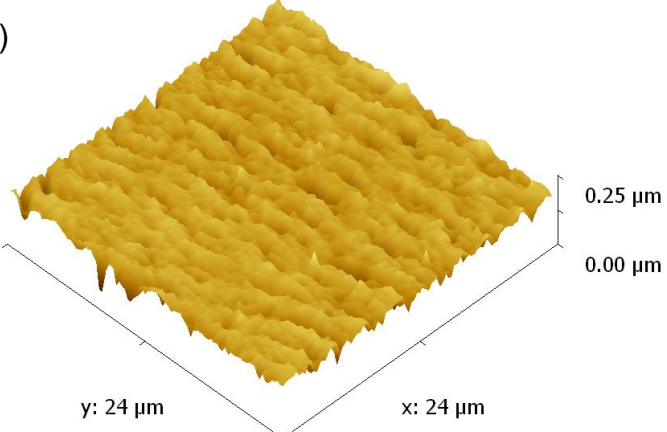
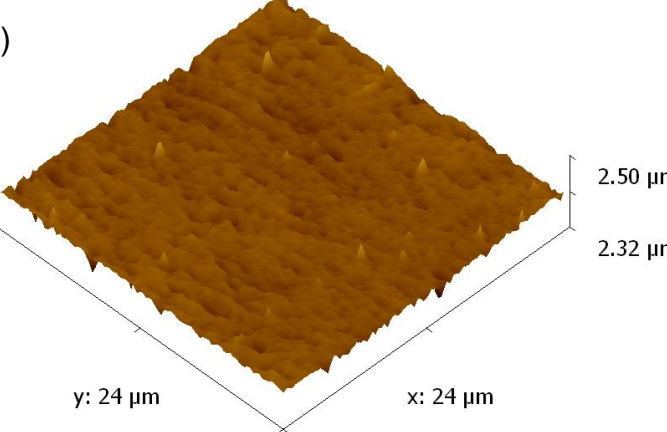
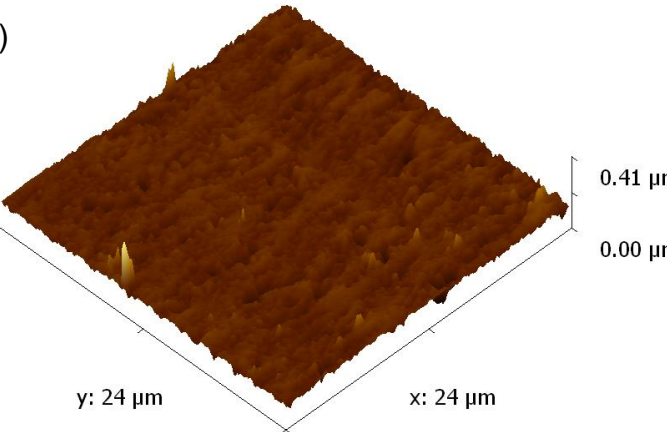
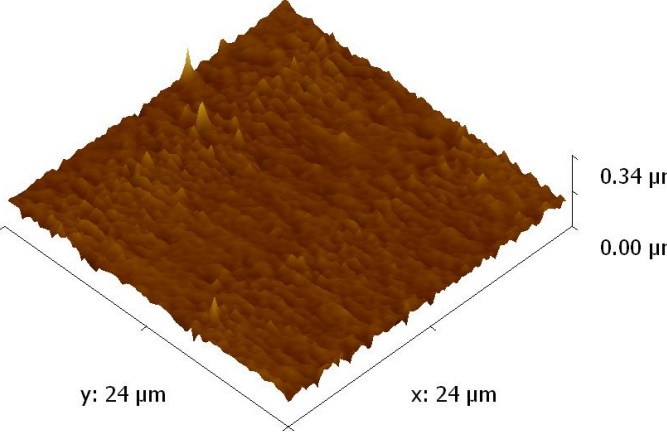
From this analysis, experimental values were found to be very close to theoretically roughness values within margin of few nanometres. Increasing feedrate yielded a

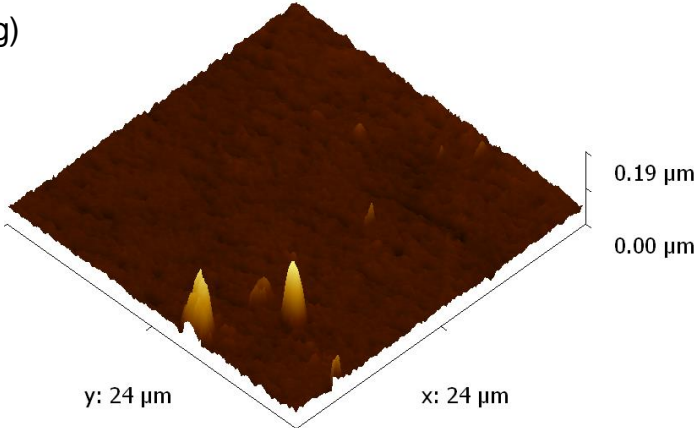
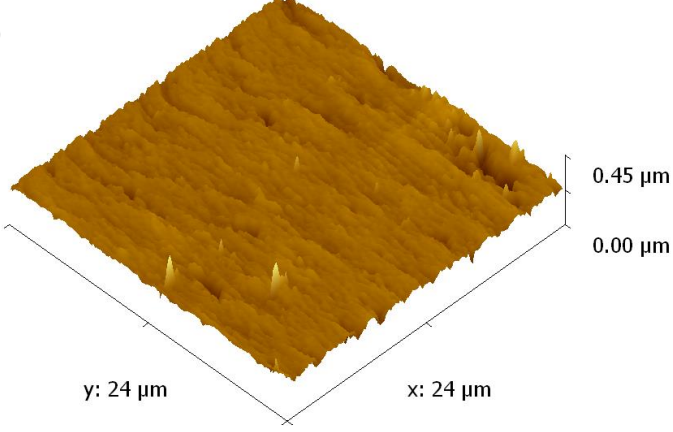
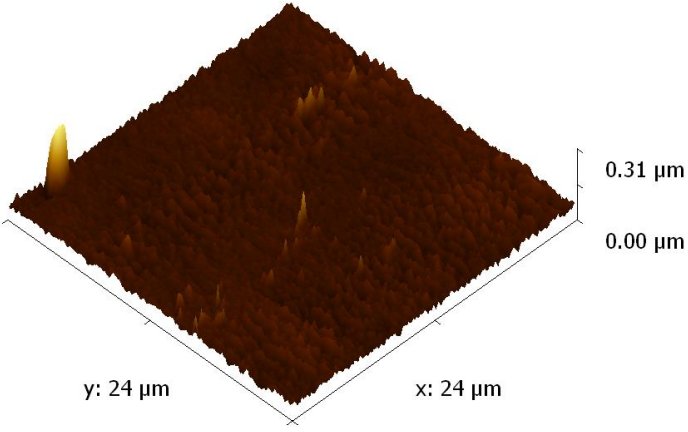
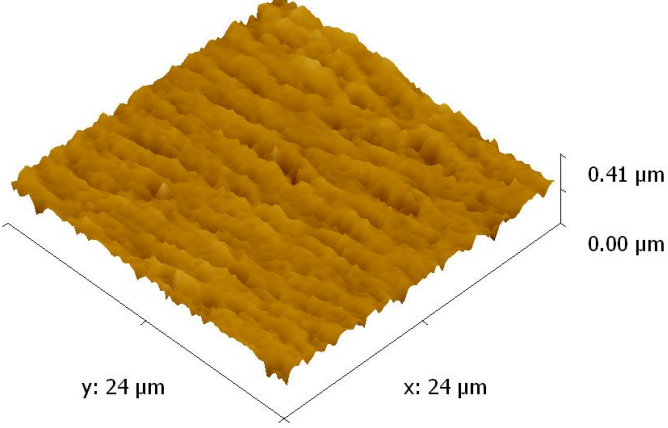
corresponding rise in surface roughness, for both experimental and theoretical predictions. However, a fall in surface roughness is found as the feedrate increases to 12 $\mu\text{m}/\text{rev}$.

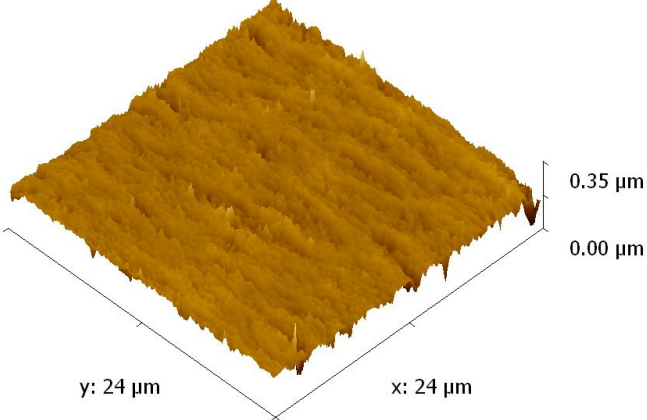
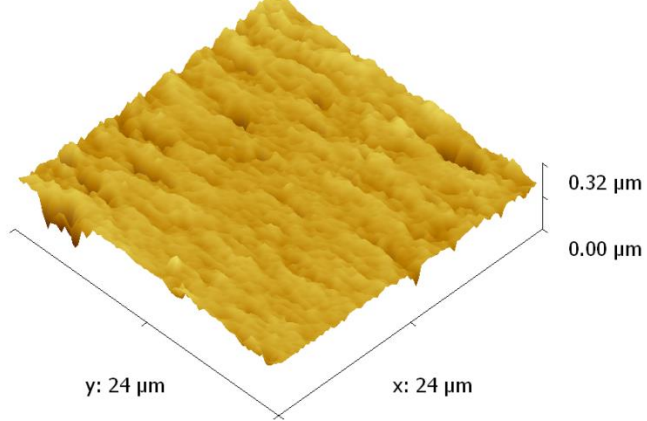
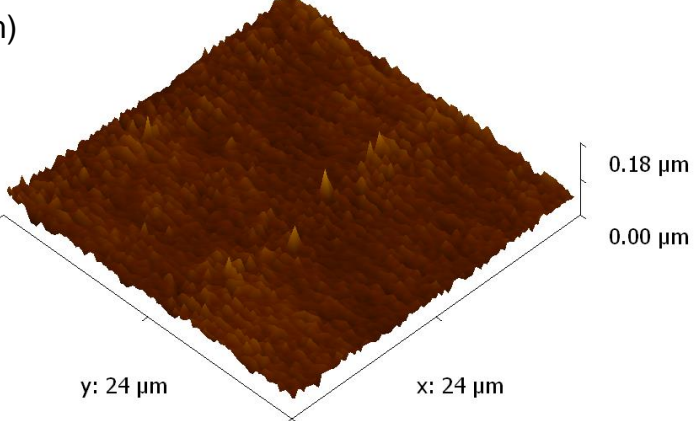
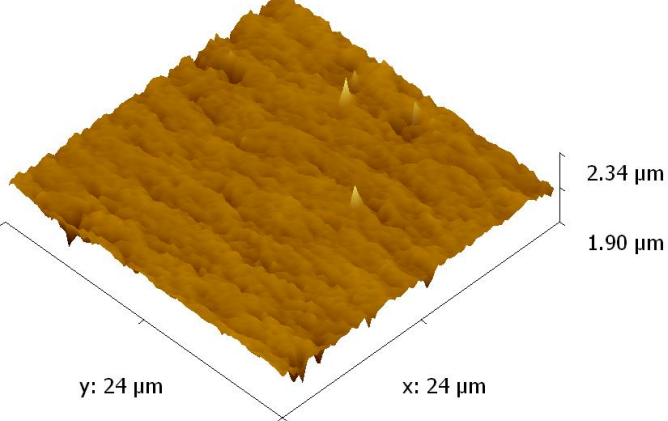
According to Hwang and Zhang [142], on their analysis of elastoplastic deformation on machined surfaces they identified differences in amplitude of the surface roughness profile could be attributed to the elastoplastic deformation and the elastic recovery process. This phenomenon is also believed to be responsible for the fall in experimental roughness values at higher feedrates. It can be postulated that a combination of high compressive forces and temperatures at the primary shear zone yields a high phase transformation of the properties of the material and influences the obtained results. Also, a post effect of the elastic recovery process could yield further influence on achievable surface results for materials of high plasticity. Additional conditions such as the change in the effect of the rubbing action of tool chips found at surface of workpiece may also be of importance.

Figure 5.4 shows the AFM 3D images result for the individual lens surfaces.



<p>(c)</p>  <p>y: 24 μm x: 24 μm</p>	<p>Average value: 187.4 nm Minimum: 0.0 nm Maximum: 254.4 nm Median: 191.5 nm Ra: 14.0 nm Rms: 19.8 nm</p>
<p>(d)</p>  <p>y: 24 μm x: 24 μm</p>	<p>Average value: 90.2 nm Minimum: 0.0 nm Maximum: 188.1 nm Median: 91.8 nm Ra: 6.1 nm Rms: 9.0 nm</p>
<p>(e)</p>  <p>y: 24 μm x: 24 μm</p>	<p>Average value: 142.6 nm Minimum: 0.0 nm Maximum: 407.5 nm Median: 144.7 nm Ra: 11.2 nm Rms: 15.8 nm</p>
<p>(f)</p>  <p>y: 24 μm x: 24 μm</p>	<p>Average value: 132.0 nm Minimum: 0.0 nm Maximum: 338.9 nm Median: 132.7 nm Ra: 12.9 nm Rms: 17.2 nm</p>

<p>(g)</p> 	<p>Average value: 46.7 nm Minimum: 0.0 nm Maximum: 192.8 nm Median: 46.4 nm Ra: 4.5 nm Rms: 8.9 nm</p>
<p>(h)</p> 	<p>Average value: 254.6 nm Minimum: 0.0 nm Maximum: 454.6 nm Median: 257.6 nm Ra: 13.6 nm Rms: 20.1 nm</p>
<p>(i)</p> 	<p>Average value: 66.8 nm Minimum: 0.0 nm Maximum: 311.4 nm Median: 65.7 nm Ra: 9.8 nm Rms: 15.2 nm</p>
<p>(j)</p> 	<p>Average value: 247.3 nm Minimum: 0.0 nm Maximum: 410.3 nm Median: 253.6 nm Ra: 20.4 nm Rms: 28.2 nm</p>

<p>(k)</p>  <p>y: 24 μm x: 24 μm</p>	<p>Average value: 202.4 nm Minimum: 0.0 nm Maximum: 351.0 nm Median: 206.6 nm Ra: 14.6 nm Rms: 21.0 nm</p>
<p>(l)</p>  <p>y: 24 μm x: 24 μm</p>	<p>Average value: 239.5 nm Minimum: 0.0 nm Maximum: 321.1 nm Median: 243.5 nm Ra: 15.5 nm Rms: 23.0 nm</p>
<p>(m)</p>  <p>y: 24 μm x: 24 μm</p>	<p>Average value: 52.5 nm Minimum: 0.0 nm Maximum: 177.8 nm Median: 52.4 nm Ra: 8.8 nm Rms: 11.2 nm</p>
<p>(n)</p>  <p>y: 24 μm x: 24 μm</p>	<p>Average value: 250.8 nm Minimum: 0.0 nm Maximum: 442.4 nm Median: 255.6 nm Ra: 17.3 nm Rms: 24.7 nm</p>

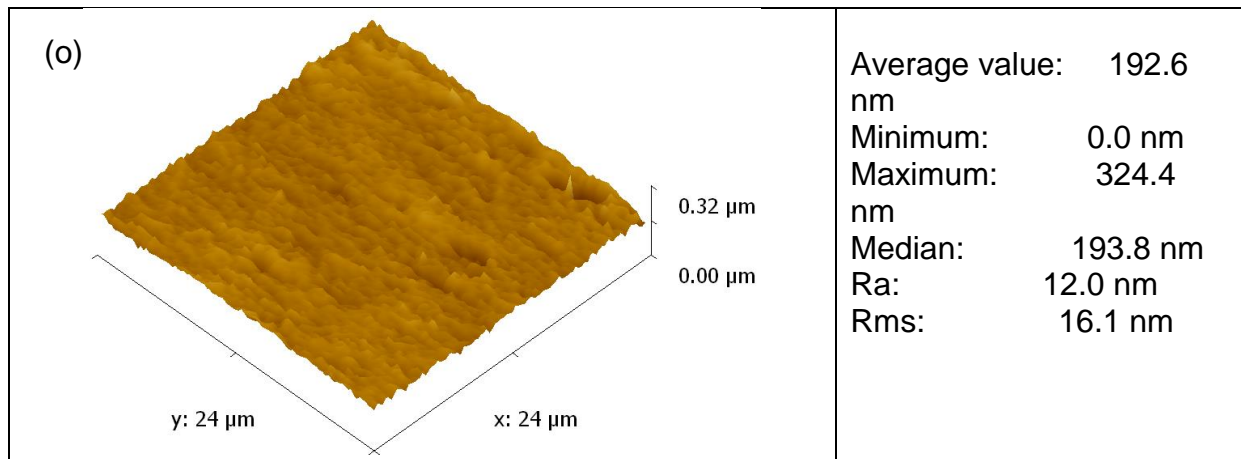


Figure 5.4 Surface AFM topographic images of contact lens

From the images in Figure 5.4 and results in Table 5.1, a trend could be identified of high roughness values with higher speeds and average feed values. This was postulated to be based on interaction of cutting parameters on experimental surface values. The samples in Figure 5.4 with large feedrate ($f = 12 \mu\text{m}/\text{rev}$) are seen to reflect the following conditions: they showed little or no sign of cutting edge damage from the measured profiles, and had a more uniform machined groove profile formed on the lens surface. An elastic recovery process could also be identified on some image acquisition as shown in sample (j) & (l) of Figure 5.4.

These qualitative results are further supported by the peak-to-valley roughness result. To clearly understand the relationship between these parameters on the surface roughness, a statistical analysis using the Box Behnken response surface method was employed. This analysis is shown in the next section.

5.1.2 Determination of appropriate polynomial equation to represent RSM model

An RSM data analysis was carried out using statistical software. The determination of a suitable polynomial equation to represent the relationships between input parameters and the surface roughness (output response) was done by carrying out a sum of squares sequential model and lack of fit test shown in Table 5.2 and Table 5.3. From these two tables various source equations are evaluated and the best suited in predictability and lack of fit form to the problem is identified. The result from the sequential model indicates a “linear vs mean” approach; however, the lack of fit

test suggests a linear equation approach. Figure 5.2 shows a scatter plot of the Box-Behnken statistical model.

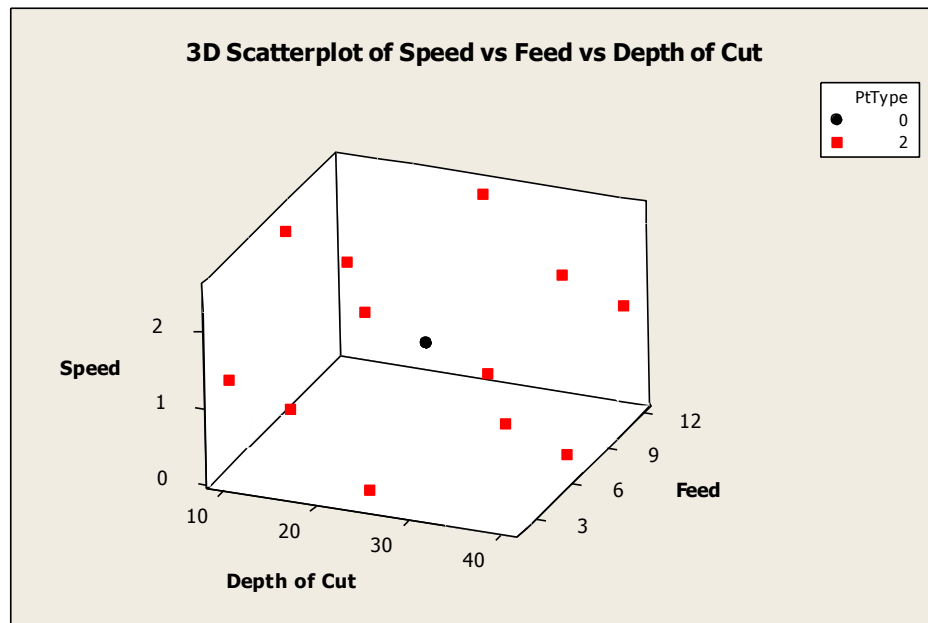


Figure 5.5 Box-Behnken statistical model

Table 5.2 Sequential model sum of squares (SMSS) analysis for surface roughness

Source	DF	Seq SS	Adj MS	F	P	Remark
Mean vs Total	<u>1</u>	<u>2210.69</u>	<u>2210.69</u>			<u>Suggested</u>
Linear vs Mean	3	66.53	22.18	1.39	0.2975	
2FI vs Linear	3	46.74	15.58	0.97	0.4541	
Quadratic vs 2FI	<u>3</u>	<u>95.61</u>	<u>31.87</u>	<u>4.79</u>	<u>0.0621</u>	<u>Suggested</u>
Cubic vs Quadratic	3	27.06	9.02	2.92	0.2655	Aliased
Residual	2	6.18	3.09			
Total	15	2452.81	163.52			

Table 5.3 Lack of fit test for surface roughness

Source	DF	Seq SS	Adj MS	F	P	Remark
Linear	9	169.40	18.82	6.09	0.1489	
2FI	6	122.66	20.44	6.62	0.1371	
Quadratic	<u>3</u>	<u>27.06</u>	<u>9.02</u>	<u>2.92</u>	<u>0.2655</u>	<u>Suggested</u>
Cubic	0	0.000				
Pure Error	2	6.18	3.09			

The lack of fit tests suggests the use of a quadratic model equation which shows the least significant lack of fit. Also, the sequential test considers a model equation where additional terms remain significant to the model with “Quadratic vs 2FI” having the highest “F-value”. Therefore, based on these suggestions, the quadratic equation approach was utilised for modelling the surface roughness.

5.1.2.1 ANOVA analysis of the response surface quadratic model for surface roughness

The analysis of variance have been performed to check whether the model is adequate as well as to check the significance of the individual model coefficients. Table 5.4 shows the ANOVA for surface roughness. The Model F-value of 5.60 implies the model is significant. The P-value indicates the percentage probability of occurrence due to noise of the resulting F-value obtained. In the table below, a 1.40% chance is identified for the stated F-Value".

Table 5.4 ANOVA for model coefficient for Surface Roughness in UHPM of contact lens polymer

Source	DF	Seq SS	Adj MS	F	P	Remark
Model	3	146.36	48.79	5.60	0.0140	significant
B-Feed	<u>1</u>	9.25	9.25	1.06	0.3249	
C-Depth of cut	<u>1</u>	43.25	43.25	4.97	0.0476	
B²	<u>1</u>	93.87	93.87	10.78	0.0073	
Residual	11	95.76	8.71			
Lack of fit	9	89.58	9.95	3.22	0.2593	<i>not significant</i>
Pure Error	2	6.18	3.09			
Cor Total	14	242.12				

The "Lack of Fit F-value" of 3.22 within the ANOVA estimations implies that lack of fit is not significant relative to the pure error. For this value a 25.93% chance of occurrence due to noise is obtained. A non-significant lack of fit is a good result, since a fitting model is desired.

Normal plot of residuals

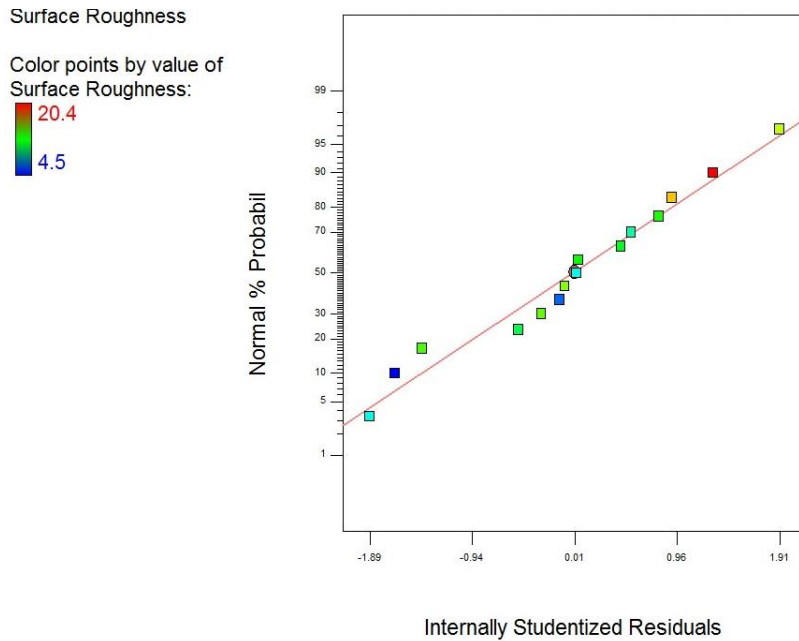


Figure 5.6 Normal probability plot of residuals in surface roughness modelling

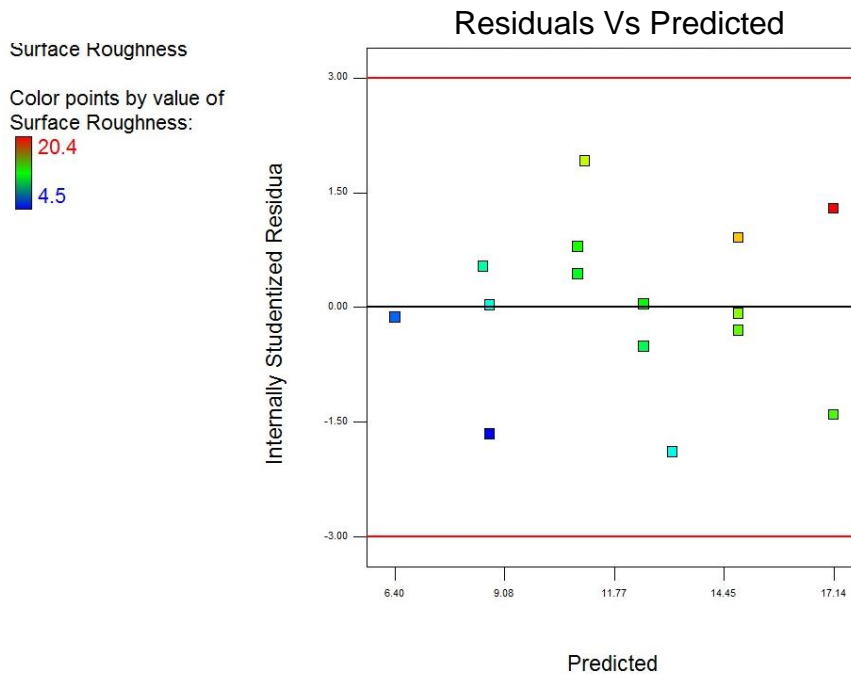


Figure 5.7 Probability plot of residuals vs. predicted points

The normal probability plot of the residuals and the plot of residuals versus the predicted response seen in Figure 5.6 and Figure 5.7 show a close correlation of the data points to the straight probability line and no obvious and unusual structure found. This indicates that the model possesses adequate normality of residuals and no constant error.

5.1.2.2 Determination of significant factors influencing surface roughness

In determining the cutting parameters influential to the surface roughness the results from the ANOVA (Table 5.4) were studied. Based on a probability value greater than the F-value and less than 0.005, significant terms to the model were identified. In this case the feed rate, depth of cut and the square effect of the feed were identified as the significant model parameters linked to the surface roughness. The behaviour of surface roughness in response to variations of feed rate was also compared to research work compiled by other researchers to support the validation of the model.

- The surface roughness response in Figure 5.8 indicates that as the feed increases from 2 to 7 $\mu\text{m}/\text{rev}$, surface roughness increases from 8.725 to about 15nm with a diminishing rate. Beyond 7 $\mu\text{m}/\text{rev}$, increase in feed leads to a gradual fall in surface roughness of the lens. A curved correlation is shown to exist with increase in feed. This is believed to be as a result of the change in tool width of the chips during machining. At this stage a reduced amount of chip is found at the diamond tip causing a relative improvement in achieved surface roughness.

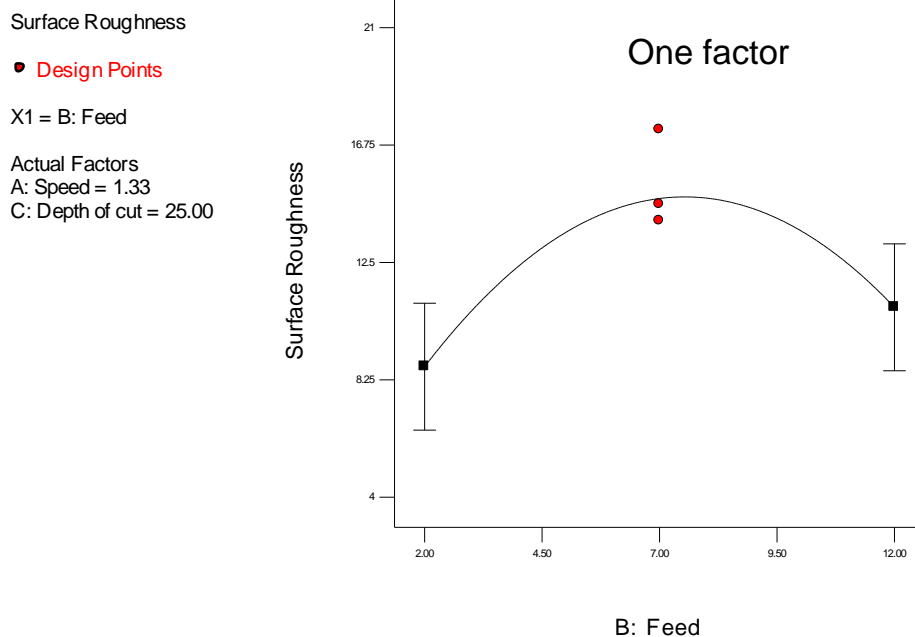


Figure 5.8 Normal Probability plot of surface roughness vs speed

However, the behaviour of surface roughness in response to variations of depth of cut shows a straight-line relationship. The surface roughness response in Figure 5.9 indicates that as the depth of cut increases from 10 to 40 μm , the surface roughness of the lens improves with a decrease from 17.13 to 12nm. Furthermore, the graphical representation of the contour plot in Figure 5.10 shows the combined effects of depth of cut and feed rate on surface roughness. This poorer surface finish at low depth of cut is believed to be also attributed to the elastoplastic deformation and the elastic recovery process. Various sub-structural surface effects occur within the compressive shear zone in polymer machining. These effects caused by the influence of tool shape, negative rake angle, material properties and temperature inhibit a phase transformation within the ductile cutting regime for elastoplastic deformation. This effect in combination with the concern of the light cutting chips across the face of the workpiece during cutting laps damages the achievable surface finish. This occurs as low weight chips bundle and entangle around the tool tip. A rapid depreciation in surface roughness is observed during such conditions.

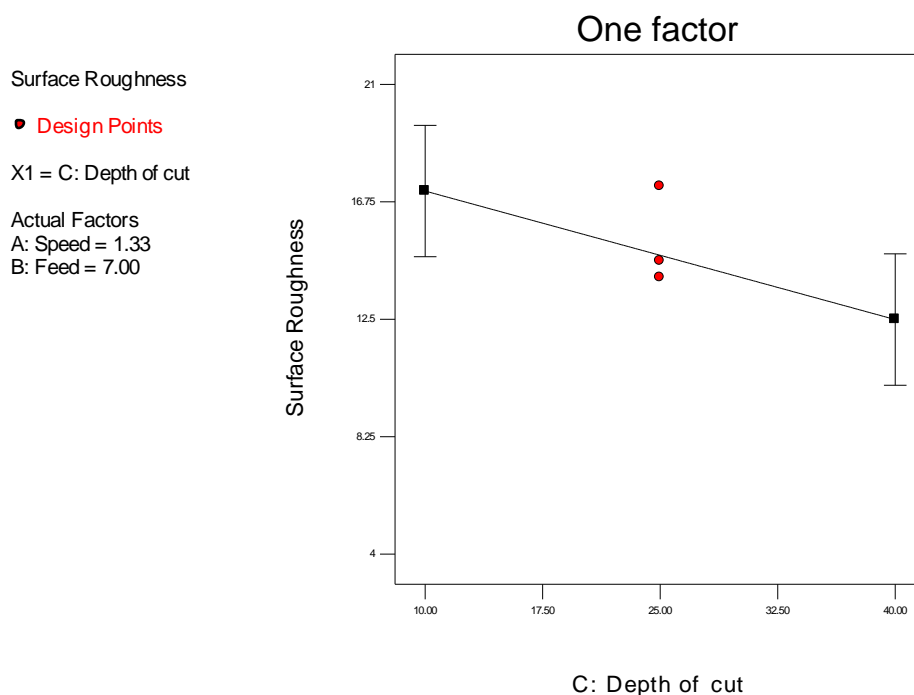


Figure 5.9 Normal Probability plot of surface roughness vs depth of cut

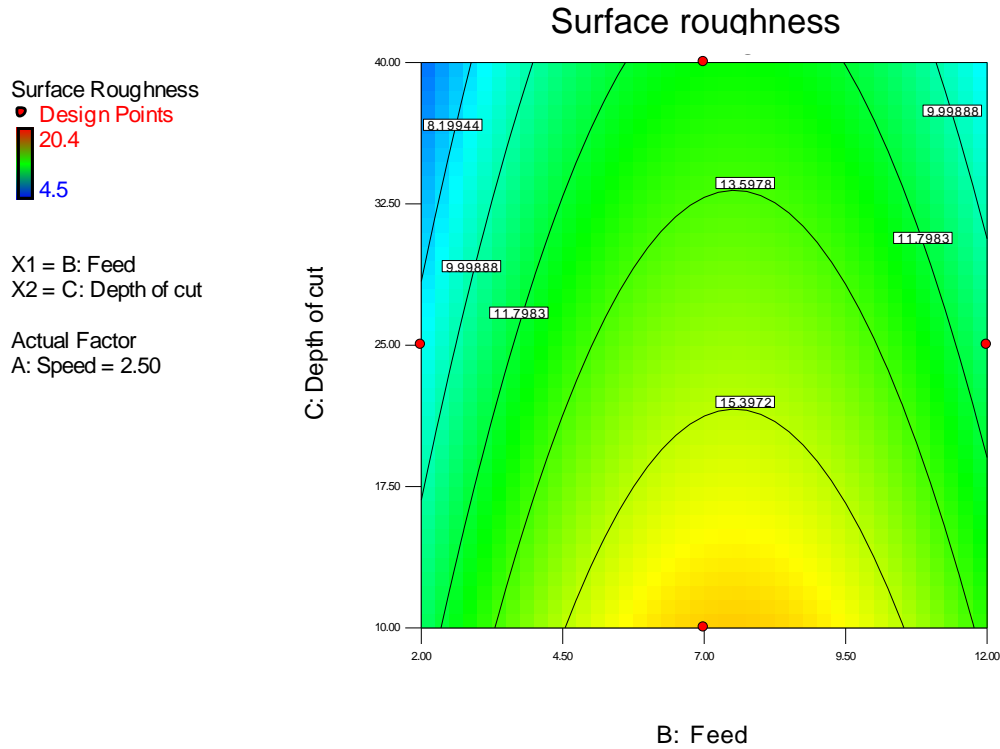


Figure 5.10 2D Normal Probability plot of surface roughness vs feed and depth of cut

From the surface response modelling the quadratic polynomial model equation developed to relate the input parameters to the surface roughness is shown in Eq. 4.2 below.

$$\text{Surface roughness (Ra)} = 7.35629 + 3.02300 F - 0.15500 D - 0.20057 F^2$$

where: $F = \text{Feed } (\mu\text{m/rev})$, $D = \text{depth of cut } (\mu\text{m})$ (4.2)

From the graphical perspective of the model equation using a 3D surface plot, in (Figure 5.11), the effects of varying the depth of cut and feed while keeping the speed constant is shown. Figure 5.11 shows the curved relationship of the feed rate over an increased depth of cut for lower surface roughness. This graph shows a reflection of the combination of various factors in establishing surface roughness. This is however, largely attributed to the chip formation at the tool chip. As chips form and leave the surface of the polymer and tool, magnitudes in electrostatic accumulations are varied.

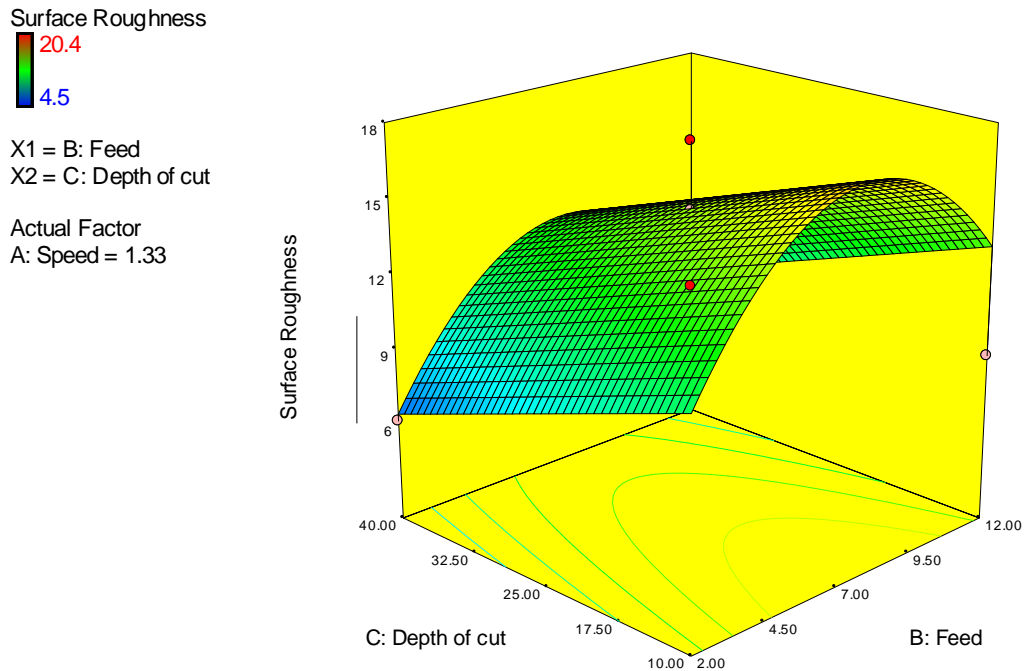


Figure 5.11 3D Plot of the influence of feed and depth of cut on surface roughness

Another train of thought on the analysis of the results is based on the mechanics of polymer machining. In Figure 5.54, it can be seen that during polymer machining numerous underlining cutting effects occur. This complex phenomenon could result as a consequence on the shape of the tool, choice of rake angle, composition of the polymer material and temperature at the cutting point.

Deviations are known to exist between the real surface roughness measured and the calculated theoretical surface profile. These deviations are primarily attributed to other underlining machining conditions such as tool wear, vibration of the tool during machining, build-up edge at tool tip, resolution of the measurement machine, etc. Fundamentally also the theoretical calculation only considers the feedrate and tool radial dimensions. However, research has shown [143] that this theoretical modelling approach can be used for the prediction of the surface finish in comparison with the measured surface roughness values to investigate the influence of the work-material, tool behaviour, cutting parameters, and other effects on the machined surface.

Model validation

The validation of the model is used to ascertain if the developed model can sufficiently predict the surface roughness output generated during cutting. Three sets

of parameters were chosen for validation. As seen in Table 5.5, the actual predicted values are compared using the residual error. A margin of 25% is used to determine the adequacy of the model at a confidence prediction level of 80%.

Table 5.5 Experimental run and results of surface roughness

Run	Factors			Responses	
	A: Speed (m/s)	B: Feed ($\mu\text{m}/\text{rev}$)	C: Depth of cut (μm)	Predicted Surface Roughness (nm)	Actual Surface Roughness (nm)
1	2.5	2	25	8.72501	8.8
2	1.33	2	40	6.40001	6.1
3	0.15	7	10	10.87521	12

It can be concluded that the table attests that the model presents an acceptable depiction of the roughness effects on the surface of a lens based on the selected cutting parameters during the machining of Roflufocon E.

5.1.3 Analysis of cutting chips

An evaluation of the cutting chips gives a clearer depiction of the effects generated from the change in tool chip width to its influence on machining dynamics. Table 5.6, Table 5.7 and Table 5.8 show a classification of cutting chips at high depth, low feed, low depth and low speeds. With these classification tables, an overview of the changes in morphology of the chip is understood.

Chip removal in the nanomachining of polymers takes place by virtue of plastic deformation rather than brittle fracture. Literature has shown this possibility of machining brittle materials in the ductile-regime [137]. Table 5.6, depicts the surface micro topography and morphology of the lamella structure obtained during machining. Some experimental tests with high cutting depth generated high micro-cracking and structural ripples on cutting chips. Lamellar chip formation thus represents a form of continuous, periodic chip formation process similar to that of the pure continuous chip formation in ductile materials. However, this differs by the existence of variations in the deformation process that cause more or less significant cleavages or even concentrated shear bands on chip profiles (Figure 5.12). Lamellae structures are believed to be produced due to thermal or elastomechanical

processes with a high formation frequency [144]. These observations were mainly identified at high depth of cut ($40\ \mu\text{m}$) and high cutting speed ($2.5\ \text{m/s}$). Nevertheless, they are commonly known to occur with highly ductile workpiece materials with an increased strength, especially at high cutting speeds.

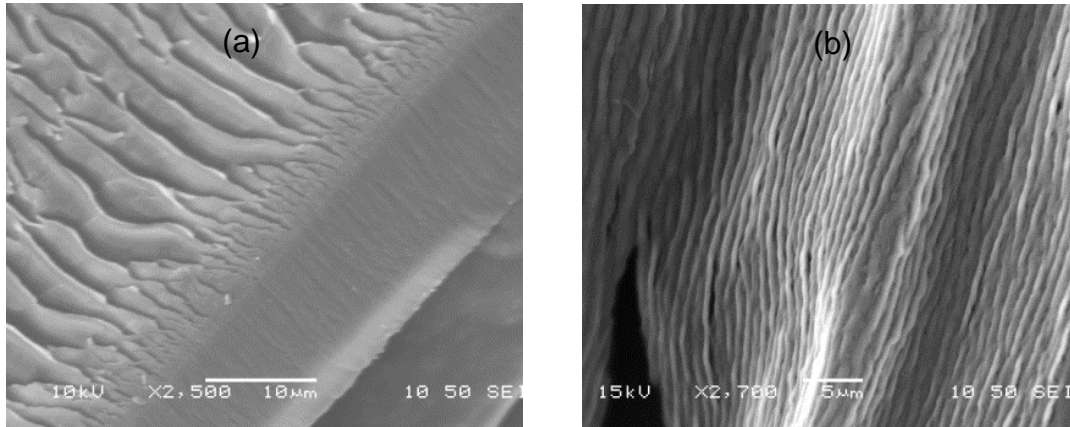


Figure 5.12 Lamella structure on the cutting chip (a) 2.5m/s , $7\ \mu\text{m/rev}$, $40\ \mu\text{m}$ (b) 2.5m/s , $2\ \mu\text{m/rev}$, $25\ \mu\text{m}$

At such high speed and cutting depth value, thick chips were obtained. The core of the lamella is generated by the plastic deformation which takes place in the primary shear zone in the form of shear deformation, due to high shear forces occurring on the cutting plane. Lamellae sizes were observed to vary based on the choice of feed employed. Higher feed values greatly increased ripple sizes and generated scaling/segmented chip structure with low yield strength and macro cracks. Research by Jasinevicius et al. [141] on the surface integrity of Al-Mg alloy on the in ultra-precision machining identified similar chip topography from their experiments. In their study, they identified the lamella to vary based on the grain structure of the material and the crystallographic orientation of the crystal grains (Figure 5.13).

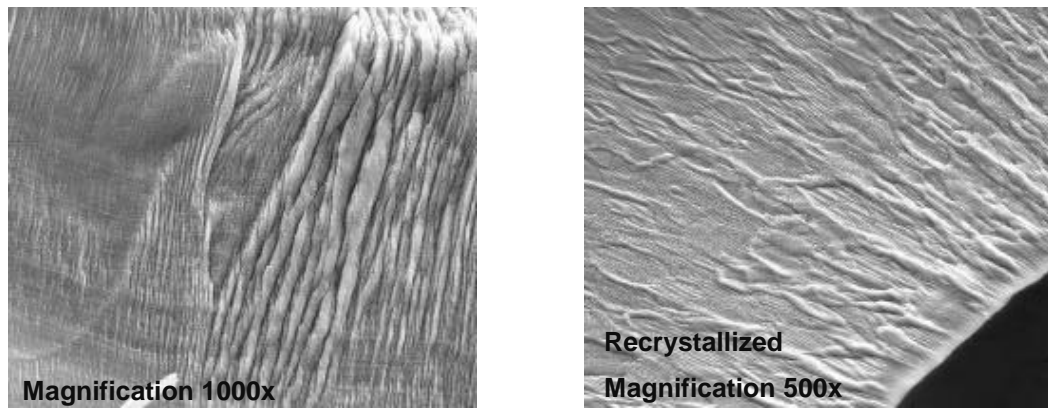


Figure 5.13 Photomicrographs made by SEM of cutting chips (Cutting conditions: $f = 30 \mu\text{m}/\text{rev}$, depth of cut = $10 \mu\text{m}$) Jasinevicius et al. [138]

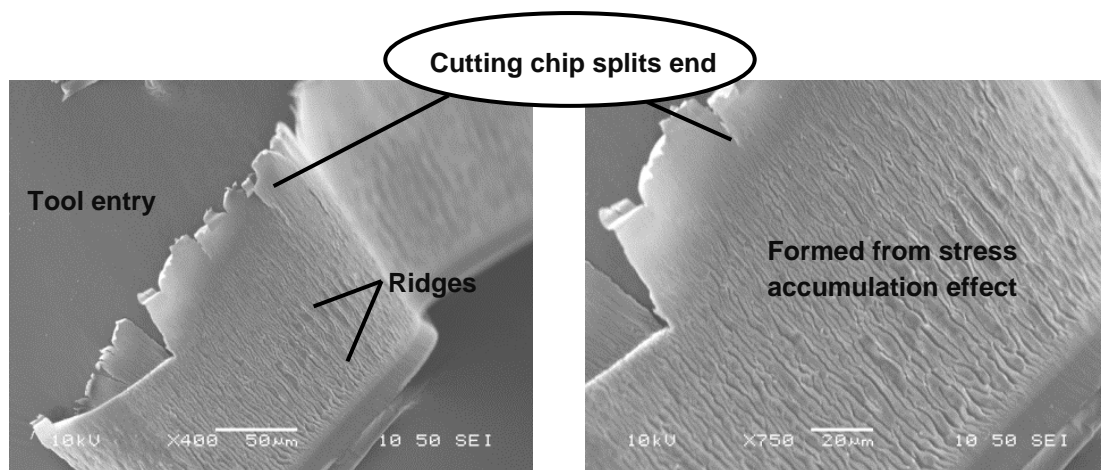
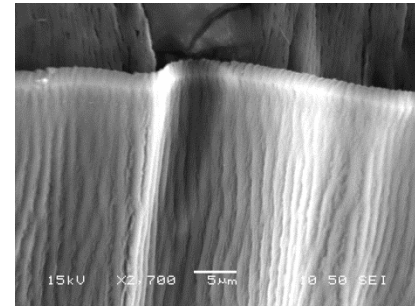
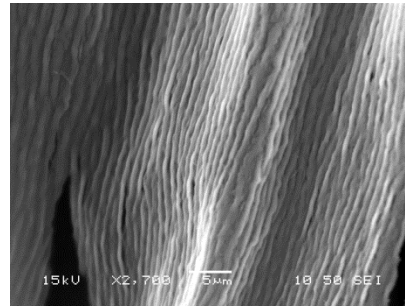
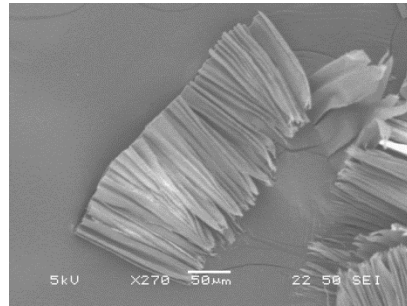
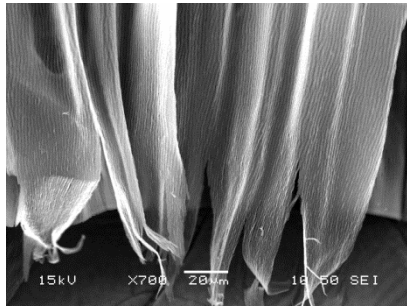


Figure 5.14 Photomicrographs made by SEM of cutting chip splits (Cutting conditions: $f = 30 \mu\text{m}/\text{rev}$, depth of cut = $10 \mu\text{m}$)

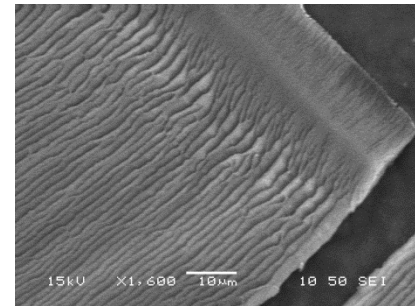
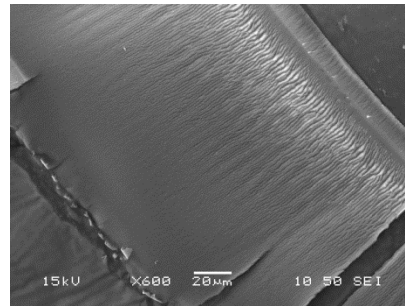
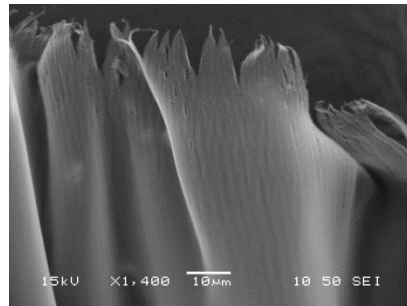
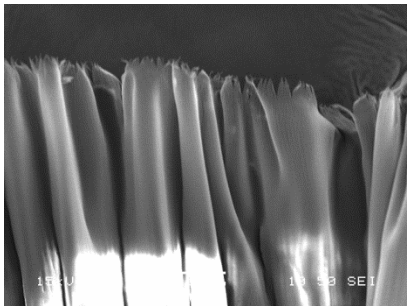
Figure 5.14, shows a photomicrographs made by scanning electron microscope during the course of this research. It is found that the cutting chip splits out at the starting position of ridges. These splits which are probably formed by the stress accumulation effect are at the tool entry side of cutting chips and along the cutting direction. The thickness of cutting chips is thinner at the tool entry, which is easy to split under the effect of stress accumulation. However, with the increase of thickness across the cutting direction, the splitting is stopped. The generation of splits can help locate the ridges from cutting action formed on the chips [145].

Table 5.6 shows cracking and microstructural ripple occurrence on cutting chips based on high cutting depth

Table 5.6: Cracking and microstructural ripple occurrence on cutting chips based on high cutting depth at SEM different image magnification

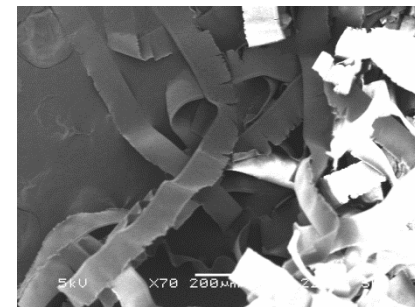
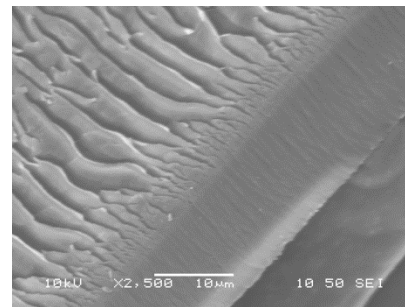
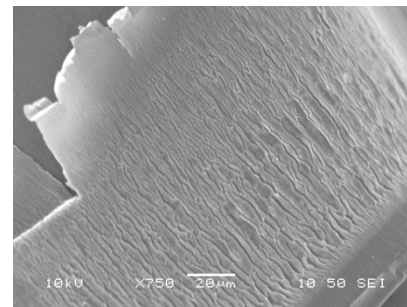
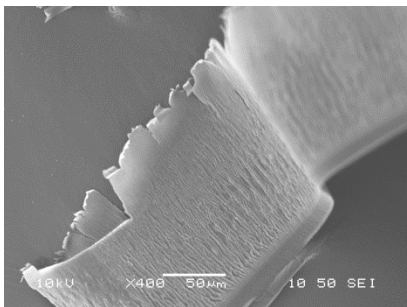


Experiment 1 (2.5m/s, 2µm/rev, 25µm, 0.060N)

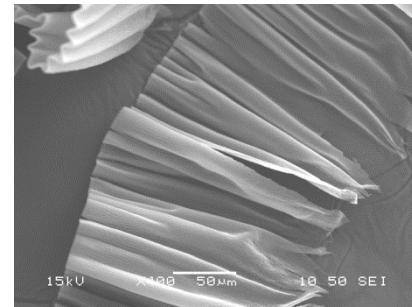
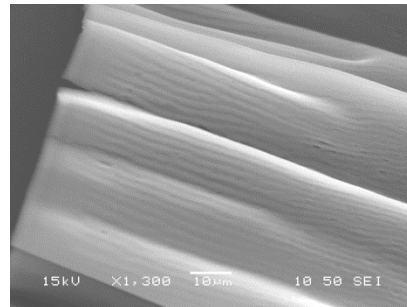
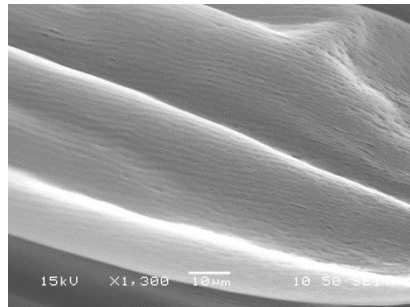
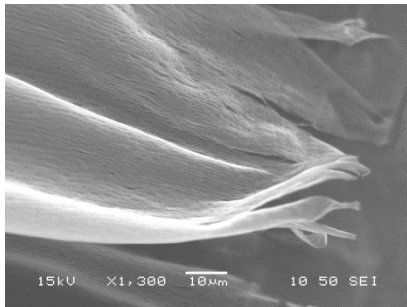


Experiment 5 (2.5m/s, 7µm/rev, 40µm, 0.060N)

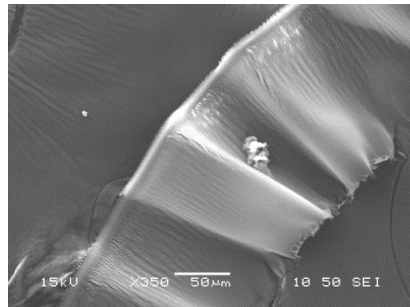
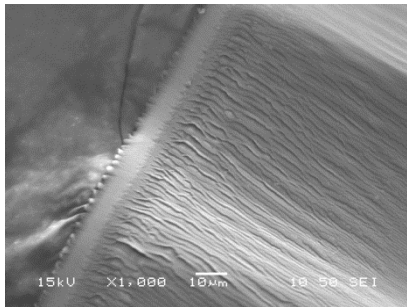
Experiment 6 (2.5m/s, 12µm/rev, 25µm, 0.060N)



Experiment 15 (2.5m/s, 7µm/rev, 40µm, 0.060N)

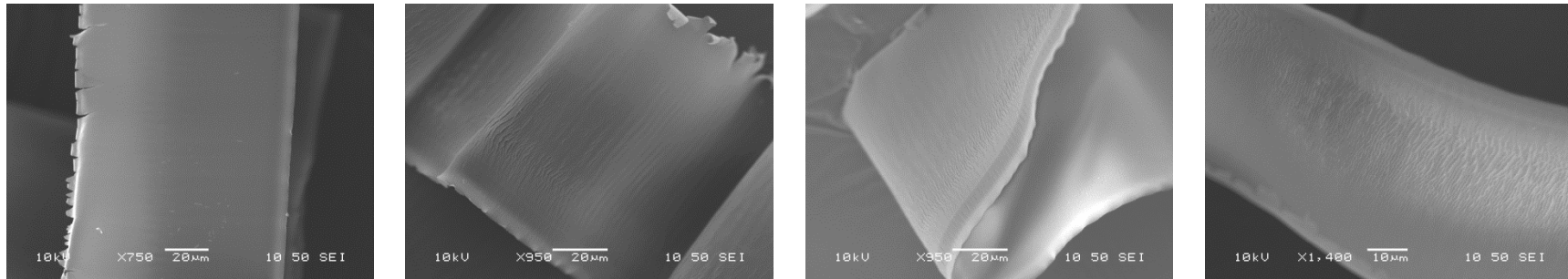


Experiment 4 (1.325m/s,2um/rev,40µm,0.060N)

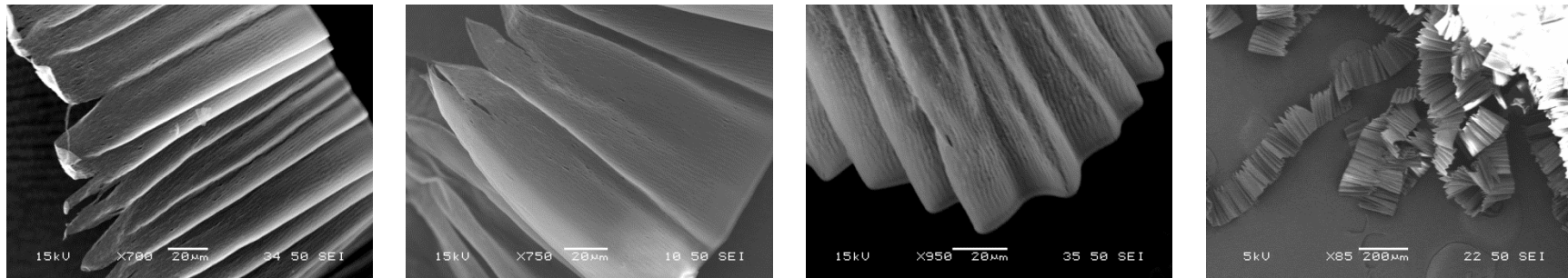


Experiment 2 (1.325m/s,12um/rev,40µm,0.060N)

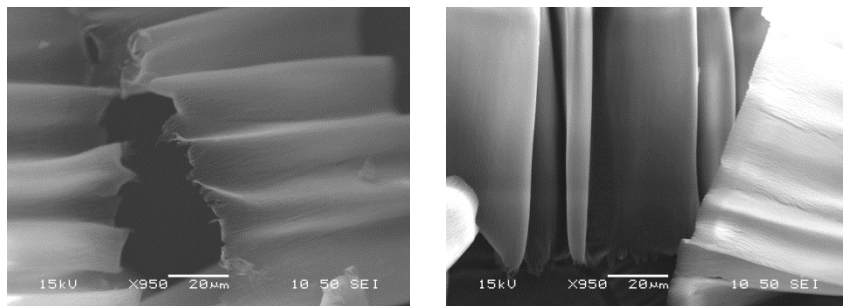
Table 5.7 Smooth and large folding on cutting chips based on low cutting feed



Experiment 13 (2.5m/s,2µm/rev,25µm,0.060N)

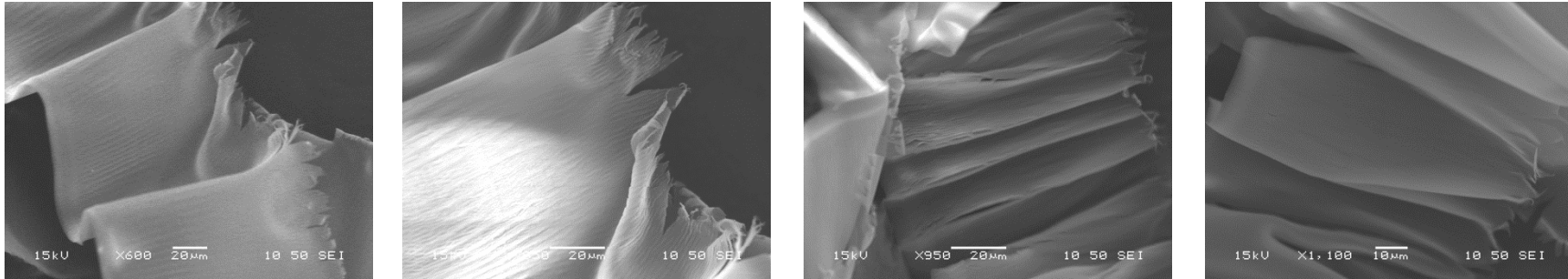


Experiment 7 (0.15m/s,2µm/rev,25µm,0.060N)

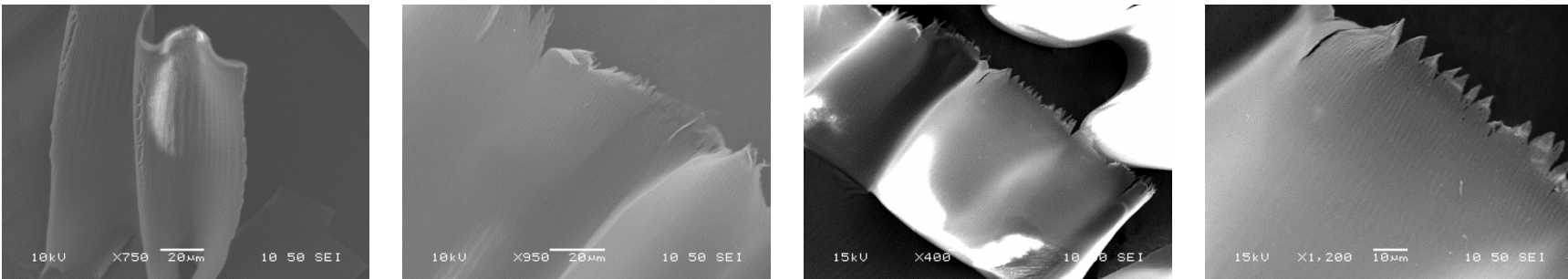


Experiment 12 (1.325m/s,2µm/rev,10µm,0.060N)

Table 5.8 Tear edges on cutting chips at low depth of cut and cutting speed

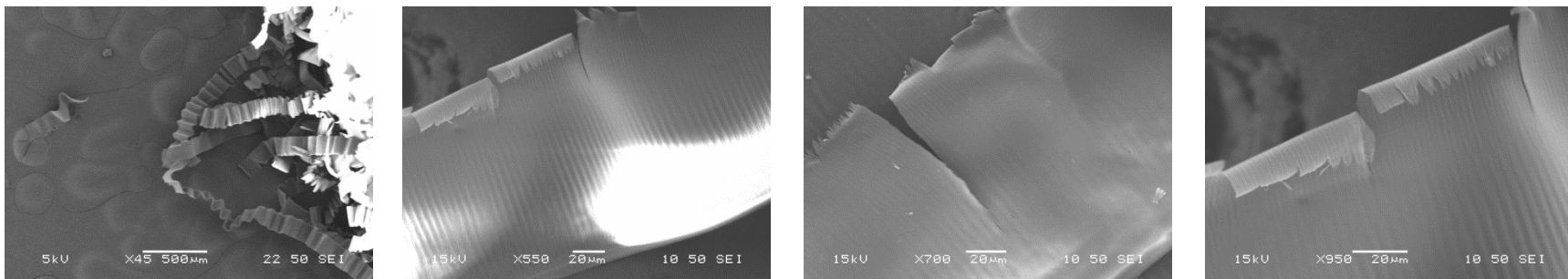


Experiment 8 (0.15m/s,7µm/rev,10µm,0.060N)



Experiment 14 (1.325m/s,7µm/rev,25µm,0.060N)

Experiment 3 (1.325m/s,7µm/rev,25µm,0.060N)



Experiment 11 (1.325m/s,7µm/rev,25µm,0.060N)

The machining of polymers and quasi-isotropic polymer composites (such as paper-filled, short-fiber-filled, and particulate-filled thermoplastics) is to a great extent similar to the machining of homogeneous metals [146]. For ductile thermoplastics, a continuous shear-type chip is largely formed by plastic deformation in a well-defined shear plane. An exception to this is the formation of continuous elastic-type chip that occurs when machining polymers that show high rubber-like elasticity (such as polyethylene) at low cutting speeds. On the other hand, machining of the stiffer and stronger thermosets is marked by fracture and discontinuous chip formation. The resulting surface quality is much better when machining takes place with a continuous chip. The results in this thesis show a high rubber-like elastic chip flow from the Roflufocon E polymer. The chips in Table 5.8 (magnification less than X600) show the smooth continuous flow as predicted for low cutting speeds.

Polymer machining behaviour is also known to be affected by process parameters such as tool material, rake angle, cutting edge radius, depth of cut and cutting speed [146]. From literature it is seen that thermosets and thermoplastics react differently to applied load variations. Thermosets show a more brittle nature but thermoplastics are more ductile with a high strain to fracture ratio. Over an increasing deformation rate, materials however could show transition from ductile to brittle behaviour. Based on this reason, chip formation and the quality of surface finish attainable in machining vary widely on cutting parameters. From Jamal [2] a high rake angle and low depth of cut results in a reduction in the amount of deformation the material undergoes to form the chip. However, higher cutting speeds create high strain on the material to yield a brittle nature during machining.

5.1.3.1 The influence of rake angle on material properties of the workpiece

From the Table 5.7, smooth and large folds are observed on cutting chips. This is as a result of the low cutting feed. This also reflects a reduction in the cutting shear strain in the primary zone from cutting. This cutting process is characterised by a long and continuous chip flow. Continuous chip formation shown in these images is promoted by: the uniform, fine-grained structure and high ductility of the workpiece material, high cutting speeds and low friction on the rake face, the rake angle and a low undeformed chip thickness [144]. Goel et al. [147], in their review paper on the diamond machining of silicon, discuss the effect of a negative rake angle tool on the

machining mechanics and force distribution. In this study they identify that a negative rake angle tool compression force is experienced on the cutting tool instead of bending stress. Additionally, they describe the negative rake angles of the tool to exert a hydrostatic stress state in the workpiece, which inhibits crack propagation and leads to a ductile response from brittle materials during nanometric cutting [147-149]. Similar conclusions could be drawn from the SEM images at low cutting feed and at high cutting speeds.

5.1.3.2 The influence of cutting parameters on material properties of the workpiece

In general, the machining behaviour of thermoplastics is dependent on cutting speed and rake angle. From the results in this thesis, the use of the negative rake angle yields to an increase in the compressive force acting directly over the primary shear zone/high pressure phase transition zone which leads to a phase transition from ductile to brittle regime. This influence of the rake angle on the machining process also influences the trailing elastic recovery zone after the tool has passed the cutting zone. Furthermore, a transition from ductile to brittle behaviour takes place as the cutting speed is increased. This is attributed to the sensitivity to heat of the polymers. It is shown by the increase in the lamella at higher speeds on the cutting chips (Table 5.6). In this research, it is observed that based on the high capacity for elastic deformation this polymer possesses; a continuous elastic chip is produced at low cutting speeds and a large positive rake angle. This type of chip is almost entirely formed by elastic deformation, but for the effect of the separation of the polymer chains needed to form the chip which is not elastic. Another type of continuous chip is the shear-flow type chip which is observed when cutting at higher cutting speeds (Table 5.6) and is caused by plastic deformation of the material as it passes through a shear plane.

The combination of the low cutting feed and low speed furthermore created cone-like chip edges formation. Various combinations of speed values influenced either a tear on chip edges or created fillet like cone structures. This, as mentioned earlier was attributed to the small chip thickness at tool entry into the workpiece, having a lower yield strength based on the high compressive forces obtained with a negative rake angle tool on the chip. These tears are witnessed in a large number of machining experiments and vary in shapes based on parametric values.

Research studies have shown that chips with a very small chip thickness ($h = 0.1 \mu\text{m}$), have shown a corrugated shape. In contrast to chips with higher thickness, these chips have imperfections such as fringed edges or dents. For much higher thicknesses of $h = 10 \mu\text{m}$, the chip forms are seen to change into a segmented chip. This was attributed to the fact that for larger undeformed chip thicknesses the state of stress changes and exceeds the deformation capacity of the material [150]. Cristino et al. [151] in their study also attribute the shape of chip curvature to the undeformed chip thickness. In their study they identify that with rising undeformed chip thickness the radius of curvature of the chip decreases. Nonetheless, experimental investigations show that with rising chip contact length the radius of curvature increases [152].

As can be seen in Table 5.8, smooth chip edge in combination with a shredded edge is obtained at low cutting speeds. This could be explained based on the time for a cleaner rupture of the edge of the chip from the workpiece. As the speed increases, the ductility improves, based on heat generated in the cutting zone. This condition reduces the frequency of tear found at the edges and it is also dependent on the thickness of the chip at the time.

5.1.4 Experimental observations of factors affecting surface finish

During these experimental tests the minimum achieved surface roughness was obtained at a 0.15 m/s , $2 \mu\text{m/rev}$ and $25 \mu\text{m}$. During modelling, feed rate and depth of cut were identified as significant influential factors in the determination of surface roughness; however, changes in the feed rate had greater influence than any other factors. This situation is assumed to be due to a decrease in the distance between cutting passes by the diamond tip, creating a form of overlapping between cutting grooves. Also, this could be attributed to the rubbing action originating from tool chip magnetised to the cutting tool from a triboelectric effects. These chips as the feed gradually increases increase in width and cause disturbance during the cutting process (Figure 5.15).

However, as the feed further increases beyond $7 \mu\text{m/rev}$, a point is achieved where a balance semi-balance can be found between increase in the width of chips and chip clearance (due to size) from the surface of the lens during machining. At this stage a

reduced amount of chip is found at the diamond tip causing a relative improvement in achieved surface roughness.



Figure 5.15 (a) Diamond machining of a contact lens button (b) top surface of mounted lens button

At a feed rate of $7\mu\text{m}/\text{rev}$ and a very low depth of cut of $10\mu\text{m}$, a very rough lens surface of 20.4nm is achieved during machining. This poorer surface finish is presumed to be attributed to the compounding effect of a reduced chip thickness due to a low depth of cut. These further compounds initial observations and a huge ball of chip entangled around the tool tip as shown in Figure 5.15. A rapid depreciation in surface roughness is observed during such conditions.

An overview of the cutting shows that cutting depth influenced the thickness (width) of the cutting chip. This generated light or thick chips which generated an effect on continuous and non-continuous chip flow. Lamellae structures which represented a high shear force occurring in the primary shear zone also were also used to explain shearing mechanics of chips during machining. The effects of this high shearing force are also reflected at the edges of the chip which possess a lower chip thickness. They cause rupture and tear of the continuous chip flow and these effects are enhanced at lower speed and feed. Also, the feed rate was identified to have a high effect on the structural surface of the tool chip. The speed of entry of the tool into the workpiece influences compressive stress zones found during chip formation and also affects their topography and structure. This also contributed in chip breaking. However, it is postulated that the combination of feed and speed led to a variation in chip edges. This variation ranged from cone-like, fillet-shaped to actual

tear. A combination of these observations on the cutting chip can be used to explain the formation of tool chip at the tool tip during machining.

Furthermore, at high cutting speeds, the shearing bands are more conspicuous. This was linked to the phenomenon of localized deformation in the primary shear zone that becomes more important with the increase in the temperature. Based on the low thermal conductivity of the polymer, a high rise in temperature is presumed to occur at the cutting zone. This temperature concentration caused a decrease in the mechanical properties of material by reducing its resistance to the plastic deformation and leads shearing of the chips. From literature Salem et al. [153] also explain this phenomenon to be as a results of periodic catastrophic thermoplastic instability where the decrease in material flow stress due to thermal softening more than offsets the associated strain hardening [154].

It is also seen that due to the viscous behaviour of the material, the ultimate strength of the material increases and elongation to fracture decreases as the rate of load application is increased. In addition, increasing the rake angle and decreasing the depth of cut results in reducing plastic deformation and promotes continuous shear-type chip formation. Because of the low thermal conductivity and high heat capacitance of polymers, they are more capable of retaining the heat from machining than metals. This in turn results in increasing the material temperature and ductility [146].

As observed from the RSM model, negligible effect of cutting speed is experienced during the prediction of surface roughness within the selected parameters. Further experimentation with a wider range of parameters may however produce difference in results.

5.1.5 Summary of results

It can be seen from the research that understanding the effects of the chip is also essential in the investigation the influence of cutting parameters. Chips additionally influence the achievable surface quality of lenses when entangled at the tool tip from prolonged rubbing action.

In conclusion, the results of surface roughness measurements indicate a rise in roughness value with a low depth of cut, and increasing feed to a certain value. The study identifies feed rate as the main influential cutting parameter towards the achievement of high surface accuracy based on significant changes feed rate has on surface roughness and cutting tool chip.

The next section addressed results observed in the estimation of the influence of cutting parameters on cutting force and the predictive modelling of cutting force occurring at the tool tip.

5.2 Predictive modelling of cutting force at the tool tip

In determining the force at the tool-tip, the force equation by Fetecau and Stan [155] was used in the study while the governing equations for the analysis are premised on a multivariate total derivative function and Runge-Kutta's fourth order non-linear finite series scheme [155].

$$\text{Given that } F_c = \frac{w}{l} \left(\frac{Eh^2}{6} \right) \varepsilon \quad (4.3)$$

Adapted source: Fetecau and Stan [155]. Where,

F_c =Cutting force

w =Width of tool

l = Length of tool

h =Tool thickness

E =Young's modulus of material

ε =Strain

Consider a multivariate derivative function expressed in terms of $F_c = f(l, w, \varepsilon)$ such that the tool length (l), width (w) and strain (ε) are simultaneously changing along the tool length, then a total derivative function of the variants can be expressed as in (1):

$$dF_c = \frac{\partial F_c}{\partial l} \partial l + \frac{\partial F_c}{\partial w} \partial w + \frac{\partial F_c}{\partial \varepsilon} \partial \varepsilon \quad (4.4)$$

Hence,

$$dF_c = \frac{Ewh^2\varepsilon}{6l^2} \partial l + \frac{Eh^2\varepsilon}{6l} \partial w + \frac{Ewh^2}{6l} \partial \varepsilon \quad (4.5)$$

$$dF_c = \frac{Eh^2}{6l} \partial l \left[\frac{-w}{l} \partial l + \varepsilon \partial w + w \partial \varepsilon \right] \quad (4.6)$$

From Runge-Kutta's fourth order scheme, let

$$y = y_0 + \frac{1}{6} (\xi_1 + 2\xi_2 + 2\xi_3 + \xi_4) \quad (4.7)$$

Where, ξ_1, ξ_2, ξ_3 and ξ_4 represent the terms for each order of the equation

$$\xi_1 = \varphi f(x_n, y_n) \quad (4.8)$$

$$\xi_2 = \varphi f(x_0 + \frac{h}{2}, y_0 + \frac{\xi_{11}}{2}) \quad (4.9)$$

$$\xi_3 = \varphi f(x_0 + \frac{h}{2}, y_0 + \frac{\xi_2}{2}) \quad (4.10)$$

$$\xi_4 = (x_0 + h, y_0 + \xi_2) \quad (4.11)$$

$\varphi = \text{simulationg interval}$

Then

$$\xi_1 = \varphi f(l, w, \varepsilon, F_c) = \frac{\varphi E h^2}{6l} \left[\frac{-w}{1} \partial l + \varepsilon \partial w + w \partial \varepsilon \right] \quad (4.12)$$

$$\xi_2 = \varphi f \left[1 + \frac{\varphi}{2}, w + \frac{\varphi}{2}, \varepsilon + \frac{\varphi}{2}, F_c + \frac{\xi_1}{2_0} \right] \quad (4.13)$$

$$= \varphi f \left[1 + \frac{\varphi}{2}, w + \frac{\varphi}{2}, \varepsilon + \frac{\varphi}{2}, F_c + \frac{\varphi E h^2}{12l} \left[\frac{-w}{1} \partial l + \varepsilon \partial w + w \partial \varepsilon \right] \right] \quad (4.14)$$

$$= \varphi \left[F_c + \frac{\varphi E h^2}{12(1+\frac{\varphi}{2})} \left(\frac{-(w+\frac{\varphi}{2})}{1+\frac{\varphi}{2}} \right) \partial l + \left(\varepsilon + \frac{\varphi}{2} \right) \partial w + \left(w + \frac{\varphi}{2} \right) \partial \varepsilon \right] \quad (4.15)$$

$$\xi_3 = \varphi f \left[1 + \frac{\varphi}{2}, w + \frac{\varphi}{2}, \varepsilon + \frac{\varphi}{2}, F_c + \frac{\xi_2}{2_0} \right] \quad (4.16)$$

$$= \varphi f \left[1 + \frac{\varphi}{2}, w + \frac{\varphi}{2}, \varepsilon + \frac{\varphi}{2}, F_c + \frac{\varphi}{2} \left[F_c + \frac{\varphi E h^2}{12(1+\frac{\varphi}{2})} \left(\frac{-(w+\frac{\varphi}{2})}{1+\frac{\varphi}{2}} \right) \partial l + \right. \right. \\ \left. \left. \left(\varepsilon + \frac{\varphi}{2} \right) \partial w + \left(w + \frac{\varphi}{2} \right) \partial \varepsilon \right] \right] \quad (4.17)$$

$$= \varphi \left[F_c + \frac{\varphi}{2} \left[F_c + \frac{\varphi E h^2}{12(1+\frac{\varphi}{2}+\frac{\varphi}{2})} \left(\frac{-(w+\frac{\varphi}{2}+\frac{\varphi}{2})}{1+\frac{\varphi}{2}+\frac{\varphi}{2}} \right) \partial l + \left(\varepsilon + \frac{\varphi}{2} + \frac{\varphi}{2} \right) \partial w + \right. \right. \\ \left. \left. \left(w + \frac{\varphi}{2} + \frac{\varphi}{2} \right) \partial \varepsilon \right] \right] \quad (4.18)$$

$$\begin{aligned}
\xi_4 &= \varphi f[l + \varphi, w + \varphi, \varepsilon + \varphi, F_c + \xi_3] \\
&= \varphi f \left[l + \varphi, w + \varphi, \varepsilon + \varphi, F_c + \varphi \left[F_c + \frac{\varphi}{2} \left[F_c + \right. \right. \right. \\
&\quad \left. \left. \left. \frac{\varphi E h^2}{12 \left(1 + \frac{\varphi}{2} + \frac{\varphi}{2} \right)} \left(\frac{-(w + \frac{\varphi}{2} + \frac{\varphi}{2})}{1 + \frac{\varphi}{2} + \frac{\varphi}{2}} \right) \partial l + \left(\varepsilon + \frac{\varphi}{2} + \frac{\varphi}{2} \right) \partial w + \left(w + \frac{\varphi}{2} + \frac{\varphi}{2} \right) \partial \varepsilon \right] \right] \right]
\end{aligned} \tag{4.19}$$

$$F_c^l = F_c^{l-1} + \frac{1}{6} (\xi_1 + 2\xi_2 + 2\xi_3 + \xi_4) \tag{4.20}$$

$$\varepsilon = \frac{F_c}{w} \left(\frac{6}{E h^2} \right) \tag{4.21}$$

*NOTE: Using the method-of-lines approach, a system of ordinary differential equations is integrated, with the generally denoted functions

$$\frac{d}{dx} y(t) = f(t, y) \tag{4.22}$$

The analysis of the cutting force at the tool-tip was conducted from the derived Eq. 4.19. In the course of the analysis, a segmental interpretation of the gradual change in force based on the shape of the tool is evaluated. It is assumed that as the force dissipates through the cutting inserts, it loses its value based on the increased area and distance from the point of machining. This is taken into account from the modelling of the tool shape and value of Young's modulus of 1.426 Gpa obtained from the nano-indenter, as seen in Eq. 4.21. Figure 5.16 shows the segmented approach of force transfer and loss across the tool insert. Table 5.9 below shows the results of the model for the set of fifteen experimental parameters used. This table gives overview of the cutting combinations, their respective measured force, changes in length and breadth and the resulting strain.

Calibration steps were also conducted during no cutting action to ensure that no load is applied on the sensor. During these steps force sensor was tested with no present load and results were recorded. An additional calibration step with a change in

sensor position was also done along to base of the tool to access the accuracy of the sensor for measurement. The sensor was then Pre-set for measurement.

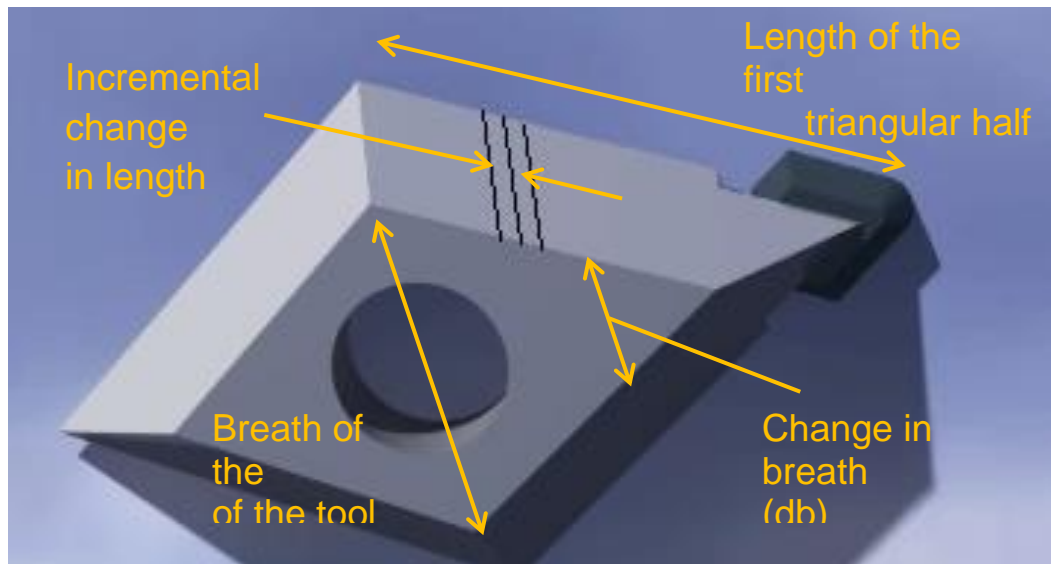


Figure 5.16 Evaluation of force dissipation across the cutting tool

Table 5.9 Analysis of Force at the tool-tip for the experimental runs

Exp	Speed (m/s)	Feed ($\mu\text{m}/\text{rev}$)	Depth (μm)	force (N)	Change in length dl (m)	Change in strain (d ϵ)	Strain (ϵ)
1	2.50	2.00	25.00	0.06	0.001	0.00000066	0.000180098
2	0.15	7.00	40.00	0.06	0.001	0.00000066	0.00018
3	1.33	7.00	25.00	0.054	0.001	0.00000059	0.000162088
4	1.33	2.00	40.00	0.074	0.001	0.00000081	0.000222121
5	2.50	7.00	40.00	0.098	0.001	0.00000107	0.00029416
6	2.50	12.00	25.00	0.074	0.001	0.00000081	0.000222
7	0.15	2.00	25.00	0.061	0.001	0.00000067	0.0001831
8	0.15	7.00	10.00	0.054	0.001	0.00000059	0.000162088
9	1.33	12.00	40.00	0.126	0.001	0.00000138	0.000378806
10	2.50	7.00	10.00	0.045	0.001	0.00000049	0.000135073
11	1.33	7.00	25.00	0.079	0.001	0.00000086	0.000237429
12	1.33	2.00	10.00	0.042	0.001	0.00000046	0.000126069
13	1.33	12.00	10.00	0.141	0.001	0.00000155	0.000424131
14	1.33	7.00	25.00	0.067	0.001	0.00000073	0.000201109
15	0.15	12.00	25.00	0.109	0.001	0.00000119	0.000327178

Table 5.10 Experimental run 15 ($0.15\text{m}^{-\text{sec}}$, $12\ \mu\text{m}^{-\text{rev}}$ and $25\ \mu\text{m}$) analysis of Force at the tool-tip

Exp	force (N)	breadth (m)	length (m)	Phi (m)	Change in length dl (m)	Change in breath db(m)	Change in strain (d ϵ)	Strain (ϵ)
0	0.109	0.00292	0.0105	0.001	0	0	0.00000000	0.00113728
1	0.109	0.00396	0.0095	0.001	0.001	0.00104	0.00037855	0.000758733
2	0.109	0.005	0.0085	0.001	0.001	0.00104	0.00022107	0.000537662
3	0.109	0.00604	0.0075	0.0006	0.001	0.00056	0.00014494	0.000392722
4	0.109	0.00666	0.0069	0.001	0.0006	0.00058	0.00006505	0.000327669
5	0.109	0.00569	0.0059	0.001	0.001	0.00103	-0.00000028	0.000327945
6	0.109	0.00473	0.0049	0.001	0.001	0.00016	0.00000031	0.000327639
7	0.109	0.00376	0.0039	0.001	0.001	0.00097	-0.00000041	0.000328048
8	0.109	0.0028	0.0029	0.001	0.001	0.00096	0.00000048	0.000327567
9	0.109	0.00183	0.0019	0.001	0.001	0.00097	-0.00000080	0.00032837
10	0.109	0.00087	0.0009	0.0009	0.001	0.00096	0.00000119	0.000327178
11	0	0	0	0	0.0009	0.00087		

Experiment 15 (Table 5.10) was selected from this table to further explain the progressive estimation of the strain on the cutting insert. This experimental run was chosen due to the fact that it generated the highest force magnitudes. From the experiment in Table 5.10, the measured force, breath and length at various segments, the step distance (Phi) of the tool and their corresponding incremental changes in strain is observed. Based on the rhombic tool shape, the tool area dimensions were dissection in ten constant incremental steps (Phi) of 0.001m and correlating length and breadth dimensions of the tool at those steps was recorded. Incremental estimation of strain based on Eq. 4.21 was performed at individual step distances. The final strain estimated at the tool tip was recorded at the final step distance.

5.2.1 Summary of results

From the results in Table 5.9 and Table 5.10, it can be seen that the final strain achieved for each experiment was very small. This is reflected by the negligible difference between the measured force from the sensor and that estimated at the tool tip.

Based on the findings, one can conclude that for this experimental set on the effects of sensor positioning along the tool poses an insignificant effect on the recorded force readings. The next section moves further on force analysis and performs an evaluation of the influence of cutting parameters on these measured force results.

5.3 Predictive modelling of cutting force and the influence of cutting parameters

The successful application of contact lenses is heavily dependent on their form accuracy and surface integrity. The cutting force plays a key role in the diamond turning of contact lenses as it has a negative influence on the form accuracy and surface integrity. It is recorded from literature that there exist a high influence of cutting parameters such as feed rate and depth of cut on cutting force and invariably this affects achievable surface quality [156, 157]. In addition, cutting force is also important for other aspects of diamond turning of contact lenses such as tool wear. One way to manage the effect of the cutting force and reduce its negative effect on surface finish could be realised through optimisation and modelling. Therefore, the prediction of cutting forces in contact lens manufacturing is deemed essential for the sake of high quality optical surfaces. There are several factors that affect the extent of the cutting force developed in diamond turning. An example of these factors is the selection of cutting parameters and thus, the establishment of a statistical model for the reliable prediction of cutting forces which is linked to specific optical quality is of high importance in lens cutting.

In this study, a cutting force model based on the response surface statistical method is developed for the reliable prediction of cutting forces in the high-precision machining of contact lenses. The model obtained from fifteen experimental tests

determines the effects of cutting speed, feed rate and depth of cut on force and how various combinations of parameters relate to surface quality.

Via a set of polynomial mathematical equations, RSM analysis is utilised to define the relationship between the input variables (speed, feed and depth of cut) and the output variable (cutting force). The obtained results are validated to ascertain if they comply with some statistical conditions. These conditions are:

1. To predict the suitability of the validation run outcome based on input parameters within a 95% of its predictive confidence
2. To determine residual error between experimental value and predicted value within a range of accuracy of 5%.

Table 5.11 shows the results of the experimental cutting force

Table 5.11 Experimental run and results of cutting Force

Run	Factor 1	Factor 2	Factor 3	Response 1
	A: Speed (m/s)	B: Feed ($\mu\text{m}/\text{rev}$)	C: Depth of cut (μm)	Cutting force (N)
1	2.50	2.00	25.00	0.06
2	0.15	7.00	40.00	0.06
3	1.33	7.00	25.00	0.054
4	1.33	2.00	40.00	0.074
5	2.50	7.00	40.00	0.098
6	2.50	12.00	25.00	0.074
7	0.15	2.00	25.00	0.061
8	0.15	7.00	10.00	0.054
9	1.33	12.00	40.00	0.126
10	2.50	7.00	10.00	0.045
11	1.33	7.00	25.00	0.079
12	1.33	2.00	10.00	0.042
13	1.33	12.00	10.00	0.141
14	1.33	7.00	25.00	0.067
15	0.15	12.00	25.00	0.109

Determination of an appropriate polynomial equation to represent RSM model

An RSM data analysis was carried out using statistical software. The determination of a suitable polynomial equation to represent the relationships between input parameters and the cutting force (output response) was done by carrying out the sum of squares sequential model and lack of fit test shown in Table 5.12 and Table 5.13. The results from the sequential model indicate a “linear vs mean” approach; however the lack of fit tests suggests a linear equation approach.

Table 5.12 Lack of fit test for cutting Forces

Source	DF	Seq SS	Adj MS	F	P	Remark
Linear	9	5.505E-003	6.117E-004	3.91	0.2201	<u>Suggested</u>
2FI	6	4.112E-003	6.853E-004	4.38	0.1974	
Quadratic	3	1.739E-003	5.796E-004	3.71	0.2197	
Cubic	0	0.000				Aliased
Pure Error	2	3.127E-004	1.563E-004			

Table 5.13 Sequential model sum of squares (SMSS) analysis for cutting Forces

Source	DF	Seq SS	Adj MS	F	P	Remark
Mean vs Total	1	0.087	0.087			
Linear vs Mean	3	6.399E-003	2.133E-003	4.03	0.0368	<u>Suggested</u>
2FI vs Linear	3	1.393E-003	4.645E-004	0.84	0.5092	
Quadratic vs 2FI	3	2.373E-003	7.909E-004	1.93	0.2433	
Cubic vs Quadratic	3	1.739E-003	5.796E-004	3.71	0.2197	Aliased
Residual	2	3.127E-004	1.563E-004			
Total	15	0.099	6.631E-003			

The lack of fit tests suggested the model equation with the least significant lack of fit and the sequential test considered a model equation where additional terms remain significant to the model. Therefore, based on these suggestions the linear source approach was utilised for modelling the cutting force.

ANOVA analysis of the Response surface Quadratic Model for cutting force

The ANOVA has been performed to check whether the model is adequate, as well as to check the significance of the individual model coefficients. Table 5.14 shows

the ANOVA for cutting forces. The Model F-value of 11.26 implies the model is significant. The percentage chance of the occurrence of this “F-value” to originate from noise within the analysis is only a 0.52%.

Table 5.14 ANOVA for model coefficient for Cutting Forces in UHPM of contact lens polymer

Source	DF	Seq SS	Adj MS	F	P	Remark
Model	1	5.671E-003	5.671E-003	11.26	0.0052	
B-Feed	<u>1</u>	5.671E-003	5.671E-003	11.26	0.0052	significant
Residual	13	6.546E-003	5.035E-004			
Lack of fit	11	6.233E-003	5.666E-004	3.62	0.2360	Not-significant
Pure Error	2	3.127E-004	1.563E-004			
Cor Total	14					

The "Lack of Fit F-value" of 3.62 implies the Lack of Fit is not significant relative to the pure error. In the same manner, there is only a 23.60% chance that a "Lack of Fit value" could result from noise interference during analysis. Non-significant lack of fit is a desired trait for a fitting model.

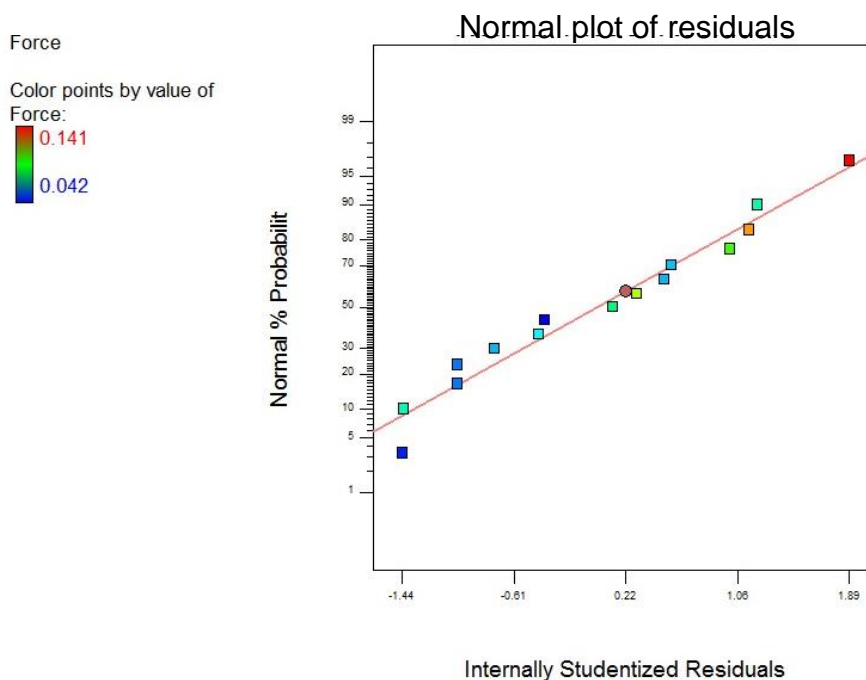


Figure 5.17 Normal probability plot of residuals in cutting force modelling

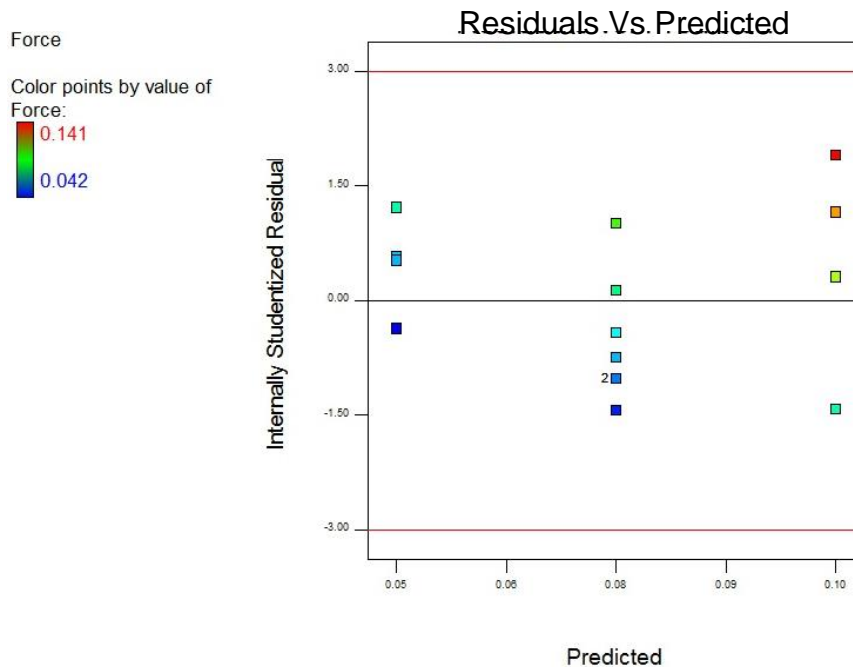


Figure 5.18 Probability plot of residuals vs predicted in cutting force modelling

The normal probability plot of the residuals and the plot of residuals versus the predicted response shown in Figure 5.17 and Figure 5.18 show a close correlation of the data points to the straight probability line and no obvious and unusual structure found. This indicates that the model possesses adequate normality of residuals and no constant error.

Determination of significant factors influencing cutting force

In determining the cutting parameters influential to the cutting force the results from the ANOVA Table 5.14 were studied. Based on a probability value greater than F-value and less than 0.005, significant terms to the model were identified. In this case the feed was identified as the only significant model term linked to the cutting force. The behaviour of the cutting force in response to variations of the feed rate was also compared to research work compiled by other researchers to support the validation of the model. The feed rate line in Figure 5.19 indicates that as the feed increases from 2 to 12 $\mu\text{m}/\text{rev}$, the cutting force increases from 0.45 to 0.102N. A direct correlation is shown to exist with increase in feed.

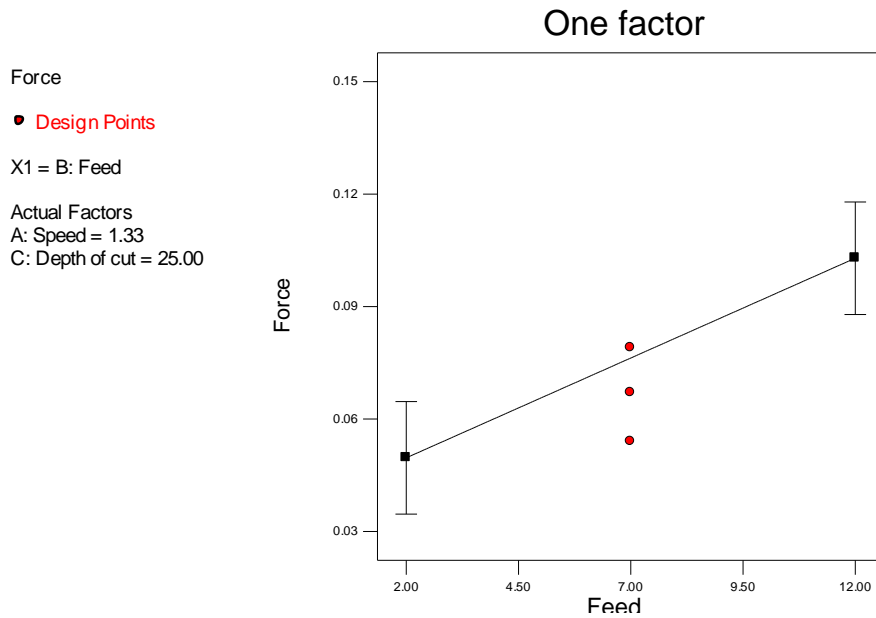


Figure 5.19 Normal Probability plot of feed on cutting force

From the surface response modelling the linear polynomial model equation developed to relate the input parameters to the cutting force is shown in Eq. 4.23.

$$\text{Cutting Force (N)} = 0.039 + 5.32500E - 003 * \text{Feed} \quad (4.23)$$

From the graphical perspective of the model equation using a 3D surface plot, in Figure 5.20, the effects of varying the depth of cut and feed while keeping the speed constant is shown. Figure 5.14 shows that as the feed increases a corresponding increase in cutting force is observed. However, the depth of cut shows no effects on force values.

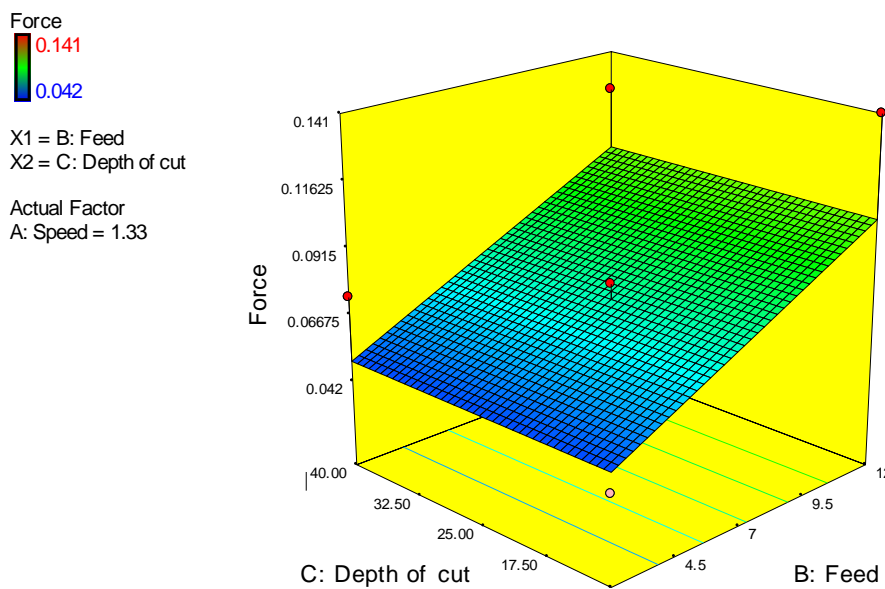


Figure 5.20 3D Plot of the influence of feed and depth of cut on cutting force

Model validation

The validation of the model is used to ascertain if the developed model can sufficiently predict the output cutting force generated during cutting. Using the point tool from the statistical software, three sets of parameters were chosen for validation. As seen in Table 5.15 below, the actual and predicted values are compared using the residual error. A margin of 20% is used to determine the adequacy of the model at a confidence prediction level of 80%. From the table, it can be seen that the results fall within the 20% margin to determine model adequacy but below the 10% confidence prediction level.

Table 5.15 Experimental run and results of cutting Force

Run	Factor 1	Factor 2	Factor 3	Response 1	Response 2
	A: Speed	B: Feed	C: Depth of cut	Predicted force	Actual force
1	2.50	12.00	25.00	0.0953	0.078
2	2.09	10.57	22.81	0.0953	0.061
3	1.33	7.00	30	0.0762	0.062

5.3.1 Summary of results

In this section, it can be identified that the feed rate is the main influence in cutting force generation in diamond machining of polymers. The RSM model implemented also postulates that negligible or no influence is perceived from depth of cut and speed during UHPM of polymer. However, the validation of the model falls below a 10% confidence prediction level needed in general statistics despite a prior modelling of the exact force at the tool tip. This value indicates an underlining challenge in the model. This could be attributed to challenges in micro-force acquisition based on the scale of machining. It is recommended that more tests be conducted with a combination of multiple sensors to predict force effects on cutting parameters.

In conclusion, it can be seen that higher feed rates and high cutting speeds adversely affect the quality of machined lenses in the high precision machining of contact lenses.

5.4 Statistical evaluation of triboelectricity

Using the RSM Box-Behnken statistical second order model a set of 15 experimental parameters was generated. This was created to model the effects of three machining on the triboelectric phenomenon as listed in Table 5.16. Humidity measurements of experimental tests were taken using a humidity meter.

Table 5.16 Experimental run and results of Surface Roughness

Run	Factor 1	Factor 2	Factor 3	Response 1	Response 2	Response 3
	A: Speed	A: Feed	A: Depth of cut	Statics at 60%	Statics at -40%	Statics at 20%
1	2.50	2.00	25.00	1.958	-0.6291	0.000354
2	0.15	7.00	40.00	0.57	-2.317	0.2254
3	1.33	7.00	25.00	0.629	-2.152	-0.01902
4	1.33	2.00	40.00	1.114	-0.2365	-7.979
5	2.50	7.00	40.00	0.506	-3.12	-0.5758
6	2.50	12.00	25.00	0.475	-2.244	-8.462
7	0.15	2.00	25.00	0.544	-0.5299	-0.1097
8	0.15	7.00	10.00	0.626	-0.613	0.00011
9	1.33	12.00	40.00	0.484	-1.609	0.000171
10	2.50	7.00	10.00	0.696	-0.6361	4.88E-05
11	1.33	7.00	25.00	0.795	-1.999	4.88E-05
12	1.33	2.00	10.00	1.725	-0.1207	-22.23
13	1.33	12.00	10.00	0.605	-0.4678	-0.6981
14	1.33	7.00	25.00	1	-1.764	-0.5382
15	0.15	12.00	25.00	0.847	-3.449	-1.232

5.4.1 Analysis for triboelectric phenomenon at 60% relative humidity

The influence of the cutting parameters (speed, feed and depth of cut) on the response variables selected has been assessed at 60% relative humidity. Fluctuations found in acquired signals represent charges formed both at the surface of the lens button (positive charges) based on the placement of the polymer on the triboelectric series.

Experimental tests firstly identified the effects of mist coolant. During these tests, high humidity prevented any form of static generation to be formed and served as

calibration guideline for the sensor. All subsequent tests were performed in dry operation. During the dry machining tests at this humidity value, a tool chip build-up at the tool edge was observed. This occurred at experimental tests of low speed and mostly high depth of cut. This was on account of continuous chip formation which tangled around the workpiece and tool (Figure 5.21). Further examination of the statics reading exposed that only a minimal amount of electrostatic charge was formed at such humidity level. This was thus explained to be due to adhesive reaction that occurred due to change in polarity between chips and workpiece [56].



Figure 5.21 Chip build up on the diamond tool [55]

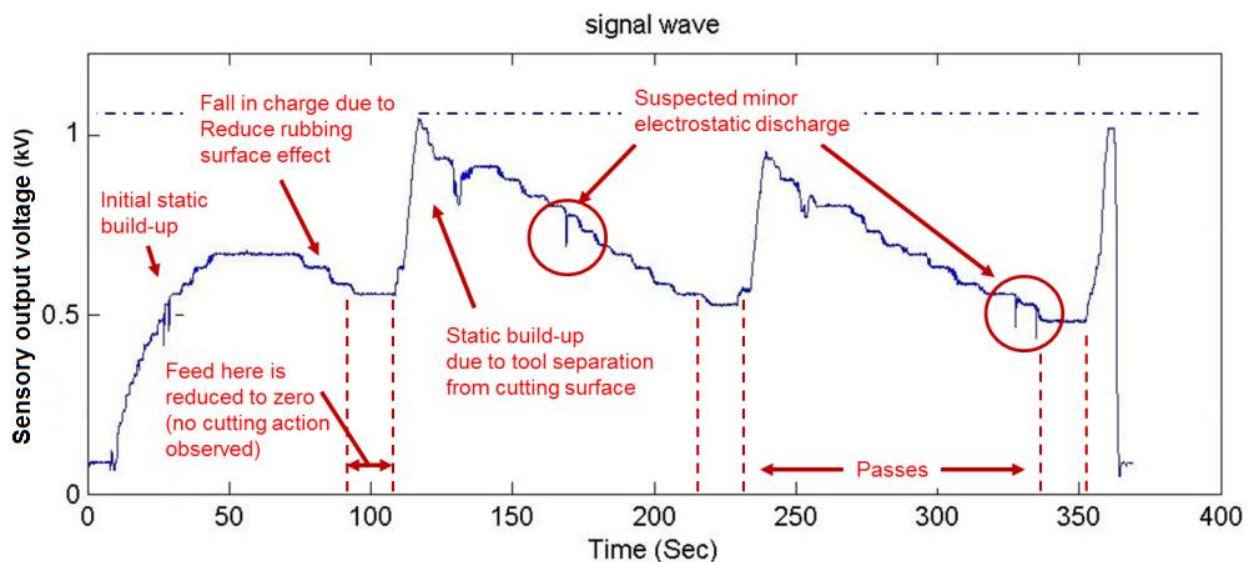


Figure 5.22 Basic cycle chart of the static charging during diamond machining of polymers [55]

Figure 5.22 shows the progression of an acquired static charge. It can be seen that these results agree with those found by Gubbels [66]. During initial tool and workpiece contact, an initial static build-up is observed. This initial rise increases to an optimal level but is preceded by a gradual fall in charge. This as stated by Gubbels et al. [66] could be explained from the reduced rubbing effect due to a reduction on surface contact of the tool. At minimal surface contact (when the tool is at the centre of the circular piece), a dead zone in static charging and discharging is observed. During this state, no depth of material is cut to release additional ions to the material surface, but ions already present at the surface maintain the currently acquired static charge.

As the tool gradually separates from the workpiece, an ion exchange from one material surface to the next is experienced, yielding a sudden surge in static charge and then based on the ionization reaction with moisture in the air, static charge is lost. According to Gubbels [9], an electrostatic charge of 7.4eV is needed for discharge to occur. However, during this charging cycle, suspected minor electrostatic discharges were observed. These suspected sharp negative static peaks suggest the presence of minor discharges. This phenomenon could be explained due to the dry flow of coolant during machining which could spurge minor discharge. However this is not sufficiently high to cause any damage to the tool.

Figure 5.23 shows the events experienced during the 13th experimental run with cutting parameters of speed at 2109 rpm, feed at 12 μ m and 10 μ m depth of cut. During this test acquisition, various cutting passes were recorded. The figure shows a negative trend line as opposed to subsequent machining tests. This is postulated to be as a result of the combination of high feed and low depth of cut and short tool separation times between passes. This condition was characterised by a faster rubbing action and reduced discharge action. The residual magnitude of the charge at the end of the cutting shows the magnitude of the actual number of ions formed after final tool separation when the electrons have been transferred to another statically charged surface. Based on the limited amount of conduction in the machined compartment, the magnitude is seen to remain charged until it is manually discharged.

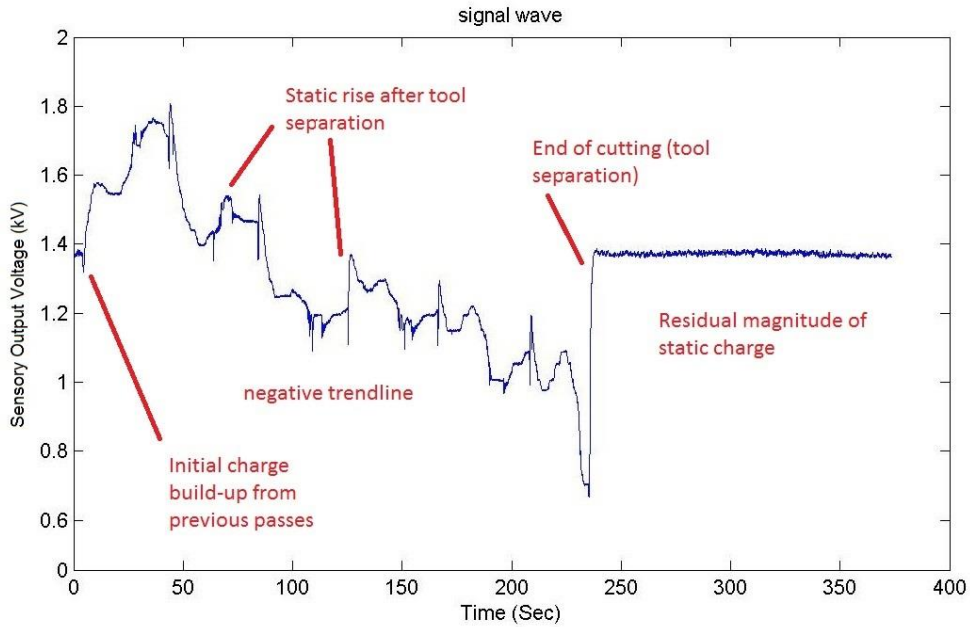


Figure 5.23 Static charging effects in experiment 13 (60% - humidity)

Furthermore, indications of small statistical magnitudes ranging from 0.5kV to 2kV were generated at 60% humidity as shown in Figure 5.24. This concurs within the 60 to 70% humidity transition zone of weak static formation [56]. From this study, it is believed that at humidity of 60% upwards, the hydrophilic surface of the polymer absorbs initial humidity from the atmosphere which in turn prevents rapid rise of static formation. After, excessive machining passes, progressive static values were obtained in experimental runs because new surfaces with less humidity had a lower static dissipation constant. The section below analyses the effects of each cutting parameter using the RSM modelling methodology.

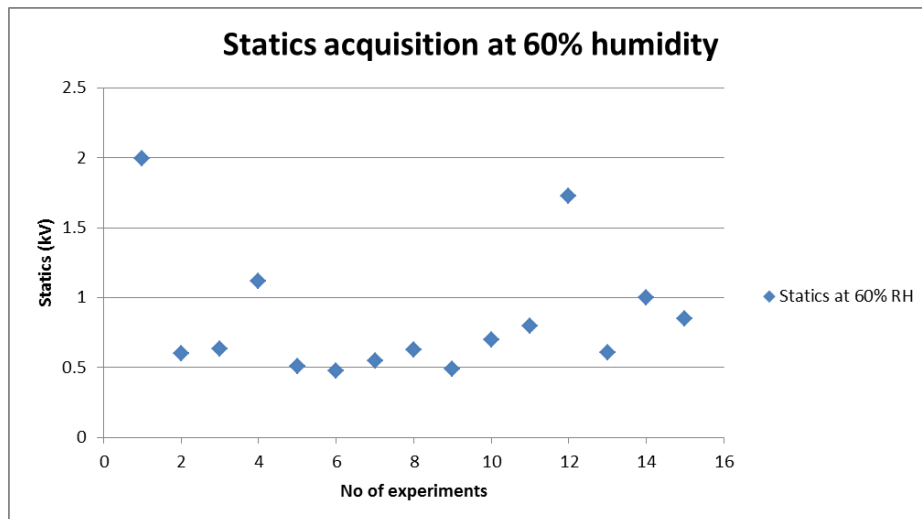


Figure 5.24 Static magnitudes at 60% humidity experiments

Determination of appropriate polynomial equation to represent RSM model

By carrying out the sum of squares sequential model and lack of fit test shown in Table 5.17 and Table 5.18, the determination of a suitable polynomial equation representing the relationships between input parameters and the electrostatics at 60% humidity (output response) was done. This RSM data analysis was carried out using statistics.

Table 5.17 Sequential model sum of squares (SMSS) analysis for electrostatics at 60% humidity

Source	DF	Seq SS	Adj MS	F	P	Remark
Mean vs Total	<u>1</u>	<u>10.76</u>	<u>10.76</u>			<u>Suggested</u>
Linear vs Mean	3	1.35	0.45	3.20	0.0661	
2FI vs Linear	<u>3</u>	<u>0.90</u>	<u>0.30</u>	<u>3.66</u>	<u>0.0630</u>	<u>Suggested</u>
Quadratic vs 2FI	3	0.36	0.12	2.09	0.2203	
Cubic vs Quadratic	3	0.22	0.074	2.13	0.3351	Aliased
Residual	2	0.069	0.035			
Total	15	13.66	0.91			

Table 5.18 Lack of fit test for electrostatics at 60% humidity

Source	DF	Seq SS	Adj MS	F	P	Remark
Linear	9	1.48	0.16	4.77	0.1853	
2FI	<u>6</u>	<u>0.58</u>	<u>0.097</u>	<u>2.82</u>	<u>0.2847</u>	<u>Suggested</u>
Quadratic	3	0.22	0.074	2.13	0.3351	
Cubic	0	0.000				Aliased
Pure Error	2	0.069	0.035			

The sequential test considered a model equation where additional terms remain significant to the model thereby identifying “2FI vs Linear” with the highest “F-value”. Also, the lack of fit tests suggested that the “2FI model” equation to which vis-à-vis its relatively low “p-value” points is the least significant lack of fit of the two. Therefore, based on these suggestions the 2FI equation approach was utilised for modelling the statics at 60% humidity.

The ANOVA performed were utilised to check the adequacy of the model, as well as the significance of its individual coefficients. Table 5.19 shows the ANOVA for the electrostatics at 60% humidity. The “F-value” of 9.12 suggests that the model is significant to the results. A probability of 0.25% of noise occurrence is obtained for this model.

Table 5.19 ANOVA for model coefficient for the electrostatics at 60% humidity in UHPM of contact lens polymer

Source	DF	Seq SS	Adj MS	F	P	Remark
Model	3	2.07	0.69	9.12	0.0025	significant
A-Speed	<u>1</u>	0.14	0.14	1.84	0.2017	
B-Feed	<u>1</u>	0.10	1.10	14.55	0.0029	
AB	<u>1</u>	0.83	0.83	10.97	0.0069	
Residual	11	0.83	0.076			
Lack of fit	9	0.76	0.085	2.46	0.3225	not significant
Pure Error	2	0.069	0.035			
Cor Total	14	2.91				

The "Lack of Fit F-value" of 2.46 also indicates that this Lack of Fit is not significant due to the pure error. There is only a 32.25% chance that such a fit could result from noise. A non-significant lack of fit such as this is good property for modelling. It is a desirable quality for the model to fit.

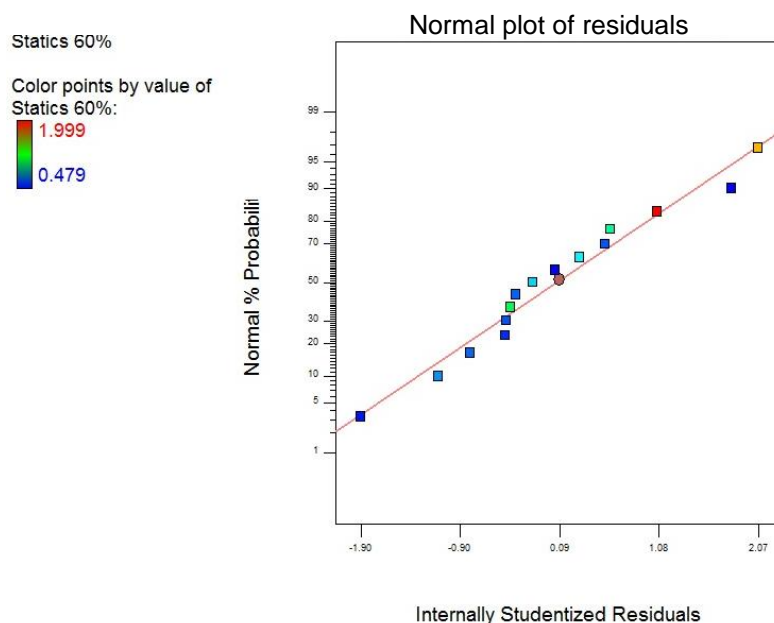


Figure 5.25 Normal probability plot of residuals of statics at 60% humidity

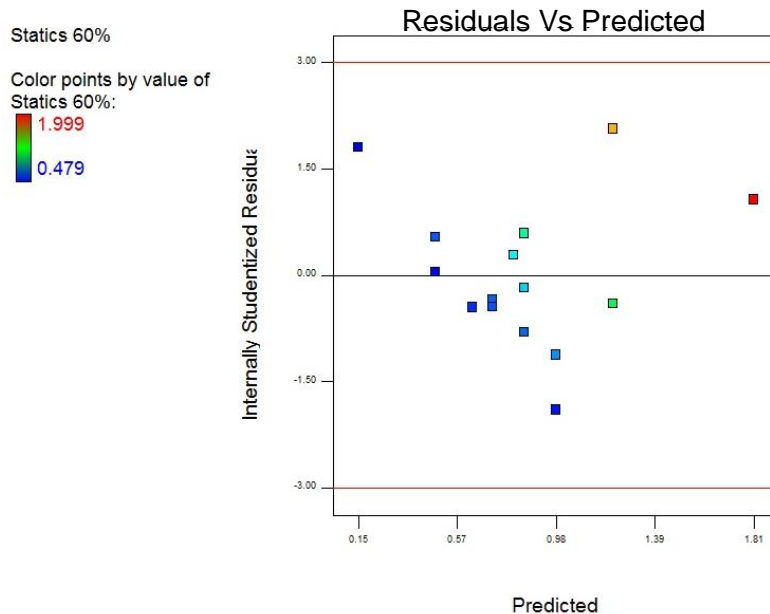


Figure 5.26 Probability plot of residuals vs predicted response for the statics at 60% humidity

The normal probability plot of the residuals and the plot of residuals versus the predicted response are shown in Figure 5.25 and Figure 5.26 above. These plots show that a close correlation of the data points to the straight probability line and no obvious or unusual structure was found. They indicate that the model possesses adequate normality of residuals and no inherent constant error within its model.

Determination of significant factors influencing the electrostatics at 60% humidity

In determining the cutting parameters influential to the electrostatics at 60% humidity, the results from the ANOVA Table 5.19 were studied. Based on a probability value greater than F-value and less than 0.005, significant terms to the model were identified. In this case the speed, feed rate, and the interaction effect between the two were identified as the significant model parameters linked to electrostatics at 60% humidity. The figures below show the one-point parameter effect on the electrostatic values and discuss them.

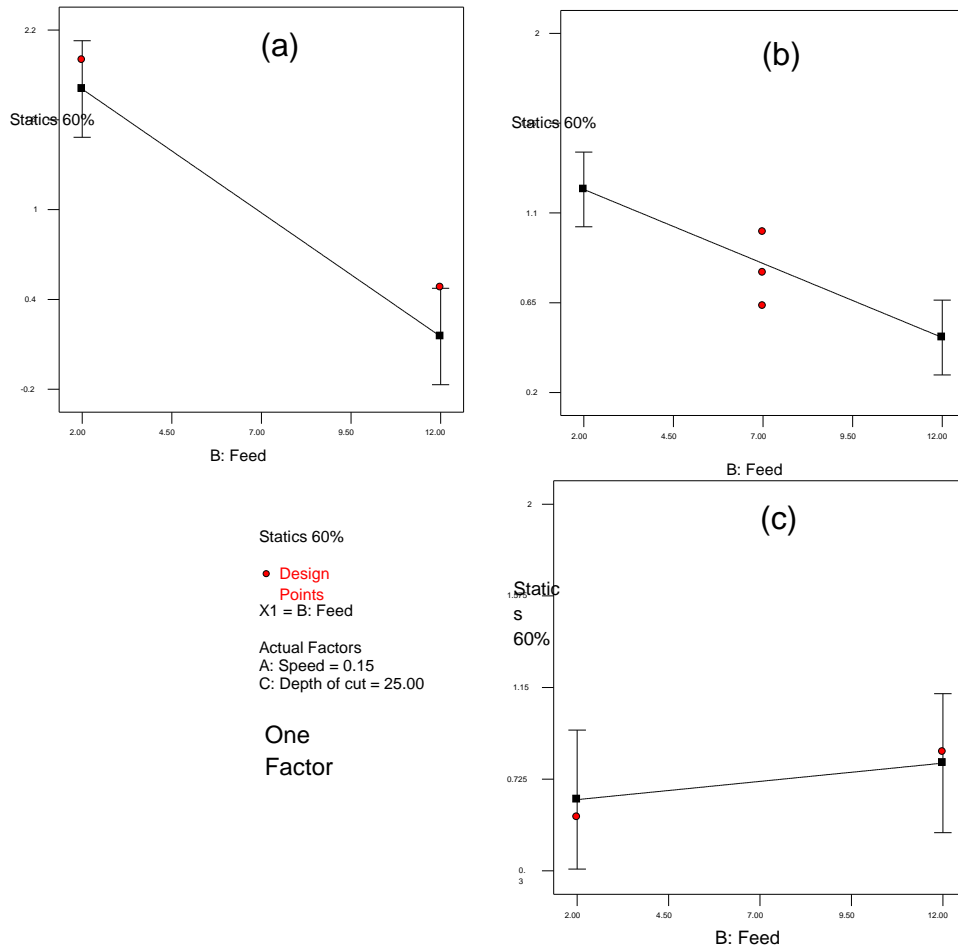


Figure 5.27 Behaviour of 60% RH in response to variation in feed at (a) 239 rpm (b) 2109 rpm (c) 3979 rpm

- From Figure 5.27, the plot of electrostatic magnitudes versus feed rates changes over the three different speeds. This figure indicates that as the feed increases a corresponding increase in statics generated is obtained. This condition is experienced at 239 rpm (Figure 5.27(a)) and at 2109 rpm (Figure 5.27(b)). A downward line is observed with statics output in these graphs but an upward line is obtained at speed values of 3979 rpm (Figure 5.27(c)). Electrostatic discharge values are seen to range from 2.0 kV to 0.3 kV in Figure 5.27(a), and from 1.2kV to 0.5Kv in Figure 5.27(b) respectively. But a smaller range is observed in Figure 5.27(c) which is from 0.5kV to 0.8kV. This trend decrease and subsequent increase reflects a curved reaction in the effect of feed on static charge.
- The electrostatic value for the cutting speed of 3979 rpm in the figure below changes over distinct feed rates. Figure 5.28(a),(b) and (c) in the same

manner as the speed increases, initial increase over lower speeds generates a rising slope in statics but at higher speed value falls with a downward slope to statics generated. Electrostatics values here are seen to range from 0.5 kV to 1.3 kV in Figure 5.28(a), from 0.6Kv to 0.9kV in Figure 5.27(b) and a range of 0.8kV to 0.3kV is observed in Figure 5.28(c). At high speeds, this may reflect a change in the amount of tool chip found at the surface of the lens.

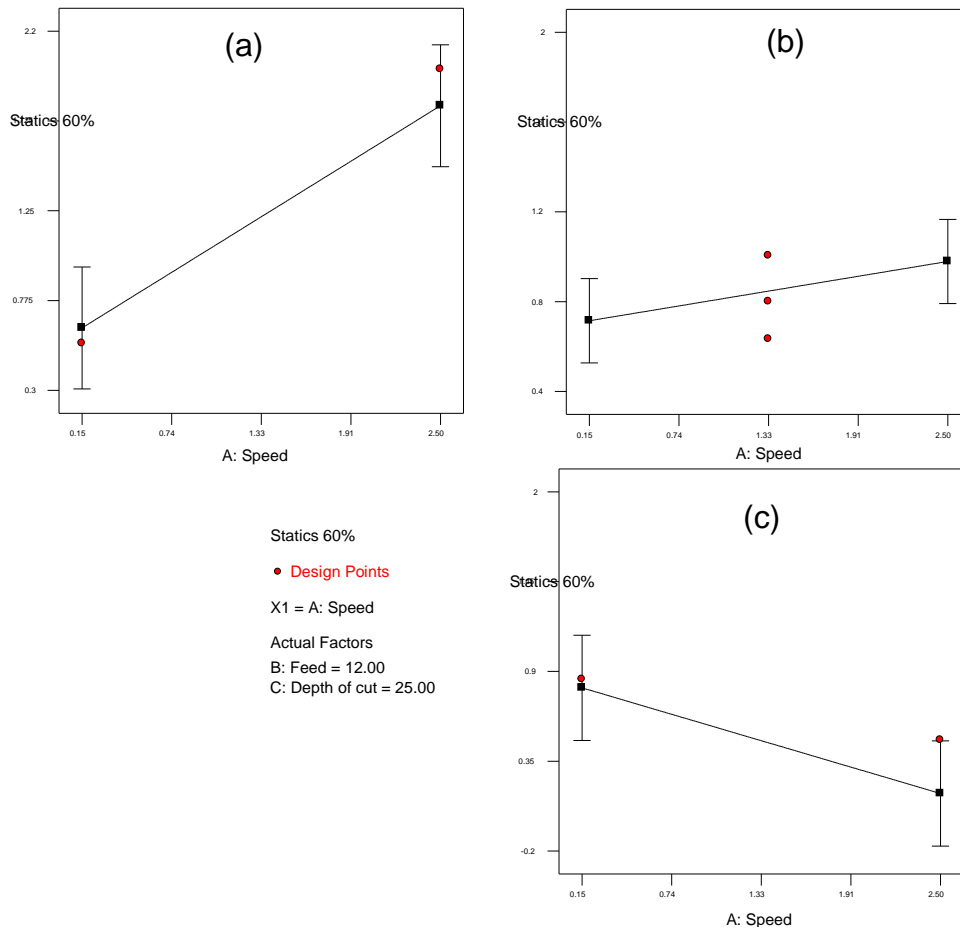


Figure 5.28 Behaviour of 60% humidity in response to variation in speed at (a) $2\mu\text{m/rev}$ (b) $7\mu\text{m/rev}$ (c) $12\mu\text{m/rev}$

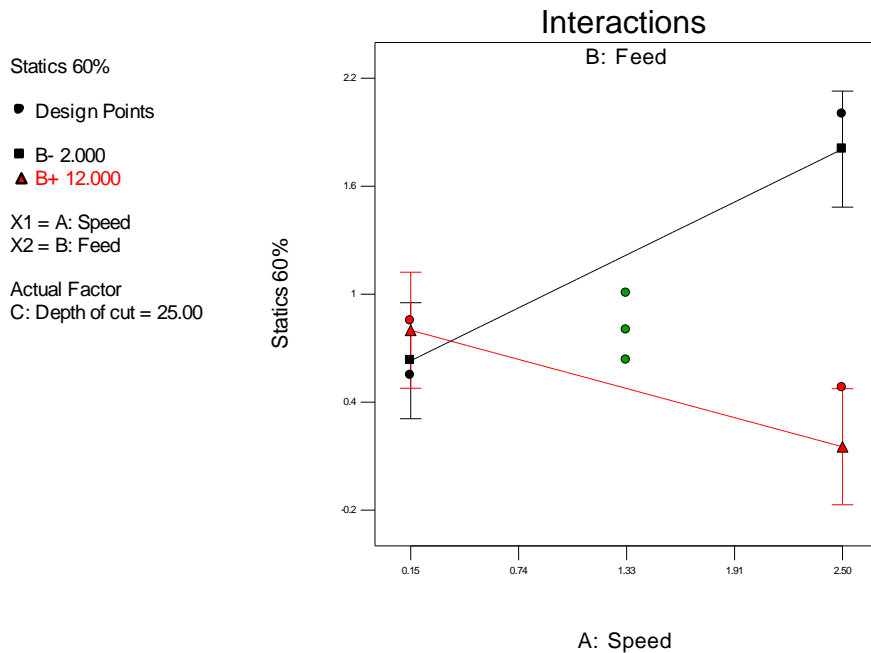


Figure 5.29 Behaviour of 60% humidity relative to interaction between feed and speed

- The ANOVA analysis also revealed that one of the significant factors influencing the generation of electrostatic charge at 60% relative humidity is the interaction between the feed and speed. As shown in Figure 5.29, at low feed rates, the increase in cutting speeds generates an increased amount of electrostatic charges. However, at higher levels of feed an opposite case was observed with a decrease in static generation as the speed value increased. This condition is explained by the reduced rubbing time from high speed and feed conditions leading to a downward interaction slope. However at low feeds, more rubbing time is available for static build and increase speeds enhances friction and thus static generation. Figure 5.30 shows a contour plot of that interaction between speed and feed. From the plot, the interaction earlier stated can be observed as well. High feeds generated statics found within the low static region on the top part of the plot. Lower feeds however, at the extreme levels of speeds generated much higher statics magnitudes.

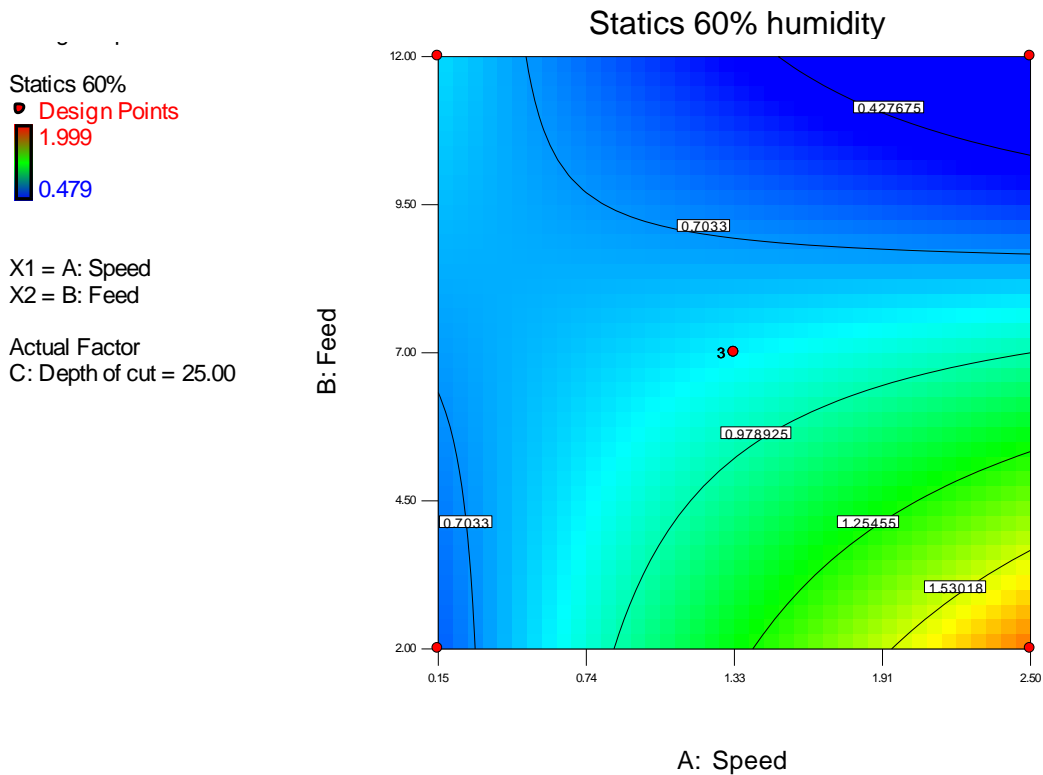


Figure 5.30 Normal Probability plot of 60% relative humidity

Polynomial equation of the electrostatic model at 60% relative humidity

From the surface response modelling the quadratic polynomial model equation developed to relate the input parameters to the electrostatic charges generated at the 60% level humidity is shown in Eq. 4.24 below.

$$\text{Electrostatics at 60\% humidity} = 0.49788 + 0.65547 S + 0.028561 F - 0.077574 S * F \quad (4.24)$$

Where: $F = \text{Feed}$, $S = \text{Speed}$

From the graphical perspective of the model equation using a 3D surface plot, in Figure 5.31, the effects of varying the speed, feed and depth of cut are shown. The last figure (Figure 5.31) shows the curved relationship of the feed rate and speeds over the generated statics.

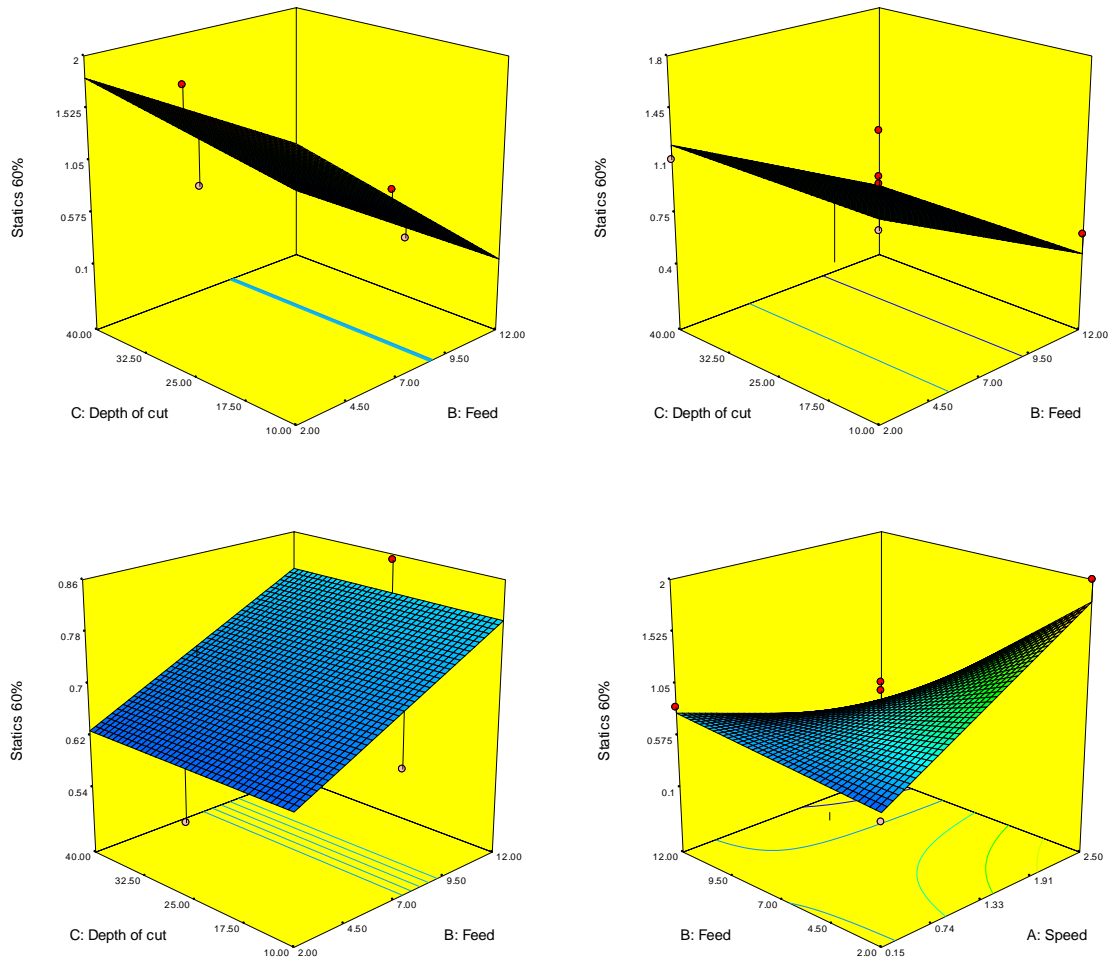


Figure 5.31 3D Plot of the influence of feed and depth of cut on cutting force

5.4.2 Analysis for triboelectric phenomenon at 40% relative humidity

At 40% relative humidity, both positive and negative polarity electrostatic readings are observed. This dual polarity represents charges formed both at the surface of the lens button (Positive charges) and those formed on the chips (negative charged) as explained from the triboelectric series (Figure 2.18).

During experimental tests at a lower relative humidity of 40%, a marginally higher indication of triboelectricity occurring during machining is experienced. However, these tests generated static value with interchanging polarities. Generally similar levels of positive static charges were obtained but with higher negative statics values (Figure 5.32) as low as -3kV. These were detected during chip build-up at the cutting tool that tool chips carried on them emitted electrons from the workpiece surface and were thus obtained inherent negative charges. Their presence during acquisition influenced the strength of negative statics accumulation around the tool tip.

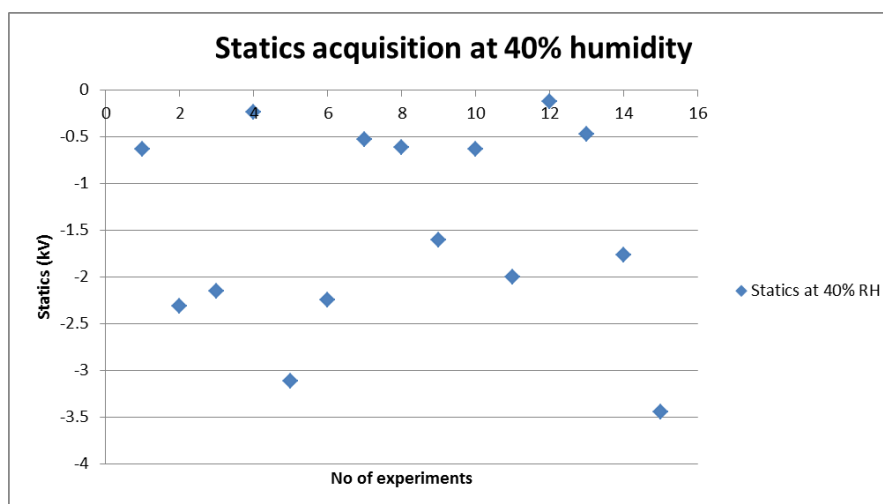


Figure 5.32 Static magnitudes in high humidity experiments (40% humidity)

Some notable experiments are discussed below. These experiments are: experiment 4 ($s = 2109$ rpm, $f = 2\mu\text{m}/\text{rev}$, $d = 40\mu\text{m}$), 12 ($s = 2109$ rpm, $f = 7\mu\text{m}/\text{rev}$, $d = 25\mu\text{m}$) and 15 ($s = 239$ rpm, $f = 12\mu\text{m}/\text{rev}$, $d = 25\mu\text{m}$).

From results in experiment 4 as seen in Figure 5.33, with cutting parameters of speed at 2109 rpm, feed at $2\mu\text{m}$ and $40\mu\text{m}$ depth of cut, major tool chip build is formed at the tool tip. This chip build-up causes a negative rise in statics up to levels

as low as -0.2kV . However, based on the uneven chip formation, frequent fluctuations in statics can be observed. These conditions are summed with frequent loading and offloading of heavy chip bundles on the tool tip leading to a reversal of statics values in the positive ranges. Figure 5.34 shows the chip build-up and electrostatic charging effects during machining at 40% humidity.

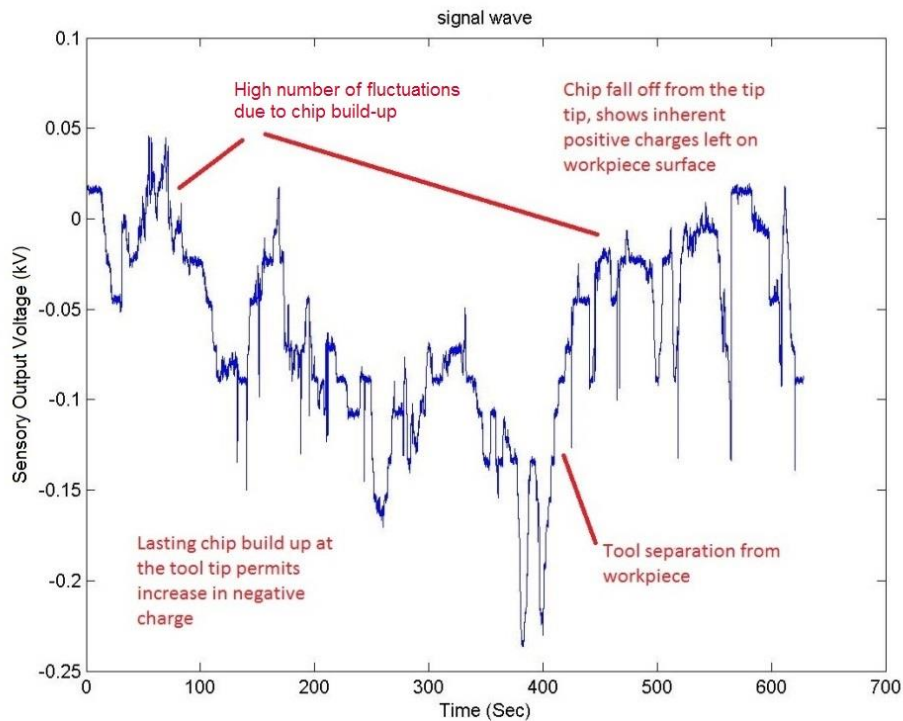


Figure 5.33 Static charging fluctuations in experiment 4 at $s = 2109$ rpm, $f = 2\mu\text{m}/\text{rev}$, $d = 40\mu\text{m}$ and 40% humidity)

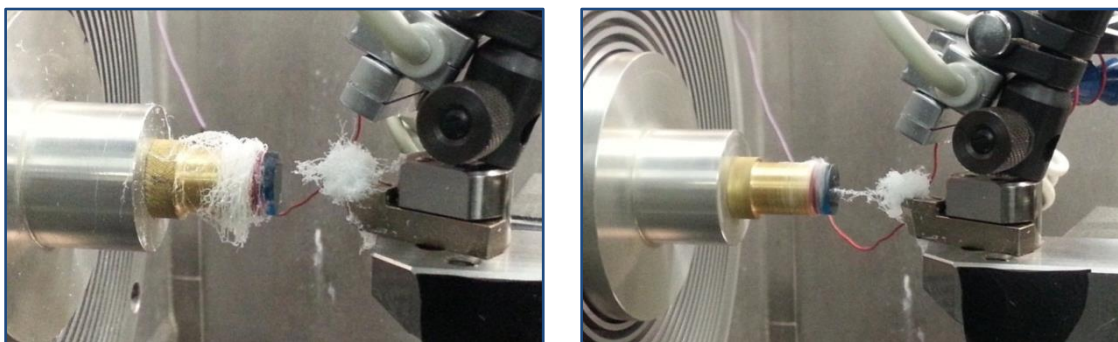


Figure 5.34 Chip builds up and static charging effects (40% humidity)

In experiment 12 (Figure 5.35), with cutting parameters of speed at 2109 rpm, feed at $7\mu\text{m}/\text{rev}$ and $25\mu\text{m}$ depth of cut, shows a clearer trend as depicted. In this experiment, clear fluctuations from positive to negative static generation are

observed. These are postulated to be as a combined cause of tool separation at the end of each pass and cumulatively chip off. Minor oscillations are seen within the gradual descent as compared to the previously analysed experiment; this is as a result of a higher feed rate in this experiment, creating a shorter time for rubbing action of the tool and chips against the mechanical surface.

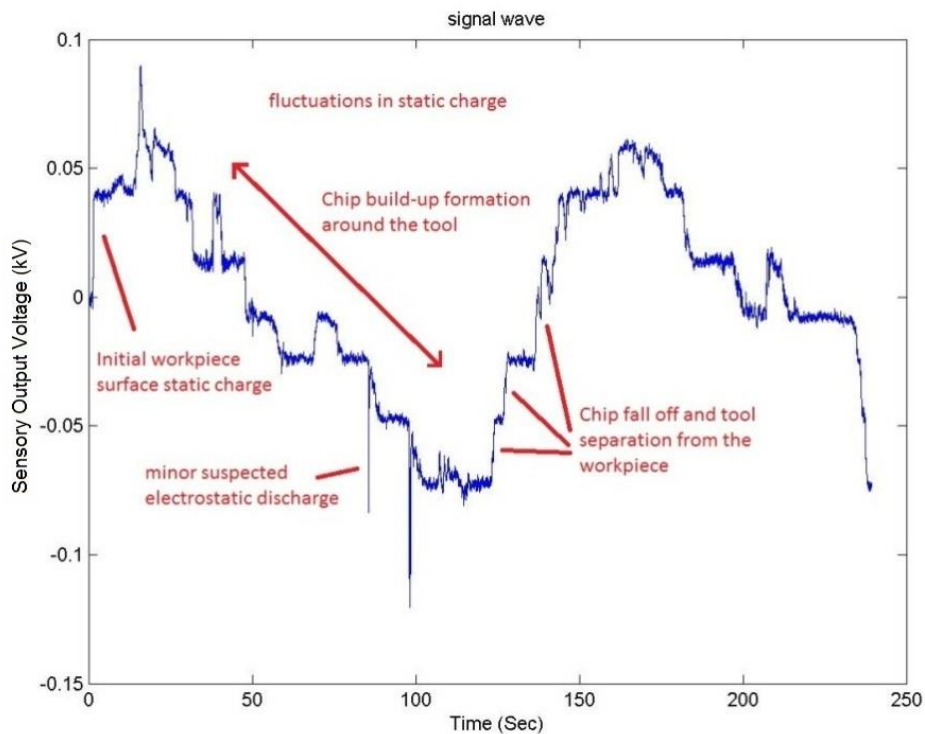


Figure 5.35 Static charging effects in experiment 12 at $s = 2109$ rpm, $f = 7\mu\text{m}/\text{rev}$, $d = 25\mu\text{m}$ and 40% humidity

In experiment 15 (Figure 5.36), at 239 rpm, $12\mu\text{m}/\text{rev}$ and $25\mu\text{m}$, a clearer trend of static signals is shown. At low speeds and high feeds a large amount of chipping is formed at the tool tip. This led to negative static values of -3kV . Little or no time was left between the passes for tool separation static build; this led to a rapid rise in negative magnitude.

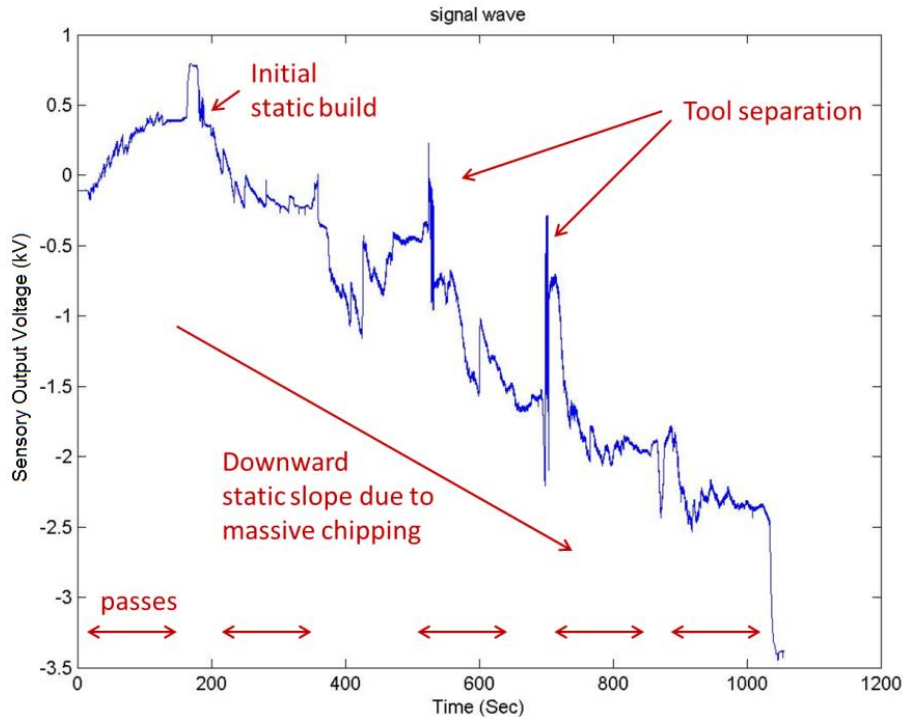


Figure 5.36 Static charging effects in experiment 15 at $s = 239$ rpm, $f = 12\mu\text{m}/\text{rev}$, $d = 25\mu\text{m}$ and 40% humidity

Determination of an appropriate polynomial equation to represent RSM model positive static readings

An RSM data analysis was carried out to determine a polynomial equation which represents the relationships between input parameters and the output response (at 40% humidity). This was done by carrying out a sum of squares sequential model and lack of fit test shown in Table 5.20 and Table 5.21.

Table 5.20 Sequential model sum of squares (SMSS) analysis for electrostatics at 40% RH

Source	DF	Seq SS	Adj MS	F	P	Remark
Mean vs Total	1	<u>19.78</u>	<u>19.78</u>			<u>Suggested</u>
Linear vs Mean	3	7.58	2.53	1.16	0.3692	
2FI vs Linear	3	9.16	3.05	1.65	0.2542	
Quadratic vs 2FI	3	<u>7.00</u>	<u>2.33</u>	<u>1.49</u>	<u>0.3244</u>	<u>Suggested</u>
Cubic vs Quadratic	3	7.60	2.53	22.80	0.0423	Aliased
Residual	2	0.22	0.11			
Total	15	51.33	3.42			

Table 5.21 Lack of fit test for electrostatics at 40% RH

Source	DF	Seq SS	Adj MS	F	P	Remark
Linear	9	23.76	2.64	23.74	0.0411	
2FI	<u>6</u>	14.60	2.43	21.89	0.0443	
<u>Quadratic</u>	3	<u>7.60</u>	<u>2.53</u>	<u>22.80</u>	<u>0.0423</u>	<u>Suggested</u>
Cubic	0	0.000				Aliased
Pure Error	2	0.22	0.11			

The sequential test considered a model equation where additional terms remain significant to the model. The term “Quadratic vs 2FI” from the Table 5.20 possesses the significant “F-value” relevant for term significance. Also, from the lack of fit tests displayed in Table 5.21, suggests that the quadratic model term (with a relatively low “p-value” point) is the least significant lack of fit from the suggested terms in Table 5.20. Therefore, based on these suggestions a quadratic model equation approach was utilised for modelling the statics at 40% humidity.

To assess the adequacy of the model, the ANOVA was performed. Table 5.22 shows the ANOVA for the electrostatics at 40% humidity. The Model F-value of 4.61 implies the model is significant with only a 2.31% chance of occurring from noise interference.

Table 5.22 ANOVA for model coefficient for the electrostatics at 40% humidity in UHPM of contact lens polymer

Source	DF	Seq SS	Adj MS	F	P	Remark
Model	5	22.69	4.54	4.61	0.0231	significant
A - Speed	1	2.81	2.81	2.86	0.1253	
B-Feed	1	4.75	4.75	4.82	0.0557	
C-Depth of cut	1	0.014	0.014	0.014	0.9087	
AC	1	8.42	8.42	8.55	0.0169	
C2	1	6.70	6.70	6.80	0.0284	
Residual	9	8.86	0.98			
Lack of fit	7	8.64	1.23	11.10	0.0851	not significant
Pure Error	2	0.22	0.11			
Cor Total	14	31.56				

From the analysis, “F” values less than 0.05 indicate significant terms. In this case, AC, C2 are significant model terms.

The "Lack of Fit F-value" of 11.10 also indicates a low percentage chance of being influenced from noise samples. Therefore, this lack of fit is a bad representation of the sample, since it is desired to generate a fitting model. This relatively low probability (<10%) is troubling.

The normal probability plot of the residuals and the plot of residuals versus the predicted response shown in Figure 5.37 and Figure 5.38 show some outliers points from the straight probability line. This creates an unusual structure in establishing the reliability of the model at 95% confidence. It further indicates that the model barely conforms to adequate normality of residuals and may possess a constant error.

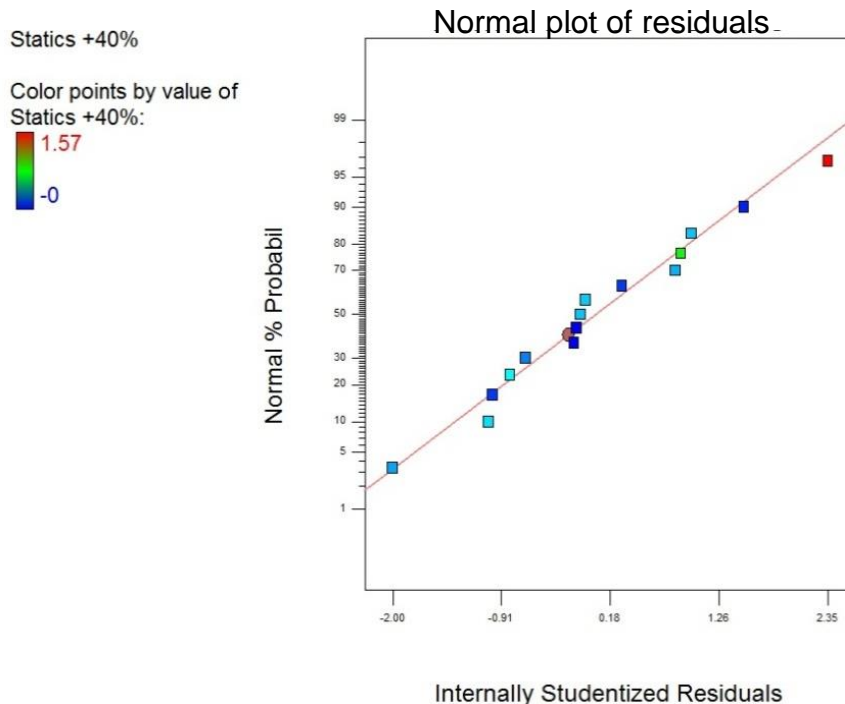


Figure 5.37 Normal probability plot of residuals of statics at 40% humidity

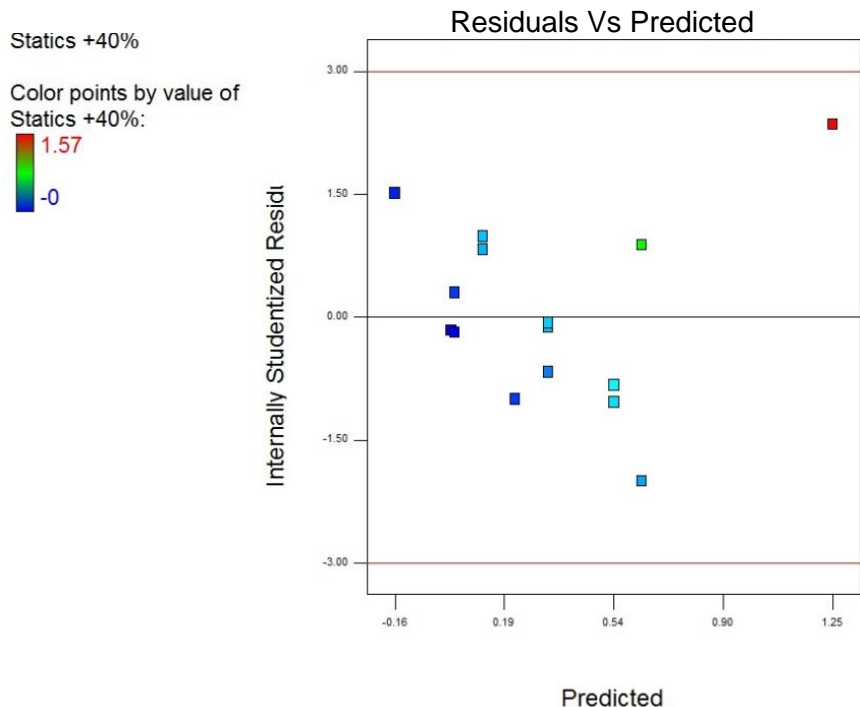


Figure 5.38 Probability plot of residuals vs. predicted for the statics at 40% humidity

Determination of significant factors influencing the electrostatics at 40% humidity

In determining the cutting parameters influential to the electrostatics at 40% humidity, the results from the ANOVA (Table 5.22) were studied. Based on a probability value greater than F-value and less than 0.005, significant terms to the model were identified. In this case the speed, depth of cut, and the interaction effect between the two were identified as the significant model parameters linked to the electrostatics at 40% humidity. Figure 5.39 shows the one-point parameter effect on the statics values and discusses them.

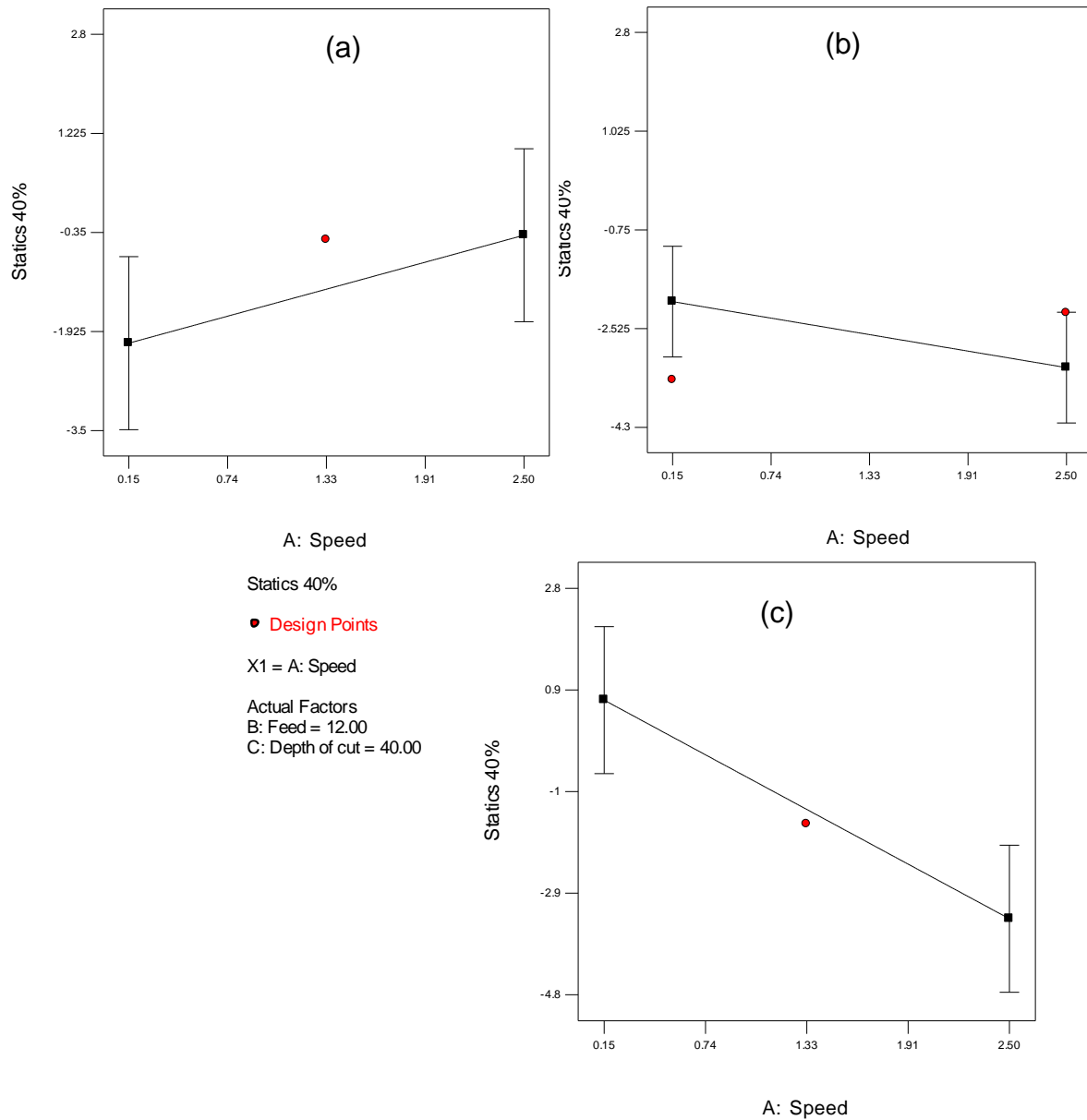


Figure 5.39 Behaviour of 40% RH in response to variation in speed at (a) 10 μm (b) 25 μm (c) 40 μm

- The plot of electrostatic magnitudes versus speeds in Figure 5.39 changes over the three different depths of cut at fixed feeds of 12 $\mu\text{m}/\text{rev}$. The Figure 5.39 indicates that as the Depth of cut changes from 25 μm in (Figure 5.39(b)) to 40 μm (Figure 5.39(c)), an increase in depth of cut generates a downward line but at a low depth of cut of 10 μm an upward trendline is obtained (Figure 5.39(a)). Statics values are seen to range from -1.9 kV to -0.4 kV in Figure 5.39(a), and from -1.8Kv TO -3.1kV in Figure 5.39(b) and a range of 0.8kV to -3.0kV in Figure 5.39(c). This condition could reflect the high rubbing action from the tool chips found at the tool tip.

- The change in the electrostatic values from the depth-of-cut plots at different speeds is shown below. Figure 5.40(a), (b) and (c) shows the depth of cut influence at 239, 2109 and 3979 rpm. A curve which reflects changing electrostatic conditions over an increase in depth of cut is seen at all the different speeds. This is explained by a variation of electrostatic response at both extremes in depth conditions. Statics values here are seen to range from -2.0 kV to 1.1 kV in Figure 5.40(a), from -0.9kV to -0.9kV in Figure 5.40(b) and a range of -0.2kV to -3.0kV is observed in Figure 5.40(c).

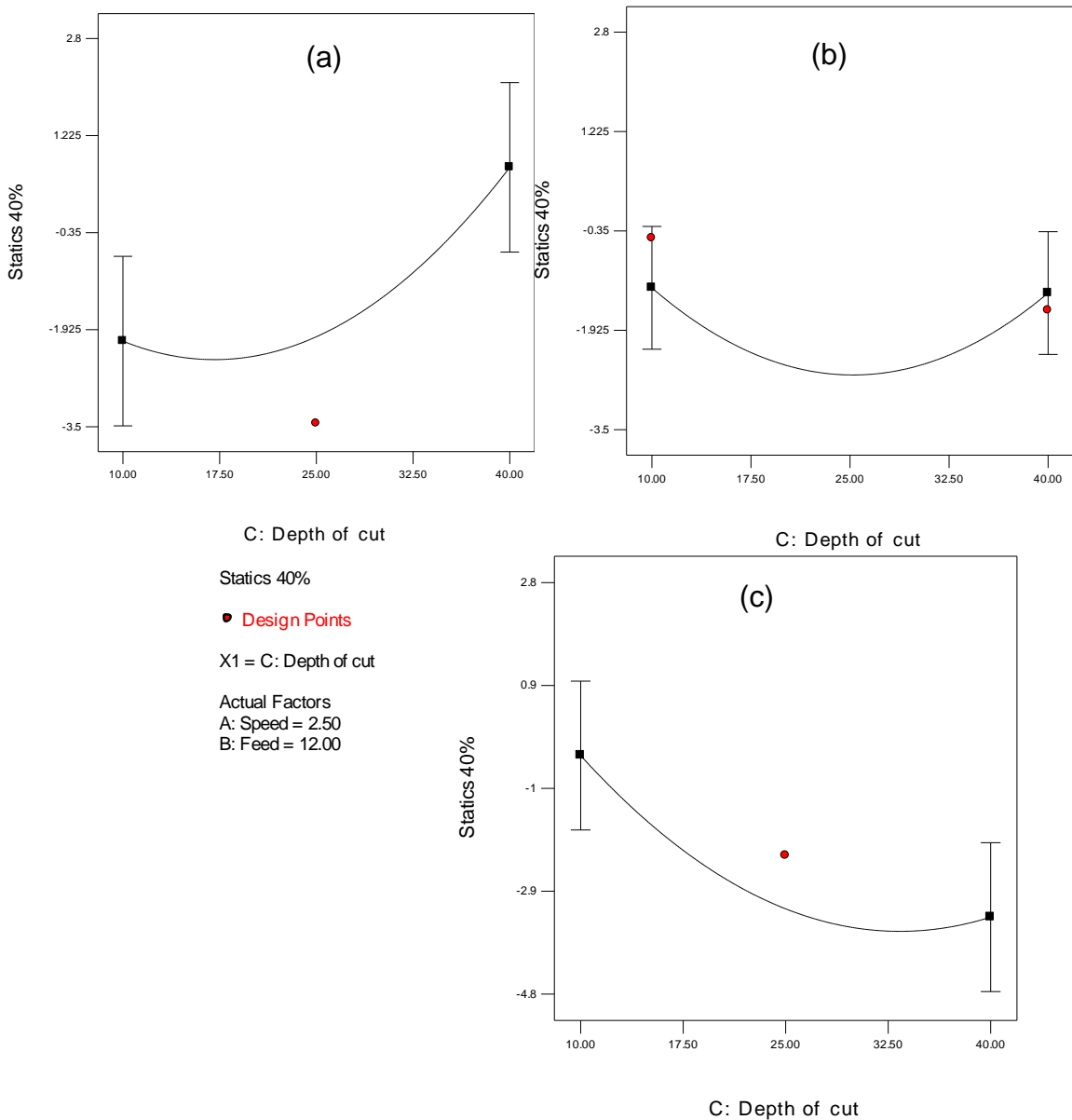


Figure 5.40 Behaviour of 40% humidity in response to variation in depth of cut at (a) 239 rpm (b) 2109 rpm (c) 3979 rpm

- The ANOVA analysis also revealed that one of the significant factors influencing the generation of electrostatic charge at 40% relative humidity is the interaction between the speed and the depth of cut. As shown in Figure 5.41, at low depth of cut, the increase in speeds leads to an increased amount of static charges. However, at higher levels of depth of cut an opposite reaction was observed. This is shown by the downward trending red line. The condition was identified with a decrease in static generation as the speed value increased.

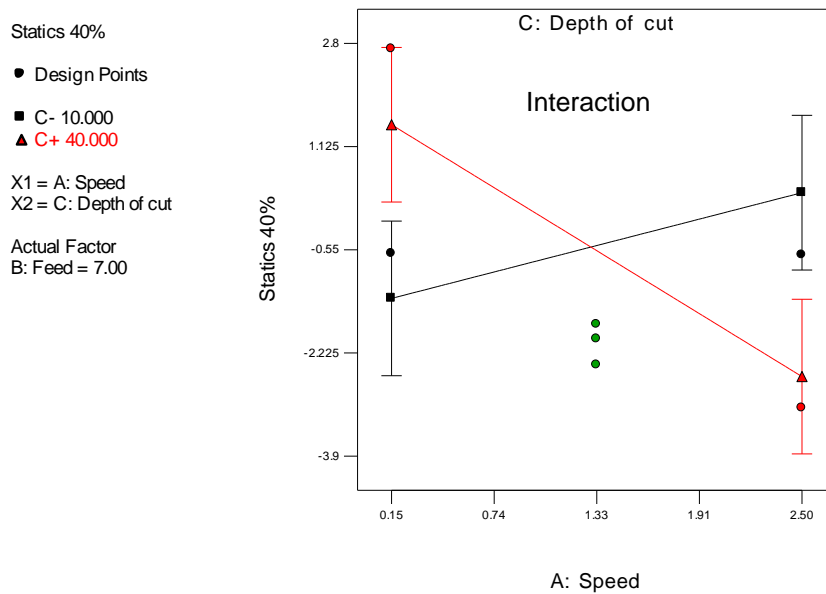


Figure 5.41 Interaction between feed and depth of cut (at 239 rpm)

Figure 5.42 shows a contour plot of that interaction between speed and depth of cut. From this contour plot, the interactions earlier stated can be observed. At very low depth of cut, an increase in speed reaches higher static values (extreme right corner). But at high depth of cut and high speeds, extremely low negative electrostatic readings are obtained (right top corner). The various region scaling also presents the curved relationships spoken in earlier sections (Figure 5.40(a), (b) and (c)).

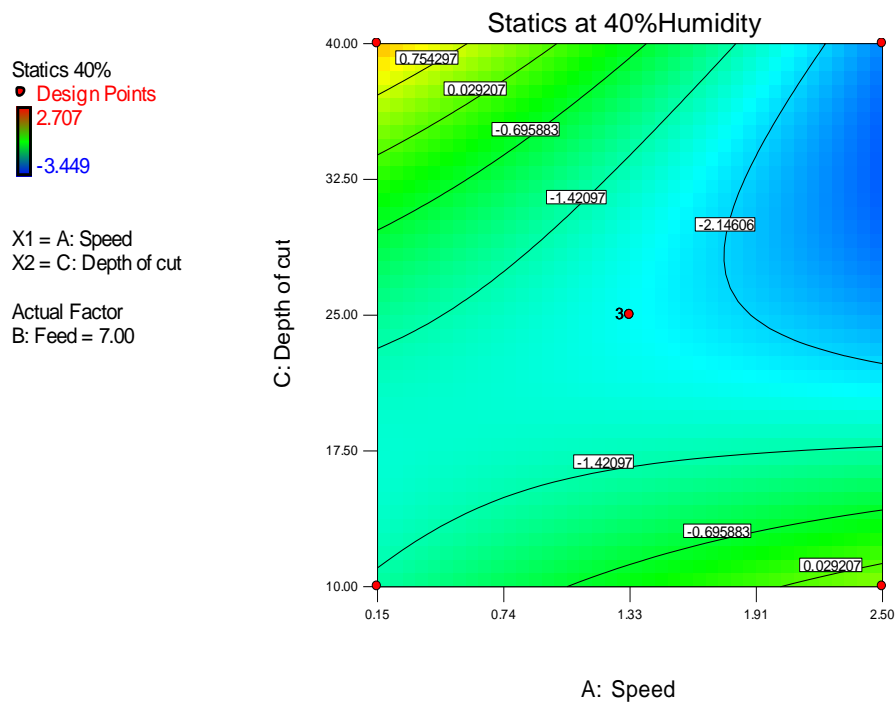


Figure 5.42 Normal probability plot of electrostatic discharge at 40% relative humidity

Polynomial equation of the electrostatic model at 40% relative humidity

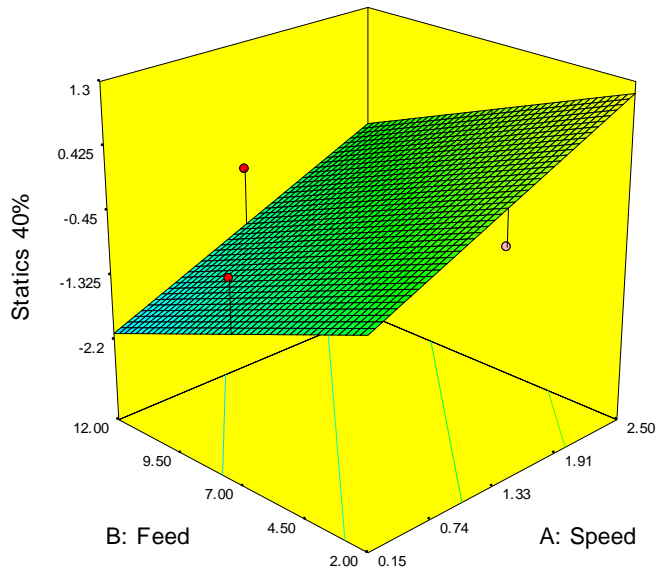
From the surface response modelling the quadratic polynomial model equation developed to relate the input parameters to the electrostatic charges generated at the 40% level humidity is shown in Eq. 5.24 below.

$$\text{Statics (+40\%)} = 0.94678 + 1.55341 S - 0.15409 F - 0.19127 D - 0.082325 S * D + 5.95185E - 003 D^2 \quad (5.24)$$

Where: $F = \text{Feed}$, $S = \text{Speed}$, $D = \text{Depth of cut}$

From the model it is seen that the speed and depth of cut and their interactions are most influential to the amount of static force generated at this humidity level. From the graphical perspective of the model equation using a 3D surface plot, in Figure 5.43, the effects of varying the speed, and depth of cut is shown. Figure 5.43(b) shows the curved relationship of the speed rate and depth of cut over the generated statics.

Statics 40%
 2.707
 -3.449
 X1 = A: Speed
 X2 = B: Feed
 Actual Factor
 C: Depth of cut = 10.00



Statics 40%
 2.707
 -3.449
 X1 = C: Depth of cut
 X2 = A: Speed
 Actual Factor
 B: Feed = 12.00

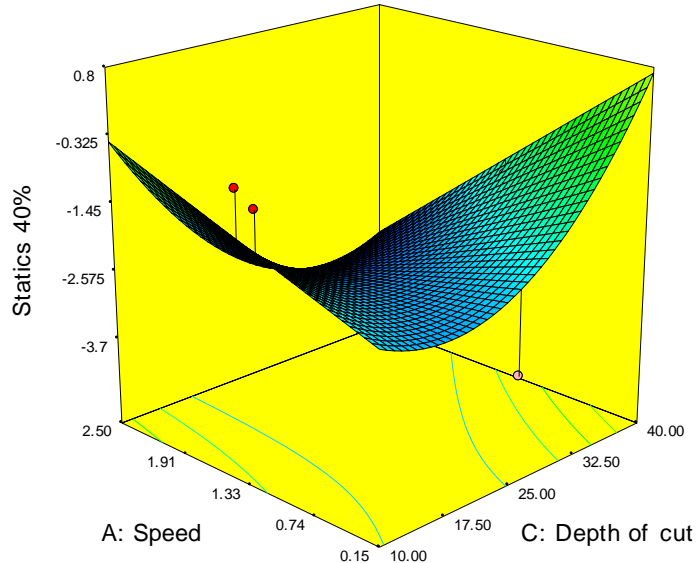


Figure 5.43 3D Plot of the influence of parameters on electrostatic discharge at 40% humidity

5.4.3 Analysis for triboelectric phenomenon at 20% relative humidity

At very low humidity (20% relative humidity) within the machine chamber further tests were conducted. At this level a huge increment in static charge generation was observed. This is believed to be based on the reduced atmospheric conductivity.

At this humidity level, static readings of high values were recorded with visual effects. Chipping formed at the tool occasionally created a flying bridge effect during tool separation with the workpiece as seen in Figure 5.44. This effect was still maintained within distances of about 40 μ m from the workpiece.



Figure 5.44 Strong triboelectric effects at very low humidity

During experiment 4 (at 2109 rpm, 2 μ m/rev and 40 μ m), a massive response in generated statics was first observed. At these parameters a negative voltage value of -5kV was generated at the third machining pass (Figure 5.45). This is postulated to be due to a massive rubbing effect from large chips from the high depth of cut followed by a low feed which increased the time for a pass. Heavy chipping is often observed at reduced humidity. This is due to the lack of presence of atmospheric

humidity which makes the hydrophilic workpiece material less porous and hard at the machining surface yielding to a better chip flow.

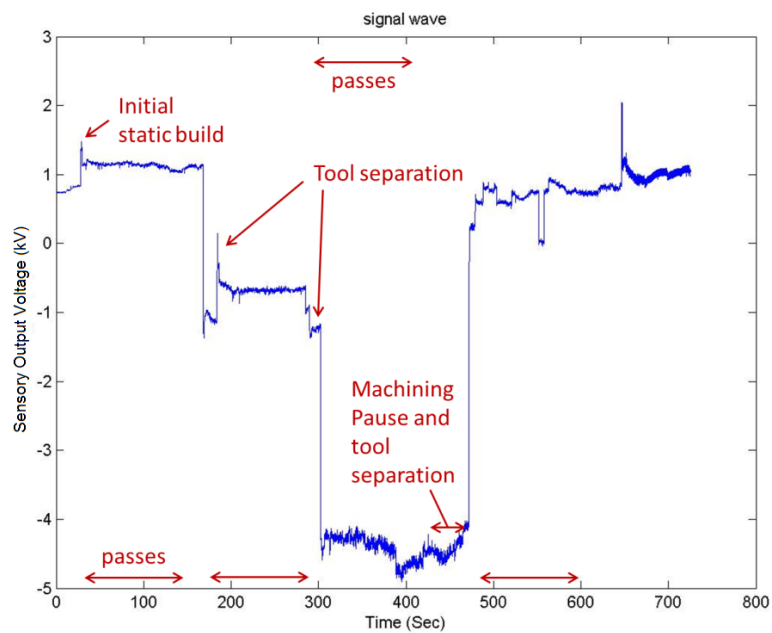


Figure 5.45 Triboelectric discharge effects during experiment 4 at $s = 2109$ rpm, $f = 2\mu\text{m}/\text{rev}$, $d = 40\mu\text{m}$ (20% humidity)

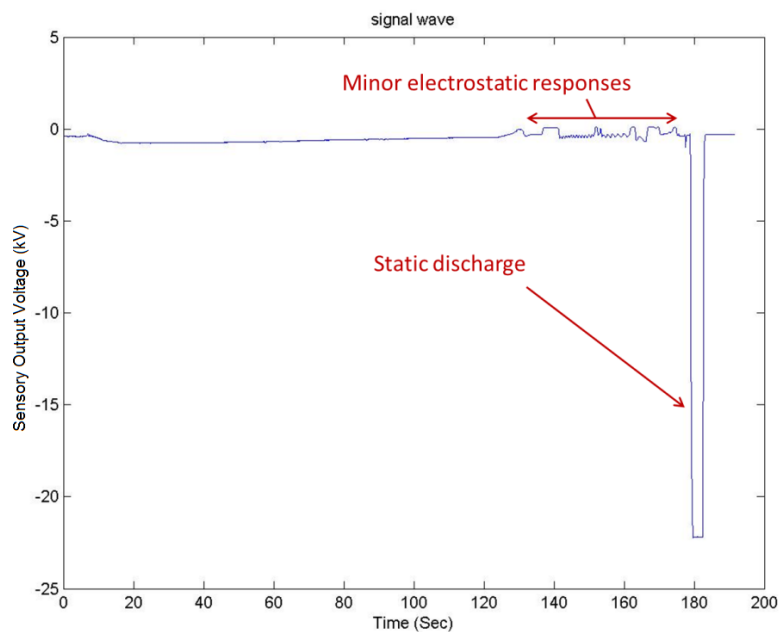


Figure 5.46 Triboelectric effect and sudden discharge at experiment 12 at $s = 2109$ rpm, $f = 7\mu\text{m}/\text{rev}$, $d = 25\mu\text{m}$ and 20% humidity

Using the same parameters but a reduced depth of cut in experiment 12 led to a static discharge of -22kV (Figure 5.46). This was obtained at the third pass. These chips are of similar width as found in experiment 4 but lighter due to reduced depth

of cut as shown in Figure 5.47. The massive static discharge at the experimental level is believed to be due to the light nature of the chips which enabled an easy build-up of larger volume than the previous experiment.

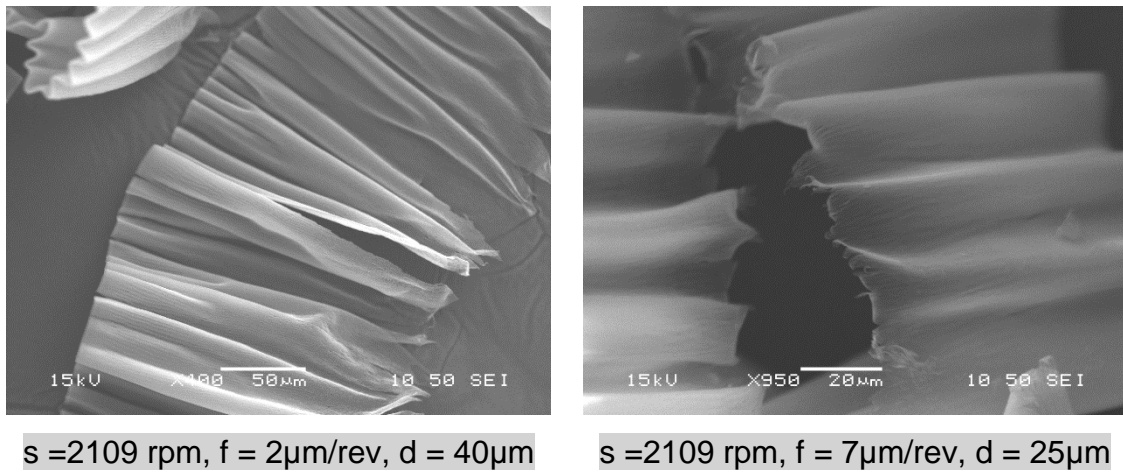


Figure 5.47 Comparison of cutting chip in experiment 4 & 12

Other experimental conditions such as experiment 6 with cutting parameters of speed at 3979 rpm, feed at 12µm/rev and 25µm depth of cut, also experienced huge static discharges of magnitudes of about -15kV (Figure 5.48). This was however, explained based on the high material removal rate possessed at this parameter combination.

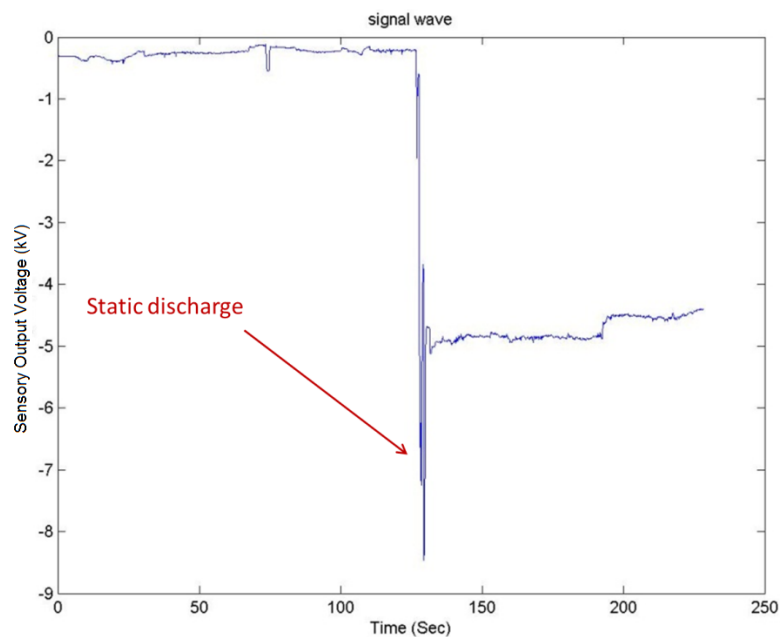


Figure 5.48 Triboelectric effect and sudden discharge at experiment 6 at $s = 4109$ rpm, $f = 12\mu\text{m}/\text{rev}$, $d = 25\mu\text{m}$ and 20% humidity

Experiment 6 possessed the highest material removing rate (MRR) with a feed of 47.75 mm/min and a cutting time of 0.13 seconds. In so doing, this selection produced the fastest rubbing action leading to sudden static discharge reactions during its short passes.

Determination of appropriate polynomial equation to represent RSM model positive static readings

Using an RSM data analysis, a suitable polynomial equation was obtained to represent the relationships between the input parameters and the electrostatics. The sum of squares sequential model and lack of fit test are both shown in Table 5.23 and Table 5.24.

Table 5.23 Sequential model sum of squares (SMSS) analysis for negative electrostatics at 20% humidity

Source	DF	Seq SS	Adj MS	F	P	Remark
Mean vs Total	<u>1</u>	<u>115.47</u>	<u>115.47</u>			<u>Suggested</u>
Linear vs Mean	3	84.12	28.04	0.71	0.5643	
2FI vs Linear	3	59.55	19.85	0.43	0.7400	
Quadratic vs 2FI	3	147.50	49.17	1.09	0.4337	
Cubic vs Quadratic	3	225.31	75.10	805.22	0.0012	Aliased
Residual	2	0.19	0.093			
Total	15	632.13	42.14			

Table 5.24 Lack of fit test for negative electrostatics at 20% humidity

Source	DF	Seq SS	Adj MS	F	P	Remark
Linear	9	432.36	48.04	515.06	0.0019	
2FI	6	372.81	62.14	666.18	0.0015	
Quadratic	3	225.31	75.10	805.22	0.0012	
Cubic	0	0.000				Aliased
Pure Error	2	0.19	0.093			

The sequential test considered a model equation where additional terms remain significant to the model with “Mean vs Total” having the highest “F-value”. But no appropriate lack of fit tests were found for the model. From the analysis all

polynomial models had significant lack of fit. Therefore, it can be concluded that these current results may not be modelled due to significant constant errors. A wider range in experimental parameters could be effectively used to rectify this challenge and provide enough data for modelling.

5.4.4 Modelling summary

The relationship between the speed, feed and depth of cut for the various relative humidity was successfully developed. The models are represented as polynomial equations and shown in Table 5.25.

Table 5.25 Polynomial equations to represent the developed models

Performance	Polynomial models
Statics at 60%	Statics 60% = $0.49788 + 0.65547 S + 0.028561 F - 0.077574 S * F$
Statics at +40%	Statics (+40%) = $0.50383 - 0.074167 F - 0.023567 D + 5.36667E - 003 F * D$
Statics at 20%	Not applicable

Significant process parameters that influence the generation of static charges at the various humidity levels are also listed in Table 5.26 below.

Table 5.26: Cutting parameters and interactions that significantly influence the triboelectric effect

Models	Significant influencing parameters	Significant interaction factor
Statics at 60%	Speed, feed	Speed vs feed
Statics at 40%	Speed, feed and Depth of cut	Speed vs Depth of cut
Statics at 20%	-	-

5.4.5 Conclusion and physics of the triboelectric phenomenon

From the triboelectric tests it was found that at 60% relative humidity increase in cutting speeds generates an increased amount of electrostatic charges. This, however, was influenced by the interaction of the feed rate. In such a case that at higher levels of feed an opposite response was observed with a decrease in static generation as speed value increased. This condition is explained by the reduced rubbing time from high speed and feed conditions. However, at low feeds, more rubbing time is available for static build and increased speed enhances friction and thus static generation.

At the 40% humidity stage, high chip build up around the tool was frequently observed during machining. This chip build-up causes a negative rise in statics up to levels as low as -3.0kV. Based on an additional influence of uneven chip formation, frequent fluctuations in statics were observed. These conditions are caused by a frequent loading and offloading of heavy chip bundles at the tool tip leading to a reversal of statics values in the positive ranges. From this experiment stage, it was identified that tool chips carried negatively charged ions and these increased negative electrostatic readings when formed. Higher feed rate in these experiments also created weaker electrostatic signals due to the shorter time for rubbing action of the tool and chips against the workpiece surface. High depth of cut and high speeds also generated extremely low negative electrostatic readings from these conditions previously mentioned. During tests at 40% humidity, it was concluded that additional experimentation is needed to perfectly model the effect of cutting parameters. The sensitivity of statics readings to various conditions posed to be a challenge in generating a high confidence model.

From the last triboelectric experimental (at 20% humidity), massive static discharge was observed in average cutting conditions. This is believed to be due to the light nature of the chips which enabled an easy build-up of larger volume than the previous experiment in combination with an extremely dry workpiece surface. Also it can be explained based on the high material removal rate possessed at the feed and speed value. The highest material removing rate (MRR) with a feed of 47.75 mm/min and a cutting time of 0.13 seconds was obtained in experiment 6 at $s = 4109$ rpm, $f =$

12 μ m/rev, $d= 25\mu$ m. Therefore, this cutting selection produced the fastest rubbing action leading to sudden static discharge reactions during its short passes.

5.4.6 Summary of results

Ultra-high precision machining of a contact lens polymer is shown to generate tribocharging characteristics under different conditions. The effects of each cutting parameters could be varied based on environmental conditions such as relative humidity. However, cutting speed which influences the shape of cutting chips and time of a cutting pass was seen to be the crucial parameters influential parameter in static formation. Various interactions, however, are responsible for static generation which are mostly linked to tool chip formation.

An observation of the tool chip, showed the importance of chipping in the triboelectric effect. Tribocharging was discovered to be founded derived from the short rubbing action of tool and workpiece or due to the rubbing action of massive chip formation on the tool tip. Both of these conditions are causing agents for electric fields formation during machining and static discharges. It was, however, confirmed that humidity could be used to control tribocharging.

In conclusion, tribocharging is an important factor in polymer machining. This phenomenon linked to cutting parameters within specific ranges could yield high voltages capable of causing triboelectric wear.

5.5 Molecular modelling overview of polymer nanomachining

5.5.1 Introduction

The MD cutting process of fluorosilicon acrylate polymer had varying results linked to force interaction parameters, iterations and tool size. Some experimental cutting runs have shown an elastic spring effect of the polymer while others exhibited a direct atomic break in the lattice depicted by a clear scattering of atoms. MD cuts were followed by an investigation of atomic shift. A process as seen in Figure 5.49 which studied various visual drawing representations (such as CPK, bonds and VDW) as well as thermodynamic data was applied.

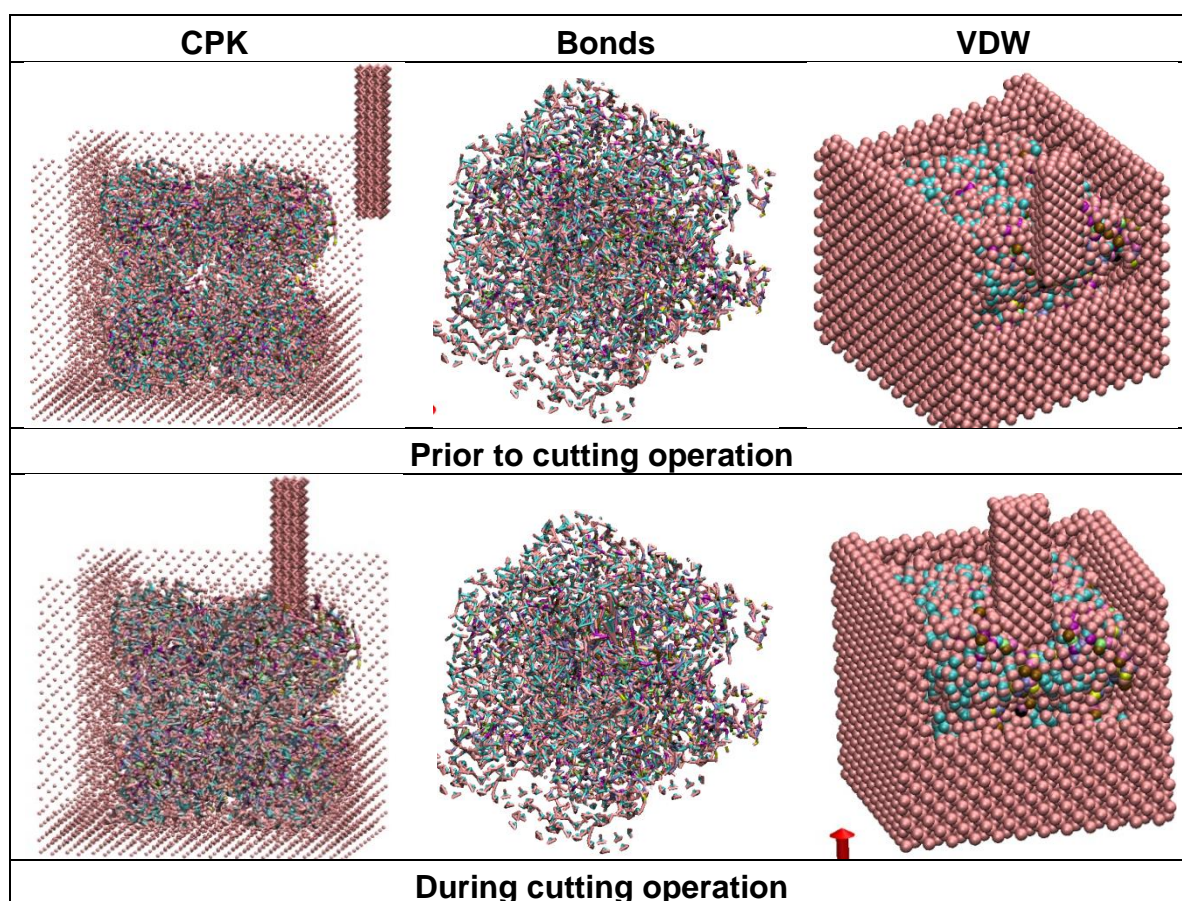


Figure 5.49 Various cutting conditions during MD simulation

5.5.2 Thermodynamic information analysis

During thermodynamic evaluation, observations of the temperature, as well as the potential energy, were analysed. Initial tests were done to ascertain stabilization of the MD ensemble at ambient temperature levels.

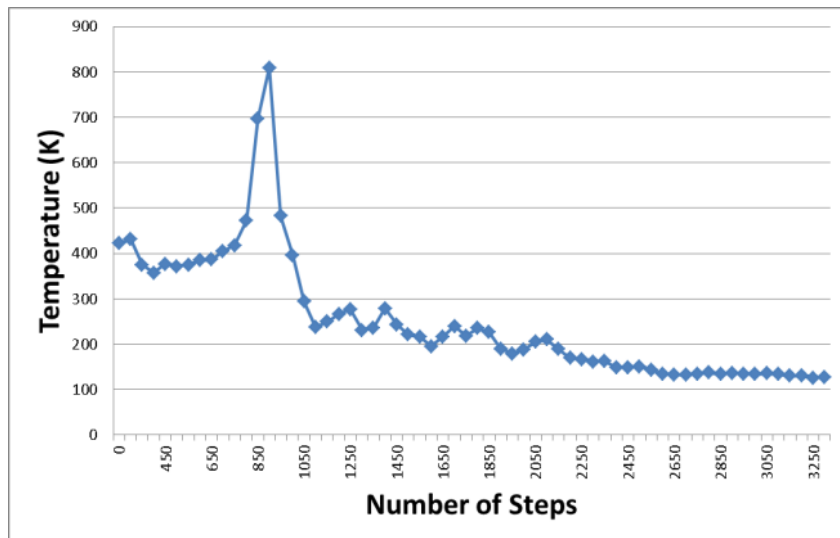


Figure 5.50 MD simulation of (a) temperature

Temperature results as seen in Figure 5.50 had initial spikes to values as high as 800K. This was believed to be associated with early tool entry and eventually these temperature values eventually stabilised to values about 200K as cutting was in progress. This condition is allegedly used to represent conditions experienced in an actual cutting process such as rubbing action of tool and workpiece or molecular displacement of atoms but reflects a huge loss of heat from boundary atoms. However, an actual cutting process of the polymer reflected here displays the recreation of a satisfactory dynamic representation of the process.

Similarly, in the machining of metals, a high proportion of the heat generated is removed from the cutting area by the chip [1]. Despite the high conductivity present metallic materials, the huge portion of heat present at the interfacial layer on the surface of the workpiece plays an important role in heat removal by conduction. Literature shows [158] that the amount of heat carried away from the primary shear zone by the chip is as high as 90% for higher cutting speeds. This initial simulation outcome shows the boundary conditions acting as a high source of heat dissipation from the interfacial layer of the surface of the workpiece. Also, based on the constrictions of the size of the simulated workpiece by computational demands, heat dissipation could be a significant challenge, acting as cutting chips would in metal machining but reversing realistic temperature levels.

Subsequent tests were built on this experiment model. Figure 5.50 and Figure 5.51 show the initial temperature and energy results from MD tests.

Also, results from the potential energy and total energy of these experimental runs as shown in Figure 5.51, depict the overall loss in energy of the system. Energy loss in the molecular dynamic system are known to occur (Oluwajobi [84]) but should be anticipated and adjusted accordingly during simulations. Oluwajobi [84] in his research found values of ultimate low of -500000eV found during the MD nanomachining of copper using LJ parameters.

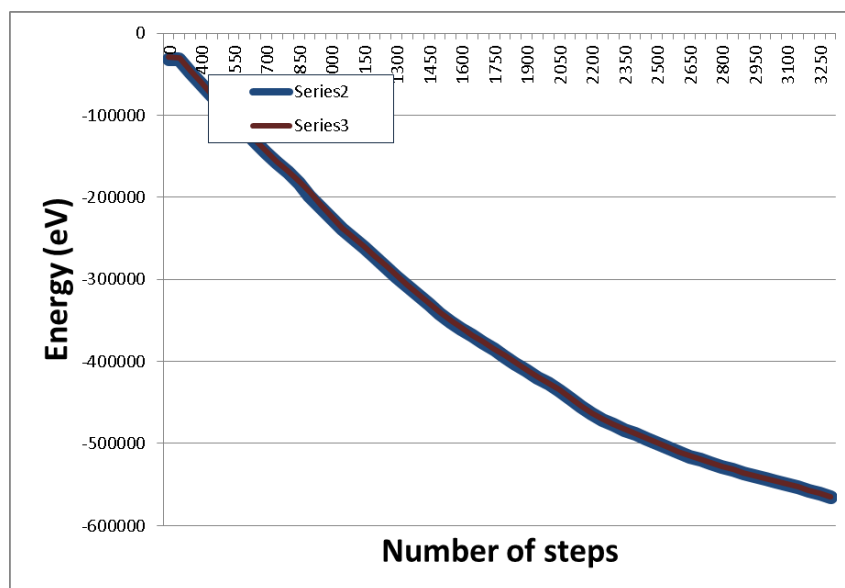


Figure 5.51 MD simulation of energy

Furthermore, for these temperature and energy results, a rubbery reaction was observed as shown in Figure 5.52. This results from the high interactive forces acting between workpiece atoms.

In plastic machining, because of their low thermal conductivity, heat generated in the primary shear zone does not quickly dissipate. This condition is characterised by concentrated heat generation in the cutting zone, yielding to an increased range in mobility of the molecular chain of the material and thus improved material ductility. Parameters such as molecular weight and the glass transition factor are the determining factors as to which these cutting effects become dominant [158].

However, this transition extends from a glassy state to a rubbery state based on machining conditions. Heat generation is a determining factor in glass transition states. In actual machining, this heat is generated by the shear in the primary deformation zone, by friction between the chip and the tool face and between the workpiece and the tool clearance side.

From the simulation results, the high loss in temperature mentioned above is assumed to be thus responsible for the resultant higher molecular force interaction between molecules. The tool in these instances experienced difficulty in rupturing molecular chains of the polymer leaving an imprint of its shape within the workpiece. The action induced a form of spring back action from the workpiece. This situation is reflected by the rapid fall in temperature and the energy trendline further highlights the elasticity in the material.

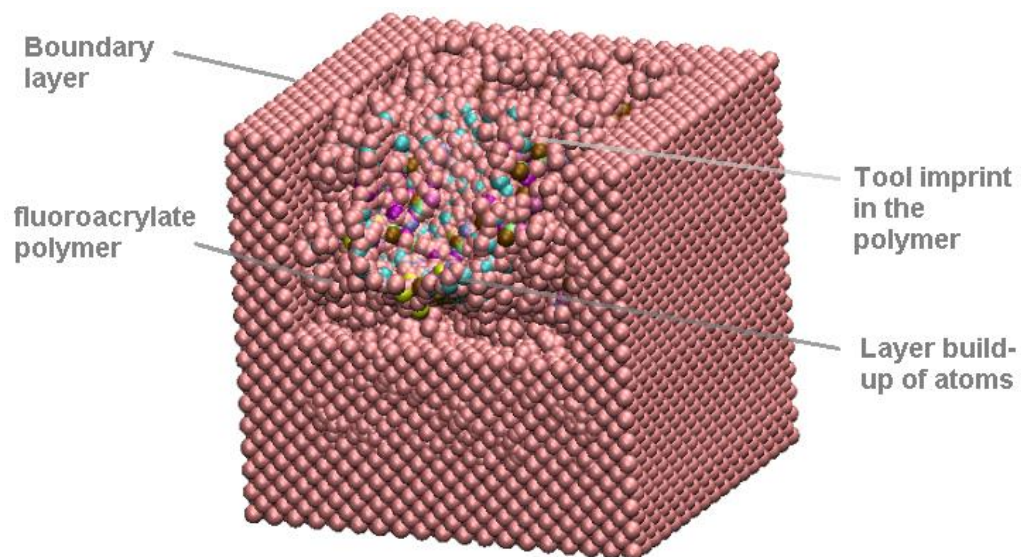


Figure 5.52 Hyper-elastic polymer property

Additional experimental runs in simulation had changes in interacting force potential values to reduce the high elasticity obtained during simulations and allow cutting action. Comparison of the effect of altering parameters was linked to elasticity and studied.

5.5.3 Comparison of various potentials between tool and workpiece

Numerous MD tests were run to access the effects of some parameters on MD results; however this section of the thesis reflects the results of MD test linked to the

combined effects from molecular interacting force parameters and speed. Experimental tests investigated the effects of using only the Lennard-Jones force potential and also a hybrid force setup of the Lennard-Jones in combination with Tersoff force potentials. The force potential depicting interactions between the tool and workpiece was additionally set during MD simulation tests from LAMMPS. A number of combinations of LJ parameters were tested and these results are shown in Table 5.27. Variation of the LJ parameters was done following the estimation based on the chart by Aziz [131] shown in Figure 3.12. The tool in some test had a smoother cutting effect through the workpiece. This was found to be linked to the hybrid combination of LJ and Tersoff force potentials which created a more appropriate representation of force interaction during cutting simulation.

Table 5.27 Comparison of various LJ force potentials during MD simulation

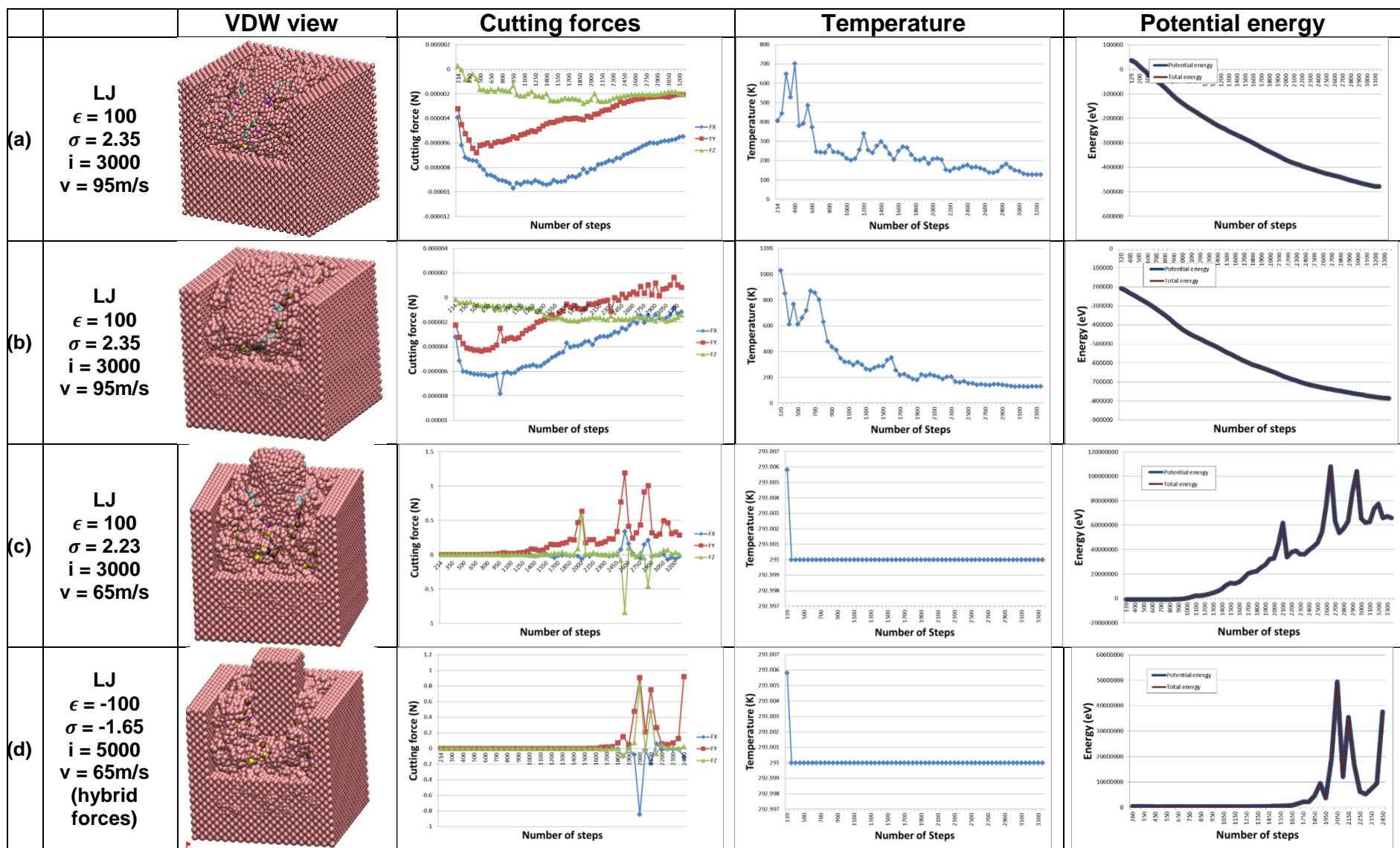


Table 5.27 shows variations in simulation observed during tests. The results in Table 5.27(a) show that the tangential force components of cutting forces (f_x) varied in the range from around -4×10^{-6} N to -5×10^{-6} N with an average of -1×10^{-5} N; the potential energy had a progressive downward slope, falling to low values of about -500000 eV, towards the end of the simulation at 3200 steps. Initial high temperature was observed but these later stabilised during the simulation run due to optimised cutting conditions. The phenomenon of ploughing was not observed due to the high elasticity of the workpiece but an imprint of the tool was seen on the workpiece.

For the subsequent experimental test in Table 5.27(b), an increase in the tool size from the number of atoms and the structural dimension produced similar results to other experiments. However, over the same number of experimental iterations, tangential force further increased to more positive values of -4×10^{-6} N to 2×10^{-4} N. During these tests, high attractive forces between atoms of the tool were also experienced. These high interactive forces depict an inherent imbalance in force application of the system on tool atoms. Similar temperature results from initial force potentials tests in Table 5.27 were observed in this test. A mild build-up at atoms was observed from the tool imprint.

Further tests in Table 5.27(c), show the varied atomic distance between tool and workpiece atoms, at reduced cutting speed. As the temperature values stabilised, the test produced a very soft workpiece with loosely attached atoms. However, the presence of excessive attractive forces was still present on the tool. This was identified to be as a result of the inadequate relaxation time for the system. At this stage evaluation of the cutting force showed positive values with rise from values ranging between 1×10^{-2} N to about 3×10^{-1} N. In this test positive energy value of 1×10^8 eV over 3200 steps and a stable temperature of 293K was observed. These results reflected pure cutting action but with plastic deformation. A mild ploughing phenomenon was identified at this stage with about 2 layers of atoms.

Finally, to improve the relaxation stage of the simulation a higher number of iteration and LJ parameters (from Table 5.27(d)) were selected. A pure cutting condition was achieved without plastic deformation. In this test, the atoms behave more like solids and show cohesiveness. The potential energy and total energy of this experiment shows a progressive stable rise before 1800 steps with a positively inclined energy

value but it has fluctuations towards its end due to compression effect from atomic pile up with the fixed boundary atoms. The tangential force component started with 1×10^{-5} N to high values of 3N towards the end of the pass. In this simulation the atoms behave a lot more like solids with higher attractive forces between them and more resistance in cutting action. A ploughing phenomenon was observed with a pile-up of three layers of atoms from the external Van der Wall (VDW) simulation drawing method. A steady stable temperature value of 293K was observed from the temperature which indicates stabilisation and heat dissipation within the model. This is a desired quality for a model and the best cutting condition.

From the results in Table 5.27(d), an additional test run performed at a higher number of iterations and an introduction of Tersoff force potential between the tool and the workpiece to achieve stabilisation. This is added due to the suitability of Tersoff in modelling carbon force interaction with other elements. Simulated results of these findings are expanded in Table 5.28. A clearer representation of the MD visualisation with varying colours based on MD component parts is shown in Figure 5.53 for visual inspection. This final test is conducted over 6000 iterations with the additional hybrid Tersoff potential.

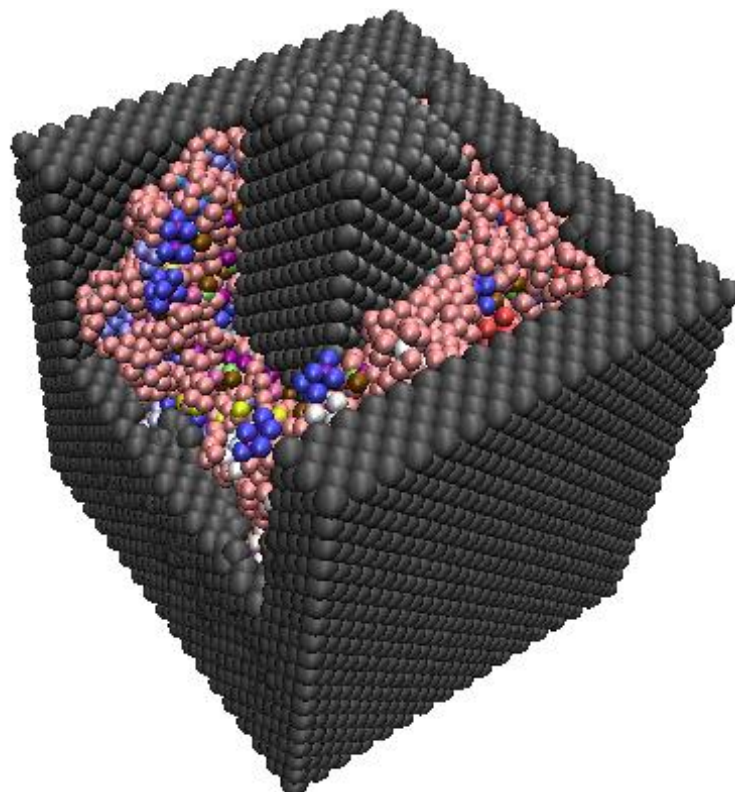
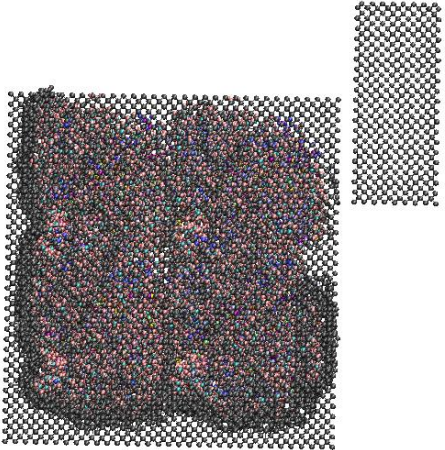
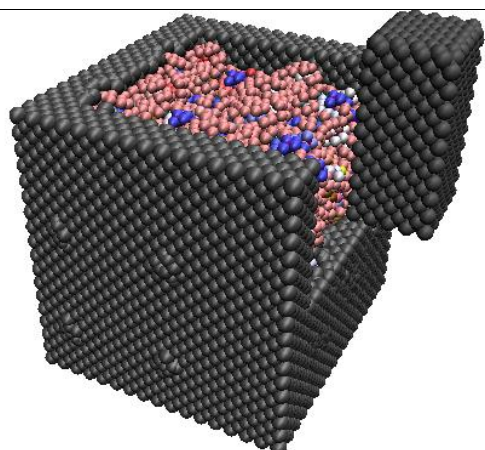
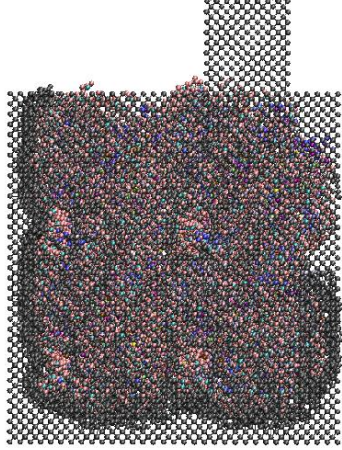
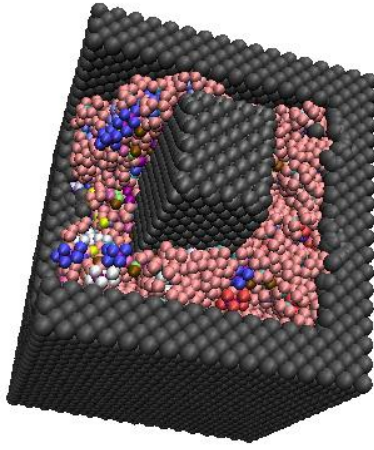
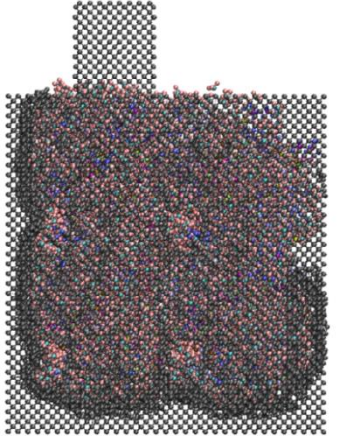
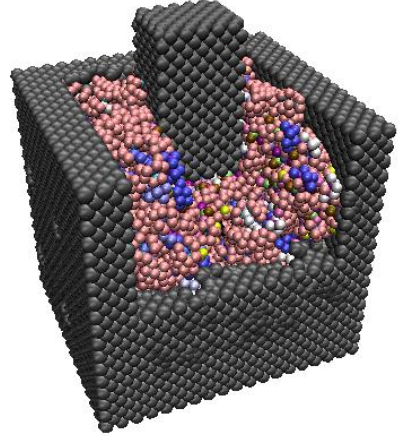


Figure 5.53 MD of simulation model of Roflufocon

Table 5.28 Hybrid force simulation with (a) CPK; (b) VDW representation

	CPK drawing representation	VDW representation
(a)		
(b)		
(c)		

The effect of the number of iterations on the plasticity of the material can be better observed in this test. It could be postulated that a smaller number of iterations didn't provide adequate time for ideal force representation between atoms and thus yielded plasticity. A higher range in iterations generated a more cohesive solid nature of the polymer. This is also believed to be linked to the influence that iterations may have

on the simulated velocity of cutting. VDW and CPK drawing representation shown in Table 5.28 show the progressive shift of atoms experienced as the cutting process is done. Figures in the table seek to infer effects occurring due to shifting of atoms within the compression and lattice slip zone. Observations show that the effect of an underlining cushion bed of atoms formed within the workpiece attest to the fact that the compressive stress zone present in this polymer simulation is greater than that found by bigger than metals opposites [82] based on the choice of force potentials and bonds present.

The CPK drawing method shows the more robust internal ploughing phenomenon experienced in polymers. A build-up of about 4 layers of atoms can be seen from a closer view. This is attributed to a pure cutting and shift of atoms from the tool atoms. In the last CPK figure, the atomic layers are seen to overflow from its boundary box region. Though some elasticity is retained in this simulation, its VDW representation could be identified as adequately mimicking an ideal polymer cutting process from the combination of the force potentials acting within the workpiece and with the tool.

5.5.4 Correlation of MD results to machining conditions

Figure 5.54 shows the cutting dynamics complexities in polymers machining. From the figure a depiction of known dynamic principles guiding orthogonal cutting are also reflected.

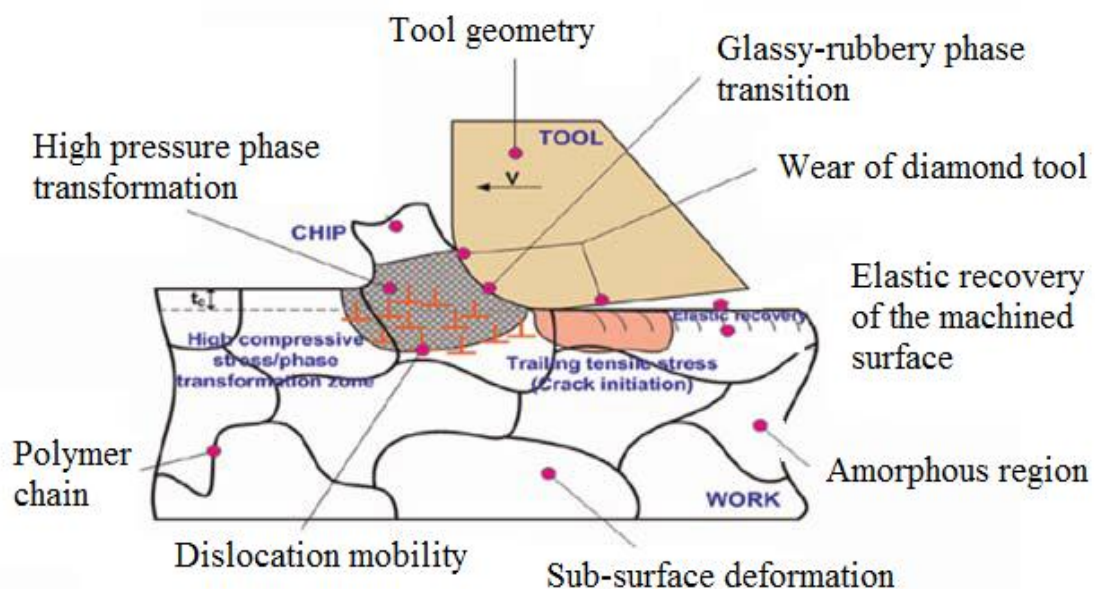


Figure 5.54 Various complexities involved in the cutting of polymers [147]

As mentioned in Chapter 2, polymers undergo a transition from a glassy state to a rubbery state with increase in temperature. From experimental results in previous sections, the effect of temperature and pressure applied at various cutting parameters creates a ductile regime cutting characterised by a glass-rubbery effect and continuous chip flow formation. This condition is also reflected in MD by the elasticity of the workpiece during tool passes.

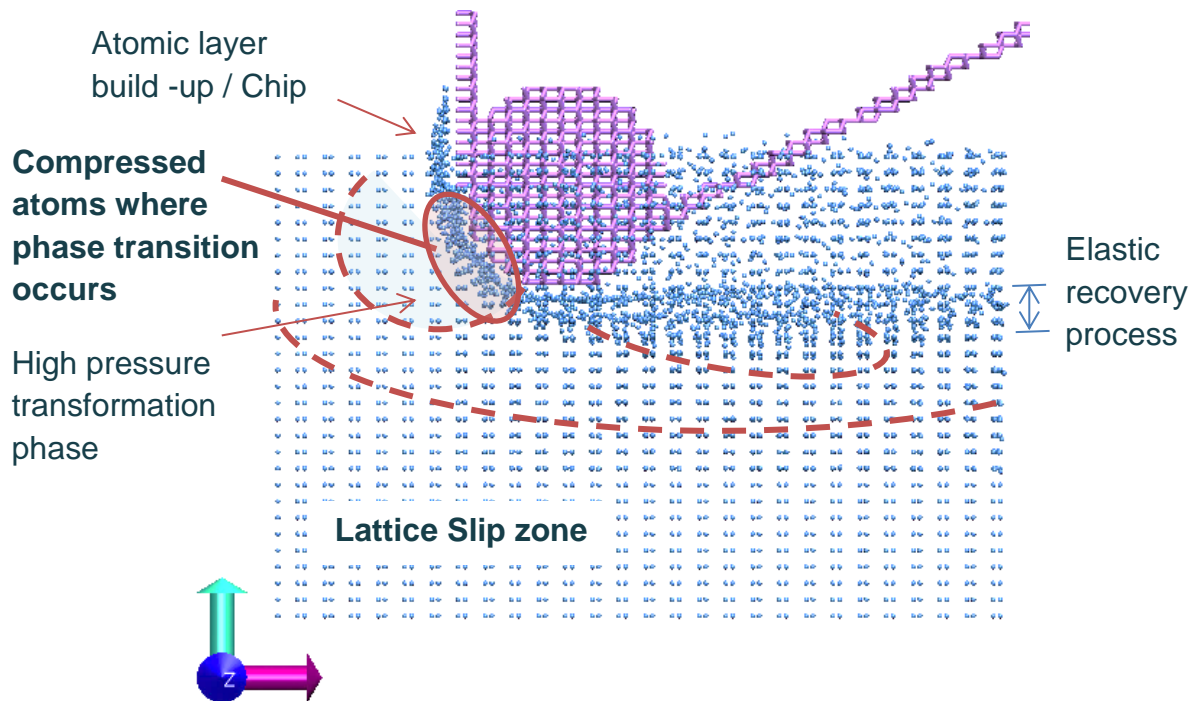


Figure 5.55 MD showing atomic movement within the silicon workpiece

The effect of increased feedrates leading to high rubbing experienced at the surface of the workpiece was shown by the increase in simulated cutting speeds. Similar reactions with increased cutting velocity influenced simulated temperature output. High elastoplastic and plastic deformation observed in both simulation and cutting operation are thus seen to occur in the primary shear zone or high compressive stress/phase transformation zone (Figure 5.55). Figure 5.55 which shows this atomic movement within a workpiece gives a better depiction of the movement of atoms within the material during molecular dynamic simulated conditions. The reaction from micro-structural cracks which occur along the trailing tensile stress zone are however difficult to identify from simulated diagrams.

Figure 5.56-58 show the observations of the temperature and cutting force (f_x, f_y and f_z), as well as the potential energy which is also analysed for the hybrid condition. From the figure, force components as seen in the simulation show an initial start in the values of 0.02 – 0.1N before rising to values of 0.8N. This is believed to be as a result of the dimensional constraints of the simulated environment as the tool approaches the boundary atoms. It can thus be seen that the outcome of simulated sub-surface machining phenomena correlates with postulated findings from force and surface experiments in previous sections of the thesis.

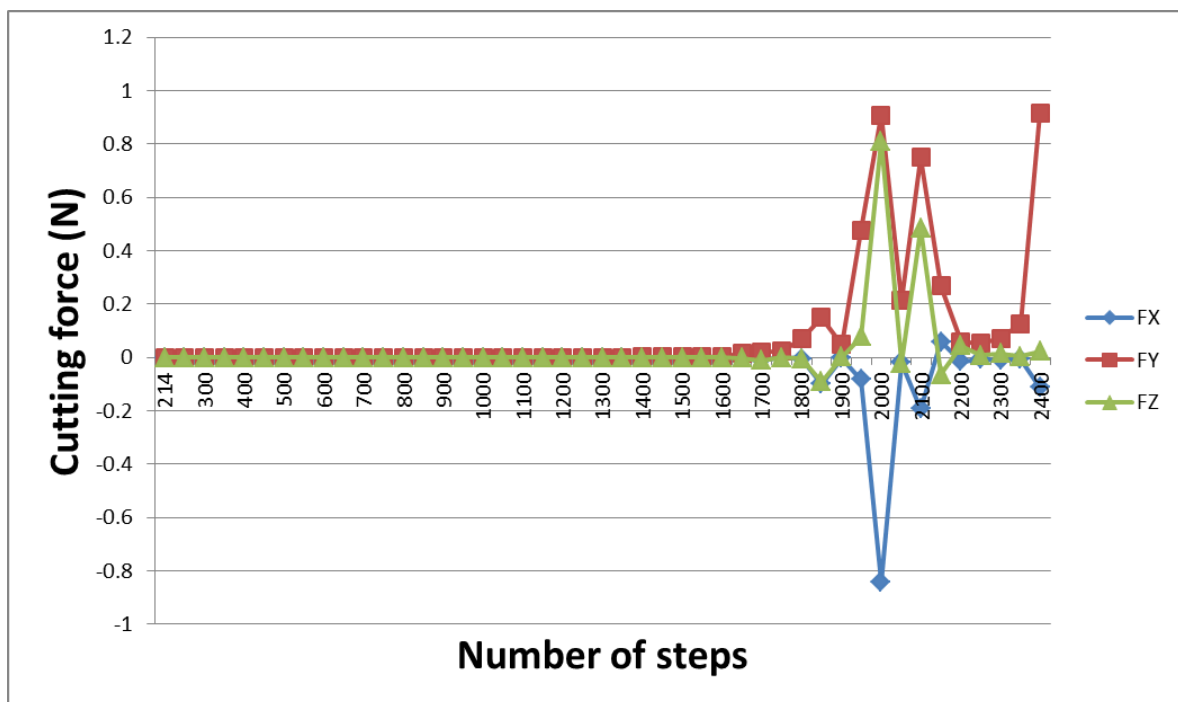


Figure 5.56 Cutting force component of MD simulation of polymer

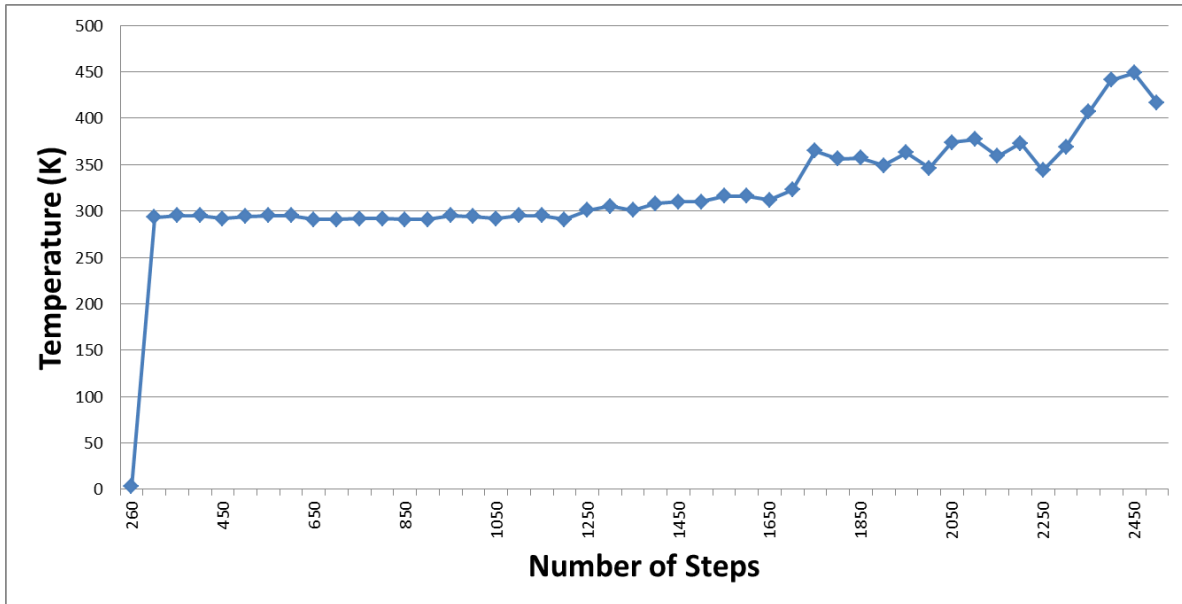


Figure 5.57 Temperature component of MD simulation of polymer

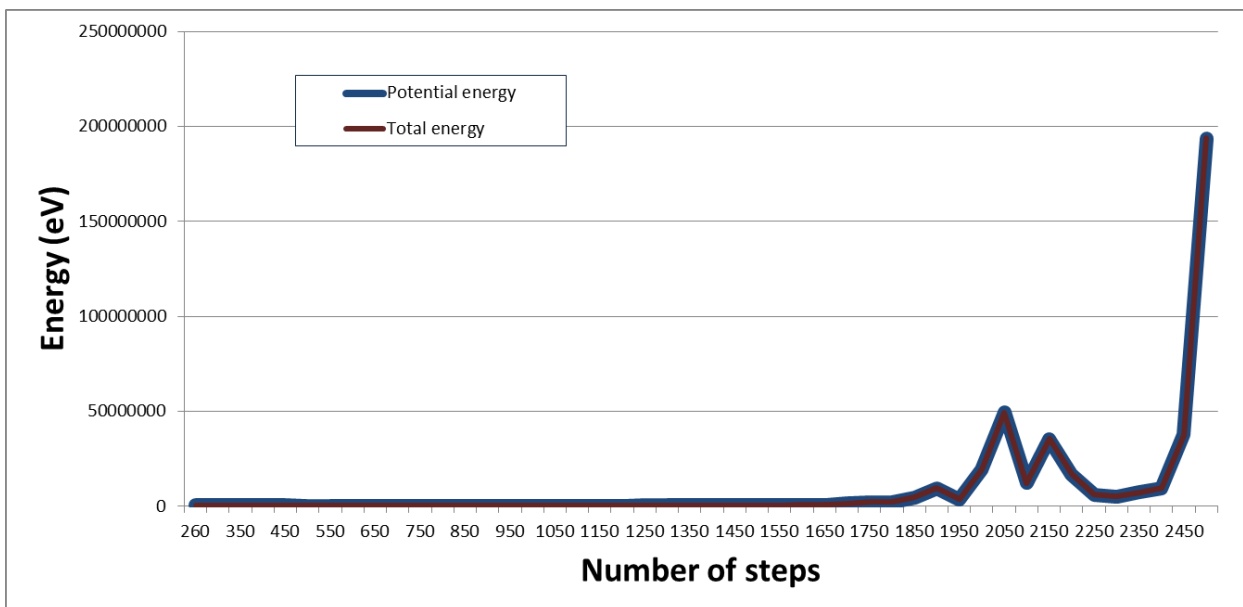


Figure 5.58 Energy observed during MD simulation of polymer

A brief initial stable temperature which indicated a stable thermodynamic system was seen (Figure 5.57). This was later characterised with a gradual increase in temperature as the tool atoms are compressed against the fixed boundary atoms. This condition reflects the effects discussed from the heat generated in the compressive cutting zone. As the specific heat of polymers is usually greater than that of metals and its thermal conductivity significantly lower, therefore, temperature

rise in the polymer is normally larger and concentrated to a smaller area when a given quantity of heat is applied to equal volumes of a polymer and a metal. Also because of the concentration and the scission of molecular chains to form an atomic build-up layer, heat is believed to be generated. MD simulation however takes into consideration the overall increase in temperature of the simulated system in the thesis. In an experimental setup, this also results due to localized heating from continuous tool rubbing at the machined surface, leading to excessive heating. This further may create a burning in the machined surface of thermosetting polymers or the elastoplastic effects experienced in thermoplastic polymers.

Force signal observed had an initial stable start, few oscillations at 1750 steps which gradually increased to higher energy values (Figure 5.58). This observation may further display the influence on sub-surface compressive force actions as responsible for change in material condition during cutting. Higher forces, increased temperature and energy release explain the importance of the effects of cutting parameters on sub-surface conditions to determine achievable lens output. Also, an influence of the post effect of the elastic recovery process as seen in Figure 5.55 may form a combined effect for these results. This could further influence achievable surface results for materials of high plasticity. Additional conditions such as the change in the effect of the rubbing action of tool chips found at surface of workpiece which wasn't covered in this simulation may also be of importance.

5.5.5 Summary

Despite the difficulty in estimating force interaction between elements in a polymer during machining action, this study was able to reproduce an actual MD investigation into nanoscale machining of polymers. Results of the force components during initial simulated cutting reflected similar values as seen in section 4-2. An evaluation into sub-surface microstructural phenomena during nanometric machining reinforced known orthogonal theory of sub-surface effects. Potential energy release from the simulated system provided results which correspond to an increased scission of molecular chains. This is presumed to be from the generation of a form of tool chip from the atomic build-up layer. Increased rubbing action between tool and workpiece could reflect on the high electrostatics addressed in section 4.4. The combined effect of the compression zone found in polymers, ploughing phenomenon and build-up of layers of atoms are believed to be conditions associated with high rubbing for static charging. High elasticity in polymers and close atomic attraction may also contribute to this. Despite the replication of this cutting process using simulations, it must however be noted that MD simulations only observe a nano-portion of the cutting effect which does not proportionally apply to an experimental larger scale nanomachining process based on force interaction over a larger volume.

Conclusion

The objectives of this research work were aimed at investigating postulated facts on the UHPM of polymers and evaluate the performance of ultra-high precision manufacturing of contact lens polymers. This was done on the commercially available contact lens polymer, Roflufocon E, and performed on the Precitech Nanoform Ultra-grind 250 precision machining.

An extensive literature review, as presented in Chapter 2, discussed in details optical polymers and the UHPM process in general. It then addressed barriers and current available evaluation techniques that could be employed in analysing conditions occurring in polymer cutting.

The reviewed literature revealed the challenges faced in polymer machining from various wear mechanisms which could drastically influence surface accuracy of the optical profile attainable; and how current machining parameters employed in the fabrication of high-end optical polymers have produced Liechenberg cracks on diamond tools from high static.

The identified knowledge gap in the literature depicts that there exists no report on an established process scheme for efficient UHPM of polymers. The lack thereof affects the understanding of the influence of cutting factors in machining. Also, detailed quantification and understanding of the underlining triboelectric phenomena between diamond tools and polymers as studied in this thesis does not exist. In addition, there is no published work on the molecular dynamics simulation of a contact lens polymer and its nano-machining replication.

The detailed experimental procedures employed were portrayed in this thesis in Chapter 3. These comprised a detailed overview of a commercially available contact lens polymer workpiece, specific diamond tooling and state-of-the-art nano-machining equipment. This chapter further consists of the method employed for the determination of optical surface quality. This directly considered the effects of machining parameters such as feed rate, speed and depth of cut. The deductions from these tests were based on the analysis of machining cuts. Various combinations of cutting parameters were considered; and selection of the machining

final matrix was based on the Box-Behnken RSM modelling method and utilised for modelling. This methodology permitted prediction within and above selected ranges of parameters. The selection of the statistical analysis method considered the number of factors to be evaluated and provided a lower number of experiments for predictions. It was seen that this response surface technique aided in the selection of cutting parameters not at the extreme ranges of the Ultra-precision machine based on its spatial modelling arrangement which aided in predictions.

Other conclusions based on the investigation were on the evaluation of the cutting parameters effects on relevant condition monitoring practices such as force monitoring and triboelectricity that best described the influences of cutting factors.

During the evaluation of surface roughness, experimental tests achieved the minimum surface roughness at 239 rpm speed, $2\mu\text{m}/\text{rev}$ and $25\mu\text{m}$ depth of cut. During modelling, feed rate and depth of cut were identified as significant influential factors in the determination of surface roughness; however changes in the feed rate had greater influence than any other factors. This situation was assumed to be due to a decrease in the distance between cutting passes by the diamond tip, creating a form of overlapping between cutting grooves. Also, this could be attributed to the rubbing action originating from tool chip magnetised to the cutting tool from a triboelectric effects. These chips as the feed gradually increased, increased in width and caused disturbance during the cutting process. However, as the feed further increased beyond $7\mu\text{m}/\text{rev}$ a point was achieved where a balance/semi-balance could be found between increase in the width of chips and chip clearance (due to size) from the surface of the lens during machining. At this stage a reduced amount of chip was found at the diamond tip causing a relative improvement in achieved surface roughness. At a low depth of cut of $10\mu\text{m}$, a very rough lens surface of 20.4nm was achieved during machining. This poorer surface finish was presumed to be attributed to the compounding effect of a reduced chip thickness due to a low depth of cut.

An overview of the cutting shows that cutting depth influenced the thickness (width) of the cutting chip. This generated light or thick chips which generated an effect on continuous and non-continuous chip flow. Also, the feed rate was identified to have a greater effect on the structural surface of the tool chip. Chips with rough surface and

high cracks were obtained at high feeds. This also contributed in chip breaking. However, it was postulated that the speed led to a variation in chip edges. This variation ranged from cone-like, fillet-shaped to actual tear. A combination of these observations on the cutting chip could be used to explain the formation of tool chip at the tool tip during machining.

During the force evaluation, from the analysis of force at the tool tip, it was concluded that the effects of sensor positioning along the tool poses an insignificant effect on the recorded force readings. Furthermore, the effect of the feed rate was identified as the only significant model term linked to the cutting force. The RSM model implemented also postulates that negligible or no influence is perceived from depth of cut and speed during UHPM of polymer. However, the validation of the model falls below a 10% confidence prediction level needed in general statistics despite a prior modelling of the exact force at the tool tip. This value indicated an underlining challenge in the model. This was attributed to challenges in micro-force acquisition based on the scale of machining. Thus, it was concluded that this model might not take all factors involved into consideration. It is recommended that more tests be conducted with a combination of multiple sensors to predict force effects on cutting parameters.

A careful analysis of the cutting parameters linked to static charging as presented in Chapter 4, showed a high correlation of feed and speed at higher humidity value and speed and the depth of cut at lower humidity. UHPM of a contact lens polymers was here shown to generate tribocharging characteristic under a range of conditions. However, speed rate which influences the shape of cutting chips and time of a cutting pass was seen to be the most influential parameter in static formation. This factor was identified also to be a linked non-continuous chip flow which greatly reduced chip build-up.

From the triboelectric tests, it was found that at 60% relative humidity increase in the cutting speeds generates an increased number of negative electrostatic charges at low feed rates. At the 40% humidity stage, high chip build up around the tool was frequently observed during machining. This chip build-up also causes a negative rise in statics up to levels as low as -3.0kV. However, at this humidity stage, it was concluded that additional experimentation is needed to perfectly model the effect of

cutting parameters. This was attributed to wide variations in statics readings based on loading and offloading of tool chips at the tool tip.

From the last tribo-electric experimental (at 20% humidity), massive static discharge was observed average cutting conditions. This was believed to be due to the working on extremely dry workpiece surface. Also it could be explained based on the high material removal rate possessed at the feed and speed value.

The importance of chipping in the tribo-electric effect could not be undervalued. Tribo-charging was discovered to be founded derived from a short rubbing action of tool and workpiece or due to the rubbing action of massive chip formation on the tool tip. Both of these conditions were causing agents for electric fields formation during machining and static discharges. It was, however, confirmed that humidity could be used to control tribocharging.

From the experimental evaluation of triboelectric phenomena, it was found that each of the cutting parameters influenced chipping, some more than others. Some basic interactions from cutting parameters contributed most to this condition and had high electrostatic charging effects. It was concluded that an independent look on parameter interactions on the tool chip could generate a way to determine possible electrostatic magnitudes.

In conclusion, the results validated the fact that feed rate had a high influence in polymer machining surface roughness. As observed from the RSM model, negligible effect of the cutting speed was experienced during the prediction of surface roughness. Further experimentation with a wider range of parameters may however, produce different variations and show underlining interactions with other cutting parameters. Results of surface roughness measurements indicated a rise in roughness value with a low depth of cut, and increasing feed. Feed rate was identified as influential towards high surface accuracy based on significant changes it has on the cutting tool chip. Conclusively, it could be said that force sensor positioning had negligible interference in force recordings. However, extensive amounts of cutting parameter combinations need to be done to adequately model cutting force influence in diamond machining.

In addition, tribocharging is an important factor in polymer machining. This phenomenon is linked to cutting parameters and relative humidity. It could rise to magnitudes as high as 22kV and could be the cause for severe wear formation in diamond tooling. It was concluded that at high humidity, low feeds and high depth of cuts produced higher static charges while at moderate humidity levels, speed and depth of cut had greater influence. This was solely attributed to changing conditions in ion conductivity during machining process. Therefore, it can be concluded that humidity greatly affects the top surface of the lens and its air-borne discharge rate, creating a less effective rubbing action at faster speed and feed.

From the MD study a clearer understanding is achieved of sub-structural effects during nanometric machining. These simulations were able to reproduce an actual MD investigation into nanoscale machining of polymers. Results of the force components during initial simulated cutting reflected similar values as seen in section 4-2. An evaluation into sub-surface microstructural phenomena during nanometric machining reinforced known orthogonal theory of sub-surface effects as caused from high compressive forces in the cutting zone leading to an increase in temperature and transition in material state, Potential energy release from the simulated system also provided results which correspond to an increased scission of molecular chains presumed to reflect the generation of tool chip. Furthermore, increased rubbing action between tool and workpiece may reflect on the high electrostatics previously addressed in Section 4.4.

From all these conclusions, it can be generally concluded that in all experimental tests to achieve highest quality finish in optical manufacture, the feed rate would be seen as a vital factor to be considered in a factory-conditioned environment.

Recommendation

In spite of an enormous amount of work carried out in this study, there remain some aspects that would require further investigation. These include:

- The need to ascertain level of influence of the feed rate on output quality within a wider range of cutting parameters;
- Further study into the UHPM of polymers should consider a wider range of polymer types based on their Food and Drug Administration classifications and area of application within the society;
- Further experimentation for an adequate model of cutting force could provide initial ground for the introduction of an automated force-controlled manufacturing system;
- Analysis of the influence of cutting parameters on temperature occurring during polymer machining on the tool flank;
- A classification of polymers into triboelectric magnitude generated during polymer machining could greatly improve costs in general polymer cutting and save tool cost.

These in addition to the work completed in this study would constitute a comprehensive study on the ultra-high precision machining of contact lens polymers. This research as mentioned earlier could provide a ground for the establishing of a customised design contact lens based on racial specifications for the African populace. Therefore, the need to design an optical equation based on racial profiles and manufacturing based on the research specifications given in this study would create both a local and an affordable solution to the creation of an African contact lens.

References

1. Refojo MF, editor Polymers and devices in ophthalmology. Biomedical Engineering Conference; 1995 7-9 Apr 1995; Shreveport, Louisiana: IEEE.
2. Gupta H, Aqil M. Contact lenses in ocular therapeutics. Drug discovery today. May 2012;17(9-10):522-7.
3. Heinrich M, Wildsmith C, editors. Need for precision engineering in astigmatic contact lenses. Proceedings of the ASPE Topical Meeting on Freeform Optics; 2004.
4. Mamalis AG, Lavrynenko SN. On the precision single-point diamond machining of polymeric materials. J Mater Process Tech. 2007 Jan 1;181(1-3):203-5. PubMed PMID: ISI:000241963900041. English.
5. Taniguchi N, editor On the basic concept of nanotechnology. Proceedings of the International Conference of Production Engineering 1974; Tokyo, Part II: Japan Society of Precision Engineering.
6. Pawade KJR, Balasubramaniam R, editors. Some investigations on surface characteristics in precision turning of nylon and polypropylene. 1st International Conference on Recent Trends in Engineering & Technology, ; 2012 March Special Issue of International Journal of electronics, Communication & Soft Computing Science & Engineering.
7. Saini V, Sharma D, Kalla S, Chouhan T. Optimisation of process parameter in ultra-precision diamond turning of polycarbonate material. International Conference on Manufacturing Excellence, MANFEX 2012; 29-30 March, 2012; Noida, India2012.
8. Venkatesh VC. Precision manufacture of spherical and aspheric surfaces on plastics, glass, silicon and germanium. Curr Sci India. 2003 May 10;84(9):1211-9. PubMed PMID: ISI:000183086000021. English.
9. Gubbels GPH. Diamond turning of glassy polymers [Doctoral thesis]: Technische Universiteit Eindhoven; 2006.
10. Barr J, MS F. Contact Lens Spectrum's annual report of major corporate and product developments and events in the contact lens industry in 2004, as well as predictions for 2005 [article on the Internet cited on 2006 March 3] 2005.

11. Nichols JJ. Annal report: Contact lenses 2011. Contact Lens Spectrum. 2012;27 (January 2012):20 - 5.
12. Brinksmeier E, Glaebe R, Osmer J. Surface integrity demands of high precision optical molds and realization by a new process chain. Procedia Engineering. 2011;19:40-3.
13. Oluwajobi AO. Nanomachining technology development [Doctorate thesis]: University of Huddersfield; 2012.
14. Ramsden J, Allen D, Stephenson D, Alcock J, Peggs G, Fuller G, et al. The design and manufacture of biomedical surfaces. CIRP Annals-Manufacturing Technology. 2007;56(2):687-711.
15. Apple DJ, Ram J, Foster A, Peng Q. Evolution of cataract surgery and intraocular lenses (IOLs): IOL quality. Survey of Ophthalmology. 2000;45, Supplement 1(0):S53-S69.
16. Nicolson PC, Vogt J. Soft contact lens polymers: an evolution. Biomaterials. 2001 Dec;22(24):3273-83. PubMed PMID: ISI:000171759500008. English.
17. Lloyd AW, Faragher RGA, Denyer SP. Ocular biomaterials and implants. Biomaterials. 2001 April;22(8):769-85. PubMed PMID: ISI:000167120000003. English.
18. Efron N. Contact lens practice. Second ed: Elsevier Health Sciences; 2010.
19. Hough D. Contact lens standards. Contact Lens and Anterior Eye. 1998;21(Supplement 1):S41-S5.
20. Rattier BD, Hoffman AS, Schoen FJ, Lemons JE. Biomaterials science: an introduction to materials in medicine. Journal of Clinical Engineering. 1997;22(1):26.
21. Maldonado-Codina C, Efron N. Hydrogel lenses-material and manufacture: A review. Optometry in Practice. 2003;4:101-15.
22. Brievogel S. A primer on contact lens polymer. Eyewitness Second quarter - A publication of the Contact lens Society of America. 2002:32-5.
23. Snyder C. A primer on contact lens materials. Contact Lens Spectrum. 2004;19(2):34-9.
24. Giedd B. Understanding the nuances of contact lens materials. Contact lens Spectrum. 1999;14:23-8.
25. Optical Filters: ADC cast optical sheet: Optical Polymer International; 2009. Available from: <http://alcat.typepad.com/opi/display--readout-windows--->

[optical--filters-----adc-cast-optical-sheet-display-applications----the--continual-adv.html](#).

26. Cavagnaro JM. Polymer optics: Progress in plastic optics follows advances in materials and manufacturing 2011. Available from: <http://www.laserfocusworld.com/articles/print/volume-47/issue-9/features/polymer-optics-progress-in-plastic-optics-follows-advances-in-materials-and-manufacturing.html>.
27. Heinrich M, Wildsmith C, editors. Need for precision engineering in astigmatic contact lenses 2004.
28. Bennett ES, Weissman BA. Clinical contact lens practice: Lippincott Williams & Wilkins; 2005.
29. Selby AP. Nanoindentation of soft contact lens materials [Doctorate thesis]: The University of Manchester; 2012.
30. Dick L, Risse S, Tünnermann A. Injection molded high precision freeform optics for high volume applications. Advanced Optical Technologies. 2012;1(1):39-50.
31. Chunning Huang MS. Investigation of injection molding process for high precision polymer lens manufacturing [Doctorate Thesis]. Ohio: The Ohio State University; 2008.
32. Chiu W, Lee W. Development of ultra-precision machining technology. Fifth International Conference on FACTORY 2000 - The Technology Exploitation Process; 2-4 April 1997; Cambridge, UK 1997. p. 486 – 90.
33. Hsu A. The development of ultra-precision machining technology in ITRC. In: Center ITR, editor. Presentation. Port-Elizabeth: National Applied Research Laboratories; 2013.
34. Riemer O, editor Advances in ultraprecision manufacturing. Proceedings of Japan Society of Precision Engineers; 2011.
35. Chapman G. Ultra-precision machining systems; an enabling technology for perfect surfaces. Moore Nanotechnology Systems. 2004.
36. Bylinsky G. Closing In on perfection: Ultraprecision machine tools are putting manufacturers within nanometers of absolute accuracy 2003 28th January, 2014. Available from: http://money.cnn.com/magazines/fortune/fortune_archive/2003/06/23/344598/

37. Freedonia.Market.Research. World Machine Tools to 2014: Alacra Store; Apr 01, 2011 [Feb 19, 2014]. Available from:
<http://www.alacrastore.com/storecontent/Freedonia-Market-Research/World-Machine-Tools-to-2014-2039-427>.
38. Franse J. Manufacturing techniques for complex shapes with submicron accuracy. Reports on Progress in Physics. 1990;53(8):1049.
39. Davies MA, Evans CJ, Vohra RR, Bergner BC, Patterson SR, editors. Application of precision diamond machining to the manufacture of microphotronics components. Optical Science and Technology, SPIE's 48th Annual Meeting; 2003: International Society for Optics and Photonics.
40. Contour Fine Tooling. Diamond tools for contact lenses and IOL's2008. Available from: <http://www.contour-diamonds.com/en/about-us/brochures/>.
41. Gauthier C, Lafaye S, Schirrer R. Elastic recovery of a scratch in a polymeric surface: experiments and analysis. Tribology International. 2001;34(7):469-79.
42. Friedrich K, Sue H, Liu P, Almajid A. Scratch resistance of high performance polymers. Tribology International. 2011;44(9):1032-46.
43. Lane B, Dow T, Scattergood R. Thermo-chemical wear model and worn tool shapes for single-crystal diamond tools cutting steel. Journal of Wear. 2013;300(1):216-24.
44. Abou-El-Hossein K, Olufayo O, Mkoiko Z. Diamond tool wear during ultra-high precision machining of rapidly solidified aluminium RSA 905. Journal of Wear. 2013 Apr-May;302(1-2):1105-12. PubMed PMID: ISI:000322682800032. English.
45. Gubbels GPH, van der Beek GJFT, Hoep AL, Delbressine FLM, van Halewijn H. Diamond tool wear when cutting amorphous polymers. Cirp Annals-Manufacturing Technology. 2004;53(1):447-50. PubMed PMID: ISI:000222519700106. English.
46. Shi M. Thermo-chemical tool wear in orthogonal diamond cutting steel and stainless steel [Master's dissertation]: North Carolina State University; 2010.
47. Jasinevicius RG, Duduch JG, Porto AJ. Investigation on diamond turning of silicon crystal-generation mechanism of surface cut with worn tool. Journal of the Brazilian Society of Mechanical Sciences. 2001;23(2):241-52.

48. Abdel-Aal HA, Smith ST, Patten JA. On the development of surface temperatures in precision single-point diamond abrasion of semiconductors. *International Communications in Heat and Mass Transfer*. 1997;24(8):1131-40.
49. Hurt H, Decker D, editors. Tribological considerations of the diamond single-point tool. 28th Annual Technical Symposium; 1984: International Society for Optics and Photonics.
50. Shin I. Cutting-temperature measurement by means of photodiodes in diamond turning of hard alloys. *Measurement Techniques*. 1984;27(10):899-901.
51. Ueda T, Sato M, Nakayama K. The temperature of a single crystal diamond tool in turning. *Cirp Annals-Manufacturing Technology*. 1998;47(1):41-4.
52. Overcash JL, Cuttino JF. In-process modeling of dynamic tool-tip temperatures of a tunable vibration turning device operating at ultrasonic frequencies. *Precision Engineering*. 2009;33(4):505-15.
53. Goel S, Luo X, Reuben RL. Wear mechanism of diamond tools against single crystal silicon in single point diamond turning process. *Tribology International*. 2013;57:272-81.
54. Gubbels G, Van Der Beek G, Hoep A, Delbressine F, Van Halewijn H. Diamond tool wear when cutting amorphous polymers. *CIRP Annals-Manufacturing Technology*. 2004;53(1):447-50.
55. Olufayo OA, Abou-El-Hossein K, editors. Preliminary Investigation of surface finish of a contact lens polymer in ultra-precision diamond turning. 6th Robotics and Mechatronics Conference (RobMech); 2013; Durban, South Africa, October 30-31, 2013.
56. Contour Fine Tooling. Diamond tool wear during cutting of plastics 2008. Available from:
http://www.zimmerman.com.tw/download2.asp?file=uploads/07_cuttingplastic.pdf.
57. Zhou M, Ngoi B, Yusoff M, Wang X. Tool wear and surface finish in diamond cutting of optical glass. *J Mater Process Tech*. 2006;174(1):29-33.
58. Rhorer RL, Evans CJ. Fabrication of optics by diamond turning. *Handbook of Optics*. 1995:41.1-.13.

59. Olufayo O, Abou-El-Hossein K, Kadernani M. Tribo-electric Charging in the Ultra-high Precision Machining of Contact Lens Polymers. *Procedia Materials Science*. 2014;6:194-201.
60. Kaplan A, McReynolds B, Selvaduray G. Dielectric characteristics of materials-electrostatic discharge. *Experimental Methods In Materials Engineering*. November 2002.
61. Williams MW, editor Mechanisms of triboelectric charging of insulators, a coherent scenario. Proceedings of ESA Annual Meeting on Electrostatics 2011 June 14-16, 2011; Case Western Reserve University, Cleveland OH: Electrostatic Society of America.
62. Liu L, Seyam AM, Oxenham W. Frictional electrification on polymeric flat surfaces. *Journal of Engineered Fibers and Fabrics*. 2013;8(1):126 -36.
63. Jasti VK. Electrostatic charge generation and dissipation on woven fabrics treated with antistatic and hydrophilic surface finishes [Doctorate thesis]: North Carolina State University; 2012.
64. Williams MW. Triboelectric charging of insulating polymers—some new perspectives. *AIP Advances*. 2012;2(1):-.
65. Asuni N. Introduction to static electricity: An introduction to ESD Technick.net - Electronic Hardware Information, Guides and Tools1998 [15th November, 2013]. Available from: http://www.technick.net/public/code/cp_dpage.php?aiocp_dp=guide_esd_001.
66. Gubbels G, van der Beek G, Delbressine F, Schellekens P, editors. Electrostatic tool wear in diamond turning of amorphous polymers. Euspen international conference; 2004; Glasgow, Scotland, UK: European Society of Precision Engineers.
67. Mason GW, Griffen DT, Merrill JJ, Thorne JM. Physical science concepts Brigham Young University Print Services; 1997.
68. Diaz A, Felix-Navarro R. A semi-quantitative tribo-electric series for polymeric materials: the influence of chemical structure and properties. *Journal of Electrostatics*. 2004;62(4):277-90.
69. Xie L, Han K. Influence of relative humidity on the aeolian electric field. *Aeolian Research*. 2012;7:45-50.
70. Carr JW, Feger C. Ultraprecision machining of polymers. *Journal of Precision Engineering*. 1993;15(4):221-37.

71. Khan GS. Characterization of surface roughness and shape deviations of aspheric surfaces [Doctoral Thesis]: Friedrich-Alexander-Universität Erlangen-Nürnberg; 2008.
72. Gubbels GP, Delbressine F, Govaert L, Schellekens PH, editors. Precision cutting of glassy polymers: influence of aging on the cutting process. Optical Systems Design; 2004: International Society for Optics and Photonics.
73. Roblee J. Factors affecting surface finish in diamond turning: Precitech, Inc; 2007. Available from: http://www.precitech.com/about/white_papers.html.
74. Ghosh R, Knopf JA, Gibson DJ, Mebrahtu T, Currie G, editors. Cryogenic machining of polymeric biomaterials: An intraocular lens case study. Medical Device Materials IV: Proceedings of the Materials & Processes for Medical Devices Conference 2007, September 23-27, 2007, Palm Desert, California, USA; 2008: ASM International.
75. CSM. Atomic Force Microscope (AFM): CSM instruments; 2013 [cited 2013 8th May]. Available from: <http://www.csm-instruments.com/en/Atomic-Force-Microscope>.
76. Li L. Investigation of the optical effects of single point diamond machined surfaces and the applications of micro machining [Doctorate thesis]: The Ohio State University; 2009.
77. Whitehouse DJ. Handbook of surface metrology: CRC Press; 1994.
78. Dandekar CR, Shin YC. Modeling of machining of composite materials: a review. International Journal of Machine Tools and Manufacture. 2012;57:102-21.
79. Dandekar CR, Shin YC. Multiphase finite element modeling of machining unidirectional composites: prediction of debonding and fiber damage. Journal of Manufacturing Science and Engineering. 2008;130(5):051016.
80. Goggins DA. Response surface methods applied to submarine concept exploration [Master's dissertation]: Massachusetts Institute of Technology; 2001.
81. Minbo C. Study of nanoscale ductile mode cutting of silicon using molecular dynamics simulation [Doctorate thesis]: National university of Singapore; 2008.
82. Olufayo OA, Abou-El-Hossein K. Molecular dynamics modeling of nanoscale machining of silicon. Procedia CIRP. 2013;8:503-8.

83. Oluwajobi A, Chen X. The effect of interatomic potentials on the molecular dynamics simulation of nanometric machining. *International Journal of Automation and Computing*. 2011;8(3):326-32.
84. Oluwajobi A. Molecular dynamics simulation of nanoscale machining. In: Wang PL, editor. *Molecular dynamics - Studies of synthetic and biological macromolecules*: InTech Publishers; 2012.
85. Oluwajobi AO, Chen X, editors. The effect of depth of cut on the molecular dynamics (MD) simulation of multi-pass nanometric machining. 17th International Conference on Automation and Computing (ICAC); 2011: IEEE.
86. Oluwajobi AO, Chen X, editors. The effect of interatomic potentials on nanometric abrasive machining. *Proceedings of the 16th International Conference on Automation & Computing*; 2010; University of Birmingham, Birmingham: Chinese Automation and Computing Society in the UK.
87. Aly MF, Eugene N, Veldhuis SC. Cutting force prediction using molecular dynamics assisted finite element simulation model. 19th Annual meeting of American Society for precision Engineers (ASPE); Orlando, Florida: American Society for precision Engineers (ASPE); 2004.
88. De Chiffre L, Kunzmann H, Peggs G, Lucca D. Surfaces in precision engineering, microengineering and nanotechnology. *Cirp Annals-Manufacturing Technology*. 2003;52(2):561-77.
89. Cai MB, Li XP, Rahman M. Study of the mechanism of nanoscale ductile mode cutting of silicon using molecular dynamics simulation. *International Journal of Machine Tools and Manufacture*. 2007;47(1):75-80.
90. Chang W-Y, Fang T-H, Lin S-J, Huang J-J. Nanoindentation response of nickel surface using molecular dynamics simulation. *Molecular Simulation*. 2010;36(11):815-22.
91. Sushko G, Verkhovtsev A, Yakubovich A, Solov'yov A, editors. Molecular dynamics simulation of nanoindentation of nickel-titanium crystal. *Journal of Physics: Conference Series*; 2013: IOP Publishing.
92. Lai M, Zhang X, Fang F, Wang Y, Feng M, Tian W. Study on nanometric cutting of germanium by molecular dynamics simulation. *Nanoscale Research Letters*. 2013;8(1):1-10.
93. Zhu P, Fang F. Molecular dynamics simulations of nanoindentation of monocrystalline germanium. *Applied Physics A*. 2012;108(2):415-21.

94. Chen YH, Fang FZ, Zhang XD, Hu XT. Molecular dynamics investigation of cutting force in nanometric cutting of monocrystalline silicon. *American Journal of Nanotechnology*. 2010;1(2):62-7.
95. Komanduri R, Chandrasekaran N, Raff LM. Effect of tool geometry in nanometric cutting: a molecular dynamics simulation approach. *Journal of Wear*. 1998;219(1):84-97.
96. Goel S, Luo X, Reuben RL, Rashid WB. Atomistic aspects of ductile responses of cubic silicon carbide during nanometric cutting. *Nanoscale Research Letters*. 2011;6(1):1-9.
97. Arefin S, Li X, Cai M, Rahman M, Liu K, Tay A. The effect of the cutting edge radius on a machined surface in the nanoscale ductile mode cutting of silicon wafer. *Proceedings of the Institution of Mechanical Engineers, Part B: Journal of Engineering Manufacture*. 2007;221(2):213-20.
98. Fang T-H, Wu J-H. Molecular dynamics simulations on nanoindentation mechanisms of multilayered films. *Computational Materials Science*. 2008;43(4):785-90.
99. Harmandaris VA. Atomistic molecular dynamics simulations of polymer melt viscoelasticity [Doctorate thesis]: University of Patras; 2001.
100. Rocha JR, Yang KZ, Hilbig T, Brostow W, Simoes R. Polymer indentation with mesoscopic molecular dynamics. *Journal of Materials Research*. 2013;28(21):3043-52.
101. Starr FW, Schröder TB, Glotzer SC. Molecular dynamics simulation of a polymer melt with a nanoscopic particle. *Macromolecules*. 2002;35(11):4481-92.
102. Chen Y-C, Nomura K-i, Kalia RK, Nakano A, Vashishta P. Molecular dynamics nanoindentation simulation of an energetic material. *Applied Physics Letters*. 2008;93(17):171908.
103. Promyoo R. Molecular dynamics simulation of nanometric machining under realistic cutting conditions using LAMMPS: Purdue University; 2008.
104. Plimpton S. LAMMPS user's manual. Sandia National Laboratory. 2005.
105. Allen MP. Introduction to molecular dynamics simulation. *Computational Soft Matter: From Synthetic Polymers to Proteins*. 2004;23:1-28.

106. Rasmussen WLC. Novel carbazole based methacrylates, acrylates, and dimethacrylates to produce high refractive index polymers [Doctorate thesis]: Virginia Polytechnic Institute and State University; 2001.
107. Brar A, Singh G, Shankar R. Structural investigations of poly (methyl methacrylate) by two-dimensional NMR. *Journal of Molecular Structure*. 2004;703(1):69-81.
108. Souto-Maior R, Tavares M, Monteiro E. Solid State ¹³C NMR study of methyl methacrylate-methacrylic acid Copolymers. *Ann Magn Reson* 2005 4(3):69-72.
109. Uhlig F, Marsmann HC. ²⁹ Si NMR some practical aspects. Available from: <http://www.pascal-man.com/periodic-table/29Si.pdf>.
110. Shimada S, Ikawa N. Molecular dynamics analysis as compared with experimental results of micromachining. *CIRP Annals-Manufacturing Technology*. 1992;41(1):117-20.
111. Rentsch R, Inasaki I. Molecular dynamics simulation for abrasive processes. *CIRP Annals-Manufacturing Technology*. 1994;43(1):327-30.
112. Komanduri R, Chandrasekaran N, Raff L. Some aspects of machining with negative-rake tools simulating grinding: a molecular dynamics simulation approach. *Philosophical Magazine B*. 1999;79(7):955-68.
113. Shimada S, Tanaka H, Ikawa N, editors. Atomistic mechanism of surface generation in micromachining of monocrystalline silicon. *Proceedings of 1st International Conference of the European Society for Precision Engineering and Nanotechnology 1999*; Bremen, Germany: European Society for Precision Engineering (euspen).
114. Han X, Lin B, Yu S, Wang S. Investigation of tool geometry in nanometric cutting by molecular dynamics simulation. *J Mater Process Tech*. 2002;129(1):105-8.
115. Ye Y, Biswas R, Morris J, Bastawros A, Chandra A, editors. Simulation of nanoscale polishing of copper with molecular dynamics. *MRS Proceedings*; 2002; San Francisco, California: Cambridge Univ Press.
116. Lin B, Yu S, Wang S. An experimental study on molecular dynamics simulation in nanometer grinding. *J Mater Process Tech*. 2003;138(1):484-8.
117. Cheng K, Luo X, Ward R, Holt R. Modeling and simulation of the tool wear in nanometric cutting. *Journal of Wear*. 2003;255(7):1427-32.

118. Rentsch R, Inasaki I. Effects of fluids on the surface generation in material removal processes:—molecular dynamics simulation—. *CIRP Annals-Manufacturing Technology*. 2006;55(1):601-4.
119. Shimizu J, Zhou L, Eda H. Molecular dynamics simulation of vibration-assisted cutting: influences of vibration, acceleration and velocity. *International Journal of Nanomanufacturing*. 2006;1(1):105-16.
120. Pei Q, Lu C, Fang F, Wu H. Nanometric cutting of copper: a molecular dynamics study. *Computational Materials Science*. 2006;37(4):434-41.
121. Cai MB, Li XP, Rahman M. Characteristics of "dynamic hard particles" in nanoscale ductile mode cutting of monocrystalline silicon with diamond tools in relation to tool groove wear. *Journal of Wear*. 2007 Sep 10;263:1459-66. PubMed PMID: ISI:000249754500077. English.
122. Shimizu J, Zhou L, Eda H. Molecular dynamics simulation of effect of grinding wheel stiffness on nanogrinding process. *International Journal of Abrasive Technology*. 2008;1(3):316-26.
123. Noreyan A, Amar J. Molecular dynamics simulations of nanoscratching of 3C SiC. *Journal of Wear*. 2008;265(7):956-62.
124. Du K, Tang Y, Zhang J, Xu F, Yan Y, Sun T. Velocity-dependent nanoscratching of amorphous polystyrene. *Current Nanoscience*. 2013;9(1):153-8.
125. Sun J, Fang L, Han J, Han Y, Chen H, Sun K. Abrasive wear of nanoscale single crystal silicon. *Journal of Wear*. 2013;307(1):119-26.
126. Schlick T. *Molecular Modeling and Simulation: An Interdisciplinary Guide: An Interdisciplinary Guide*: Springer Science & Business Media; 2010.
127. Bicerano J. *Computational modeling of polymers*: CRC press; 1992.
128. Arab B, Shokuhfar A. Molecular dynamics simulation of cross-linked epoxy polymers: the effect of force field on the estimation of properties. *Journal of Nano-& Electronic Physics*. 2013;5(1).
129. Komanduri R, Raff L. A review on the molecular dynamics simulation of machining at the atomic scale. *Proceedings of the Institution of Mechanical Engineers, Part B: Journal of Engineering Manufacture*. 2001;215(12):1639-72.
130. Han XS, Hu YZ, Yu S. Molecular dynamics analysis micro-mechanism of ductile machining single crystal silicon by means of nanometric cutting

- technology. *Eur Phys J-Appl Phys*. 2008 Jun;42(3):255-62. PubMed PMID: ISI:000257337500012. English.
131. Aziz RA. A highly accurate interatomic potential for argon. *The Journal of Chemical Physics*. 1993;99(6):4518-25.
 132. Rzepa HS. The theory of conformational analysis 2010 [cited 2014 13th June]. Available from:
http://www.ch.ic.ac.uk/local/organic/conf/c1_theory.html#a1.
 133. Fang T-H, Chang W-J. Effects of AFM-based nanomachining process on aluminum surface. *Journal of Physics and chemistry of Solids*. 2003;64(6):913-8.
 134. Risbood KA, Dixit US, Sahasrabudhe AD. Prediction of surface roughness and dimensional deviation by measuring cutting forces and vibrations in turning process. *J Mater Process Tech*. 2003 1/10;132(1-3):203-14.
 135. de Agustina B, Rubio E, Sebastián M. Surface roughness model based on force sensors for the prediction of the tool wear. *Sensors*. 2014;14(4):6393-408. PubMed PMID: doi:10.3390/s140406393.
 136. Molinari A, Moufki A. The merchant's model of orthogonal cutting revisited: A new insight into the modeling of chip formation. *International Journal of Mechanical Sciences*. 2008;50(2):124-31.
 137. Xiao K, Zhang L. The role of viscous deformation in the machining of polymers. *International journal of mechanical sciences*. 2002;44(11):2317-36.
 138. Luo X, Cheng K, Holt R, Liu X. Modeling flank wear of carbide tool insert in metal cutting. *Journal of Wear*. 2005;259(7):1235-40.
 139. SMC. Electrostatic sensor monitor Series IZD10 user manual. 2013.
 140. Cheung C, Lee W. Study of factors affecting the surface quality in ultra-precision diamond turning. *Materials and Manufacturing Processes*. 2000;15(4):481-502.
 141. Jasinevicius R, De Campos G, Montanari L, Tsukamoto R, Garcia J, Camargo R, et al. Influence of the mechanical and metallurgical state of an Al-Mg alloy on the surface integrity in ultraprecision machining. *Journal of the Brazilian Society of Mechanical Sciences and Engineering*. 2003;25(3):222-8.
 142. Hwang T-W, Zhang G. Analysis of elastoplastic deformation observed on machined surfaces. 1993.

143. Qu J, Shih AJ. Analytical surface roughness parameters of a theoretical profile consisting of elliptical arcs. *Machining science and technology*. 2003;7(2):281-94.
144. Toenshoff HK, Denkena B. *Basics of cutting and abrasive processes*: Springer; 2013.
145. Zhang G, To S. A novel surface quality evaluation method in ultra-precision raster milling using cutting chips. *J Mater Process Tech*. 2014.
146. Sheikh-Ahmad JY. *Machining of polymer composites*: Springer; 2009.
147. Goel S, Luo X, Agrawal A, Reuben RL. Diamond machining of silicon: A review of advances in molecular dynamics simulation. *International Journal of Machine Tools and Manufacture*. 2015;88:131-64.
148. Nakasuji T, Koderu S, Hara S, Matsunaga H, Ikawa N, Shimada S. Diamond turning of brittle materials for optical components. *CIRP Annals-Manufacturing Technology*. 1990;39(1):89-92.
149. Cai M, Li X, Rahman M, Tay A. Crack initiation in relation to the tool edge radius and cutting conditions in nanoscale cutting of silicon. *International Journal of Machine Tools and Manufacture*. 2007;47(3):562-9.
150. Schneider F, Lohkamp R, Sousa F, Müller R, Aurich J. Analysis of the Surface Integrity in Ultra-precision Cutting of Cp-titanium by Investigating the Chip Formation. *Procedia CIRP*. 2014;13:55-60.
151. Cristino V, Rosa P, Martins P. Cutting under active and inert gas shields: A contribution to the mechanics of chip flow. *International Journal of Machine Tools and Manufacture*. 2010;50(10):892-900.
152. Jawahir I, Van Luttervelt C. Recent developments in chip control research and applications. *CIRP Annals-Manufacturing Technology*. 1993;42(2):659-93.
153. Salem SB, Bayraktar E, Boujelbene M, Katundi D. Effect of cutting parameters on chip formation in orthogonal cutting. *Journal of Achievements in Materials and manufacturing Engineering*. 2012;50(1):7-17.
154. Komanduri R, Brown R. On the mechanics of chip segmentation in machining. *Journal of Manufacturing Science and Engineering*. 1981;103(1):33-51.
155. Fetecau C, Stan F. Study of cutting force and surface roughness in the turning of polytetrafluoroethylene composites with a polycrystalline diamond tool. *Measurement*. 2012;45(6):1367-79.

156. Lin WS, Lee BY, Wu CL. Modeling the surface roughness and cutting force for turning. *J Mater Process Tech.* 2001;108(3):286-93.
157. Özel T, Hsu T-K, Zeren E. Effects of cutting edge geometry, workpiece hardness, feed rate and cutting speed on surface roughness and forces in finish turning of hardened AISI H13 steel. *Int J Adv Manuf Technol.* 2005 2005/02/01;25(3-4):262-9. English.
158. Sheikh-Ahmad J, McKenzie W, editors. Measurement of tool wear and dulling in the machining of particleboard. *Proceedings of the 13th International Wood Machining Seminar, Vancouver, Canada; 1997.*

Publications

1. **O.A. Olufayo**, K. Abou-El-Hossein, Molecular dynamics modelling of nanoscale machining of silicon, *Procedia CIRP*, Volume 8, 2013, Pages 504-509, ISSN 2212-8271, <http://dx.doi.org/10.1016/j.procir.2013.06.141>. (<http://www.sciencedirect.com/science/article/pii/S2212827113004186>)
2. **Olufayo, O.A**; Abou-El-Hossein, K., "Preliminary investigation of surface finish of a contact lens polymer in ultra-high precision diamond turning," *Robotics and Mechatronics Conference (RobMech)* , Durban South-Africa, 2013 6th , vol., no., pp.117,122, 30-31 Oct. 2013, <http://dx.doi.org/10.1109/RoboMech.2013.6685502><http://ieeexplore.ieee.org/stamp/stamp.jsp?tp=&arnumber=6685502&isnumber=6685470>
3. **O.A. Olufayo**, K. Abou-El-Hossein, M.M. Kadernani, Tribo-electric Charging in the Ultra-high Precision Machining of Contact Lens Polymers, *Procedia Materials Science*, Volume 6, 2014, Pages 194-201, ISSN 2211-8128, <http://dx.doi.org/10.1016/j.mspro.2014.07.024>. (<http://www.sciencedirect.com/science/article/pii/S2211812814003897>)
4. Yuan-Chieh Cheng; Wei-Yao Hsu; Khaled Abou-El-Hossein; **O.A. Olufayo**; Timothy Otieno, Investigation of diamond turning: of rapidly-solidified aluminium alloys, *Proceedings. SPIE 9192*, Vol. 9192: Current Developments in Lens Design and Optical Engineering X, Current Developments in Lens Design and Optical Engineering XV, 919214; <http://dx.doi.org/10.1117/12.2060176>
5. K. Abou-El-Hossein, **O.A. Olufayo**, Z. Mkoko, Performance of diamond inserts in ultra-high precision turning of Cu₃Cr₃Zr alloy, *Wear*, Volume 302, Issues 1–2, April–May, 2013, Pages 1098-1104, ISSN 0043-1648, <http://dx.doi.org/10.1016/j.wear.2013.01.062>. (<http://www.sciencedirect.com/science/article/pii/S0043164813000847>)
6. K. Abou-El-Hossein, **O.A. Olufayo**, Z. Mkoko, Diamond tool wear during ultra-high precision machining of rapidly solidified aluminium RSA 905, *Wear*, Volume 302, Issues 1–2, April–May 2013, Pages 1105-1112, ISSN 0043-1648, <http://dx.doi.org/10.1016/j.wear.2012.12.060>. (<http://www.sciencedirect.com/science/article/pii/S0043164813000100>)
7. K. Abou-El-Hossein, **O.A. Olufayo**, Diamond Machining of Rapidly Solidified Aluminium for Optical Mould Inserts, *Procedia Materials Science*, Volume 6, 2014, Pages 1077-1082, ISSN 2211-8128, <http://dx.doi.org/10.1016/j.mspro.2014.07.178>. (<http://www.sciencedirect.com/science/article/pii/S2211812814005434>)

8. Ayomoh, M.K.O.; Abou-El-Hossein, K.A; **Olufayo, O.A**, "Cutting force prediction for single point diamond tool-tip," Robotics and Mechatronics Conference (RobMech), Durban South-Africa, 2013 6th , vol., no., pp.123,128, 30-31 Oct. 2013, <http://dx.doi.org/10.1109/RoboMech.2013.6685503><http://ieeexplore.ieee.org/stamp/stamp.jsp?tp=&arnumber=6685503&isnumber=6685470>
9. **O. A. Olufayo**, K. Abou-El-Hossein, Predictive modelling of cutting force and its influence on surface accuracy in Ultra-high precision machining of contact lenses, 15th CIRP Conference On Modelling Of Machining Operations, Karlsruhe, Germany 11 – 12 June 2015 (*Published to be linked online*)
<http://dx.doi.org/10.1016/j.procir.2015.03.042>
10. **O. A. Olufayo**, K. Abou-El-Hossein, Evolution of high precision contact lens manufacturing and its application of light metals, 7th Light Metals Technology (LMT) conference - 27 July, 2015 . DOI: [10.4028/www.scientific.net/MSF.828-829.374](http://dx.doi.org/10.4028/www.scientific.net/MSF.828-829.374)

Appendix A: Ultra-precision G-code

```
;DIFFSYS Version 3.92 jobfile:
;Technical Support : contact info@westernisle.com
;DSF file          : [unsaved]
;Created           : Monday, April 29, 2013 12:58
;Units            : mm
;Z Offset          : 0.00000 mm
;Reference Point   : Front-most point
;Tool Radius       : 0.5 mm
;Rake Angle        : 0.000 degrees
;Tilt Angle        : 15.000 degrees
;Orientation       : 0.000 degrees
;X-axis direction  : Edge to Center
;Spindle direction : Clockwise X coordinates are +ve
;Design type       : 2D Flat
;
;P1 = depth of cut
;P2 = no of cycles
;P43 = offset of cut depths
;P44 = pass counter
;
P1=0.040
P2=100
;
;watch:p44=pass counter
;watch:p2=# of cycles
;
;----- PART INFO DATA -----
;CUSTOM DESIGN
;-----
;
;PROLOG data:
G01
G71
G90
T1
G18
M3S200

P44=0
WHILE (P44<P2)
P43=P43-P1
G59Z (P43)
GOSUB1000
```

P44=P44+1
ENDWHILE

M5
EXIT
N1000
X9Z2F200

;End of PROLOG data

```
;
X10.000000Z0.000000 ; 7.000000, 0.000000
F2
X6.900000Z-0.000000 ; 6.900000, 0.000000
X6.800000Z-0.000000 ; 6.800000, 0.000000
X6.700000Z-0.000000 ; 6.700000, 0.000000
X6.600000Z-0.000000 ; 6.600000, 0.000000
X6.500000Z-0.000000 ; 6.500000, 0.000000
X6.400000Z-0.000000 ; 6.400000, 0.000000
X6.300000Z-0.000000 ; 6.300000, 0.000000
X6.200000Z-0.000000 ; 6.200000, 0.000000
X6.100000Z-0.000000 ; 6.100000, 0.000000
X6.000000Z-0.000000 ; 6.000000, 0.000000
X5.900000Z-0.000000 ; 5.900000, 0.000000
X5.800000Z-0.000000 ; 5.800000, 0.000000
X5.700000Z-0.000000 ; 5.700000, 0.000000
X5.600000Z-0.000000 ; 5.600000, 0.000000
X5.500000Z-0.000000 ; 5.500000, 0.000000
X5.400000Z-0.000000 ; 5.400000, 0.000000
X5.300000Z-0.000000 ; 5.300000, 0.000000
X5.200000Z-0.000000 ; 5.200000, 0.000000
X5.100000Z-0.000000 ; 5.100000, 0.000000
X5.000000Z-0.000000 ; 5.000000, 0.000000
X4.900000Z-0.000000 ; 4.900000, 0.000000
X4.800000Z-0.000000 ; 4.800000, 0.000000
X4.700000Z-0.000000 ; 4.700000, 0.000000
X4.600000Z-0.000000 ; 4.600000, 0.000000
X4.500000Z-0.000000 ; 4.500000, 0.000000
X4.400000Z-0.000000 ; 4.400000, 0.000000
X4.300000Z-0.000000 ; 4.300000, 0.000000
X4.200000Z-0.000000 ; 4.200000, 0.000000
X4.100000Z-0.000000 ; 4.100000, 0.000000
X4.000000Z-0.000000 ; 4.000000, 0.000000
X3.900000Z-0.000000 ; 3.900000, 0.000000
X3.800000Z-0.000000 ; 3.800000, 0.000000
X3.700000Z-0.000000 ; 3.700000, 0.000000
X3.600000Z-0.000000 ; 3.600000, 0.000000
```

```

X3.500000Z-0.000000 ; 3.500000, 0.000000
X3.400000Z-0.000000 ; 3.400000, 0.000000
X3.300000Z-0.000000 ; 3.300000, 0.000000
X3.200000Z-0.000000 ; 3.200000, 0.000000
X3.100000Z-0.000000 ; 3.100000, 0.000000
X3.000000Z-0.000000 ; 3.000000, 0.000000
X2.900000Z-0.000000 ; 2.900000, 0.000000
X2.800000Z-0.000000 ; 2.800000, 0.000000
X2.700000Z-0.000000 ; 2.700000, 0.000000
X2.600000Z-0.000000 ; 2.600000, 0.000000
X2.500000Z-0.000000 ; 2.500000, 0.000000
X2.400000Z-0.000000 ; 2.400000, 0.000000
X2.300000Z-0.000000 ; 2.300000, 0.000000
X2.200000Z-0.000000 ; 2.200000, 0.000000
X2.100000Z-0.000000 ; 2.100000, 0.000000
X2.000000Z-0.000000 ; 2.000000, 0.000000
X1.900000Z-0.000000 ; 1.900000, 0.000000
X1.800000Z-0.000000 ; 1.800000, 0.000000
X1.700000Z-0.000000 ; 1.700000, 0.000000
X1.600000Z-0.000000 ; 1.600000, 0.000000
X1.500000Z-0.000000 ; 1.500000, 0.000000
X1.400000Z-0.000000 ; 1.400000, 0.000000
X1.300000Z-0.000000 ; 1.300000, 0.000000
X1.200000Z-0.000000 ; 1.200000, 0.000000
X1.100000Z-0.000000 ; 1.100000, 0.000000
X1.000000Z-0.000000 ; 1.000000, 0.000000
X0.900000Z-0.000000 ; 0.900000, 0.000000
X0.800000Z-0.000000 ; 0.800000, 0.000000
X0.700000Z-0.000000 ; 0.700000, 0.000000
X0.600000Z-0.000000 ; 0.600000, 0.000000
X0.500000Z-0.000000 ; 0.500000, 0.000000
X0.400000Z-0.000000 ; 0.400000, 0.000000
X0.300000Z-0.000000 ; 0.300000, 0.000000
X0.200000Z-0.000000 ; 0.200000, 0.000000
X0.100000Z-0.000000 ; 0.100000, 0.000000
X-0.000000Z-0.000000 ; 0.000000, 0.000000
;
;EPILOG data:
G01
Z0.5
F100Z10M7
X12F200
;End of EPILOG data
ret
;

```

Appendix B: Polymer USAN worksheet

STATEMENT ON A NONPROPRIETARY NAME ADOPTED BY THE USAN COUNCIL

USAN	ROFLUFOCON E
PRONUNCIATION	roe floo foe' kon
INGREDIENT FUNCTION	contact lens material (hydrophobic)
CHEMICAL NAMES	
	1) 2-propenoic acid, 2-methyl-, polymer with 2-hydroxyethyl 2-methyl-2-propenoate, methyl 2-methyl-2-propenoate, 2,2,2-trifluoro-1-(trifluoromethyl)ethyl 2-methyl-2-propenoate and 3-[3,3,3-trimethyl-1,1-bis[(trimethylsilyl)oxy]disiloxanyl]propyl 2-methyl-2-propenoate
	2) 2-methylprop-2-enoic acid polymer with 2-hydroxyethyl 2-methylprop-2-enoate, methyl 2-methylprop-2-enoate, 2,2,2-trifluoro-1-(trifluoromethyl)ethyl 2-methylprop-2-enoate and 3-[3,3,3-trimethyl-1,1-bis[(trimethylsilanyl)oxy]disiloxanyl]propyl 2-methylprop-2-enoate
MOLECULAR FORMULA	$(C_4H_6O_2)_v(C_6H_{10}O_3)_w(C_5H_8O_2)_x$ $(C_7H_6F_6O_2)_y(C_{16}H_{38}O_5Si_4)_z$
TRADEMARK	Contaperm
MANUFACTURER	Contamac Ltd. (England)
WATER CONTENT (at ambient temperature (23±2°C))	<1.0%
OXYGEN PERMEABILITY at 35°C (Dk Value)	130±2 x 10 ⁻¹¹ (cm ² /sec)(ml O ₂ /mlxmm Hg)
CAS REGISTRY NUMBER	583883-80-1

Appendix C: LAMMPS

```
# in.roflufocon
# ----- Initialize Simulation -----
clear
units metal
dimension 3
boundary p p p
atom_style full
bond_style class2
angle_style class2
dihedral_style class2
improper_style class2

pair_style hybrid lj/class2/coul/cut 10.0 tersoff
#echo both

# ----- Create Atoms -----

read_data data1.Roflu

#~~~~~
# New section for boundary concept

region      bott block -4 13 -3 -1 -1 15
region      left block -4 -1 -3 14 -1 15
region      back block -4 13 -3 14 -1 1
region      right block -4 13 13 15 -1 15
region      front block -4 4 -3 14 13 15

region      exc union 5 left bott right back front      # atoms that won't
move
group       mobi union hydrogen carbon oxygen fluorine Silicon

group       exc region exc
group       mob subtract mobi exc      # moveable copper atoms

#group      pin region pin            # indenter

group       bott region bott          # bottom layer
group       right region right        # right layer
group       back region back          # bck layer
group       left region left          # left layer
group       front region front        # side layer

lattice     diamond 3.57
create_atoms 16 region exc

#~~~~~

pair_coeff * * tersoff ../lammops-16Aug12/potentials/SiC.tersoff NULL C C
NULL NULL NULL C NULL NULL NULL C NULL NULL C C C

pair_coeff 1 1 lj/class2/coul/cut 0.0200000000 2.9950000000
pair_coeff 2 2 lj/class2/coul/cut 0.0540000000 4.0100000000
pair_coeff 3 3 lj/class2/coul/cut 0.0540000000 4.0100000000
```

pair_coeff 4 4 lj/class2/coul/cut 0.1200000000 3.8100000000
pair_coeff 5 5 lj/class2/coul/cut 0.2400000000 3.4200000000
pair_coeff 6 6 lj/class2/coul/cut 0.2670000000 3.3000000000
pair_coeff 7 7 lj/class2/coul/cut 0.0540000000 4.0100000000
pair_coeff 8 8 lj/class2/coul/cut 0.0130000000 1.1100000000
pair_coeff 9 9 lj/class2/coul/cut 0.2400000000 3.5350000000
pair_coeff 10 10 lj/class2/coul/cut 0.0130000000 1.0980000000
pair_coeff 11 11 lj/class2/coul/cut 0.0540000000 4.0100000000
pair_coeff 12 12 lj/class2/coul/cut 0.0598000000 3.2000000000
pair_coeff 13 13 lj/class2/coul/cut 0.0700000000 4.2840000000
pair_coeff 14 14 lj/class2/coul/cut 0.2400000000 3.3500000000
pair_coeff 16 16 lj/class2/coul/cut 0.0000000000 0.0000000000

pair_coeff 1 2 lj/class2/coul/cut 0.032863353 3.465537476
pair_coeff 1 3 lj/class2/coul/cut 0.032863353 3.465537476
pair_coeff 1 4 lj/class2/coul/cut 0.048989794 3.378009769
pair_coeff 1 5 lj/class2/coul/cut 0.0692820323 3.200453093
pair_coeff 1 6 lj/class2/coul/cut 0.0730753036 3.143803429
pair_coeff 1 7 lj/class2/coul/cut 0.032863353 3.465537476
pair_coeff 1 8 lj/class2/coul/cut 0.0161245154 1.823307434
pair_coeff 1 9 lj/class2/coul/cut 0.0692820323 3.253816989
pair_coeff 1 10 lj/class2/coul/cut 0.01612451549 1.813424936
pair_coeff 1 11 lj/class2/coul/cut 0.032863353 3.465537476
pair_coeff 1 12 lj/class2/coul/cut 0.0345832329 3.095803611
pair_coeff 1 13 lj/class2/coul/cut 0.0374165738 3.581979899
pair_coeff 1 14 lj/class2/coul/cut 0.06928203230 3.167530584
pair_coeff 1 15 lj/class2/coul/cut 0.2400000000 3.3500000000
pair_coeff 1 16 lj/class2/coul/cut 0.2400000000 3.3500000000

pair_coeff 2 3 lj/class2/coul/cut 0.0540000000 4.0100000000
pair_coeff 2 4 lj/class2/coul/cut 0.080498447 3.908721018
pair_coeff 2 5 lj/class2/coul/cut 0.113841996 3.703268826
pair_coeff 2 6 lj/class2/coul/cut 0.120074977 3.637719066
pair_coeff 2 7 lj/class2/coul/cut 0.0540000000 4.0100000000
pair_coeff 2 8 lj/class2/coul/cut 0.026495283 2.10976302
pair_coeff 2 9 lj/class2/coul/cut 0.113841996 3.7650166
pair_coeff 2 10 lj/class2/coul/cut 0.026495283 2.098327906
pair_coeff 2 11 lj/class2/coul/cut 0.0540000000 4.0100000000
pair_coeff 2 12 lj/class2/coul/cut 0.05682605 3.582178108
pair_coeff 2 13 lj/class2/coul/cut 0.061481705 4.144736421
pair_coeff 2 14 lj/class2/coul/cut 0.113841996 3.665173939
pair_coeff 2 15 lj/class2/coul/cut 0.113841996 3.665173939
pair_coeff 2 16 lj/class2/coul/cut 0.2400000000 3.3500000000

pair_coeff 3 4 lj/class2/coul/cut 0.080498447 3.908721018
pair_coeff 3 5 lj/class2/coul/cut 0.113841996 3.703268826
pair_coeff 3 6 lj/class2/coul/cut 0.120074977 3.637719066
pair_coeff 3 7 lj/class2/coul/cut 0.0540000000 4.0100000000
pair_coeff 3 8 lj/class2/coul/cut 0.026495283 2.10976302
pair_coeff 3 9 lj/class2/coul/cut 0.113841996 3.7650166
pair_coeff 3 10 lj/class2/coul/cut 0.026495283 2.098327906
pair_coeff 3 11 lj/class2/coul/cut 0.0540000000 4.0100000000
pair_coeff 3 12 lj/class2/coul/cut 0.05682605 3.582178108
pair_coeff 3 13 lj/class2/coul/cut 0.061481705 4.144736421
pair_coeff 3 14 lj/class2/coul/cut 0.113841996 3.665173939
pair_coeff 3 15 lj/class2/coul/cut 0.113841996 3.665173939
pair_coeff 3 16 lj/class2/coul/cut 0.2400000000 3.3500000000

pair_coeff 4 5 lj/class2/coul/cut 0.169705627 3.609736833
pair_coeff 4 6 lj/class2/coul/cut 0.178997207 3.545842636

```

pair_coeff 4 7 lj/class2/coul/cut 0.080498447 3.908721018
pair_coeff 4 8 lj/class2/coul/cut 0.039496835 2.056477571
pair_coeff 4 9 lj/class2/coul/cut 0.169705627 3.669925067
pair_coeff 4 10 lj/class2/coul/cut 0.039496835 2.045331269
pair_coeff 4 11 lj/class2/coul/cut 0.080498447 3.908721018
pair_coeff 4 12 lj/class2/coul/cut 0.084711274 3.491704455
pair_coeff 4 13 lj/class2/coul/cut 0.091651514 4.040054455
pair_coeff 4 14 lj/class2/coul/cut 0.169705627 3.572604092
pair_coeff 4 15 lj/class2/coul/cut 0.169705627 3.572604092
pair_coeff 4 16 lj/class2/coul/cut 0.240000000 3.350000000

pair_coeff 5 6 lj/class2/coul/cut 0.253140277 3.359464243
pair_coeff 5 7 lj/class2/coul/cut 0.113841996 3.703268826
pair_coeff 5 8 lj/class2/coul/cut 0.05585696 1.948383946
pair_coeff 5 9 lj/class2/coul/cut 0.240000000 3.47702459
pair_coeff 5 10 lj/class2/coul/cut 0.05585696 1.937823521
pair_coeff 5 11 lj/class2/coul/cut 0.113841996 3.703268826
pair_coeff 5 12 lj/class2/coul/cut 0.119799833 3.308171701
pair_coeff 5 13 lj/class2/coul/cut 0.129614814 3.827699048
pair_coeff 5 14 lj/class2/coul/cut 0.240000000 3.38481905
pair_coeff 5 15 lj/class2/coul/cut 0.240000000 3.38481905
pair_coeff 5 16 lj/class2/coul/cut 0.113841996 2.411223756

pair_coeff 6 7 lj/class2/coul/cut 0.120074977 3.637719066
pair_coeff 6 8 lj/class2/coul/cut 0.058915193 1.913896549
pair_coeff 6 9 lj/class2/coul/cut 0.253140277 3.415479469
pair_coeff 6 10 lj/class2/coul/cut 0.058915193 1.90352305
pair_coeff 6 11 lj/class2/coul/cut 0.120074977 3.637719066
pair_coeff 6 12 lj/class2/coul/cut 0.126359012 3.249615362
pair_coeff 6 13 lj/class2/coul/cut 0.136711375 3.759946808
pair_coeff 6 14 lj/class2/coul/cut 0.253140277 3.324906014
pair_coeff 6 15 lj/class2/coul/cut 0.253140277 3.324906014
pair_coeff 6 16 lj/class2/coul/cut 0.240000000 3.350000000

pair_coeff 7 8 lj/class2/coul/cut 0.026495283 2.10976302
pair_coeff 7 9 lj/class2/coul/cut 0.113841996 3.7650166
pair_coeff 7 10 lj/class2/coul/cut 0.026495283 2.098327906
pair_coeff 7 11 lj/class2/coul/cut 0.054000000 4.010000000
pair_coeff 7 12 lj/class2/coul/cut 0.05682605 3.582178108
pair_coeff 7 13 lj/class2/coul/cut 0.061481705 4.144736421
pair_coeff 7 14 lj/class2/coul/cut 0.113841996 3.665173939
pair_coeff 7 15 lj/class2/coul/cut 0.113841996 3.665173939
pair_coeff 7 16 lj/class2/coul/cut 0.240000000 3.350000000

pair_coeff 8 9 lj/class2/coul/cut 0.05585696 1.980871021
pair_coeff 8 10 lj/class2/coul/cut 0.013 1.103983696
pair_coeff 8 11 lj/class2/coul/cut 0.026495283 2.10976302
pair_coeff 8 12 lj/class2/coul/cut 0.027881894 1.884675038
pair_coeff 8 13 lj/class2/coul/cut 0.030166206 2.180651279
pair_coeff 8 14 lj/class2/coul/cut 0.05585696 1.928341256
pair_coeff 8 15 lj/class2/coul/cut 0.05585696 1.928341256
pair_coeff 8 16 lj/class2/coul/cut 0.240000000 3.350000000

```